# Flow-Induced Segregation and Dynamics of Red Blood Cells in Sickle Cell Disease

By

**Xiao Zhang**

A dissertation submitted in partial fulfillment of the

requirements for the degree of

Doctor of Philosophy

(Chemical Engineering)

at the

**UNIVERSITY OF WISCONSIN – MADISON**

2020

Date of final oral examination: February 19, 2020

The dissertation is approved by the following members of the Final Oral Committee:

Michael D. Graham, Professor, Chemical Engineering

Daniel J. Klingenberg, Professor, Chemical Engineering

Reid C. Van Lehn, Assistant Professor, Chemical Engineering

Naomi C. Chesler, Professor, Biomedical Engineering

© Copyright by Xiao Zhang 2020

All Rights Reserved

*In loving memory of my grandfather.*

# Acknowledgments

I would like to first thank Prof. Michael D. Graham for his guidance in my research – I had not even scratched the surface of the field of fluid mechanics before grad school, and without him I would never had tasted the "flavor of blood". I will also remember his kind support beyond my research through the years, especially in my difficult times. He is the best advisor and mentor I could ask for.

I would also like to express my sincere gratitude to the rest of my thesis committee: Prof. Klingenberg, who also served on my prelim and 4th-year talk committees; Prof. Van Lehn, who helped a lot with scheduling my defense; and Prof. Chesler, who taught one of my favorite courses in grad school and skipped her group meeting for my defense. Their insightful comments on my research are highly appreciated.

My research on sickle cell disease was performed in collaboration with Wilbur A. Lam. I have benefited from the helpful discussions with him and his colleagues Christina Caruso and Yumiko Sakurai, who provided enlightening insight into my work from experimental perspectives.

I have also learned a lot from a number of professors at UW-Madison, including Prof. Qin Li, Prof. Christopher Rutland, and Prof. Leslie Smith. The knowledge I acquired from their classes has benefited my research, and will definitely be applied

to solving engineering problems in my future career.

I thank Rafael Henríquez Rivera, Kushal Sinha, and Sarit Dutta, among other former members of the Graham group, for their great help at the beginning of my research. I will miss the stress-relieving chats with Ashwin Shekar, Eric Yu, RJ Hommel, and Zehua Wei, as well as the great amount of joy they brought me. I have also enjoyed working with Alec Linot, Kevin Zeng, Carlos Perez De Jesus, Oliver Köhn, Daniel Floryan, Hayden Boline, and Xiaopo Cheng.

The staff of the Department of Chemical and Biological Engineering have been extremely obliging to me. Special thanks to Susann Eva S. Ely, Kate Fanis, Rosalind Mckennon, Michael Morris, Theresa Neisius, and Russ Poyner, for all the warm-hearted help and joyful conversations.

Being abroad alone for more than five years has not been easy. Fortunately, I have made many amazing friends in and out of the department who have been there through my ups and downs. I will miss the two-hour badminton games every Saturday afternoon and a lot more beyond with Songyang Cheng, Jiayue He, Kefeng Huang, Yingzhou Liu, Yuying Shi, Lifeng Zhang, Zhongrui Zhang, and Ante Zhu. I thank Yifei Liu for hosting the Chinese Spring Festival party every year and making me feel at home. I wish all the best for Parvathi Madathil Kooloth, who has been bearing with my complaints every week and witnessed my changes over the years. I will always be grateful to Yaning Wang for everything she did for me towards the end of my grad life. Also, it has been a big blessing to be friends with Kaiwen Ma and Can Li, who have given me so much support and care in either Madison or Pittsburgh. I have had wonderful time with Yue Zhang and Xu'er Shi, from undergrad to grad school, and from China to the US. I wish I knew Jing Wang earlier so we could have

had more Karaoke fun together. I owe thanks to many other friends, including Hui Geng, Shujin Jiang, Mike Jindra, Mingyuan Tian, Wenzhao Wu, Yaqing Wu, and Yuxin Zhang.

Big thanks to Elliot Parens and his entire family – before coming to the US I could never imagine I would have an American family here. Thank you all for always being there, sending generous love and sharing my moments and feelings, big and small, regardless of any differences between us.

I can never repay my teachers and professors from middle school to undergrad, every one of them. I will forever be grateful to them, for not only helping me establish a solid foundation in a variety of subjects, from science and engineering to Chinese and English, which have benefited every stage of my academic experiences, but also teaching me to dream big while taking firm steps.

Finally, to my parents and family: 我最挚爱的爸爸妈妈，能够做你们的儿子是我最大的幸福。在这个特殊的时刻，我想你们一定和儿子一样，感慨万千。近二十二年求学之路，感恩你们对我的全部叮嘱与教诲，呵护与疼爱。我想说，这不仅是我个人的漫长旅程，于你们而言，也是一场鏖战。一路走来，荣耀与失意交杂，喜悦与纠结相伴，曾怀有海阔凭鱼跃天高任鸟飞的年少轻狂，也体味过心力交瘁几近放弃时的黯然神伤。幸而有你们随时给予我的鼓励与开解，穿越时空界限，让我们虽无法时常触碰彼此，心却愈发贴近。我亲爱的家人们，感激你们虽远隔重洋却从未迟到的挂念，感激你们对我父母的照顾与陪伴，让我得以安心在外求学。我深知，这一份外人眼中所谓的优异与光鲜，何尝不是借由了整个家族的成全。你们是我在这个世界上的全部牵挂与寄托，若非因为你们，我的一切努力将失去意义。纸短情长，伏惟珍重，亟盼重逢。

# Abstract

Blood is a classic archetype of multicomponent suspensions. During blood flow, red blood cells (RBCs) tend to migrate away from the vessel walls, forming a cell-free layer next to the walls, while white blood cells and platelets tend to reside in the near-wall region, a phenomenon known as margination. This segregation behavior in blood flow, characterized by the non-uniform cross-stream distribution of different cellular components, substantially arises from their shape, size, and rigidity contrasts.

Blood flow in sickle cell disease (SCD), however, can substantially differ from the normal due to alterations in the physical properties of sickle RBCs. Chronic complications, such as inflammation of endothelial cells that line the blood vessels, are associated with SCD, for reasons that are unclear. Using direct simulations, we investigate a number of binary suspensions containing primarily flexible healthy RBCs and a small fraction of stiff cells with different rest shapes in confined pressure-driven flow. We predict that sickle cells, modeled as stiff curved prolate capsules, are largely drained from the bulk flow and strongly marginate towards the walls, due to their increased rigidity and reduced size compared to healthy RBCs. Furthermore, we quantify the hydrodynamic effects of different suspensions on the walls, and show that in contrast to the case with purely healthy RBCs, large local wall shear stress peaks

are induced in the cases of binary suspensions due to the proximity of the marginated stiff cells to the walls. In addition, we also perform systematic investigations on the orbital dynamics of a single deformable straight and curved prolate capsule in unbounded simple shear flow, and determine the effects of a number of parameters, in terms of membrane mechanics of the capsule and flow conditions, on the dynamics.

Overall, our work represents a pioneering effort towards understanding the dynamics of flowing suspensions of cells in complex scenarios such as SCD. As endothelial cells are known to mechanotransduce physical forces such as aberrations in shear stress and convert them to physiological processes such as activation of inflammatory signals, our results may aid in understanding mechanisms for endothelial dysfunction in SCD from a purely physical perspective.

# Contents

**Acknowledgements** **ii**

**Abstract** **v**

**List of Figures** **xi**

**1 Summary** **1**

**2 Background** **11**

2.1 Blood as a flowing multicomponent suspension . . . . . 12

2.1.1 Major components and physiological functions . . . . . 12

2.1.2 Non-uniform distribution of blood cells and segregation phenomena during flow . . . . . 14

2.1.3 Understanding flow-induced segregation in confined multicomponent suspensions: state of the art . . . . . 17

2.2 Sickle cell disease and complications . . . . . 21

2.2.1 Physical properties of sickle cells: pathological morphologies and biomechanics . . . . . 22

2.2.2 Vasculopathy associated with sickle cell disease: insufficient understanding of pathophysiology . . . . . 24
2.3 Red blood cells and other deformable capsules . . . . . 28
2.3.1 Dynamics of red blood cells in shear flow . . . . . 28
2.3.2 Dynamics of other deformable capsules in shear flow . . . . . 31

**3 Model and methods for direct simulations 36**
3.1 Problem formulation . . . . . 36
3.2 Model and discretization for capsule membrane . . . . . 38
3.3 Flow field and fluid motion . . . . . 42

**4 Dynamics of single sickle cells as deformable curved prolate capsules in shear flow 46**
4.1 Introduction . . . . . 46
4.2 Model formulation . . . . . 53
4.2.1 Model and discretization . . . . . 53
4.2.2 Fluid motion . . . . . 57
4.2.3 Model validation . . . . . 57
4.3 Results and discussion . . . . . 59
4.3.1 Dynamics of deformable straight prolate capsules . . . . . 59
4.3.2 Dynamics of deformable curved prolate capsules . . . . . 63
4.4 Conclusion . . . . . 71

**5 Flow-induced segregation and dynamics of red blood cells in sickle cell disease 74**
5.1 Introduction . . . . . 74

5.2 Model formulation . . . . . 84
5.2.1 Model and discretization . . . . . 84
5.2.2 Fluid motion . . . . . 89
5.3 Results and discussion . . . . . 91
5.3.1 Cross-stream distribution and dynamics of cells in different suspensions . . . . . 92
5.3.2 Effect of marginated cells on the walls in binary suspensions . 104
5.3.3 Mechanism for flow-induced segregation and margination . . . 111
5.3.4 Implications on SCD vasculopathy . . . . . 118
5.4 Conclusion . . . . . 119

**6 Dynamics of deformable prolate capsules in shear flow: multiplicity of stable orbits 124**

6.1 Introduction . . . . . 124
6.2 Model formulation . . . . . 129
6.2.1 Model and discretization . . . . . 129
6.2.2 Fluid motion . . . . . 131
6.2.3 Particle stress in a dilute suspension of capsules . . . . . 132
6.3 Results and discussion . . . . . 134
6.3.1 Dynamics of prolate capsules with small bending stiffness . . . 134
6.3.2 Dynamics of prolate capsules with large bending stiffness . . . 142
6.4 Conclusion . . . . . 154

**7 Conclusions 156**

**8 Future directions: extending the present study on blood flow in sickle cell disease** **161**

8.1 Effects of heterogeneity in cell properties and flow parameters . . . . 161

8.1.1 Direct simulation . . . . . 162

8.1.2 Mechanistic theory . . . . . 163

8.2 Effects of vessel geometry . . . . . 166

8.3 Novel biophysical therapeutic strategies . . . . . 169

**A Parallel computing using message passing interface** **171**

A.0.1 High performance computing resources . . . . . 172

A.0.2 Code performance and scaling . . . . . 174

**Bibliography** **178**

# List of Figures

1.1 Schematic of our hypothesis of vasculopathy in SCD. Yellow indicates endothelial dysfunction. . . . . 5

2.1 (a) Cell-free layer formation [Ng *et al.*, 2016] and (b) margination of WBCs (transparent circles next to the walls) [Shevkoplyas *et al.*, 2005] in microfluidic devices. . . . . 13

2.2 Healthy and sickle RBCs under a microscope. . . . . 22

2.3 Microfluidic fabrication of prolate-shaped microcapsules containing a calcium ion solution [Schneeweiss and Rehage, 2005]. . . . . 32

2.4 Polyelectrolyte capsules (PECs) with independently controlled size and shape by combining particle stretching with soft template layer-by-layer (LBL) deposition [Zan *et al.*, 2015]. . . . . 33

3.1 Schematic of the simulation domain for flowing suspensions of deformable capsules subjected to a unidirectional pressure-driven flow in a planar slit bounded by two parallel rigid walls. . . . . 38

4.1 Schematic of the initial orientation of a curved prolate capsule in unbounded simple shear flow. . . . . 54

4.2 Evolution of inclination angle $\phi$ for a stiff prolate spheroid (Ca = 0.06) with (a) $r_p = 2.0$ and (b) $r_p = 4.8$, respectively. Solid blue lines are predictions by Jeffery's theory and red dashed lines are simulation results. 58

4.3 Trajectories on the unit sphere of (a) **p** and (b) **n** for a prolate spheroid ($r_p = 4.8$, Ca = 0.12) with initial orientation $\alpha = 0$ (up to $\dot{\gamma}t = 2000$). 59

4.4 Trajectories on the unit sphere of **p** ((a) and (b) ($y$-$z$ view)) and **n** ((c) and (d) ($x$-$z$ view)) for a prolate spheroid ($r_p = 4.8$, Ca = 0.12) with initial orientation $\alpha = \pi/36$. . . . . 60

4.5 The evolution of the $p_z$ and $n_z$ for a prolate spheroid ($r_p = 4.8$, Ca = 0.12) with initial orientation $\alpha = \pi/36$. . . . . 61

4.6 Trajectories of **p** (a) and **n** (b) for a curved prolate capsule with initial orientation $[\alpha, \beta] = [0,0]$ at the early stage of simulation ($0 < \dot{\gamma}t < 500$). 63

4.7 Early-stage trajectories on the unit sphere of the **p** (blue) and **n** (red) vectors of a curved prolate capsule with initial orientation $[\alpha, \beta] = [0,\pi/6]$ ($0 < \dot{\gamma}t < 500$) (a,d), $[0,\pi/2]$ ($0 < \dot{\gamma}t < 100$) (b,e), and $[\pi/6,\pi/3]$ ($0 < \dot{\gamma}t < 400$) (c,f), respectively. . . . . 65

4.8 Time sequence images (front view) of the early-stage (a) and long-time (b) motions of a curved prolate capsule with initial orientation $[\alpha, \beta] = [0,\pi/6]$. The dashed arrow in each image represents the **p** vector at the corresponding time spot. . . . . 65

4.9 Long-time trajectories on the unit sphere of the **p** (blue) and **n** (red) vectors of a curved prolate capsule with initial orientation $[\alpha, \beta] = [0,\pi/6]$ (a,d), $[0,\pi/2]$ (b,e), and $[\pi/6,\pi/3]$ (c,f), respectively. . . . . 66

4.10 Evolution of $y$- and $z$-components $y_{cm}$ and $z_{cm}$ of the center-of-mass position of curved prolate capsules with initial orientations $[\alpha, \beta] =$ [0,$\pi$/6] (a), [0,$\pi$/2] (b), and [$\pi$/6,$\pi$/3] (c). . . . . 68

4.11 The long-time trajectory (blue curve) of a curved prolate capsule in terms of $\phi$ and $\theta$ and the average trajectory (black circles). The red curve represents the fit of the average trajectory using Eq. 4.5. The black dashed line corresponds to $\phi = \pi$. $\Delta\theta^+$ and $\Delta\theta^-$ denote the maximum positive and negative deviations, respectively, of the instantaneous trajectory from the mean when $\phi = \pi$. (a) Ca = 0.12, $K =$ 0.36, $\lambda = 1$; (b) Ca = 0.06, $K = 0.39$, $\lambda = 5$. . . . . 69

4.12 The dependencies of (a) the effective orbit constant $C_{\text{eff}}$ of the long-time orbit and (b) the effective aspect ratio $\ell_{\text{eff}}$ on the deformability Ca and the degree of curvature $K$ of the curved prolate capsules. . . . 70

5.1 Rest shapes of a biconcave discoidal capsule (top) as a model for healthy RBCs, a straight prolate capsule (bottom left), and a curved prolate capsule (bottom right) as a model for typical sickle cells. . . . 85

5.2 (a) Wall-normal number density profile $\hat{n}$ for healthy RBCs assuming different spontaneous shapes ($c_0$) in a homogeneous suspension at steady state. (b) Hematocrit profile for the healthy RBC suspension. The two positions at $y/a = 0$ and $y/a = 5$ correspond to the wall and centerplane of the channel, respectively. . . . . 93

5.3 Simulation snapshots for a homogeneous suspension at steady state of flexible biconcave discoidal capsules (healthy RBCs) with Ca = 1.6 assuming either a biconcave discoidal (a) or an oblate spheroidal (b) spontaneous shape. . . . . 94

5.4 Time evolution of the parameter $s = \left\langle (y_{cm} - H)^2 \right\rangle^{1/2} / a$ for flexible (red) and stiff (blue) RBCs in a binary suspension. . . . . 95

5.5 Wall-normal number density profiles $\hat{n}$ for flexible (solid red) and stiff (dotted blue) RBCs in a binary suspension at steady state. . . . . 96

5.6 Simulation snapshots ((a) side view, (b) front view) for a binary suspension of flexible (red) and stiff (blue) RBCs at steady state. . . . . 97

5.7 Time evolution of $s$ for healthy RBCs in suspension with sickle cells (solid red) and straight prolate capsules (dotted red), and for sickle cells (solid blue) and straight prolate capsules (dotted blue) in suspension with healthy RBCs, respectively. . . . . 98

5.8 Wall-normal number density profiles $\hat{n}$ for (a) healthy RBCs in suspension with sickle cells (solid red) and straight prolate capsules (dotted red), and (b) for sickle cells (solid blue) and straight prolate capsules (dotted blue) in suspension with healthy RBCs, respectively. . . . . 99

5.9 Simulation snapshots (left: side view; right: front view) for binary suspensions of healthy RBCs with sickle cells (a,b) and straight prolate capsules (c,d), respectively, at steady state. . . . . 100

5.10 Effect of the spatial period $L_x$ of the simulation domain on wall-normal number density profiles $\hat{n}$ for healthy RBCs (a) in suspension with sickle cells (b). . . . . 101

5.11 Simulation snapshots (a,b) for a steady-state binary suspension of healthy RBCs with sickle cells, as well as wall-normal number density profiles $\hat{n}$ (c,d) for both components, assuming a biconcave discoidal (a) and an oblate spheroidal (b) spontaneous shape ($c_0$) for healthy RBCs, respectively. . . . . 102

5.12 Magnitude of the $x$-$x$, $x$-$y$, $y$-$y$, and $z$-$z$ components of the tensor $\mathbf{S} = \langle \mathbf{pp} \rangle$ for sickle cells and straight prolate capsules inside the cell-free layer (labelled "CFL") and in the bulk of the suspension (labelled "bulk"), respectively. . . . . 103

5.13 Examples of the spatial distribution of the additional wall shear stress $\hat{\tau}_w$ on the bottom wall ($y = 0$) induced by a homogeneous suspension of healthy RBCs (a) and binary suspensions of healthy (flexible) RBCs with stiff RBCs (b), sickle cells (c), and straight prolate capsules (d), respectively, at steady state. . . . . 105

5.14 Time evolution of the additional wall shear stress $\hat{\tau}_w$ at a fixed wall position $(x, y, z) = (0.74a, 0, 1.67a)$ for the cases of a homogeneous suspension of healthy RBCs (a) and binary suspensions of healthy (flexible) RBCs with stiff RBCs (b), sickle cells (c), and straight prolate capsules (d), respectively, at steady state. . . . . 106

5.15 The spatially-averaged RMS $\langle (\hat{\tau}_w)_{\mathrm{RMS}} \rangle$ (a) and maximum $\langle (\hat{\tau}_w)_{\max} \rangle$ (b) of the additional wall shear stress for different suspensions at steady state. For each quantity, the error bars represent standard error. . . . 107

5.16 The ensemble-averaged magnitude $\langle(\hat{\tau}_w)_{pk}\rangle$ (a), duration $\langle\Delta t_{pk}\rangle$ (b), and frequency $\langle f_{pk}\rangle$ (c), respectively, of the wall shear stress peaks experienced by all wall positions for different suspensions at steady state, and the product $A_{pk}$ of these three quantities (d). The error bars in (a), (b), and (c) represent standard error for each quantity. . . 109

5.17 Schematic of a curved or straight prolate capsule with different initial orientations subjected to simple shear flow in a planar slit. The inset illustrates the initial orientation of a curved prolate capsule (same as FIG. 4.1). . . . . 113

5.18 Evolution of the wall-normal center-of-mass position $y_{cm}$ of a sickle RBC (Ca = 0.4) in comparison with a healthy RBC at varying Ca (a) and a straight prolate capsule with different initial orientations (b). . 114

5.19 Schematic of trajectories of capsules ('1' and '2') in a pair collision. The capsules are initially apart from each other with an offset $\delta_y$ in the $y$ direction, and experience cross-stream displacements, $\Delta^{12}$ and $\Delta^{21}$, respectively, after the collision. . . . . 115

5.20 Schematic of capsules in homogeneous (a) and heterogeneous (b,c) pair collisions with specified orientations. Healthy ('h') – healthy RBC; sickle ('s') – curved prolate capsule; prolate ('p') – straight prolate capsule. . . . . 116

5.21 Trajectories of healthy RBCs as well as curved (a) and straight (b) prolate capsules assuming specified orbits in homogeneous and heterogeneous pair collisions. . . . . 117

6.1 Schematic of the 3D orientation of a prolate capsule in unbounded simple shear flow. . . . . 130

6.2 Evolution of $\bar{\theta}$ of a prolate capsule (AR = 2.0) with $\hat{\kappa}_B = 0.02$ and $\lambda = 1$ at (a) Ca = 0.08, (b) Ca = 0.2, (c) Ca = 0.7, and (d) Ca = 1.5. Here the spontaneous shape of the capsule is assumed to be the same as its rest shape. . . . . 135

6.3 Bifurcation behavior for a prolate capsule (AR = 2.0) with $\hat{\kappa}_B = 0.02$ and varying $\lambda$. The black dashed lines at $\theta = 0°$ and $\theta = 90°$ represent the orbits for a capsule aligned with the $z$ axis and in the shear plane, respectively. . . . . 136

6.4 Time sequence images (side and front views) of a prolate capsule (AR = 2.0) with $\hat{\kappa}_B = 0.02$ and $\lambda = 1$ taking a rolling (a, Ca = 0.08), wobbling (b, Ca = 0.2), oscillating-swinging (c, Ca = 0.7), and swinging (d, Ca = 1.5) motion, respectively. The initial orientation of the capsule is $\alpha = 5°$. The markers indicate the positions of a membrane point initially on the equator of the capsule for (a), and a membrane point initially on the major axis of the capsule for (b), (c) and (d). . . . . 138

6.5 Evolution of $\bar{\theta}$ of a prolate capsule (AR = 2.0) with $\hat{\kappa}_B = 0.02$ and $\lambda = 1$ at (a) Ca = 0.08, (b) Ca = 0.2, (c) Ca = 0.8, and (d) Ca = 1.5. Here the spontaneous curvature is assumed to be zero ($c_0 = 0$ in Eq. 3.9) everywhere on the membrane surface. . . . . 140

6.6 Intrinsic viscosity (a) and dimensionless normal stress differences (b,c) predicted for a dilute suspension (with volume fraction $\Phi$) of identical prolate capsules (AR = 2.0) with $\hat{\kappa}_B = 0.02$ taking the same corresponding stable orbit at varying Ca. . . . . 142

6.7 Evolution of $\bar{\theta}$ of a prolate capsule (AR = 2.0) with $\hat{\kappa}_B = 0.2$ and $\lambda = 1$ at varying Ca. At low Ca the capsule takes a stable tumbling motion at long times ((a) Ca = 0.08 and (b) Ca = 0.2)). A tumbling-to-swinging transition is observed at moderate Ca ((c) Ca = 0.8) before swinging becomes the attractor at high Ca ((d) Ca = 1.5). . . . . 143

6.8 Evolution of $\bar{\theta}$ of a prolate capsule (AR = 2.0) with $\hat{\kappa}_B = 0.2$ and $\lambda = 5$ at (a) Ca = 0.2, (b) Ca = 0.65, and (c) Ca = 2.0. . . . . 145

6.9 Evolution of $\bar{\theta}$ of a prolate capsule (AR = 2.0) with $\hat{\kappa}_B = 0.2$ and $\lambda = 5$ at (a) Ca = 0.65, (b) Ca = 0.8, (c) Ca = 0.9, and (d) Ca = 1.0. . . . 146

6.10 (a) Bifurcation behavior for a prolate capsule (AR = 2.0) with $\hat{\kappa}_B = 0.2$ and $\lambda = 5$. The values for $\bar{\theta}_{eq}$ corresponding to the attractors are represented by the solid blue lines with filled circles, and the estimated values for $\alpha_c$ by the dashed blue line with filled circles (the error bars indicating the range for $\alpha_c$ at each Ca in the multiplicity regime). The unstable solutions at $\theta = 0°$ and $\theta = 90°$ are indicated by the dashed black lines with crosses. (b) Evolution of $\bar{\theta}$ for a capsule with $\alpha = 60°$ initially at Ca = 0.9. When a stable orbit is reached, the value of Ca is suddenly increased to 1.0, and the capsule evolves towards a new stable orbit. . . . . 147

6.11 Effects of capsule aspect ratio (a, $\lambda = 5$) and the viscosity ratio (b, AR = 3.0) on the bifurcation behavior of the attractors for a prolate capsule with $\hat{\kappa}_B = 0.2$. Again, the black dashed lines at $\theta = 0°$ and $\theta = 90°$ correspond to the orbits for a capsule aligned with the $z$ axis and in the shear plane, respectively. (c) Phase diagram of stable orbital motions for a prolate capsule (AR = 3.0) with $\hat{\kappa}_B = 0.2$ over a range of Ca and $\lambda$. The multiplicity regime is shaded in blue, and only the motion modes for the attractors on the upper branch are shown here (the attractors on the lower branch always correspond to rolling and thus are not shown here). T denotes tumbling, P precessing, and R rolling. . . . . 148

6.12 Time sequence images (side and front views) of a prolate capsule (AR = 3.0) with $\hat{\kappa}_B = 0.2$ and $\lambda = 6.0$ taking a tumbling (a, Ca = 0.6), precessing (b, Ca = 1.4), and rolling (c, Ca = 2.0) motion, respectively. The initial orientation of the capsule is $\alpha = 75°$. The markers indicate the positions of a membrane point initially on the major axis of the capsule for (a) and (b), and a membrane point initially on the equator of the capsule for (c). . . . . 150

6.13 Intrinsic viscosity (a) and dimensionless normal stress differences (b,c) predicted for a dilute suspension (with volume fraction $\Phi$) of identical prolate capsules (AR = 3.0) with $\hat{\kappa}_B = 0.2$ taking the same corresponding stable orbit(s) at varying Ca for $\lambda = 3.0$ and $\lambda = 5.0$. In each case, the squares represent the pure tumbling orbits at lower Ca, and the circles represent the pure rolling orbits at higher Ca; the downward and upward triangles represent the attractors on the upper branch (either tumbling or precessing) and the stable rolling orbits on the lower branch of the multiplicity regime (bounded by vertical dotted lines), respectively. . . . . 152

8.1 Steady-state profiles of normalized volume fractions for components in ternary (solid lines) and binary (dash-dot lines) suspensions in planar pressure-driven flow under confinement ($C = 5$). Here $\mathrm{Ca}_p = 0.5$, $\mathrm{Ca}_s = 0.08$, and $\mathrm{Ca}_t = 0.01$; $\bar{\phi}_p = 0.20$, $\bar{\phi}_s = 0.02$, and $\bar{\phi}_t = 1.0 \times 10^{-3}$; $\kappa_1 = 0.16$, $\kappa_{\alpha pc} = 0.02$, and $\kappa_{\alpha pd} = 0.07$. . . . . 164

8.2 Schematics of blood flow in a bifurcated domain (a) and a tortuous channel (b: oblique view; c: top view), respectively. . . . . 168

A.1 Scaling for benchmark simulations of a single prolate spheroidal capsule in an unbounded simple shear flow. The scaling data were obtained using Comet. It shows that the computational cost decreases approximately linearly with an increasing number of cores. . . . . 174

A.2 Scaling for benchmark simulations of a suspension of 100 capsules in a bounded domain ($\alpha = 4$). The scaling data were obtained using Comet. 176

A.3 Computational cost per step as a function of $\alpha$ for benchmark simulations of a suspension of 100 capsules in a bounded domain. All data points were obtained using 54 cores on Comet. As $\alpha$ increases, the cost of the local part decreases monotonically, while that of the global part increases monotonically. The total cost is minimal at $\alpha = 4$. . . . . 177

# Chapter 1

# Summary

Flowing suspensions of particles in confined domains are of broad interest in a large variety of fields. Advances in lab-on-a-chip microfluidic technology have enabled practical applications involving multicomponent suspensions, especially in bioengineering and pharmaceutics. Typical examples, such as rapid separation of blood cells [Shevkoplyas *et al.*, 2005, Hou *et al.*, 2010] and enhanced vascular-targeted drug delivery [Geng *et al.*, 2007, Charoenphol *et al.*, 2010, Namdee *et al.*, 2013, Thompson *et al.*, 2013, Kelley *et al.*, 2016], involve blood flow in microfluidic channels as a model for human microvasculature. Blood, a classic archetype of flowing multicomponent suspensions, is composed primarily of erythrocytes, or red blood cells (RBCs), with trace amounts of two other cellular species, namely leukocytes, or white blood cells (WBCs), and platelets. These three species of blood cells exhibit distinct contrasts in physical properties [Otto *et al.*, 2015]: normally, RBCs are fluid-filled biconcave discoids, WBCs are approximately spherical and slightly larger than RBCs, while platelets are discoids and the smallest in size; healthy RBCs are highly flexible, while

both WBCs and platelets are much stiffer. A significant feature of normal blood flow in the microcirculation, i.e., the network of microvessels ($5 - 200$ $\mu$m in diameter [Pappano and Wier, 2013]) consisting of arterioles, capillaries, and venules, is that all species of blood cells display a non-uniform distribution across the vessels. RBCs tend to migrate away from the vessel wall and form a RBC-depleted region termed cell-free layer next to the wall [Sutera and Skalak, 1993, Kumar and Graham, 2012b, Namgung and Kim, 2014, Kumar and Graham, 2015, Namgung *et al.*, 2017]. In contrast, WBCs and platelets are found to reside close to the vessel walls, a phenomenon known as margination [Tangelder *et al.*, 1985, Firrell and Lipowsky, 1989, Shevkoplyas *et al.*, 2005, Freund, 2007, Kumar and Graham, 2012b, 2015], which is of physiological significance as the prerequisite for inflammatory response and hemostasis. Under pathological conditions, however, diseased RBCs, such as those in patients suffering from sickle cell disease (SCD), often display substantial alterations in physical properties compared to healthy RBCs. These cellular-level alterations may lead to significant aberrance in the behavior of blood flow, and further cause complications such as vasculopathy. The insufficient understanding so far of both the dynamics of blood flow in SCD and the mechanism for complications associated with SCD has formed the principal motivation of the present work.

The segregation behavior in blood flow, i.e., the discrepancy in cross-stream distribution propensity of different species of blood cells, substantially arises from their shape, size, and rigidity differences. Numerous computational efforts have been made in the past decade using direct simulations to disentangle the individual effects of various physical properties of the components on the segregation behavior in confined flowing multicomponent suspensions. For example, Kumar *et al.* [2011, 2014]

numerically investigated the isolated role of rigidity difference in a binary suspension of deformable capsules subjected to either simple shear flow or pressure-driven flow in a planar slit. Here the rigidity (or deformability) of a capsule is characterized by the dimensionless capillary number, which represents the ratio of viscous stresses to elastic restoring stresses on the particle. They found that stiff capsules display a substantial margination when they are the dilute, while flexible capsules tend to enrich around the centerline of the channel, a behavior termed demargination. The effect of size contrast was also revealed [Kumar *et al.*, 2014]: in a mixture of large and small capsules with equal capillary number, the small capsules marginate while the large particles demarginate, in their respective dilute suspensions. The findings in experimental and computational investigations have also inspired the development of a number of phenomenological theories [Kumar and Graham, 2012c, Zurita-Gotor *et al.*, 2012, Kumar *et al.*, 2014, Narsimhan *et al.*, 2013, Henríquez Rivera *et al.*, 2015, Henríquez Rivera *et al.*, 2016, Qi and Shaqfeh, 2017] aiming to provide mechanistic insight into understanding the segregation behavior. Most of the theories have been grounded on taking into account two key sources of cross-stream particle fluxes in flowing suspensions under confinement: wall-induced migration flux away from the wall, which is ubiquitous for any deformable particles in a bounded flow [Smart and Leighton, 1991], and shear-induced diffusive flux due to hydrodynamic pair collisions between particles. A recent work was by Henríquez Rivera *et al.* [2016], who developed a simplified drift-diffusion (SDD) theory that describes the dynamics of flowing multicomponent suspensions. The key contribution of this work is that for binary suspensions in either simple shear flow or pressure-driven flow, several regimes of segregation are predicted based on a so-called "margination parameter" $M$, a deter-

minant of the segregation propensity that characterizes the relative significance of the wall-induced migration and the collisional fluxes. Moreover, a sharp "drainage transition", indicated by complete depletion of one component from the bulk flow towards the walls, is predicted when $M$ is below some critical value.

The substantial progress by the extensive numerical and theoretical studies has laid the groundwork for understanding the dynamics in more complex systems. In SCD, the intracellular polymerization of sickle hemoglobin (HbS) leads to formation of long fibers, which push on the cell membrane leading stereotypically to a sickle-like shape for the irreversibly sickled cells (ISCs) [Bertles and Milner, 1968]. Besides, sickle cells are typically much smaller in volume compared to healthy RBCs due to dehydration [Zucker and Cameron, 1976, Glader *et al.*, 1978], with an increase in membrane stiffness [Messer and Harris, 1970, Nash *et al.*, 1984, Evans and Mohandas, 1987, Bunn, 1997, Byun *et al.*, 2012]. Prior studies in the past several decades have demonstrated that the pathophysiology of SCD is much more complex than originally thought. In particular, SCD is now known to be a vasculopathic disease in which the endothelial cells that line the blood vessels are dysfunctional and inflamed. In many ways, SCD vasculopathy bears some resemblance to cardiovascular disease, and relatedly, stroke remains a major cause of mortality in SCD. Despite such similarities, the underlying mechanism of chronic SCD vasculopathy remains unknown. Cardiovascular bioengineering research has demonstrated that endothelial cells mechanotransduce biophysical cues, such as the shear forces of the hemodynamic microenvironment, into cellular biological signals [Harrison *et al.*, 2006, Chien, 2007, Abe and Berk, 2014]. Furthermore, pathological alterations of those forces lead to activation of pro-inflammatory signals within endothelial cells and subsequent devel-

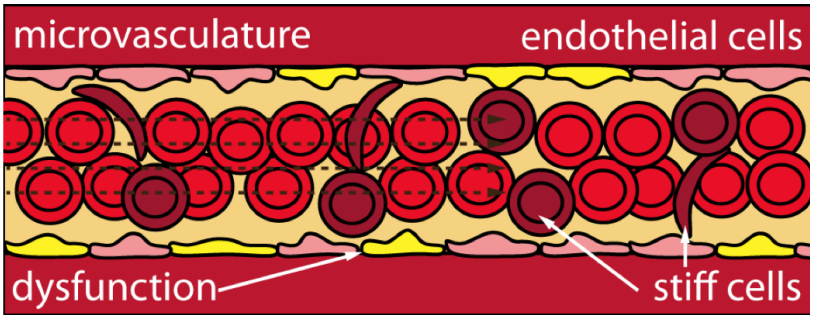



**Figure 1.1:** Schematic of our hypothesis of vasculopathy in SCD. Yellow indicates endothelial dysfunction.

opment of atherosclerotic plaques *in situ* that are prone to myocardial infarction and stroke [Abe and Berk, 2014]. In light of all these findings, how the abnormality in physical properties of sickle cells alters the dynamics of blood flow, and ultimately, how this alteration may be linked to the underlying mechanism for the complications in SCD such as endothelial dysfunction, are questions to address.

Inspired by the advances to date in understanding the segregation behavior in flowing suspensions such as blood flow, we propose an innovative paradigm-shifting biophysical hypothesis for the pathophysiology of SCD vasculopathy (FIG. 1.1). We hypothesize that the aberrant and repeated physical interactions between sickle cells and endothelium alone may be sufficient to cause endothelial dysfunction: sickle cells may first pathologically marginate towards the vessel walls due to dramatic differences in cell properties with healthy RBCs, and then exert repeated hydrodynamic effects on the endothelial cells by inducing fluctuations in local wall shear stress. This may explain the chronic nature of vasculopathy in SCD. The present study aims to take a first step towards understanding the dynamics of microvascular blood flow in SCD, and further, to validate our hypothesis regarding the pathophysiology of SCD vasculopathy. Specifically, using large-scale direct simulations, we investigate a number of binary suspensions containing primarily healthy RBCs, modeled as flexible

biconcave discoidal capsules, with a small fraction of stiff cells (capsules) with different rest shapes subjected to pressure-driven flow confined in a planar slit at zero Reynolds number. WBCs and platelets are not included in our suspension systems due to their extremely small number fractions in blood flow. Our key observation is that in a binary suspension of healthy and sickle RBCs, sickle cells, which are modeled as stiff curved prolate capsules, display strong margination towards the walls due to their increased rigidity and reduced size compared to healthy RBCs. The effects of shape, size, and rigidity differences between the components on the behavior of different suspensions are revealed by comparison. We also characterize the orbital dynamics of single cells in each suspension. Furthermore, the hydrodynamic effects of the cell suspensions on the walls, particularly the fluctuations in wall shear stress induced by the marginated stiff cells in the vicinity of the walls are quantified to establish a connection with issues in SCD such as shear-induced endothelial inflammation. We show that the orbital dynamics of the near-wall stiff cells play a nontrivial role in determining the overall physical effects on the walls.

As described above, in our study we model the typical crescent-shaped sickle cells as stiff curved prolate capsules. Therefore, prior to the work on flowing suspension systems that represent microvascular blood flow in SCD, systematic numerical investigations are first performed on understanding the orbital dynamics of a single stiff curved prolate capsule, i.e., a single sickle cell, in unbounded simple shear flow. The mechanics of the capsule membrane are described using a model incorporating both shear and bending elasticities. The parameter regime is based on the range of experimentally determined values for blood flow in the microcirculation in SCD. We reveal complicated and interesting orbits for the dynamics of single sickle cells, which

are majorly attributable to the combined effects of membrane deformability and the curvature of the capsules.

All these studies represent a pioneering effort to gain an improved understanding of both the dynamics of flowing suspensions of cells and the motion of single cells in complex scenarios, particularly the blood flow in SCD which is the focus of the present study. More importantly, the results of these studies demonstrate how the mechanical properties and distorted cell shape of sickle cells lead to distinct trajectories that may, in turn, cause pathologic biophysical activation of other cells, and may provide insight into how these disparate aspects of SCD are ultimately linked. In general, these results are of essential significance from the medical point of view by shedding light on the mechanism for complications associated with SCD, such as endothelial inflammation, that are still poorly understood, from a purely physical (non-chemical) perspective.

The present work regarding the dynamics of flowing suspensions may be extended in a number of directions. For example, given that sickle cells in SCD patients usually vary considerably in cell morphology and membrane stiffness, future simulations should attempt to incorporate the heterogeneity in cell properties, which is not considered in the present work. Other parameters of the suspensions, such as the total volume fraction and the number fraction of each component in a binary system, can also be altered in extended studies to investigate the effects of these parameters on the suspension dynamics. Furthermore, it has been observed in experiments [Loiseau *et al.*, 2015] that the flow of a suspension of sickle cells around an acute corner of a triangular pillar or a bifurcation leads to an enhanced deposition and aggregation of cells. Therefore, complex geometries of the flow domain other than a planar slit should be considered in future simulations. Finally, future studies, especially ex-

periments, are needed to elucidate if the cross-stream distribution of RBCs in the microcirculation is adversely altered in SCD, and if so, how this process may contribute to SCD vasculopathy. Such work may directly lead to a new paradigm of biophysical therapeutic strategies by mitigating the potential margination effects of the aberrant sickle RBCs.

Red blood cells are fluid-filled microcapsules in nature. More broadly, microcapsules, small liquid droplets enclosed by a thin solid membrane, have been of increasing significance in the bioengineering, pharmaceutics, and food industries. Examples include cell encapsulation for tumor progression monitoring [Alessandri *et al.*, 2013], encapsulation of cosmetic active ingredients for topical application [Casanova and Santos, 2016], development of drug delivery systems [Masuda, 2011, Degen, 2014], and artificial food particles for aquatic filter feeders [Jones *et al.*, 1974]. Particularly, non-spherical microcapsules, because of a higher surface-to-volume ratio than their spherical counterparts, can be preferable to enhance the transfer of cargoes across the capsule membrane upon arrival at the target. An example is the fabrication of prolate capsules containing a calcium ion solution by Schneeweiss and Rehage [2005] using a microfluidic channel. All of the aforementioned situations involve capsule suspensions in a fluid environment, and the dynamics of these suspensions can be greatly affected by the behavior of single capsules. Therefore, it is essential to gain a comprehensive understanding of the single capsule dynamics in flow.

Non-spherical capsules, such as oblate spheroids [Ramanujan and Pozrikidis, 1998, Sui *et al.*, 2008, Kessler *et al.*, 2008, Bagchi and Kalluri, 2009, Le and Tan, 2010, Walter *et al.*, 2011, Yazdani *et al.*, 2011, Omori *et al.*, 2012, Cordasco and Bagchi, 2013, Wang *et al.*, 2013, Dupont *et al.*, 2016] and biconcave discoids, a model for red

blood cells (RBCs) [Goldsmith *et al.*, 1972, Fischer *et al.*, 1978, Abkarian *et al.*, 2007, Skotheim and Secomb, 2007, Dupire *et al.*, 2010, Fedosov *et al.*, 2010a, 2011, Peng *et al.*, 2011, Yazdani and Bagchi, 2011, Dupire *et al.*, 2012, Cordasco *et al.*, 2014, Peng *et al.*, 2014, Sinha and Graham, 2015], have been investigated extensively in both experimental and computational studies. These studies have explored a wide range of parameters for the capsule membrane mechanics and flow properties, and revealed rich and complex orbital dynamics for the capsules. In contrast, to the best of our knowledge, there only exist a limited number of works on the motion of prolate capsules in shear flow [Walter *et al.*, 2011, Dupont *et al.*, 2013, Cordasco and Bagchi, 2013, Wang *et al.*, 2013], most of which have focused on the special case where the fluids inside and outside the capsules have the same viscosity, and neglected bending resistance of the capsule membrane. In fact, in applications, the mechanical properties of the capsule membrane can vary greatly depending on the materials and fabrication techniques, and the suspending fluid or solution and the fluid enclosed inside the capsules will generally have different viscosities.

Aiming to fill the gap in literature and gain an improved understanding of the dynamics of single deformable prolate capsules in shear flow, we perform a systematic numerical investigation over a broad domain of parameter space, and examine the effects of membrane deformability, bending stiffness, initial orientation, aspect ratio of the capsule and the viscosity ratio between the inner and outer fluids on the orbital motion of the capsule. As the key findings, we reveal parameter regimes in which either a single or multiple stable orbits exist, and show in particular that the orbits for a capsule lying in the shear plane and aligned with the vorticity axis are not always stable as the capsule evolves towards the equilibrium configuration. Furthermore, by

computing the particle contribution to the stress, we illustrate how the multiplicity of stable orbits for a prolate capsule can be linked to the resulting multiplicity in the rheological properties for a suspension of such capsules in the dilute limit. These results will motivate pertinent experimental investigations to probe the phenomenon of multiplicity in both stable orbits for a single capsule and the rheology of a dilute suspension predicted in this work.

The rest of the dissertation is organized as follows. A background introduction is provided in Chapter 2 on normal blood flow and important phenomena, blood flow in SCD, and red blood cells among other deformable capsules, with a thorough and critical review of prior studies on these topics. In Chapter 3 we describe the models for single cells and suspension systems considered in this work, as well as the numerical methods and algorithms employed to compute the flow field and cell motion in our direct simulations. In Chapter 4, we present and discuss results on the dynamics of single stiff curved prolate capsules as a model for typical sickle cells in SCD. In Chapter 5, we probe the mechanism for vasculopathy, or endothelial inflammation, in SCD, and present detailed simulation results on the dynamics of different suspensions of cells representing normal and aberrant blood flows in the microcirculation, followed by a characterization of the hydrodynamic effects of the suspensions on the walls. In Chapter 6 we investigate the orbital dynamics of single deformable prolate capsules in shear flow over a broad domain of parameters, and reveal the effects of different parameters on the capsule dynamics. Predictions of the rheological properties for a dilute suspension of prolate capsules are also reported. Finally, concluding remarks are presented in Chapter 7, with a number of future works proposed in Chapter 8.

# Chapter 2

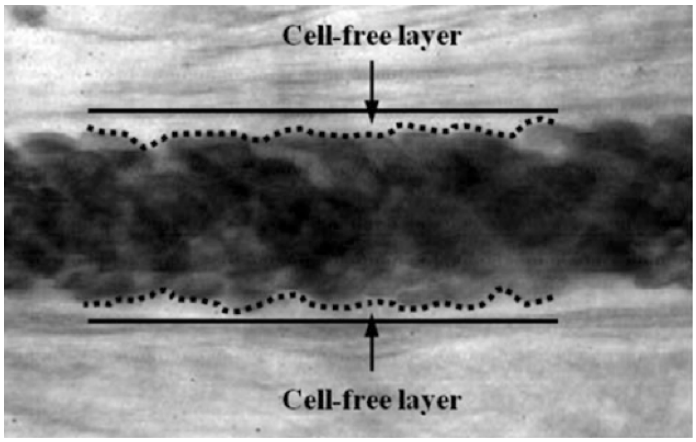
# Background

Blood is a complex biological fluid that performs a wide range of essential functions in the body. It is a typical example of multicomponent and multiphase suspensions. The dynamics of blood flow and the behavior of blood cells in the microcirculation, on which the present work is focused, are particularly complex, not only in the physiological sense due to the multifunctional nature of blood, but also in the microstructural and biomechanical sense because of various significant features and phenomena that are related to the physical properties of different cellular components in blood. A comprehensive knowledge of the dynamics of blood flow in the microcirculation as well as the principles underlying the phenomena that have long been observed in blood flow may not only provide insight into understanding the pathophysiology of blood disorders such as sickle cell disease and the associated complications, but also aid in the development of more effective diagnostic and therapeutic strategies.

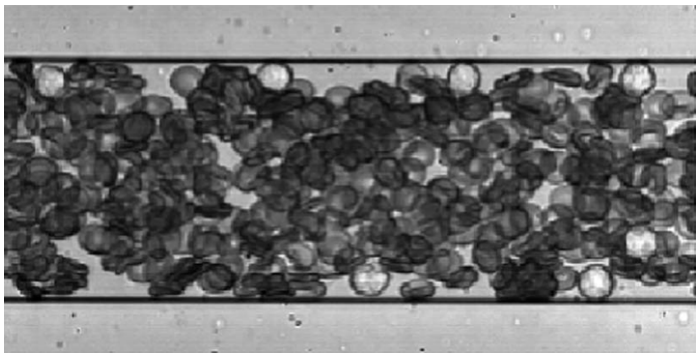
## 2.1 Blood as a flowing multicomponent suspension

### 2.1.1 Major components and physiological functions

Blood is a confined flowing suspension of various species of cells in an aqueous environment known as plasma. It is composed primarily of erythrocytes, or red blood cells (RBCs), with a hematocrit (i.e. volume fraction of RBCs) ranging from $0.1-0.3$ in the microcirculation to $0.4-0.5$ in large vessels such as arteries [Fung, 1984]. Two other major species of cells in blood, namely leukocytes, or white blood cells (WBCs), and platelets, are both considerably outnumbered by RBCs, by $\sim 500-1000:1$ and $12-32:1$, respectively [Dean, 2005]. In addition to the drastic difference in population density, these three cellular components exhibit distinct contrasts in physical properties including shape, size, and rigidity [Otto *et al.*, 2015]. Typically, RBCs are fluid-filled biconcave discoids with a radius of $\sim 3.8-4.0$ $\mu$m. This unique shape helps to increase the surface area-to-volume ratio for RBCs, which enables highly efficient material transport and diffusion across the cell membrane. Neutrophils, the majority of WBCs, are approximately spherical and slightly larger than RBCs ($10-12$ $\mu$m across) [Alberts *et al.*, 2007], while platelets are discoidal and the smallest in size ($2-3$ $\mu$m across). Mechanically, healthy RBCs are highly flexible, which allows them to squeeze through microvessels with dimensions even smaller than their size to deliver oxygen; both WBCs and platelets are much stiffer. Functionally, WBCs are significant as part of the immune system and actively involved in defending the body against infection and disease caused by foreign materials. Platelets are known for their essential roles in coagulation process, but also for their pathological significance in thrombosis and atherosclerosis [Nieswandt *et al.*, 2005]. All these cellular




**(a)**



**(b)**

**Figure 2.1:** (a) Cell-free layer formation [Ng *et al.*, 2016] and (b) margination of WBCs (transparent circles next to the walls) [Shevkoplyas *et al.*, 2005] in microfluidic devices.

components, among a great many other small molecules and proteins, are carried by plasma. Plasma, which constitutes about 55% of the total volume of blood, is mostly water so that it can be generally treated as an incompressible and Newtonian fluid with a viscosity of approximately 1.2 – 1.7 cP [Fung and Zweifach, 1971, Fung, 1984].

### 2.1.2 Non-uniform distribution of blood cells and segregation phenomena during flow

Blood is circulated throughout the body in blood vessels. In large vessels such as arteries and veins, blood can be approximately considered as a single-phase fluid. However, the dynamics of blood flow and the behavior of blood cells in the microcirculation, on which the present work is focused, are complex due to the multicomponent and multiphase nature. The microcirculation is a network of microvessels ($5 - 200$ $\mu$m in diameter [Pappano and Wier, 2013]) consisting of arterioles, capillaries, and venules. Blood flow in the microcirculation is highly laminar, with the Reynolds number (Re) much less than one based on the typical wall shear rate $\dot{\gamma}_w$ of $\sim O(10^2 - 10^3)$ s$^{-1}$ in the microvessels [Wootton and Ku, 1999, Lipowsky, 2013]. In blood flow, many phenomena have long been observed. An important phenomenon is the Fåhræus-Lindqvist effect [Fåhræus and Lindqvist, 1931, Pries and Secomb, 2005], which states that at shear rate $\gtrsim 100s^{-1}$, the apparent viscosity of blood in a tube determined in a capillary viscometer using Poiseuille's law decreases with decreasing diameter of the tube for tube diameters between 10 and 1000 $\mu$m. The origin of this effect can be related to another phenomenon called the Fåhræus effect [Barbee and Cokelet, 1971], an observation that the measured hematocrit of blood in a tube can be less than the hematocrit inferred from measurements of the blood discharged by flow out from a tube. The ratio of "tube hematocrit" to "discharge hematocrit" displays a similar tube size dependence as the apparent viscosity. The Fåhræus effect is an indication of the non-uniform distribution of RBCs across the channel; in particular, the concentration of RBCs is higher near the center of the channel where the velocity is high than near the walls where the velocity is low. This cross-stream variation

of RBC concentration in flow further leads to another classic observation in blood physiology termed plasma-skimming [Skalak *et al.*, 1989, Pries *et al.*, 1996], which is of significant relevance to blood flow in the highly-branched circulatory system: the daughter branches off a larger parent vessel have a lower hematocrit than the parent vessel. This phenomenon helps explain the relatively lower hematocrit in the microcirculation compared to that in larger vessels as noted in Section 2.1.1. Finally, related to plasma-skimming is the Zweifach-Fung effect [Svanes and Zweifach, 1968, Fung, 1973]: at an asymmetric bifurcation, the hematocrit in the daughter branch with higher flow rate is higher than in the one with lower flow rate.

All of the phenomena discussed above are consequences of a non-uniform distribution of RBCs across the vessels in blood flow, which can be qualitatively understood by considering two competing basic behaviors in confined flowing suspensions [Hudson, 2003]. On one hand, RBCs, and indeed all deformable particles [Leal, 1980, Smart and Leighton, 1991, Jendrejack *et al.*, 2004, Ma and Graham, 2005, Chen *et al.*, 2005, Doddi and Bagchi, 2008, Danker *et al.*, 2009, Graham, 2011] (capsule, drop, vesicle, flexible macromolecule) in a confined shear flow, tend to migrate away from the walls due to hydrodynamic interactions with the walls. On the other hand, neighboring particles in flowing suspensions collide with each other due to the shear effect of the flow, which drives post-collisional displacements of the particles, generating diffusive fluxes (shear-induced diffusion) as a result. The counterbalance between the effects of these two behaviors leads to the formation of a RBCs-depleted region near the vessel walls termed the "cell-free" layer (FIG. 2.1a) [Skalak *et al.*, 1989, Kim and Karrila, 2013]. A number of experimental, computational and theoretical studies [Bugliarello and Hayden, 1963, Kumar *et al.*, 2014, Narsimhan *et al.*, 2013, Kumar *et al.*, 2014,

Henríquez Rivera *et al.*, 2015, Henríquez Rivera *et al.*, 2016] have shown that the thickness of the cell-free layer decreases with increasing hematocrit.

WBCs and platelets also display non-uniform distributions in flow. In contrast to RBCs, these two cellular species are found to reside near the vessel walls in the RBCs-depleted region (i.e. cell-free layer), a phenomenon known as margination (FIG. 2.1b) [Tangelder *et al.*, 1985, Firrell and Lipowsky, 1989, Shevkoplyas *et al.*, 2005, Freund, 2007, Kumar and Graham, 2012b, 2015]. Margination is desirable as an essential prerequisite for the physiological functions of WBCs and platelets in inflammatory response and hemostasis. A large number of prior experiments [Aarts *et al.*, 1984, Goldsmith and Spain, 1984, Tangelder *et al.*, 1985, Eckstein *et al.*, 1988, Firrell and Lipowsky, 1989, Yeh and Eckstein, 1994, Pearson and Lipowsky, 2000, Abbitt and Nash, 2003, Jain and Munn, 2009, Fay *et al.*, 2016, Spann *et al.*, 2016], both in vivo and in vitro, and computational studies [Sun and Munn, 2006, Freund, 2007, AlMomani *et al.*, 2008, Crowl and Fogelson, 2011, Zhao and Shaqfeh, 2011, Zhao *et al.*, 2012, Fedosov *et al.*, 2012, Reasor *et al.*, 2013, Fedosov and Gompper, 2014, Vahidkhah *et al.*, 2014, Mehrabadi *et al.*, 2015] have attempted to characterize the effects of a variety of parameters, such as shear rate, channel width, hematocrit, and RBC aggregation, on the strength of margination of WBCs and platelets. Furthermore, margination-based cell separation has been realized using lab-on-a-chip devices. For example, motivated by WBC margination in the microcirculation, Shevkoplyas *et al.* [2005] achieved efficient separation of WBCs from whole blood using a simple network of microfluidic channels. Other examples include separation of stiffened malaria-infected RBCs from the healthy ones utilizing margination or lateral displacement of the stiff cells [Hou *et al.*, 2010, Guo *et al.*, 2016]. Recent experiments

by Fay *et al.* [2016] showed that glucocorticoid and catecholamine hormones, such as dexamethasone and epinephrine, significantly reduce the stiffness of WBCs, which, as a result, attenuates WBC margination and leads to a substantial increase in the clinical WBC count. In addition, engineering the margination process has been applied to enhance the efficacy of vascular-targeted drug delivery by optimizing the design of carrier systems for improving the diagnosis and treatment of diseases. Examples include [Geng *et al.*, 2007, Charoenphol *et al.*, 2010, Namdee *et al.*, 2013, Thompson *et al.*, 2013, Thompson and Eniola-Adefeso, 2015, Kelley *et al.*, 2016].

### 2.1.3 Understanding flow-induced segregation in confined multicomponent suspensions: state of the art

The segregation behavior in blood flow, i.e., the discrepancy in cross-stream distribution propensity of different species of blood cells, has also been observed in other multicomponent suspensions and granular systems such as macroscopic particles in air [Möbius *et al.*, 2001], polydisperse droplet suspensions [Makino and Sugihara-Seki, 2013], and foams [Mohammadigoushki and Feng, 2013]. In a more general context, for an arbitrary flowing multicomponent suspension, the segregation behavior may be largely contingent on a variety of physical factors including shape, size, and rigidity differences between the components. To clarify the individual roles of these determinants in segregation, a series of well-controlled computational studies have been performed in the past years, which represent efforts to fill the gap in prior works on multicomponent suspensions, such as whole blood, in which several physical parameters often differ simultaneously. Typical examples are the numerical investigations by Graham and co-workers [Kumar and Graham, 2011, Kumar *et al.*, 2014, Sinha and

Graham, 2016]. For example, the isolated role of rigidity difference was examined using direct simulations considering a binary suspension of flexible and stiff capsules with equal size subjected to either simple shear flow or pressure-driven flow in a planar slit [Kumar and Graham, 2011, Kumar *et al.*, 2014]. Here the rigidity (or deformability) of a capsule is characterized by the dimensionless capillary number (Ca), which represents the ratio of viscous stresses to elastic restoring stresses on the particle. The key observation is that when the stiff capsules are dilute in the suspension, they display a substantial margination; in contrast, flexible capsules tend to enrich around the centerline of the channel when they are dilute, a behavior termed demargination. The role of size contrast was revealed in a similar fashion [Kumar *et al.*, 2014]: in a mixture of large and small capsules with equal capillary number, the small capsules marginate while the large particles demarginate, in their respective dilute suspensions. Besides, shape-mediated segregation was also investigated for binary suspensions of spherical and ellipsoidal capsules in simple shear flow [Sinha and Graham, 2016]. In this work, all capules have the same capillary number, while the aspect ratio $\kappa$ of the ellipsoids is varied with either the equatorial radius or the volume of the capsules held constant; here $\kappa > 1$ and $\kappa < 1$ represent prolate and oblate spheroids, respectively. It is observed that when the ellipsoids have the same equatorial radius as the spheres, capsules with lower $\kappa$ marginate as the dilute component in a suspension containing primarily capsules with higher $\kappa$; when all capsules have the same volume, however, spherical capsules always marginate when they are dilute, while ellipsoidal (both oblate and prolate) capsules demarginate as the dilute component. Furthermore, all these controlled studies [Kumar and Graham, 2011, Kumar *et al.*, 2014, Sinha and Graham, 2016] showed that as the volume fraction

of the suspension increases, the near-wall peak in the number density distribution profile for the marginated component shifts towards the wall, with a decrease in the cell-free layer thickness that is also observed for RBCs and other deformable capsules in their homogeneous suspensions as noted in Section 2.1.2.

The extensive experimental and computational studies discussed above have not only disentangled the effects of various physical aspects on flow-induced segregation, but also inspired the development of a number of phenomenological theories aiming to provide mechanistic insight into the mechanism underlying the behavior of multicomponent suspensions such as blood flow. Most of the theories have been grounded on taking into account the two key sources of cross-stream particle fluxes described above (Section 2.1.2) in flowing suspensions under confinement: wall-induced migration flux away from the wall [Smart and Leighton, 1991], and shear-induced diffusive flux due to hydrodynamic interparticle collisions. An idealized kinetic master equation model was presented by Kumar and Graham [2012c] for a binary suspension of capsules with unequal rigidity, in which the steady-state solution is obtained using a Monte Carlo simulation technique. The mechanism for segregation in this system was shown to depend on the volume fraction of the suspension: at low volume fractions, heterogeneous pair collisions between capsules of different components drive the segregation by rigidity difference, while at higher volume fractions, wall-induced migration and heterogeneous pair collisions have comparable contributions. The authors further revealed [Kumar *et al.*, 2014] that in a binary suspension of capsules with size contrast, the segregation behavior is mainly caused by the greater wall-induced migration velocity of the larger capsules. Similar methods have been employed to understand the dynamics and particle concentration distributions in either homogeneous suspensions

or more complex binary systems [Zurita-Gotor *et al.*, 2012, Narsimhan *et al.*, 2013, Qi and Shaqfeh, 2017]. An example is a recent work by Qi and Shaqfeh [2017], who predicted the distributions of RBCs and platelets in a binary suspension subjected to pressure-driven flow.

Based on approximations that collisions only occur between closely adjacent particles and result in very small post-collisional displacements, Henríquez Rivera *et al.* [2015] simplified the master equation [Kumar and Graham, 2012c, Zurita-Gotor *et al.*, 2012, Narsimhan *et al.*, 2013] into a pair of drift-diffusion equations, and developed a "simplified drift-diffusion (SDD)" theory that describes the dynamics of confined flowing multicomponent suspensions. In simple shear flow, closed-form analytical solutions are attainable, and the predictions of cell-free layer thickness using this theory [Henríquez Rivera *et al.*, 2016] agree well with the values reported in other experimental [Bugliarello and Hayden, 1963], numerical [Kumar *et al.*, 2014] and theoretical [Narsimhan *et al.*, 2013] studies. In the solutions, a so-called "margination parameter" $M$ arises, which determines the segregation propensity that characterizes the relative significance of the wall-induced migration and the collisional fluxes. As a result, several regimes of segregation are revealed depending on the value of $M$. Besides, a sharp "drainage transition", characterized by complete depletion of one component from the bulk flow towards the walls, is also identified. The SDD theory was then employed to understand the segregation behavior in binary suspensions of spherical and ellipsoidal capsules [Sinha and Graham, 2016], as described above, and found to well capture the key qualitative features of the shape-mediated margination and demargination. Later, this theory was extended [Henríquez Rivera *et al.*, 2016] to describe suspension dynamics in pressure-driven flow, which is complicated due to

the nonuniform shear rate and in particular the fact that it vanishes at the center-plane. The numerical solutions obtained for this case predict margination regimes and a drainage transition qualitatively similar to those in the simple shear flow case, and also aid in understanding the non-monotonic dependence of WBC margination on hematocrit in blood flow observed in prior numerical studies [Fedosov *et al.*, 2012, Fedosov and Gompper, 2014].

## 2.2 Sickle cell disease and complications

The knowledge of the significant phenomena related to normal blood flow in the microcirculation as well as the substantial advances to date in probing the mechanisms underlying the flow-induced segregation in blood and other multicomponent suspensions, as thoroughly discussed above, has laid the groundwork for understanding the suspension dynamics in more complex scenarios. For example, in hematologic diseases, physical properties of pathological RBCs can be substantially different from those of healthy ones. These cellular-level alterations can further lead to aberrant blood flow and even cause complications. A typical example is sickle cell disease (SCD), one of the most common blood disorders that affects millions of people worldwide. The understanding so far of the hemodynamics in SCD is insufficient, and the mechanisms for complications associated with SCD, such as endothelial dysfunction and inflammation, remain unclear, which have formed the principal motivation of the present work.

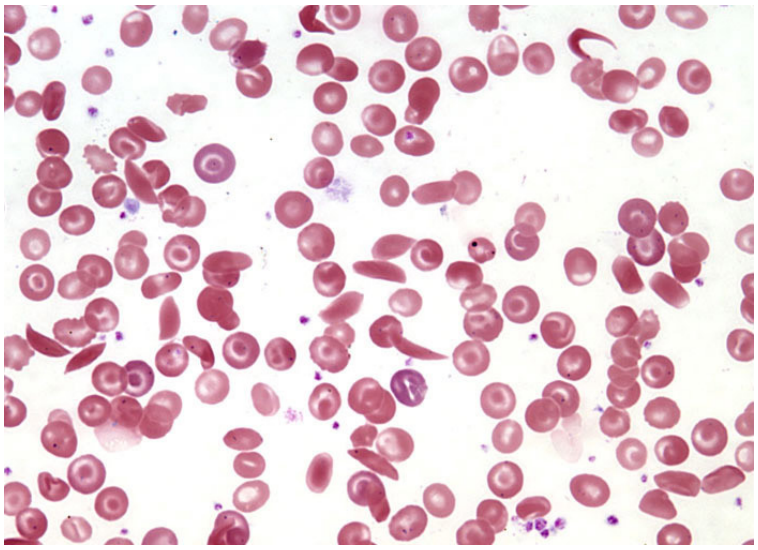


**Figure 2.2:** Healthy and sickle RBCs under a microscope. Source: https://www.microscopyu.com/gallery-images/sickle-cell-anemia-at-40x-magnification.

### 2.2.1 Physical properties of sickle cells: pathological morphologies and biomechanics

Sickle cell disease is an inherited blood disorder characterized by an abnormality in hemoglobin, the oxygen-carrying protein inside RBCs. The molecular mechanism underlying SCD was revealed more than half a century ago [Pauling *et al.*, 1949]: a point mutation in the hemoglobin gene causes the substitution of a single amino acid in the $\beta$-globin subunit, leading to the synthesis of abnormal sickle hemoglobin known as hemoglobin S (HbS). Under deoxygenated conditions, sickle hemoglobin molecules pathologically self-assemble within RBCs due to hydrophobic interactions, and polymerize into long rigid fibrils, a process often called sickling. These intracellular fibrils mechanically alter and damage the membrane of RBCs, resulting in the classic "sickled" or crescent-like shape for sickle cells [Shen *et al.*, 1949], in contrast to the typical biconcave discoidal shape for healthy RBCs (FIG. 2.2).

In fact, in addition to this characteristic sickle shape, a large variation in cell morphology has long been observed within the population of sample sickle cells. In a previous experimental study, Kaul and Xue [1991] revealed the effect of deoxygenation rate on the morphological characteristics of sickle cells using scanning electron microscopy. A gradual deoxygenation procedure favors the typical sickle shape; upon relatively fast deoxygenation, however, a majority of cells show a granular shape, characterized by a bumpy irregular surface and the presence of small spicule-like projections. Besides, cells further subjected to prolonged incubation after relatively fast deoxygenation are observed to take an elongated shape, which is shown to result from the alignment of HbS polymers into long projections. In a recent work, using diffraction phase microscopy, Byun *et al.* [2012] performed optical measurement for individual sickle RBCs, and classified them into echinocytes, discocyte, and the typical crescent-shaped irreversibly sickled cells (ISCs) based on their morphological features, similar to the observations in a prior study [Kaul *et al.*, 1983]. Here ISCs commonly refer to those subjected to irreversible membrane injury after repeated cycles of intracellular sickling that have lost membrane elasticity and remain sickle-shaped even when exposed to extensive oxygenation [Diggs and Bibb, 1939, Shen *et al.*, 1949, Bertles and Döbler, 1969]. In addition to these experiments, computer-aided numerical simulations in the past decades have also improved the understanding of the nature of HbS polymer fiber formation and growth [Dou and Ferrone, 1993, Lei and Karniadakis, 2012a, Li *et al.*, 2012, Lu *et al.*, 2016, Papageorgiou *et al.*, 2018], and corroborated experimental observations of considerable heterogeneity in cell morphologies [Li *et al.*, 2012, Lei and Karniadakis, 2012a, Xu *et al.*, 2017].

The intracellular sickling not only causes the aberrant morphologies of sickle cells

that are considerably different from the normal biconcave discoidal shape of healthy RBCs, but also results in substantial alterations in the mechanical properties of the cell membrane. Using various techniques for the characterization of cell membrane mechanics, a general increase in membrane stiffness of sickle cells compared to that of healthy RBCs has been experimentally determined, though the extent of membrane stiffening is found to vary greatly depending on the states and conditions of individual sickle cells [Messer and Harris, 1970, Nash *et al.*, 1984, Evans and Mohandas, 1987, Byun *et al.*, 2012, Li *et al.*, 2017], leading to a heterogeneity in cell biomechanics. For example, the increase in membrane stiffness for non-ISCs (namely, all sickle cells other than ISCs [Bertles and Döbler, 1969]) is found to be slight under oxygenated conditions [Nash *et al.*, 1984], but substantial upon deoxygenation [Messer and Harris, 1970]. In contrast, ISCs exhibit much greater stiffness than non-ISCs in both states [Messer and Harris, 1970, Nash *et al.*, 1984, Evans and Mohandas, 1987]. Specifically, the shear modulus for ISCs is determined to be three to four times that for healthy RBCs, though no substantial difference in shear modulus is shown between healthy RBCs and non-ISCs [Nash *et al.*, 1984, Byun *et al.*, 2012]. In addition, ISCs also have a much smaller volume than healthy RBCs due to cellular dehydration [Zucker and Cameron, 1976, Glader *et al.*, 1978].

### 2.2.2 Vasculopathy associated with sickle cell disease: insufficient understanding of pathophysiology

Approximately 200,000 infants worldwide are born with SCD annually. Signs of the disease usually begin in early childhood, and a number of complications associate with SCD, either acute or chronic, subject the patients to high morbidity and mortality

rate later in their life [Yawn *et al.*, 2014]. The pathophysiology of SCD has canonically been thought to be due to vaso-occlusive crisis, a common acute complication caused by the sickling and stiffening of RBCs upon deoxygenation that obstruct capillaries and restrict microvascular blood flow, further resulting in tissue ischemia and infarction accompanied by acute pain. Experimental studies regarding the mechanisms underlying vaso-occlusion [Kaul *et al.*, 1989, 1994, Frenette, 2002, Kaul and Fabry, 2004] suggest the role of a complex interplay of multistep and multicellular adhesive events involving sickle cells, WBCs, platelets, endothelium, and extracellular matrix proteins in initiating vaso-occlusion.

However, studies over the past decades have demonstrated that the pathophysiology of SCD is much more complicated than originally thought, particularly as SCD is now also known to be a vasculopathic disease in which the endothelial cells that line the blood vessels are dysfunctional and inflamed. Apparently, the oversimplified view of SCD pathophysiology presented above fails to incorporate this common yet poorly understood complication of SCD, chronic sickle vasculopathy. In fact, during episodes of vaso-occlusion, endothelial inflammation is often observed, and previous works [Madigan and Malik, 2006, Schaer *et al.*, 2013, Sparkenbaugh and Pawlinski, 2013] have revealed that WBC-endothelium adhesion, platelets activation, and intravascular hemolysis all likely contribute to SCD inflammatory vasculopathy. Nevertheless, many questions remain. For example, the sickling of RBCs and vaso-occlusion in SCD are only induced upon deoxygenation in the microvasculature such as postcapillary venules, but why and how does SCD vasculopathy also occur in the highly oxygenated arterial circulation in both small and large blood vessels? In addition, microvascular occlusion leading to ischemia, which results in clinical "pain crises"

in SCD patients, is known to be acute and episodic, yet SCD vasculopathy is chronic; so how can these two pathophysiologic phenomena be reconciled? To address these questions, a new pathophysiological understanding of SCD that is independent of and extends beyond vaso-occlusion is needed, particularly regarding issues including how the abnormality in physical properties of sickle cells alters the hemodynamics of blood flow, and ultimately, how this alteration may be linked to the underlying mechanisms for SCD vasculopathy. None of the investigations to date, however, have attempted to gain a mechanistic understanding of the intrinsic connection between the aberrant physical properties of sickle cells, such as the distorted shape and increased stiffness, and the endothelial dysfunction in SCD.

Yet for all this, progress in the past decades in understanding the pathophysiology of cardiovascular disease such as atherosclerosis may shed some light on the mechanism for vasculopathy in SCD. For example, endothelial dysfunction and inflammation is pervasive throughout the body in both cases, and relatedly stroke, a common cardiovascular disease often associated with ischemia, is also one of the leading yet least understood causes of mortality in SCD. Interestingly, cardiovascular research has demonstrated that endothelial cells "wisely" mechanotransduce biophysical cues, such as the shear forces of the hemodynamic microenvironment, into cellular biological signals [Harrison *et al.*, 2006, Chien, 2007, Abe and Berk, 2014]. Moreover, pathological alterations of these biophysical cues are shown to induce activation of pro-inflammatory signals within endothelial cells [Bao *et al.*, 1999, Abe and Berk, 2014] and subsequent development of atherosclerotic plaques *in situ* that are prone to myocardial infarction and stroke. A previous study by Bao *et al.* [1999], for example, explicitly examined the effects of steady and unsteady shear stresses on en-

dothelial expression of MCP-1 and PDGF-A, two atherogenesis-related genes, using laminar flows with different well-defined wall shear stress profiles, namely (1) steady flow with constant shear stress, (2) ramp flow in which shear stress was smoothly changed from zero to a maximum value and then sustained, (3) step flow in which shear stress was abruptly applied at flow onset followed by steady shear stress for a sustained period, and (4) impulse flow in which shear stress was abruptly applied and then removed. It showed that in general, rapid changes in shear stress (as in impulse flow and the onset of step flow) and steady shear stress (as in steady flow, ramp flow and the steady component of step flow) stimulate and diminish the expression of both genes, respectively. A great many other studies have also elucidated a variety of shear stress-induced signal transduction pathways of the endothelium, and revealed the opposing effects of steady and unsteady shear stresses on endothelial dysfunction and atherogenic events [Davies, 1997, De Keulenaer *et al.*, 1998, Chen *et al.*, 1999, Akimoto *et al.*, 2000, Davis *et al.*, 2001, Dekker *et al.*, 2002, Hsiai *et al.*, 2003, Sorescu *et al.*, 2004, Li *et al.*, 2005, Harrison *et al.*, 2006]. Though having been well-studied in the context of cardiovascular disease, this issue has yet to be explored in SCD.

It is known that under normal conditions, vascular wall shear stress is determined only by the viscous effect of blood plasma, given that flexible healthy RBCs are depleted in the region near the endothelium forming the cell-free layer (CFL) (Section 2.1.2). However, recent studies [Kumar and Graham, 2011, Kumar *et al.*, 2014] have demonstrated that a small fraction of stiffened or smaller cells in a heterogeneous cell suspension exhibit substantial segregation towards the walls, or margination (Section 2.1.3), which may potentially disturb the wall shear stress that is otherwise steady. This is particularly pertinent in SCD, as all patients have a small population

(1-10%) of sickle RBCs, the irreversibly sickled cells, that are permanently stiff, misshapen, and shrunken (Section 2.2.2), and the abnormal characteristics of these cells are potentially in favor of their margination during flow. Therefore, in the context of SCD, it is essential to address how the altered biophysical environment of blood flow in the vicinity of the endothelium may result from the aberrant cell properties and hemodynamics on one hand, and further lead to inflammatory vasculopathy on the other.

To this end, the present work aims to address the key questions described above and gain an improved understanding of the pathophysiology of SCD vasculopathy from a purely physical perspective. This improved understanding may further facilitate a new paradigm of biophysical therapeutic strategies directed towards mitigating the potential aberrant margination effects of diseased cells in SCD. As only a limited number of FDA-approved drugs are currently available for SCD, the potential clinical significance of this work cannot be overstated.

## 2.3 Red blood cells and other deformable capsules

### 2.3.1 Dynamics of red blood cells in shear flow

Red blood cells, the dominant cellular component in blood, have been the focus of a great many studies over the past decades due to their particular physiological significance. In contrast, few efforts have been made to explore the dynamics of sickle cells in flow either as individuals or in flowing suspensions. Indeed, the greatly altered morphological characteristic and mechanical properties of sickle cells, as described in Section 2.2.2, may lead to distinct dynamical motions of sickle cells during flow that

are different from those of healthy RBCs, which may induce pathological activation of other cells (such as endothelial cells) and further contribute to the complications (such as endothelial inflammation) in SCD. Therefore, it is essential to first gain a fundamental understanding of the dynamics of single sickle cells in flow, which has been absent in research to date and formed a motivation of our work.

A healthy human RBC can be mechanically viewed as a fluid-filled deformable biconcave discoidal capsule with an incompressible membrane comprised of a fluid lipid bilayer tethered to an elastic spectrin network [Mohandas and Evans, 1994]. The dynamics and rheology of blood flow greatly depend on the properties and behavior of individual RBCs. A large number of studies have revealed a rich spectrum of dynamical modes for individual RBCs in shear flow over a vast domain of parameter space in terms of membrane mechanics of the RBC and flow conditions [Goldsmith *et al.*, 1972, Fischer *et al.*, 1978, Abkarian *et al.*, 2007, Skotheim and Secomb, 2007, Dupire *et al.*, 2010, Fedosov *et al.*, 2010a, 2011, Yazdani and Bagchi, 2011, Dupire *et al.*, 2012, Sinha and Graham, 2015, Minetti *et al.*, 2019]. Key parameters for determining the RBC dynamics include flow shear rate, viscosity ratio between the fluids inside and out of the cell, and the shear modulus and spontaneous shape of the RBC membrane; here the spontaneous shape refers to the natural shape taken by the cell membrane from which any out-of-plane deformation would lead to restoring forces under the effect of bending elasticity of the membrane. Early studies [Goldsmith *et al.*, 1972, Fischer *et al.*, 1978] found that an isolated RBC suspended in shear flow undergoes a rigid-body-like tumbling motion at low shear rates, in which the cell flips like a coin continuously, while exhibiting a so-called tank-treading motion with the membrane rotating about the interior at higher shear rates in a sufficiently

viscous fluid. A rolling orbit, in which the axis of revolution of the RBC is aligned in the vorticity direction of the shear flow, has also been revealed during the transition from tumbling to tank-treading upon increasing shear rate [Goldsmith *et al.*, 1972, Bitbol, 1986, Dupire *et al.*, 2012]. Recent experiments and theories have observed and predicted more complex dynamics such as a swinging motion, in which the cell orientation oscillates about a fixed angle with respect to the flow direction, with the membrane simultaneously tank-treading [Abkarian *et al.*, 2007, Skotheim and Secomb, 2007]. In addition, the effect of the spontaneous shape on the dynamics of single RBCs has also been investigated in a number of computational studies [Peng *et al.*, 2014, Cordasco *et al.*, 2014, Sinha and Graham, 2015], which suggest that oblate spheroid is a better candidate than biconcave discoid for the spontaneous shape of the RBC, in that it ensures the intactness of the cell dimple during a tank-treading motion and provides better predictions for cell dynamics that are in agreement with experimental observations [Dupire *et al.*, 2012].

Most of the computational studies on healthy RBCs have adopted the same well-defined geometric model [Evans and Fung, 1972] for the biconcave discoidal rest shape of the RBC. However, the considerable morphological heterogeneity within the population of sickle RBCs poses challenges to modeling sickle RBCs and understanding their dynamics in flow. For example, the canonical shape of a sickle RBC is sickle or crescent-like with curvature, but the degree of curvature can vary with the positions of the anchor points where the intracellular sickle hemoglobin fibers come into contact with the cell membrane. A limited number of studies have addressed the dynamics of curved particles that bear resemblance to the sickle-shaped cells. An example is a recent numerical study by Wang *et al.* [2012] on the motion of isolated

rigid slightly curved fibers in shear flow at zero Reynolds number. For some initial orientations, the fibers with high aspect ratio are observed to drift in the gradient direction as a result of the combined effects of the so-called "flipping, scooping, and spinning" motions, and the drift rate strongly depends on the initial orientation, aspect ratio, and curvature of the fibers. The "flipping" and "scooping" motions in [Wang *et al.*, 2012] were predicted later by a theory [Crowdy, 2016] that describes the motion of a curved rigid two-dimensional circular-arc fiber in shear flow. Only a small number of computational works have attempted to model the behavior of sickle cells in flow. Examples are [Lei and Karniadakis, 2013, 2015, Deng *et al.*, 2019], in which simulations were performed to probe the mechanisms for vaso-occlusion in SCD by quantifying the heterogeneous adhesive interactions between sickle cells and the endothelium in a tube flow. None of these studies, nevertheless, have provided insight into understanding the fundamental dynamics of single sickle cells in flow. To fill this gap, the present work aims to take a first step towards this understanding by taking into account the pathologically altered shape and membrane mechanics of the diseased cells and illustrating the effects of various parameters, such as initial orientation, membrane deformability, and curvature of the cell, on their dynamics.

### 2.3.2 Dynamics of other deformable capsules in shear flow

Red blood cells are fluid-filled capsules in nature, and a typical crescent-shaped sickle cell might be roughly thought of as a perturbed case of a deformable prolate spheroidal capsule. More broadly, artificial microcapsules, small liquid droplets enclosed by a thin solid membrane, have been applied extensively to a variety of fields including bioengineering [Masuda, 2011, Alessandri *et al.*, 2013, Degen, 2014], pharmaceutics

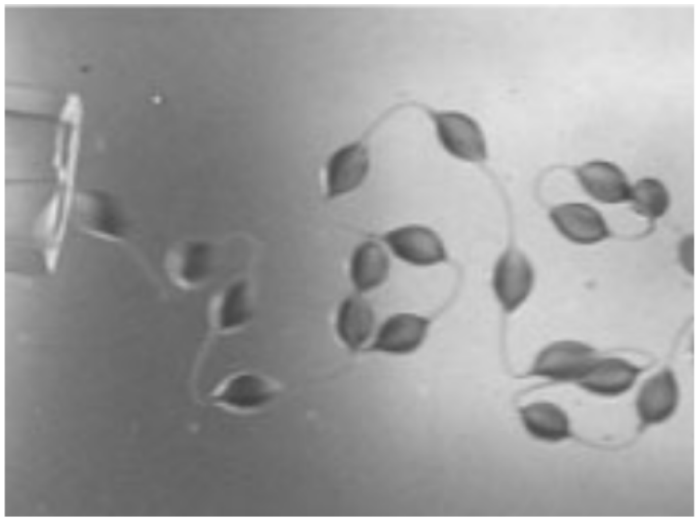


**Figure 2.3:** Microfluidic fabrication of prolate-shaped microcapsules containing a calcium ion solution [Schneeweiss and Rehage, 2005].

[Schneeweiss and Rehage, 2005] (FIG. 2.3), and food industries [Jones *et al.*, 1974]. Established fabrication techniques have achieved the production of artificial microcapsules in large quantities by adding a cross-linking agent to an emulsion, forming a membrane encapsulating the droplets [Chang *et al.*, 1966, Levy *et al.*, 1991, 1994, 1995]. Capsules obtained using these techniques are often approximately spherical in shape. However, a number of biomedical studies on vascular-targeted delivery have reported that high-aspect-ratio (prolate) microparticles/capsules exhibit considerably reduced immune clearance and increased circulation half-time compared to spheres [Geng *et al.*, 2007, Champion and Mitragotri, 2009]. Additionally, because of a higher surface-to-volume ratio than spheres, non-spherical microcapsules in general can be preferable in applications to achieve enhanced mass transfer across the capsule membrane upon arrival at the target. In fact, nature has taken this course with red blood cells, the biconcave discoidal shape of which maximizes the surface area of the cell membrane for oxygen to diffuse across. In recent years, novel fabrication methods

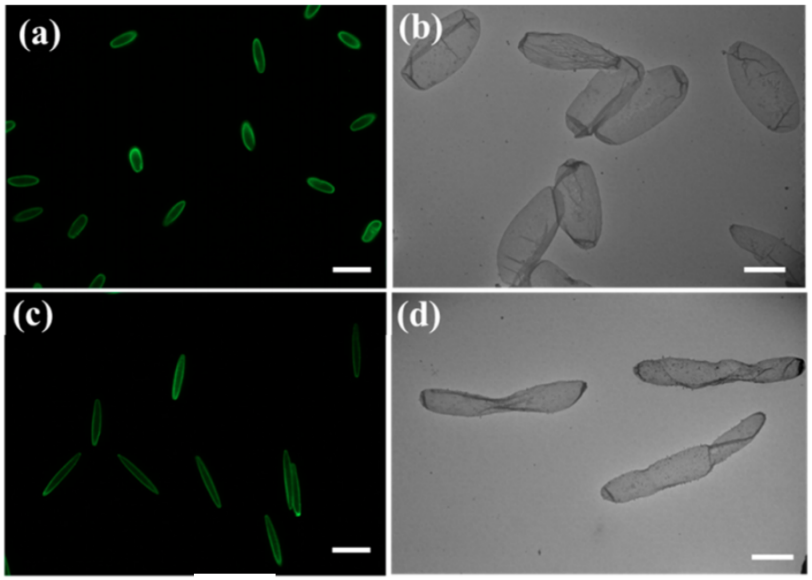



**Figure 2.4:** Polyelectrolyte capsules (PECs) with independently controlled size and shape by combining particle stretching with soft template layer-by-layer (LBL) deposition [Zan *et al.*, 2015].

[Zan *et al.*, 2015] have been developed to produce capsules with controllable size and shape (FIG. 2.4), which may facilitate the optimization of the design of a delivery system.

In analogy to blood as a cell suspension, most of the applications featuring artificial capsules involve suspensions in a microfluidic environment, in which the dynamics of single capsules can play a significant role. It has been established that a spherical deformable capsule assumes a tank-treading motion in shear flow with the membrane rotating periodically around its stationary elongated shape [Barthès-Biesel and Rallison, 1981], which is also observed for the RBC as described above. Again, the deformability of the capsule is characterized by the capillary number Ca, which represents the ratio of viscous stresses to elastic restoring stresses on the particle. For non-spherical capsules other than biconcave discoids as a model for RBCs, spheroidal capsules have also gained increasing attention in the past decade. A majority of

studies regarding spheroidal capsules, both experimental and computational, have particularly focused on oblate capsules [Ramanujan and Pozrikidis, 1998, Sui *et al.*, 2008, Kessler *et al.*, 2008, Bagchi and Kalluri, 2009, Le and Tan, 2010, Walter *et al.*, 2011, Yazdani *et al.*, 2011, Omori *et al.*, 2012, Cordasco and Bagchi, 2013, Wang *et al.*, 2013, Dupont *et al.*, 2016], possibly because of the aforementioned findings on RBC dynamics that oblate spheroid may be the best candidate for the spontaneous shape of the RBC [Peng *et al.*, 2014, Sinha and Graham, 2015]. In these works, investigations were performed in a systematic manner over a large domain of parameter space, and the roles of different parameters in leading to the complex capsule dynamics in flow were determined. To the best of our knowledge, however, only a limited number of studies have attempted to address the motion of prolate capsules in shear flow [Walter *et al.*, 2011, Dupont *et al.*, 2013, Cordasco and Bagchi, 2013, Wang *et al.*, 2013], most of which assumed the same viscosity for the fluids inside and outside the capsule and negligible bending resistance of the capsule membrane. With these simplifications, Walter *et al.* [2011] numerically determined two stable in-plane orbits, namely tumbling at low Ca and swinging at high Ca, for an isolated inertialess prolate capsule in shear flow with the major axis of the capsule initially lying in the shear plane. Richer dynamics were later revealed for a prolate capsule with off-shear-plane initial orientations [Dupont *et al.*, 2013]. In reality, the membrane mechanics of artificial capsules in applications can vary greatly depending on the materials and fabrication techniques, and the fluids or solutions suspending and enclosed within the capsules can generally have unmatched viscosities. The interplay between a non-unity viscosity ratio and non-negligible bending resistance may lead to more complex orbital dynamics for a single prolate capsule in flow. This

expectation is not groundless, since even a small additional particle inertia has been demonstrated to induce interesting behaviors of the capsule, such as the coexistence of multiple stable orbits [Wang *et al.*, 2013], that are not observed for an inertialess capsule. On account of this, another objective of the present work, in addition to the aforementioned ones regarding sickle cell dynamics in flow and the pathophysiology of sickle vasculopathy, is to gain an improved understanding of the orbital dynamics of a single prolate capsule in shear flow based on systematic investigations by particularly incorporating the effects of varying membrane bending stiffness and viscosity ratio, among other physical aspects.

# Chapter 3

# Model formulation and numerical methods for direct simulations[a]

## 3.1 Problem formulation

In this study, we perform direct numerical simulations to attain the objectives as described in Chapter 2. Specifically, either a single fluid-filled deformable capsule or a confined suspension of capsules is considered in flow depending on the objective. In this chapter, we describe the models and methods employed in our simulations.

To study the dynamics of a single prolate capsule or a sickle red blood cell (RBC), we consider an isolated neutrally-buoyant fluid-filled deformable capsule with a straight or curved prolate rest shape in unbounded simple shear flow with constant shear rate $\dot{\gamma}$. In this study, the flow and vorticity directions are $x$ and $z$, respec-

[a]This chapter includes content from: [1] Zhang, X., Lam, W. A., and Graham, M. D. (2019). Dynamics of deformable straight and curved prolate capsules in simple shear flow. Physical Review Fluids 4, 043103; [2] Zhang, X., Caruso, C., Lam, W. A., and Graham, M. D. (2019). Submitted.

tively, and $y$ denotes the wall-normal direction. The curved prolate capsule serves as a model for the typical crescent-shaped sickle RBCs in sickle cell disease (SCD). Details regarding the models for the straight and curved prolate capsules and the initial orientation of the capsules are found later in Chapters 4 and 6, respectively. The suspending fluid and the fluid enclosed by the capsule are both assumed to be incompressible and Newtonian, with viscosity $\eta$ and $\lambda\eta$, respectively, so the viscosity ratio between the fluids inside and outside the capsule is $\lambda$. The membrane mechanics of the capsule include both an in-plane shear elasticity and an out-of-plane bending elasticity. The in-plane shear modulus of the membrane is $G$ and the out-of-plane bending modulus is $K_B$. Hence the deformability of the capsule can be characterized by the dimensionless capillary number $\mathrm{Ca} = \eta\dot{\gamma}l/G$, and the bending stiffness of the capsule is expressed nondimensionally by $\hat{\kappa}_B = K_B/l^2G$; here $l$ is the characteristic length of the capsule. We will detailedly describe the model for the mechanics of the capsule membrane in Section 3.2.

To investigate the dynamics of blood flow in the microcirculation in SCD and probe the mechanism for the associated endothelial inflammation, we consider flowing suspensions of deformable capsules in a planar slit bounded by two parallel rigid walls (FIG. 3.1). In the $y$ direction, no-slip boundary conditions are applied to the two rigid walls at $y = 0$ and $y = 2H$, where $H$ is the distance from each wall to the centerplane of the slit domain. In $x$ and $z$ directions, periodic boundary conditions are imposed, with spatial periods $L_x$ and $L_z$, respectively. The suspensions are subjected to pressure-driven (Poiseuille) flow with a constant wall shear rate $\dot{\gamma}_w$. We particularly focus on a binary suspension containing primarily flexible biconcave discoidal capsules and a small fraction of stiff curved prolate capsules that represent healthy and sickle

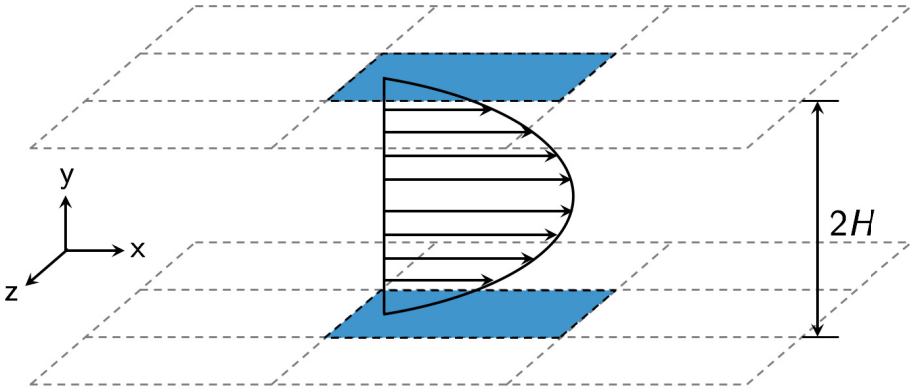



**Figure 3.1:** Schematic of the simulation domain for flowing suspensions of deformable capsules subjected to a unidirectional pressure-driven flow in a planar slit bounded by two parallel rigid walls.

RBCs, which serves as an idealized model for microvascular blood flow in SCD, along with several other suspensions containing different types of stiff capsules. The models as well as the parameters for the suspension systems considered in this work are described in detail in Chapter 5.

## 3.2 Model and discretization for capsule membrane

To describe the membrane mechanics of the capsules, we use a model that incorporates shear elasticity, area dilatation, and bending resistance. Before introducing this model, we first present the formalism used to describe the kinematics of the membrane deformation. Consider a deformation in the $x$-$y$ plane for example. The undeformed and deformed coordinates of a material point with respect to a fixed set of Cartesian axes are denoted as $(x, y)$ and $(X, Y)$, respectively, which are related by

$$X = x + u, \tag{3.1}$$

$$Y = y + v, \tag{3.2}$$

where $u$ and $v$ are the displacements of the material point in the $x$ and $y$ directions, respectively. The relation between the position vectors of two points infinitesimally close to each other before and after deformation is given by

$$\begin{bmatrix} dX \\ dY \end{bmatrix} = \begin{bmatrix} 1+\partial u/\partial x & \partial u/\partial v \\ \partial v/\partial x & 1+\partial v/\partial y \end{bmatrix} \begin{bmatrix} dx \\ dy \end{bmatrix},$$

or compactly as

$$d\boldsymbol{X} = \boldsymbol{F} \cdot d\boldsymbol{x}, \tag{3.3}$$

where $\boldsymbol{F}$ is the deformation gradient. The square of the distance between the two neighboring points before and after deformation is given by

$$dS^2 = d\boldsymbol{X} \cdot d\boldsymbol{X} = d\boldsymbol{x} \cdot \boldsymbol{G} \cdot d\boldsymbol{x}, \tag{3.4}$$

where $\boldsymbol{G} = \boldsymbol{F}^T \cdot \boldsymbol{F}$ is a symmetric, positive definite matrix. The elements of $\boldsymbol{G}$ are

$$G_{11} = \left(1 + \frac{\partial u}{\partial x}\right)^2 + \left(\frac{\partial v}{\partial x}\right)^2, \tag{3.5}$$

$$G_{12} = G_{21} = \left(1 + \frac{\partial u}{\partial x}\right)\left(\frac{\partial u}{\partial y}\right) + \left(1 + \frac{\partial v}{\partial x}\right)\left(\frac{\partial v}{\partial y}\right), \tag{3.6}$$

$$G_{22} = \left(\frac{\partial u}{\partial y}\right)^2 + \left(1 + \frac{\partial v}{\partial y}\right)^2. \tag{3.7}$$

The principal stretch ratios $\lambda_1$ and $\lambda_2$ are thus defined as the eigenvalues of $\boldsymbol{G}$, given as

$$\begin{aligned} \lambda_1^2 &= \tfrac{1}{2}\left(G_{11} + G_{22} + \sqrt{(G_{11} - G_{22})^2 + 4G_{12}^2}\right), \\ \lambda_2^2 &= \tfrac{1}{2}\left(G_{11} + G_{22} - \sqrt{(G_{11} - G_{22})^2 + 4G_{12}^2}\right). \end{aligned} \tag{3.8}$$

Now we describe the model for the mechanics of the capsule membrane. For an arbitrary capsule in this work, the total energy $E$ of the capsule membrane $S$ is given as:

$$E = \frac{K_B}{2}\int_S (2\kappa_H + c_0)^2 dS + \overline{K_B}\int_S \kappa_G dS + \int_S W dS, \tag{3.9}$$

where $K_B$ and $\overline{K_B}$ are the bending moduli, and $W$ is the shear strain energy density; $\kappa_H$ and $\kappa_G$ are the mean and Gaussian curvature of the membrane surface, respectively; $c_0 = -2H_0$ is the spontaneous curvature, $H_0$ being the mean curvature of the spontaneous shape. Here the spontaneous shape of a capsule refers to the natural shape taken by the capsule membrane from which any out-of-plane deformation would lead to restoring forces due to the effect of bending resistance of the membrane. If the spontaneous shape is a flat sheet, for example, then $c_0 = 0$ everywhere on the membrane surface. In this equation, the first two terms represent the Helfrich bending energy [Canham, 1970, Helfrich, 1973], while the third term corresponds to the shear strain energy. Specifically, the behavior of the capsule membrane in response to the in-plane shear elastic force is described using a membrane model by Skalak *et al.* [1973], in which the shear strain energy density $W$ in Eq. 3.9 is given by

$$W_{\mathrm{SK}} = \frac{G}{4}\Big[(I_1^2 + 2I_1 - 2I_2) + C_a I_2^2\Big], \tag{3.10}$$

where $G$ again is the in-plane shear modulus of the membrane, and $C_a$ characterizes the energy penalty for area change of the membrane. The two strain invariants $I_1$ and $I_2$ are functions of the principal stretch ratios $\lambda_1$ and $\lambda_2$ (Eq. 3.8), defined as

$$I_1 = \lambda_1^2 + \lambda_2^2 - 2, \quad I_2 = \lambda_1^2\lambda_2^2 - 1. \tag{3.11}$$

Barthès-Biesel *et al.* [2002] showed that for $C_a \gtrsim 10.0$, the tension of a Skalak membrane becomes nearly independent of $C_a$ under a simple uniaxial deformation, so $C_a$ is set to 10.0 for all capsules in our simulations. Sinha and Graham [2015] have validated this model for the membrane mechanics of a healthy RBC, showing that the strain hardening behavior of the membrane predicted by this model agrees very well with the experimentally determined response of an RBC membrane to optical tweezer stretching by Mills *et al.* [2004].

Taking the first variation of the total membrane energy $E$ (Eq. 3.9) gives the total membrane strain force density:

$$\mathbf{f^m} = \mathbf{f^b} + \mathbf{f^s}, \tag{3.12}$$

where $\mathbf{f^b}$ and $\mathbf{f^s}$ are bending and shear elastic force densities, respectively. Note that according to the Gauss-Bonnet theorem, the second term in Eq. 3.9, i.e., the term involving the Gaussian curvature $\kappa_G$, is a constant when no topological changes are involved, so there is no force density associated with that term [Cordasco and Bagchi, 2013]. Hence, the force density due to bending resistance is given by the first variation of only the first term in Eq. 3.9. To calculate $\mathbf{f^m}$, we first discretize the capsule membrane into $N_\triangle$ piecewise flat triangular elements; in this work $N_\triangle = 320$, resulting in 162 nodes. In addition to previous convergence tests for spherical capsules [Kumar *et al.*, 2014], we have verified that increasing the number of membrane elements from 320 to 1280 makes no difference to capsule dynamics in this work, and this mesh resolution keeps the computational cost manageable given that very long simulation times are required for the dynamics of both a single capsule and capsule suspensions to reach steady state. Based on this discretization, the calculation of the total membrane force density $\mathbf{f^m}$ then follows the work of Kumar and Graham [2012a]

and Sinha and Graham [2015] using approaches given by Charrier *et al.* [1989] for the in-plane shear force density $\mathbf{f^s}$ and Meyer *et al.* [2002] for the out-of-plane bending force density $\mathbf{f^b}$, respectively. Details regarding these calculations are found in [Kumar and Graham, 2012a] and [Sinha and Graham, 2015].

## 3.3 Flow field and fluid motion

In this section we address the calculation of the flow field. We assume that both the particle Reynolds number and the channel Reynolds number for the problems considered in this work are sufficiently small so that the fluid motion is governed by the Stokes equation. Under this assumption, the fluid velocity $\mathbf{u}$ at any point $\mathbf{x_0}$ in the simulation domain, either unbounded or confined, can be written in boundary integral form [Pozrikidis, 1992, Kumar and Graham, 2012a] as:

$$u_j(\mathbf{x_0}) = u_j^{\infty}(\mathbf{x_0}) + \sum_{m=1}^{N_p} \int_{S^m} q_i(\mathbf{x}) G_{ji}(\mathbf{x_0}, \mathbf{x}) dS(\mathbf{x}), \tag{3.13}$$

where $N_p$ is the number of capsules in the system depending on the problem, and the single layer density $\mathbf{q}(\mathbf{x_0})$ satisfies

$$\begin{aligned} &q_j(\mathbf{x_0}) + \frac{\lambda - 1}{4\pi(\lambda + 1)} n_k(\mathbf{x_0}) \sum_{m=1}^{N_p} \int_{S^m} q_i(\mathbf{x}) T_{jik}(\mathbf{x_0}, \mathbf{x}) dS(\mathbf{x}) \\ &= -\frac{1}{4\pi\mu} \Big( \frac{\Delta f_j(\mathbf{x_0})}{\lambda + 1} + \frac{\lambda - 1}{\lambda + 1} f_j^{\infty}(\mathbf{x_0}) \Big). \end{aligned} \tag{3.14}$$

Here $\mathbf{u}^{\infty}(\mathbf{x_0})$ is the undisturbed fluid velocity at a given point $\mathbf{x_0}$, $S^m$ denotes the surface of capsule $m$; $\mathbf{f}^{\infty}(\mathbf{x_0})$ is the traction at $\mathbf{x_0}$ due to the stress generated in the fluid corresponding to the undisturbed flow $\mathbf{u}^{\infty}(\mathbf{x_0})$; $\Delta\mathbf{f}(\mathbf{x_0})$ is the hydrodynamic traction

jump across the membrane interface, which relates to the total membrane force density (Eq. 3.12) by $\Delta\mathbf{f}(\mathbf{x_0}) = -\mathbf{f^m}$ assuming the membrane equilibrium condition; $\mathbf{G}$ and $\mathbf{T}$ are the Green's function and its associated stress tensor.

To fundamentally reduce the computational complexity for our simulations, such as those of suspensions containing a large number of capsules, we adopt an accelerated implementation [Kumar and Graham, 2012a] of the boundary integral method to determine the flow field. The acceleration in this implementation is achieved by the use of the General Geometry Ewald-like Method (GGEM) by Hernandez-Ortiz *et al.* [2007]. The key idea is to decompose the overall problem into a local and a global problem, specifically by splitting the Dirac-delta density $\delta(\mathbf{r})$ in the Stokes equation into a singular but exponentially-decaying (short-ranged) local density $\rho_l(\mathbf{r})$ and a smooth but long-ranged quasi-Gaussian global density $\rho_g(\mathbf{r})$. The global and local densities are respectively given by the following expressions:

$$\rho_g(\mathbf{r}) = \frac{\alpha^3}{\pi^{3/2}} e^{-\alpha^2 r^2} \left( \frac{5}{2} - \alpha^2 r^2 \right), \tag{3.15}$$

$$\rho_l(\mathbf{r}) = \delta(\mathbf{r}) - \rho_g(\mathbf{r}), \tag{3.16}$$

where $\alpha^{-1}$ represents the length scale over which the global density varies, and $\mathbf{r}$ is the position vector relative to the pole of the singularity, with $r = |\mathbf{r}|$. The solution associated with the local problem is obtained assuming free-space boundary conditions, i.e., it is independent of the geometry of interest. An important feature of the local solution is that it is short-ranged and therefore can be neglected beyond a length scale $\sim \alpha^{-1}$ from the pole of the local density. In this work, a cutoff length is taken as $r_{\text{cut}} = 4/\alpha$ with good accuracy, and a cell-linked algorithm [Allen and Tildesley,

1987] is applied to generate the near-neighbor list required for the computation of the local solution.

The solution associated with the global problem, on the other hand, is nonsingular and ensures that the boundary conditions for the overall problem are satisfied. Specifically, we compute the global solution by employing the discrete Fourier series approximation in the periodic $x$ (flow) and $z$ (vorticity) directions and the discrete Chebyshev polynomial approximation in the $y$ (wall-normal) direction. Note that in a traditional Ewald-sum-based method, the domain is triply periodic and a discrete Fourier representation is used in all three directions. In this approach, the pressure drop associated with the flow field induced by the capsules is always zero over the spatial period of the simulation domain, which ensures that the pressure drop obtained from this boundary integral implementation for any capsule suspension in this work always equals the pressure drop in the flow in the absence of the capsules. In other words, a constant pressure drop is guaranteed for these simulations.

The overall solution for the velocity or stress field is the sum of the local and global solutions. Based on extensive numerical tests [Kumar and Graham, 2012a], we set $\alpha h = 0.5$ to guarantee the convergence of the GGEM solution, where $h$ is the characteristic mesh spacing in the global problem. Once the overall solution is obtained on the mesh points, the velocity and stress at the discrete nodes on the capsule membrane are determined by 4th-order Lagrange interpolation. For a flowing suspension of capsules in a slit geometry as considered in the present study, the computational complexity of the algorithm scales as $O(N\log N)$, where $N$ is proportional to the product of the total number of capsules $N_p$ and the number of triangular elements $N_\triangle$ used for discretizing the membrane of each capsule. Details of the numerical method

and algorithm are found in [Kumar and Graham, 2012a].

Once the flow field is determined, the positions of the element nodes on the discretized capsule membrane are advanced in time using the second-order explicit Adams-Bashforth method with adaptive time step $\Delta t = 0.02\mathrm{Ca}d$, where $d$ is the minimum node-to-node distance (the closest nodes do not have to be on the same capsule). In the present work, time is nondimensionalized with either the uniform shear rate $\dot{\gamma}$ in simple shear flow or the wall shear rate $\dot{\gamma}_w$ in pressure-driven flow.

# Chapter 4

# Dynamics of single sickle cells as deformable curved prolate capsules in shear flow[a]

## 4.1 Introduction

A healthy human red blood cell (RBC) is a fluid-filled biconcave discoid with an incompressible membrane comprised of a fluid lipid bilayer tethered to an elastic spectrin network [Mohandas and Evans, 1994]. In the past decades, experimental and computational studies have revealed a rich spectrum of dynamical modes for RBCs in shear flow over a vast domain of parameter space in terms of membrane mechanics of RBC and flow conditions [Goldsmith *et al.*, 1972, Fischer *et al.*, 1978,

[a]This chapter includes content from: Zhang, X., Lam, W. A., and Graham, M. D. (2019). Dynamics of deformable straight and curved prolate capsules in simple shear flow. Physical Review Fluids 4, 043103.

Abkarian *et al.*, 2007, Skotheim and Secomb, 2007, Dupire *et al.*, 2010, Fedosov *et al.*, 2010a, 2011, Yazdani and Bagchi, 2011, Sinha and Graham, 2015, Minetti *et al.*, 2019]. In pathological cases where normal blood flow is altered, the dynamics of diseased RBCs can be very different from those of healthy ones because of differences in cell properties. In sickle cell disease (SCD), for example, the intracellular polymerization of sickle hemoglobin (HbS) leads to an abnormality in the shape of individual sickle RBCs, but a large variation in cell morphology has been revealed within the population of sample cells. Using diffraction phase microscopy, Byun *et al.* [2012] performed optical measurement for individual sickle RBCs, and classified them into echinocytes, discocyte, and the typical crescent-shaped irreversibly sickled cells (ISCs) based on their morphological features. Numerical simulations have also enhanced the understanding of the nature of HbS polymer fiber formation and growth [Dou and Ferrone, 1993, Lei and Karniadakis, 2012a, Li *et al.*, 2012, Lu *et al.*, 2016, Papageorgiou *et al.*, 2018], and corroborated experimental observations of considerable heterogeneity in cell morphologies [Li *et al.*, 2012, Lei and Karniadakis, 2012a, Xu *et al.*, 2017]. In addition, using various techniques for the characterization of cell membrane mechanics, a general decrease in deformability of sickle RBCs compared to that of normal RBCs has been determined; the extent of membrane stiffening varies greatly depending on the states and conditions of individual sickle RBCs [Messer and Harris, 1970, Nash *et al.*, 1984, Evans and Mohandas, 1987, Byun *et al.*, 2012, Li *et al.*, 2017]. The decrease in membrane deformability for non-ISCs (namely, all sickle RBCs other than ISCs [Bertles and Döbler, 1969]) is found to be slight under oxygenated conditions [Nash *et al.*, 1984], but substantial upon deoxygenation [Messer and Harris, 1970], while ISCs exhibit much lower deformability than non-ISCs in both states [Messer

and Harris, 1970, Nash *et al.*, 1984, Evans and Mohandas, 1987].

All these variations for individual sickle RBCs mentioned above pose challenges to understanding the dynamics of sickle RBCs in flow. The present work aims to take a step toward this understanding by performing a systematic computational investigation of the dynamics of a model sickle cell in simple shear flow and illustrating the effects of initial orientation, membrane deformability and curvature of the cells on their dynamical motions.

A sickle RBC might be thought of as a perturbed case of a deformable spheroidal capsule, and this is how we model it below, so here we review relevant literature on this class of particles in flow. The canonical example of this class is a simple rigid neutrally-buoyant spheroid, whose motion in simple shear flow at zero Reynolds number can be described by trajectories known as Jeffery orbits [Jeffery, 1922]. During flow the center-of-mass position of the spheroid remains on its initial streamline with no drift in any direction, while its major axis of symmetry traces out a closed periodic orbit depending on its initial orientation. Each orbit corresponds to a specific non-negative orbit constant $C$, so the quantity $C_b = C/(1 + C)$ is bounded by zero and one. When $C = C_b = 0$, the particle rolls with its major axis aligned with the vorticity direction, while $C_b = 1(C = \infty)$ corresponds to a pure tumbling motion in the shear plane. For any intermediate value of $C_b$, the major axis of the particle undergoes a so-called kayaking motion. Bretherton [1962] later showed that Jeffery's solution can be applied to describe the dynamics of any axisymmetric rigid body with fore-aft symmetry.

Jeffery orbits are highly degenerate because of the combination of symmetry, Stokes flow reversibility and rigidity. Many efforts have been made to examine the

behaviors of particles immersed in shear flow when these conditions are not strictly satisfied. For example, large changes in the orbital behaviors were observed in a number of studies when deviations from axisymmetric geometry were introduced. Hinch and Leal [1979] derived the equations for the motion of general (non-axisymmetric) ellipsoids in simple shear flow, observing that the motion of a triaxial ellipsoid with comparable axes has doubly periodic (quasiperiodic) dynamics. For triaxial ellipsoids with one axis significantly longer than the other two, Yarin *et al.* [1997] numerically observed chaotic behavior and proposed an analytical theory to explain the onset of this chaotic motion. Subramanian and Koch [2006] found through a theoretical investigation that when small but finite inertia was considered, the degeneracy of Jeffery orbits is broken and particular orbits become attractors for the long-time dynamics. In particular, they predicted that the attractor of a slightly prolate spheroid would evolve from the shear plane via an intermediate orbit towards the vorticity axis, as the ratio of particle density to fluid density decreased. Using numerical simulations, Mao and Alexeev [2014] examined the effects of fluid inertia and particle inertia on the dynamics of a solid spheroidal particle in simple shear flow, finding that at zero Reynolds number, particle inertia would cause the orientation of a prolate spheroid to drift toward a tumbling orbit in the shear plane, but the drift direction would change from in-plane tumbling to rolling around the vorticity axis when the Reynolds number exceeded a critical value.

Many computational studies have also addressed how the degeneracy of Jeffery's solution is broken in the presence of deformability as for capsules and solid elastic particles. Here capillary number, which represents the ratio of viscous stresses to elastic restoring stresses on the particle, characterizes the deformability of the particle. We

mainly focus on the works regarding prolate particles which are of direct pertinence to the present study. Most numerical studies regarding prolate capsules focused on the case where the inner and outer fluids have the same viscosity. Walter *et al.* [2011] investigated the behavior of a prolate capsule in simple shear flow with the revolution axis of the capsule initially lying in the shear plane. The membrane was modeled as a hyperelastic surface with no bending resistance. They observed that the prolate capsule took a rigid-body like tumbling motion at low shear rate (i.e. capillary number), and exhibited a fluid-like behavior termed swinging at high shear rate in which the membrane rotates around its deformed shape and the capsule elongation and orientation oscillate in shear flow. This tumbling-to-swinging transition was even found for a spheroidal compound capsule consisting of a spherical inner capsule enclosed by a spheroidal outer capsule at vanishing viscosity mismatch by increasing the inner capsule size alone [Luo and Bai, 2016]. Out-of-shear plane dynamics of prolate capsules have also gained an increasing understanding in recent years. Dupont *et al.* [2013] and Cordasco and Bagchi [2013] numerically studied three-dimensional orbital dynamics of isolated prolate capsules in simple shear flow with off-plane initial orientations, and revealed rich dynamics of the capsules irrespective of the initial orientation. In [Dupont *et al.*, 2013], the capsule membrane was modeled as an isotropic hyperelastic surface with shear elasticity and area dilatation described by either the Skalak law [Skalak *et al.*, 1973] or the neo-Hookean law and in the absence of bending rigidity. They showed that at low and high capillary number regimes, the dynamics of a prolate capsule in Stokes flow converge towards a rolling motion about the vorticity axis and an oscillating-swinging motion about the shear plane as the stable orbit, respectively, and a wobbling motion in which the capsule precesses around the vor-

ticity axis is taken at equilibrium at intermediate capillary number. This qualitative transition of motions, characterized by the change in the elastic energy stored in the membrane, was generally observed in the parameter regimes considered in this work regardless of the aspect ratio of the capsule or the membrane law. Later Cordasco and Bagchi [2013] incorporated bending stiffness into a Skalak membrane for a prolate capsule with zero spontaneous curvature, and observed a procession-to-kayaking (oscillating-swinging) transition with increasing capillary number similar to the findings by Dupont *et al.* [2013]. Solid elastic particles have also been studied [Gao *et al.*, 2012, Villone *et al.*, 2015]. Gao *et al.* [2012] theoretically predicted two in-plane dynamical modes for a neo-Hookean elastic spheroidal particle immersed in shear flow, namely trembling (similar to swinging for capsules) and tumbling, depending on the shear rate, elastic shear modulus and asphericity of the initial shape. These two regimes of motion were later observed in the numerical simulations by Villone *et al.* [2015]. These authors also revealed that a particle initially oriented out of the shear plane evolved in time towards in-plane trembling or tumbling, which differs from the stable orbits for prolate capsules observed by Dupont *et al.* [2013] and Cordasco and Bagchi [2013]. Despite all these promising results, none of the studies to date regarding deformable spheroidal particles, however, have ever considered any distortion to the original shape such as curvature, which has formed one motivation of the present work.

A limited number of studies have addressed the dynamics of curved particles such as sickle-shaped cells. Wang *et al.* [2012] simulated the motion of isolated rigid slightly curved fibers in simple shear flow at zero Reynolds number. As with triaxial ellipsoids, quasiperiodic orbit dynamics are sometimes observed. More importantly,

for some initial orientations the fibers drift in the gradient direction as a result of the combined effects of the so-called "flipping, scooping, and spinning" motions. The drift rate strongly depends on the initial orientation, aspect ratio, and curvature of the fibers – in particular drift only occurs for fibers of high aspect ratio. Crowdy [2016] derived a dynamical system governing the motion of a curved rigid two-dimensional circular-arc fiber in simple shear flow, and the analytical solutions of this dynamical system display the "flipping" and "scooping" motions observed in [Wang *et al.*, 2012]. Only a small number of numerical studies have addressed the behavior of sickle cells *per se*. Examples are [Lei and Karniadakis, 2013, 2015, Deng *et al.*, 2019], in which simulations were performed to investigate and quantify the heterogeneous adhesive interaction between sickle RBCs and the endothelium during flow, and the influence of cell morphologies and membrane rigidities. The aim of these studies was to shed light on the vasoocclusion crisis associated with SCD. None of these studies have focused on the fundamental dynamics or orbital behavior of single sickle cells in shear flow.

The aim of the present study is to take a first step toward understanding the dynamics of sickle cells in blood flow, by characterizing the dynamics of a model sickle cell in shear flow and examining this behavior in the context of what we know about the dynamics of other prolate objects in flow. Specifically, we investigate the dynamics of single straight and curved prolate capsules in unbounded simple shear flow at zero Reynolds number and discuss the effects of initial orientation, membrane deformability, and degree of curvature on their dynamics. The rest of the chapter is organized as follows: in Section 4.2 we present the model for sickle RBCs and the numerical algorithm employed to obtain the fluid field, followed by a validation

of our model and numerical simulation; in Section 4.3 we provide detailed results and discussion on the dynamics of single straight and curved prolate capsules; lastly, concluding remarks are presented in Section 4.4.

## 4.2 Model formulation

### 4.2.1 Model and discretization

We consider an isolated neutrally-buoyant fluid-filled deformable capsule with a straight or curved prolate rest shape in unbounded simple shear flow (FIG. 4.1). The shear rate is $\dot{\gamma}$, and the undisturbed flow velocity is given as $\mathbf{u}^{\infty} = (\dot{\gamma}y, 0, 0)$. Both the suspending fluid and the fluid inside the capsule are assumed to be incompressible and Newtonian, and the viscosity ratio between the fluids inside and outside the capsule is $\lambda$. The prolate spheroidal shape of the capsule derives from polar stretching and equatorial compression of a spherical capsule with radius $s$ centered at the origin. The equation for this transformation is given by

$$\mathbf{x}^p = \begin{pmatrix} c/s & 0 & 0 \\ 0 & a/s & 0 \\ 0 & 0 & a/s \end{pmatrix} \cdot \mathbf{x}^s, \tag{4.1}$$

where $\mathbf{x}^s$ and $\mathbf{x}^p$ are the positions of a point on the membrane of the original spherical capsule and the mapped point on the membrane of the resulting prolate spheroidal capsule with a polar radius $c$ and an equatorial radius $a$ (aspect ratio $r_p = c/a > 1$). The resulting prolate spheroidal capsule thus aligns with the $x$ axis. To generate a curved capsule, we then impose a quadratic unidirectional displacement of membrane

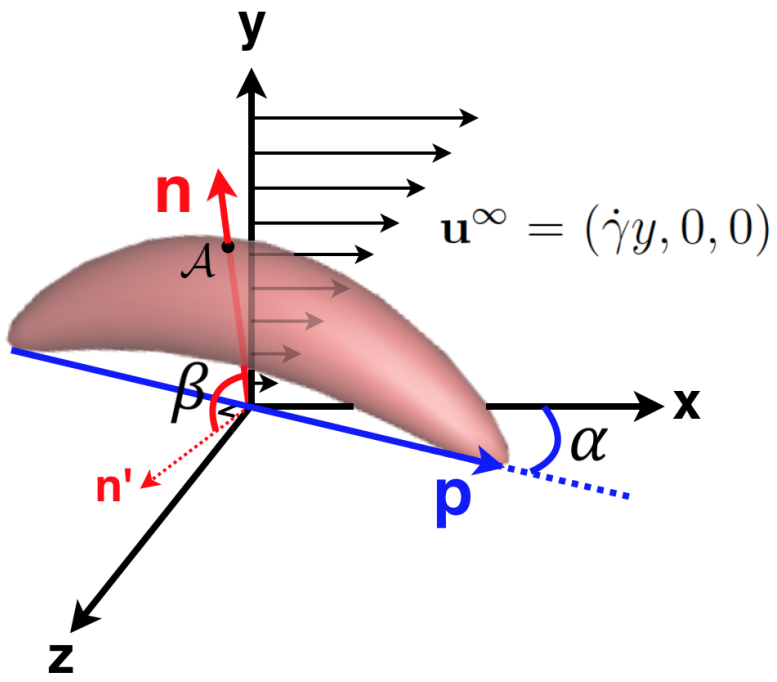



**Figure 4.1:** Schematic of the initial orientation of a curved prolate capsule in unbounded simple shear flow.

points perpendicular to the polar axis of the prolate spheroidal capsule (here in the $y$ direction),

$$x_1^c = x_1^p, \tag{4.2a}$$

$$x_2^c = x_2^p - k\left[x_1^p - \frac{1}{2}(x_1^{pl} + x_1^{pr})\right]^2, \tag{4.2b}$$

$$x_3^c = x_3^p, \tag{4.2c}$$

where $\mathbf{x}^{pl}$ and $\mathbf{x}^{pr}$ are the positions of the two ends (left- and right-most membrane points) of the prolate spheroid, and $\mathbf{x}^c = (x_1^c, x_2^c, x_3^c)$ is the position of a membrane point of the resulting curved prolate capsule mapped with the membrane point of the prolate spheroid at position $\mathbf{x}^p = (x_1^p, x_2^p, x_3^p)$; $k$ has units of inverse length, which can be nondimensionalized by $c$ to define the degree of curvature $K = kc$.

The instantaneous orientation of a curved prolate capsule is defined by two unit vectors, namely $\mathbf{p}$ and $\mathbf{n}$. The vector $\mathbf{p}$ is the normalized end-to-end vector that connects the left- and right-most membrane points of the capsule. In this work, the midpoint of the $\mathbf{p}$ vector of the capsule is initially placed at the origin of the unbounded domain. To define $\mathbf{n}$, we first mark a membrane point $\mathcal{A}$ lying in the plane of symmetry of the capsule that contains $\mathbf{p}$. The vector $\mathbf{n}$ is then uniquely defined as the unit vector passing through $\mathcal{A}$ and perpendicular to $\mathbf{p}$ that bisects $\mathbf{p}$ when the capsule is not deformed, as illustrated in FIG. 4.1. Note that for a deformed capsule, the intersection of $\mathbf{n}$ and $\mathbf{p}$ can be off-center of $\mathbf{p}$. In this work, initial conditions are chosen so that $\mathbf{p}$ is initially in the $x$-$z$ plane, and the initial angle between $\mathbf{p}$ and the $x$ axis is denoted as $\alpha$. The initial angle between $\mathbf{n}$ and its projection $\mathbf{n}'$ onto the $x$-$z$ plane is $\beta$ (note that $\mathbf{n}' \perp \mathbf{p}$). Thus the initial orientation of the capsule is given by $\alpha$ and $\beta$. For example, $[\alpha, \beta] = [0, \pi/2]$ means that the capsule is initially in the $x$-$y$ plane with $\mathbf{p}$ aligned with the $x$ axis and $\mathbf{n}$ with the $y$ axis. If the capsule is not curved, then $\beta$ is irrelevant to its orientation and dynamics.

The dynamics of the capsules are simulated using a model incorporating both shear elasticity and bending resistance. The behavior of the capsule membrane in response to the in-plane shear elastic force is described using the Skalak model [Skalak *et al.*, 1973] (Eq. 3.10), which predicts a strain hardening behavior for the membrane. The deformability of the capsule is characterized by the nondimensional capillary number $\mathrm{Ca} = \eta\dot{\gamma}c/G$, where $\eta$ is the viscosity of the suspending fluid, $c$ the half-length of the prolate capsule, and $G$ the in-plane shear modulus of the membrane. In this work the capsules are taken to be stiff in accordance with the biomechanical properties of the membrane of a sickle RBC, with Ca lower than 0.2 assuming the shear rate $\dot{\gamma}$ of blood

flow in the microcirculation $\sim 10 - 10^3$ s$^{-1}$ [Lipowsky, 2013], the characteristic length $c$ of a typical sickle RBC $\sim 5 - 6$ $\mu$m [Byun *et al.*, 2012], the viscosity of plasma $\eta \sim$ 1.71 mPa s [Laogun *et al.*, 1980], and the in-plane shear modulus of a sickle RBC membrane $G \sim 29.8$ $\mu$N/m [Byun *et al.*, 2012]. The bending modulus of the capsule $K_B$ is expressed nondimensionally by $\hat{\kappa}_B = K_B/c^2G$, which is $O(10^{-4} - 10^{-2})$ in the physiological context [Evans *et al.*, 2008, Betz *et al.*, 2009]; here we set $\hat{\kappa}_B = 0.04$ for all capsules. In this work, the natural shape for shear and the spontaneous shape for bending elasticities of the capsule membrane are both chosen to be the same as its rest shape, so that any in-plane or out-of-plane deformation would lead to an increase in the membrane energy and thus to an elastic restoring force. See Section 3.2 for details regarding the model for the mechanics of the capsule membrane.

The total membrane strain force density $\mathbf{f^m}$ can be calculated by taking the first variation of the total capsule membrane energy (Eq. 3.9), which then gives $\mathbf{f^m} = \mathbf{f^b} + \mathbf{f^s}$, where $\mathbf{f^b}$ and $\mathbf{f^s}$ are bending and shear elastic force densities, respectively. The capsule membrane is discretized into 320 piecewise flat triangular elements, resulting in 162 nodes. We have verified that increasing the number of nodes makes no difference to the cell dynamics. Based on this discretization, the calculation of the total membrane force density $\mathbf{f^m}$ follows the work of Kumar and Graham [2012a] and Sinha and Graham [2015] using approaches given by Charrier *et al.* [1989] for the in-plane shear force density $\mathbf{f^s}$ and Meyer *et al.* [2002] for the out-of-plane bending force density $\mathbf{f^b}$, respectively.

### 4.2.2 Fluid motion

As noted in Section 4.2.1, the characteristic shear rate $\dot{\gamma}$ of blood flow in the microcirculation is $\sim 10 - 10^3$ s$^{-1}$ [Lipowsky, 2013], the length scale $c$ of a typical sickle RBC $\sim 5 - 6$ $\mu$m [Byun *et al.*, 2012], the viscosity of plasma $\eta \sim 1.71$ mPa s [Laogun *et al.*, 1980], and its density $\rho \sim 10^3$ kg/m$^3$. The magnitude of the particle Reynolds number $\mathrm{Re}_p = \rho\dot{\gamma}c^2/\eta$ obtained using these parameters is $\sim O(10^{-4} - 10^{-2})$, which is assumed to be sufficiently small so that the fluid motion is governed by the Stokes equation. To determine the velocity field at each time instant, we employ a boundary integral method [Pozrikidis, 1992, Kumar and Graham, 2012a] for simulations in unbounded simple shear flow. Details of the numerical method for determining the velocity field are described in Section 3.3. Once the flow field is obtained, the positions of the element nodes on the discretized capsule membrane are advanced using a second-order Adams-Bashforth method with time step $\Delta t = 0.02\mathrm{Ca}l$, where $l$ is the minimum node-to-node distance. Time is nondimensionalized by the constant shear rate $\dot{\gamma}$.

### 4.2.3 Model validation

The implementation of the numerical methods used in this work has been validated with test problems on the velocity of rigid particles and drops between parallel walls in pressure driven flow, and the numerical algorithms for the capsule membrane mechanics including in-plane shear elasticity and out-of-plane bending elasticity have been validated with the deformation of spherical capsules in simple shear flow. For details, see [Kumar and Graham, 2012a] and [Sinha and Graham, 2015]. As a further validation, we compare here the numerically determined inclination profile for a stiff

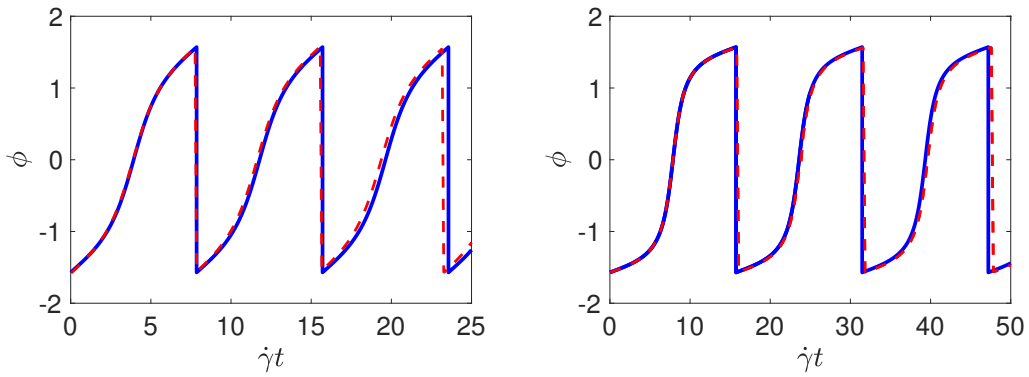



**Figure 4.2:** Evolution of inclination angle $\phi$ for a stiff prolate spheroid (Ca = 0.06) with (a) $r_p = 2.0$ and (b) $r_p = 4.8$, respectively. Solid blue lines are predictions by Jeffery's theory and red dashed lines are simulation results.

prolate spheroid (Ca = 0.06) with the prediction by Jeffery's theory [Jeffery, 1922],

$$\tan\phi = r_p \tan\left(\frac{\dot{\gamma}t}{r_p + {r_p}^{-1}} + \phi_0\right), \tag{4.3}$$

where $\phi$ is the inclination angle between the major axis of the prolate spheroid ($\mathbf{p}$) and the $y$ direction, and $\phi_0$ its initial value; here $\phi_0 = \pi/2$ since the prolate spheroid is initially aligned with the $x$ axis. Figure 4.2 shows the evolution of $\phi$ with nondimensionalized time $\dot{\gamma}t$. Good agreement between numerical simulation and Jeffery's theory (Eq. 4.3) is observed for the prolate spheroid with either a low ($r_p = 2.0$) or a high ($r_p = 4.8$) aspect ratio. The very small discrepancy in each case derives from the non-zero deformability of the prolate spheroid, and vanishes as Ca approaches zero.

## 4.3 Results and discussion

### 4.3.1 Dynamics of deformable straight prolate capsules

In this section, we investigate the dynamics of a stiff prolate spheroidal capsule ($r_p$ = 4.8, Ca = 0.12). Here we keep the viscosity ratio $\lambda = 1$. We first consider the case where the prolate capsule is initially aligned with the $x$ axis, i.e., $\alpha = 0$. The long-time trajectories (up to $\dot{\gamma}t = 2000$) of the end-to-end vector **p** and the normal vector **n** on the unit sphere are plotted in FIG. 4.3. In this case, both **p** and **n** appear to trace out a closed circle, indicating that the capsule is taking a steady symmetric tumbling motion in the $x$-$y$ plane.

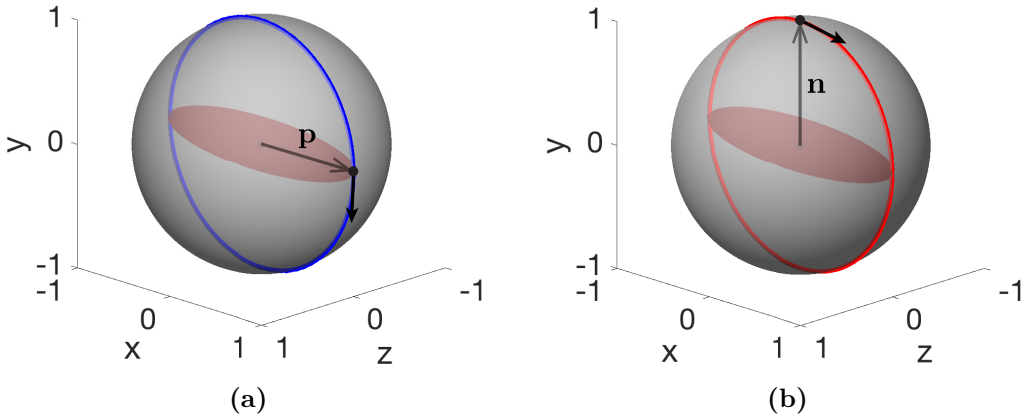



**Figure 4.3:** Trajectories on the unit sphere of (a) **p** and (b) **n** for a prolate spheroid ($r_p$ = 4.8, Ca = 0.12) with initial orientation $\alpha = 0$ (up to $\dot{\gamma}t = 2000$).

We then consider a perturbation of the initial orientation by a small angle $\alpha = \pi/36$. The trajectories of **p** and **n** vectors on the unit sphere are shown in FIG. 4.4. It can be observed that both $p_z$ and $n_z$ show an oscillation around zero whose amplitude decays to zero as time increases (FIG. 4.5), where $p_z$ and $n_z$ are the components of

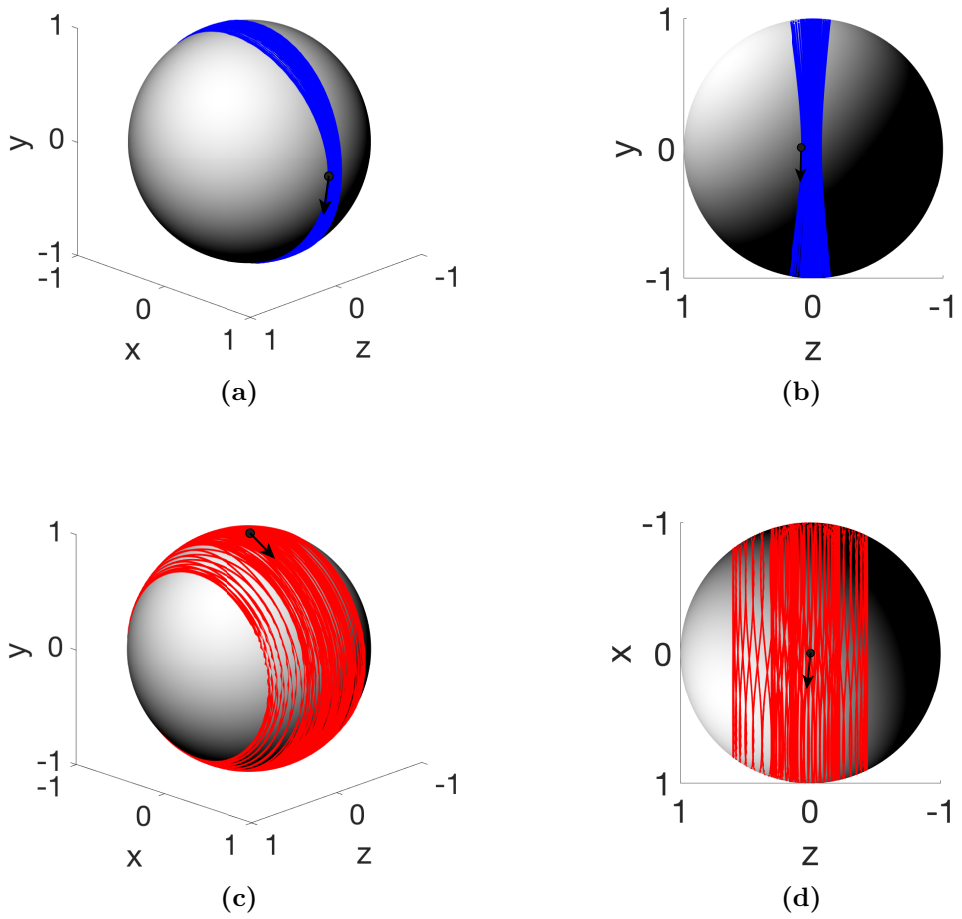



**Figure 4.4:** Trajectories on the unit sphere of **p** ((a) and (b) ($y$-$z$ view)) and **n** ((c) and (d) ($x$-$z$ view)) for a prolate spheroid ($r_p = 4.8$, Ca $= 0.12$) with initial orientation $\alpha = \pi/36$.

**p** and **n** in the vorticity direction, respectively. The director **p** crosses the $x$-$y$ plane back-and-forth (as indicated by the sign change of $p_z$ in FIG. 4.5), exhibiting non-Jeffery-like dynamics, in the sense that for Jeffery orbits, the director **p** never crosses the shear-gradient plane. The dynamics of **n** are much more complicated. The trajectory reaches a quasisteady state position on either hemisphere alternately every time $p_z$ changes its sign, as observed in FIG. 4.4d, and the quasisteady state position gets closer and closer to zero, which is consistent with the damped oscillation of $n_z$

(FIG. 4.5). All these behaviors indicate that under small perturbation, the orbit of a slightly deformable prolate spheroidal capsule evolves back towards the symmetric tumbling motion in the $x$-$y$ plane, indicating that the symmetric tumbling orbit in the $x$-$y$ plane is stable.

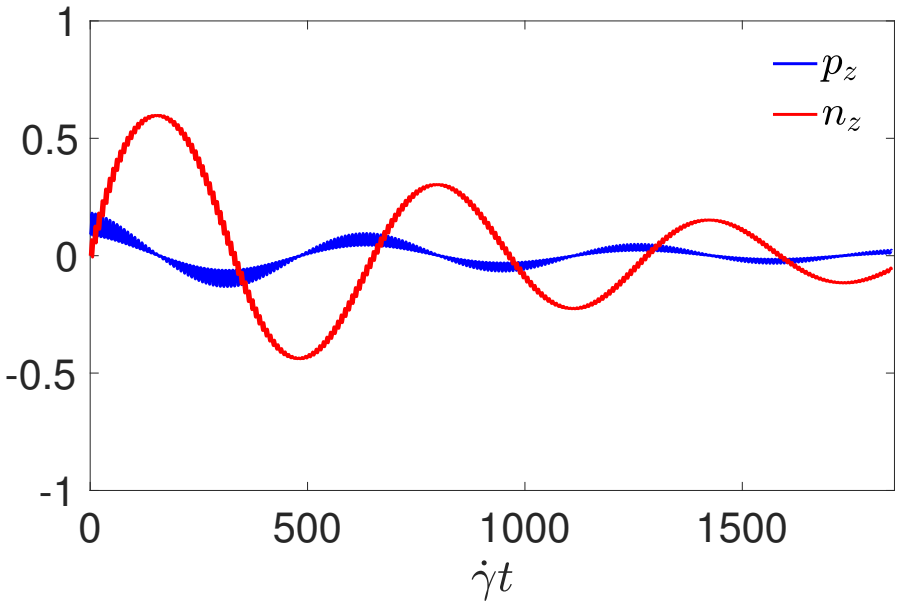



**Figure 4.5:** The evolution of the $p_z$ and $n_z$ for a prolate spheroid ($r_p = 4.8$, Ca $= 0.12$) with initial orientation $\alpha = \pi/36$.

By further increasing the initial angle $\alpha$ of the prolate spheroid off the $x$ axis, we observe that for an arbitrary $\alpha$, the orbit of the prolate spheroid evolves towards the symmetric tumbling in the $x$-$y$ plane regardless of the initial orientation. This shows that the in-plane symmetric tumbling is the globally stable state for the prolate spheroidal capsules in the parameter regime considered. This result is similar to that by Villone *et al.* [2015] for a neo-Hookean elastic solid prolate spheroid: when initially oriented off the shear plane, a stiff particle with a high aspect ratio would evolve towards tumbling motion in the shear plane with $p_z$ approaching zero. In

addition, this stable in-plane tumbling orbit that we find for an inertialess slender prolate capsule was also observed in the analytical prediction by Subramanian and Koch [2006] and the numerical investigation by Mao and Alexeev [2014] for a solid prolate particle considering particle inertia, except that in our work the degeneracy of Jeffery's solution [Jeffery, 1922] due to the linearity of the Stokes flow is broken by deformability of the capsule instead of inertial effect.

Prior to our work, Dupont *et al.* [2013] and Cordasco and Bagchi [2013] both investigated the out-of-shear plane dynamics of isolated prolate capsules in simple shear flow, revealing that a prolate capsule takes rolling, or a drifting precession towards the vorticity axis, as the stable dynamical mode at lower capillary numbers, which is different from our result. In our work, the spontaneous shape used for modeling the bending resistance of the membrane is chosen to be the same as the rest shape of the prolate capsule, while in [Cordasco and Bagchi, 2013] the spontaneous curvature was set to zero everywhere for the membrane surface, i.e., the spontaneous shape was a flat sheet; in [Dupont *et al.*, 2013], bending resistance was not even incorporated into the membrane mechanics. In addition, both Dupont *et al.* [2013] and Cordasco and Bagchi [2013] used a much lower value for the area dilatation parameter $C_a$ in the Skalak membrane model [Skalak *et al.*, 1973], i.e., $C_a = 1.0$, while we set $C_a$ to 10.0 which allows less area change of the membrane; they focused on prolate capsules with much lower asphericity ($r_p \leqslant 3.0$) as compared to the more elongated prolate capsule ($r_p = 4.8$) in our study. We have been able to reproduce Cordasco and Bagchi's result [Cordasco and Bagchi, 2013] for a prolate capsule at Ca = 0.2 with the spontaneous curvature, aspect ratio, and membrane area dilatation parameter of the capsule tuned to the same corresponding values as used in their

work, which demonstrates that the difference in the stable orbits originates from the differences in model as described above, with an indication that the capsule dynamics might be sensitive to its spontaneous shape.

### 4.3.2 Dynamics of deformable curved prolate capsules

In this section, we perform a systematic investigation of the dynamics of curved prolate spheroids at low Ca as described in Section 4.2.1, which serve as a model for the typical crescent-shaped sickle RBCs. The results for $\lambda = 1$ are presented and discussed first.

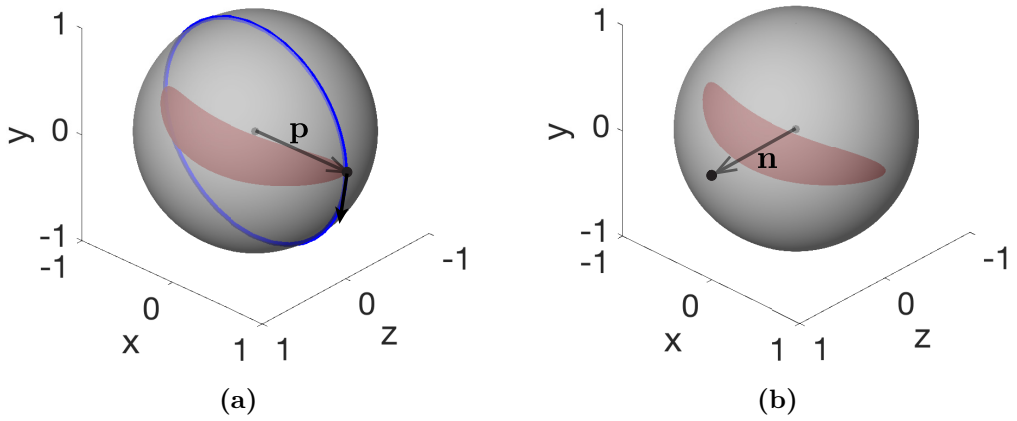



**Figure 4.6:** Trajectories of **p** (a) and **n** (b) for a curved prolate capsule with initial orientation $[\alpha, \beta] = [0,0]$ at the early stage of simulation ($0 < \dot{\gamma}t < 500$).

We first examine the early-stage dynamics ($0 < \dot{\gamma}t \lesssim 500$) of curved prolate capsules in the case of Ca $= 0.12$ and $K = 0.36$ with various initial orientations, beginning with the case where **p** is initially aligned with the $x$ direction and **n** with the $z$ direction. Here the trajectory of **p** traces out a closed circle on the unit sphere (FIG. 4.6a), while **n** remains fixed (FIG. 4.6b), which indicates that the capsule

is taking a sideways Jeffery-like tumbling motion. In the case of $[\alpha, \beta] = [0,\pi/6]$ (FIG. 4.7a and 4.7d), $\mathbf{p}$ is observed to cross the $x$-$y$ plane back and forth, exhibiting a wobbling motion which is not Jeffery-like, as shown in FIG. 4.8a. We then consider the case where $[\alpha, \beta] = [0,\pi/2]$, i.e., the capsule is completely lying in the $x$-$y$ plane initially, with $\mathbf{p}$ aligned with the $x$ direction and $\mathbf{n}$ with the $y$ direction. The closed circular orbits on the unit sphere indicate that the capsule is taking a rigid-body-like symmetric tumbling motion as its early-stage dynamics (FIG. 4.7b and 4.7e). In the case $[\alpha, \beta] = [\pi/6,\pi/3]$, a more Jeffery-like orbit is observed (FIG. 4.7c and 4.7f), in the sense that $\mathbf{p}$ does not cross the shear plane. Here it is noteworthy that in a Jeffery-like orbit, the trajectory of $\mathbf{n}$ spans both hemispheres divided by the shear plane on the unit sphere (FIG. 4.7f), while it only appears on one hemisphere of the unit sphere in the non-Jeffery-like orbit observed in the case of $[\alpha, \beta] = [0,\pi/6]$ described above (FIG. 4.7d).

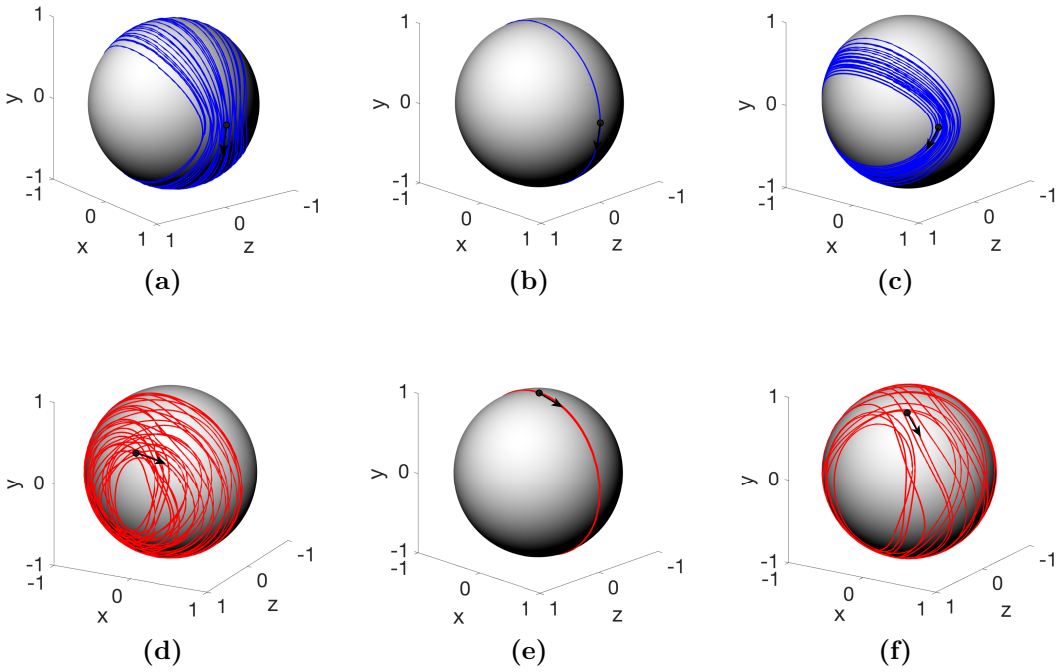



**Figure 4.7:** Early-stage trajectories on the unit sphere of the **p** (blue) and **n** (red) vectors of a curved prolate capsule with initial orientation $[\alpha, \beta] = [0,\pi/6]$ $(0 < \dot{\gamma}t < 500)$ (a,d), $[0,\pi/2]$ $(0 < \dot{\gamma}t < 100)$ (b,e), and $[\pi/6,\pi/3]$ $(0 < \dot{\gamma}t < 400)$ (c,f), respectively.

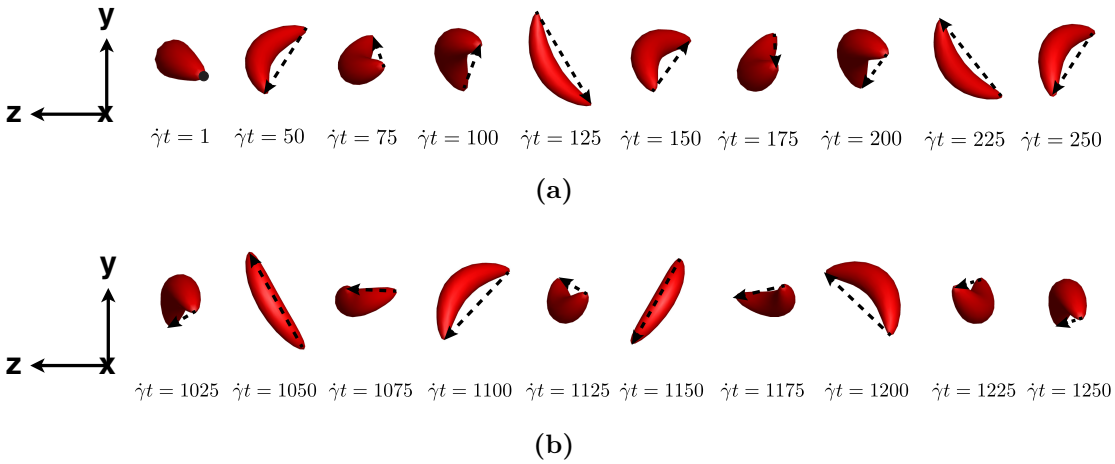



**Figure 4.8:** Time sequence images (front view) of the early-stage (a) and long-time (b) motions of a curved prolate capsule with initial orientation $[\alpha, \beta] = [0,\pi/6]$. The dashed arrow in each image represents the **p** vector at the corresponding time spot.

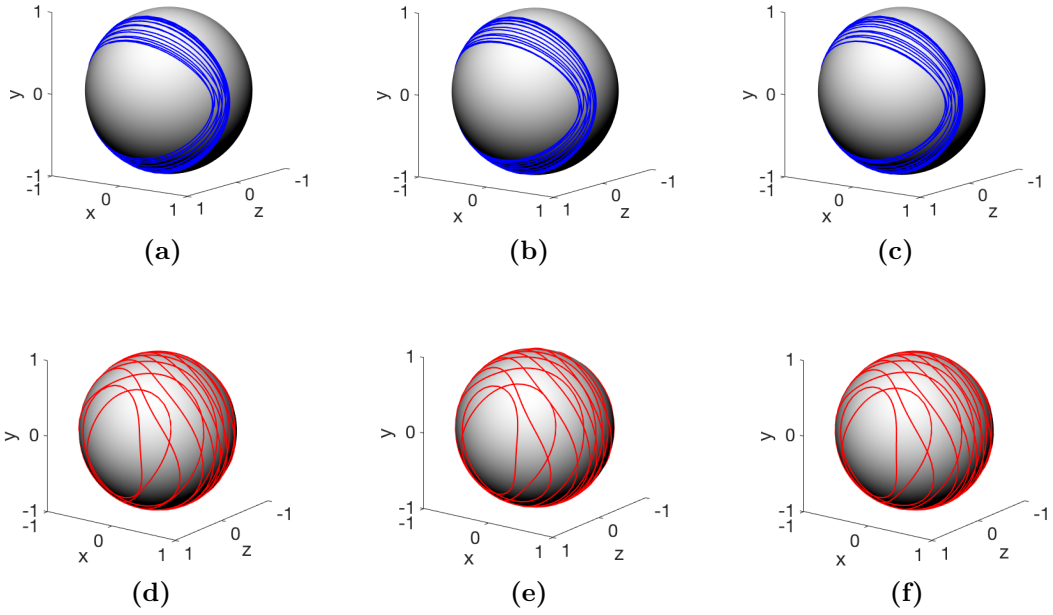
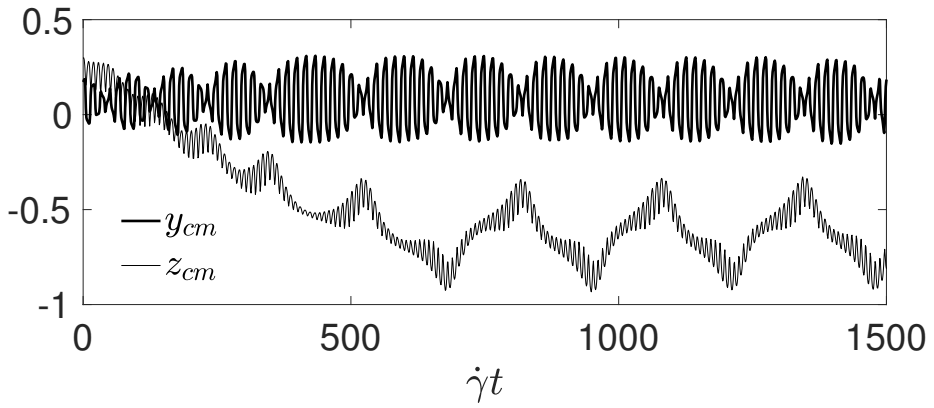



**Figure 4.9:** Long-time trajectories on the unit sphere of the **p** (blue) and **n** (red) vectors of a curved prolate capsule with initial orientation $[\alpha, \beta] = [0,\pi/6]$ (a,d), $[0,\pi/2]$ (b,e), and $[\pi/6,\pi/3]$ (c,f), respectively.

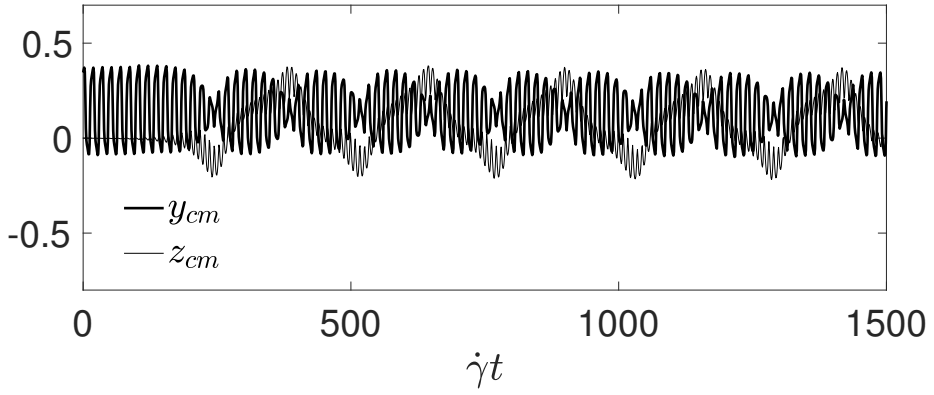
The early-stage dynamics of the curved prolate capsules described above, however, are all found to be long-lived transients. Figure 4.9 shows the long-time ($\dot{\gamma}t > 1000$) trajectories of the **p** vector of curved prolate capsules with different initial orientations on the unit sphere. The long-time dynamics of the capsules, regardless of their early-stage orbits, all evolve into a quasiperiodic kayaking motion that might be described as a "modulated Jeffery orbit". We will elaborate below on the connection to Jeffery orbit, but for the moment we simply note that the long-time motion of **p** is independent of the initial orientation of the capsules, as indicated by the nearly identical trajectories of **p** on the unit sphere (FIG. 4.9). Qualitatively, these orbits have a fast time scale corresponding to one cycle of kayaking, with a much longer time scale describing a slow modulation of the orbit. Each kayaking cycle is slightly different than the previous, a fact that can be attributed to the dynamics of **n**, which are

coupled to those of **p** for a curved particle (or indeed any nonaxisymmetric particle). Figure 4.8b shows snapshots of a long-time orbit. Recall that quasiperiodic orbits are also found for triaxial ellipsoids [Hinch and Leal, 1979] and curved rigid fibers [Wang *et al.*, 2012]. In all case this is associated with the breaking of axisymmetry and the coupling between **p** and **n**. We do not observe chaotic dynamics under any conditions considered here.

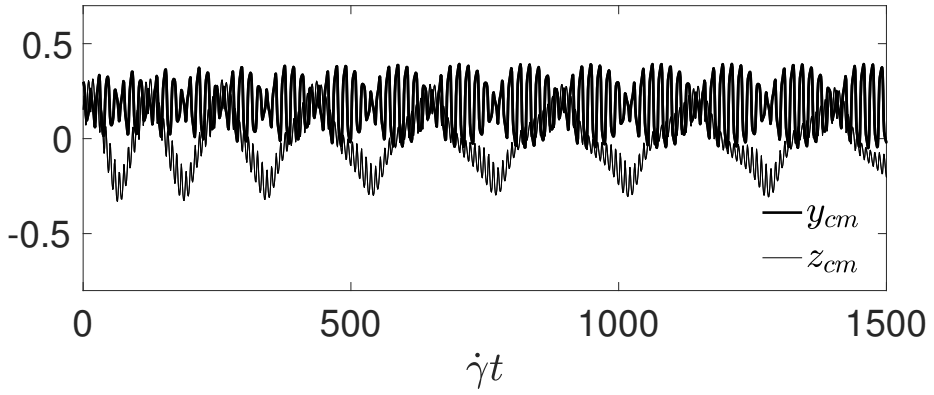
The two time scales noted above are also observed in the long-time center-of-mass position profiles shown in FIG. 4.10, with a shorter time scale representing one cycle of the kayaking motion described above superimposed onto a longer time scale corresponding to the orbit modulation. In the parameter regime considered here, we have seen no evidence of drift in the $y$ ("wall normal") direction. This is in contrast to the observations in [Wang *et al.*, 2012] for curved rigid fibers in the "flipping and scooping" regime; we believe the difference arises from the modest aspect ratios considered here, which are much smaller than those studied by Wang *et al.* [2012]. We do, however, observe a transient phase of spanwise drift in the case of the capsule initialized to perform a sideways tumbling motion. This vanishes once the cell reaches its long-time orientational trajectory. Although there is no drift at long times, both the $y$ and $z$ components of the center of mass oscillate as the cell kayaks.




**(a)**




**(b)**




**(c)**

**Figure 4.10:** Evolution of $y$- and $z$-components $y_{cm}$ and $z_{cm}$ of the center-of-mass position of curved prolate capsules with initial orientations $[\alpha, \beta] = [0,\pi/6]$ (a), $[0,\pi/2]$ (b), and $[\pi/6,\pi/3]$ (c).

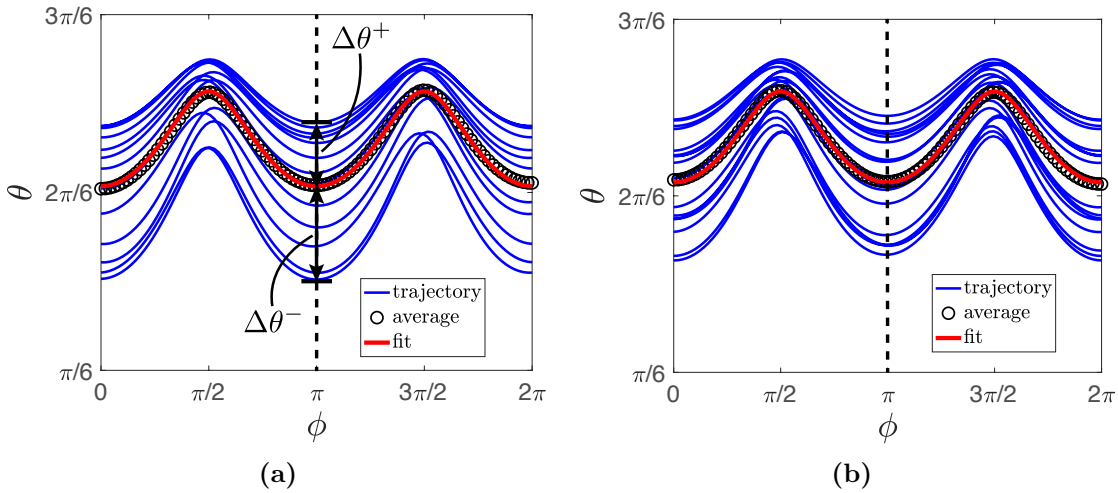



**Figure 4.11:** The long-time trajectory (blue curve) of a curved prolate capsule in terms of $\phi$ and $\theta$ and the average trajectory (black circles). The red curve represents the fit of the average trajectory using Eq. 4.5. The black dashed line corresponds to $\phi = \pi$. $\Delta\theta^+$ and $\Delta\theta^-$ denote the maximum positive and negative deviations, respectively, of the instantaneous trajectory from the mean when $\phi = \pi$. (a) Ca = 0.12, $K = 0.36$, $\lambda = 1$; (b) Ca = 0.06, $K = 0.39$, $\lambda = 5$.

Now we return to the issue of the connection with Jeffery orbits. The blue curve in FIG. 4.11a shows the long-time trajectory for the case Ca = 0.12, $K = 0.36$ (for which FIG. 4.9 shows the trajectory of $\mathbf{p}$ on the unit sphere), expressed in spherical coordinates $\phi$ and $\theta$ based on the coordinate system used in Jeffery's theory [Jeffery, 1922], i.e., $\phi$ is the azimuthal angle with respect to the $y$ axis and $\theta$ is the polar angle with respect to the $z$ axis. With this representation, we can find a mean trajectory $\bar{\theta}(\phi)$ by averaging $\theta$ over the trajectory at each $\phi$. This result is represented by the black circles in FIG. 4.11a. For a true Jeffery orbit of a rigid spheroid with orbit constant $C$ and aspect ratio $\ell$, the relation between $\phi$ and $\theta$ is given by

$$\tan\theta = \frac{C\ell}{\left(\ell^2\cos^2\phi + \sin^2\phi\right)^{1/2}}. \tag{4.4}$$

We have found that in all cases considered here, we can approximate, with very

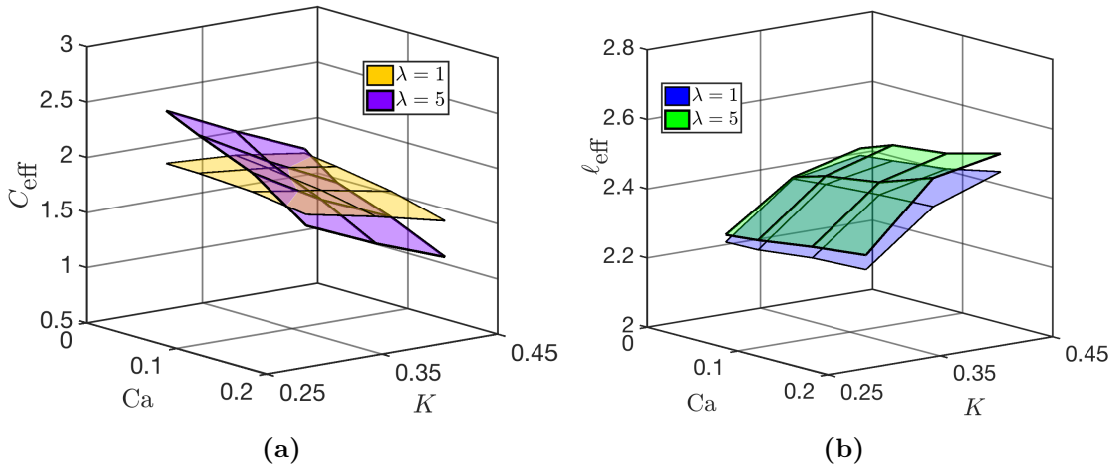



**Figure 4.12:** The dependencies of (a) the effective orbit constant $C_{\text{eff}}$ of the long-time orbit and (b) the effective aspect ratio $\ell_{\text{eff}}$ on the deformability Ca and the degree of curvature $K$ of the curved prolate capsules.

good accuracy, the curve $\bar{\theta}(\phi)$ as a Jeffery orbit for a spheroid with an effective orbit constant $C_{\text{eff}}$ and effective aspect ratio $\ell_{\text{eff}}$. That is, we can use $C_{\text{eff}}$ and $\ell_{\text{eff}}$ as fitting parameters in the expression

$$\tan\bar{\theta} = \frac{C_{\text{eff}}\ell_{\text{eff}}}{\left(\ell_{\text{eff}}^2\cos^2\phi + \sin^2\phi\right)^{1/2}}. \tag{4.5}$$

The red curve in FIG. 4.11a shows this approximation for Ca $= 0.12$, $K = 0.36$.

This observation enables us to succinctly characterize the effects of deformability and curvature on the long-time dynamics. We have computed long-time trajectories over a range of Ca and $K$ and computed the resulting values of $C_{\text{eff}}$ and $\ell_{\text{eff}}$. These results are summarized in FIG. 4.12. It is observed that $\ell_{\text{eff}}$ increases weakly as $K$ increases but shows very little dependency on Ca (FIG. 4.12b). More importantly, $C_{\text{eff}}$ decreases as either Ca or $K$ increases (FIG. 4.12a), indicating a shift of the orbit towards log-rolling motion as curvature or deformability increase.

For completeness, we briefly consider the deviations of the instantaneous trajectories from the mean curve $\bar{\theta}(\phi)$. The maximum positive and negative deviations from the mean when $\phi = \pi$ are denoted as $\Delta\theta^+$ and $\Delta\theta^-$ (FIG. 4.11a). The relative deviations $\Delta\theta/\overline{\theta}$ are found to be insensitive to the parameters in the range considered here, with $0.16 < \Delta\theta^+/\overline{\theta} < 0.19$, and $-0.35 < \Delta\theta^-/\overline{\theta} < -0.30$.

Under physiological conditions, the cytoplasmic fluid inside an RBC has a higher viscosity than the surrounding plasma [Byun *et al.*, 2012]; $\lambda \approx 5$. We have therefore also performed simulations with $\lambda = 5$, finding that the long-time trajectory of a curved prolate capsule within the parameter space considered in this work still indicates a quasiperiodic kayaking motion with no net cross-stream drift, similar to what is observed for $\lambda = 1$. Furthermore, the $\bar{\theta}(\phi)$ can still be well approximated using Jeffery's analytical solution (Eq. 4.5), with $C_{\text{eff}}$ and $\ell_{\text{eff}}$ determined by fitting. Figure 4.11b shows an example of this fit, with $\text{Ca} = 0.06$, $K = 0.39$, $\lambda = 5$. Figure 4.12 shows the values of $C_{\text{eff}}$ and $\ell_{\text{eff}}$ for $\lambda = 5$ over the same range of Ca and $K$ considered for $\lambda = 1$. The values of either parameter only show minor differences between the two viscosity ratios, so the trends with Ca and $K$ for $\lambda = 1$ still hold qualitatively for $\lambda = 5$.

## 4.4 Conclusion

We investigated the dynamics of neutrally-buoyant, slightly deformable straight and curved prolate capsules subjected to unbounded simple shear flow at zero Reynolds number using direct simulations. The curved prolate capsules in this work serve as a model for the typical crescent-shaped sickle RBCs in sickle cell disease (SCD), and we

aimed to show the effects of initial orientation, membrane deformability and curvature of the capsules on their dynamics.

The dynamics of the capsules are simulated using a full model incorporating both shear and bending elasticities. The parameter regime is based on the range of experimentally determined values for blood flow in the microcirculation. We revealed that with low deformability, straight prolate spheroidal capsules take tumbling in the shear plane as the unique globally stable orbit independent of the initial orientation. As the trajectories of the straight prolate capsules transiently evolve towards this in-plane tumbling, the director can cross the $x$-$y$ plane back and forth, showing a non-Jeffery-like motion.

Curved prolate capsules exhibit complicated and interesting dynamics due to the combined effects of membrane deformability Ca and the curvature $K$ of the capsules. At short times, a non-Jeffery-like behavior, in which the director (end-to-end vector) of the capsule crosses the shear-gradient plane periodically, is observed for specific initial orientations. Steady drift of the center of mass in the vorticity direction is also observed for some initial orientations. At long times, however, the trajectories of the curved capsules, regardless of their initial orientations, all evolve towards a Jeffery-like quasiperiodic kayaking orbit with the center-of-mass position of a curved capsule crossing the shear plane periodically instead of remaining in it. No cross-stream drift is found. Under all conditions studied, the average of the long-time orbit can be well approximated using the analytical solution for Jeffery orbits with an effective orbit constant $C_{\text{eff}}$ and aspect ratio $\ell_{\text{eff}}$. A parameter study further reveals that $C_{\text{eff}}$ decreases as the capsule becomes more deformable or curved, indicating a shift of the orbit towards log-rolling motion. This conclusion holds qualitatively as the viscosity

ratio between the fluids inside and outside the capsule increases from $\lambda = 1$ to $\lambda = 5$.

Overall, these results represent an effort to understand the motion of single sickle RBCs, taking into account the pathologically altered shape as well as the elastic and bending moduli of these diseased cells. Major aspects of the pathophysiology of SCD remain poorly understood and currently, there is an increased focus on how aberrant cell interactions, between sickle RBCs and other blood cells (i.e. platelets and leukocytes) or between sickle RBCs and endothelial cells, may contribute to phenomena such as thrombosis or vascular inflammation that are known to be vital part of the process of SCD. In particular, the effective orbit constant of a sickle cell moving near a blood vessel wall may reflect the propensity for that cell to collide with and potentially damage the wall. For example, a sickle cell with a high orbit constant tends to tumbling or kayaking motion, which physically will have a greater chance to poke and damage the vessel wall than a rolling cell with a much lower orbit constant. In addition, the comparison of our results with those by Cordasco and Bagchi [2013] with different membrane mechanics suggests that the dynamics of the capsules have a nontrivial dependence on the membrane behavior. Future work, both computational and experimental, will need to address how best to model this behavior for sickle cells in order to reflect the dynamical motions of sickle cells in blood flow. More broadly, the results of this work demonstrate how the mechanical properties and distorted cell shape of sickle RBCs lead to distinct trajectories that may, in turn, cause pathologic biophysical activation of other cells, and may provide insight into how these disparate aspects of SCD are ultimately linked. That knowledge will then lead to improved methods to diagnose complications of and new therapeutic targets for SCD.

# Chapter 5

# Flow-induced segregation and dynamics of red blood cells in sickle cell disease[a]

## 5.1 Introduction

Blood, a classic archetype of multicomponent suspensions, is composed primarily of erythrocytes, or red blood cells (RBCs), with a hematocrit (i.e. volume fraction of RBCs) ranging from $0.1-0.3$ in the microcirculation to $0.4-0.5$ in large vessels such as arteries [Fung, 1984]. Two other major species of cells in blood, namely leukocytes, or white blood cells (WBCs), and platelets, are both considerably outnumbered by RBCs, by $\sim 500-1000:1$ and $12-32:1$, respectively [Dean, 2005]. In addition to the drastic difference in population density, these three cellular components exhibit

[a]This chapter includes content from: Zhang, X., Caruso, C., Lam, W. A., and Graham, M. D. (2019). Submitted.

distinct contrasts in physical properties such as shape, size, and rigidity [Otto *et al.*, 2015]. Typically, RBCs are fluid-filled biconcave discoids with a radius of $\sim 3.8 - 4.0$ $\mu$m, WBCs are approximately spherical and slightly larger than RBCs, while platelets are the smallest. Healthy RBCs are highly flexible, while both WBCs and platelets are much stiffer. All these cellular components in blood are suspended in plasma. Under pathological conditions, however, diseased RBCs, such as those in patients suffering from sickle cell disease (SCD), often display substantial alterations in physical properties compared to healthy RBCs. These cellular-level alterations may lead to significant aberrance in the behavior of blood flow, and further cause complications. The insufficient understanding so far of both the dynamics of blood flow in SCD and the mechanism for complications associated with SCD, such as endothelial inflammation, has formed the principal motivation of the present work.

A significant feature of blood flow in the microcirculation, the network of microvessels ($5 - 200$ $\mu$m in diameter [Pappano and Wier, 2013]) consisting of arterioles, capillaries, and venules, is that all species of blood cells display a non-uniform distribution across the vessels. Flexible RBCs tend to migrate away from the vessel wall and form a RBC-depleted region termed cell-free layer next to the wall [Sutera and Skalak, 1993, Kumar and Graham, 2012b, Namgung and Kim, 2014, Kumar and Graham, 2015, Namgung *et al.*, 2017]. Stiff WBCs and platelets, in contrast, are found to reside near the vessel walls, a phenomenon known as margination [Tangelder *et al.*, 1985, Firrell and Lipowsky, 1989, Shevkoplyas *et al.*, 2005, Freund, 2007, Kumar and Graham, 2012b, 2015], which is of physiological significance as the prerequisite for inflammatory response and hemostasis. A large number of prior experiments [Aarts *et al.*, 1984, Goldsmith and Spain, 1984, Tangelder *et al.*, 1985, Eckstein *et al.*, 1988,

Firrell and Lipowsky, 1989, Yeh and Eckstein, 1994, Pearson and Lipowsky, 2000, Abbitt and Nash, 2003, Jain and Munn, 2009, Fay *et al.*, 2016, Spann *et al.*, 2016, Gutierrez *et al.*, 2018], both in vivo and in vitro, and computational studies [Sun and Munn, 2006, Freund, 2007, AlMomani *et al.*, 2008, Crowl and Fogelson, 2011, Zhao and Shaqfeh, 2011, Fedosov *et al.*, 2012, Zhao *et al.*, 2012, Reasor *et al.*, 2013, Fedosov and Gompper, 2014, Vahidkhah *et al.*, 2014, Mehrabadi *et al.*, 2015] have attempted to characterize the effects of a variety of parameters, such as cell stiffness, shear rate, channel width, hematocrit, and RBC aggregation, on the strength of margination of WBCs and platelets. For example, recent experiments by Fay *et al.* [2016] showed that glucocorticoid and catecholamine hormones, such as dexamethasone and epinephrine, significantly reduce the stiffness of WBCs, which, as a result, attenuates WBC margination and leads to a substantial increase in the clinical WBC count. Furthermore, margination-based cell separation has been realized using lab-on-a-chip devices. For example, motivated by WBC margination in the microcirculation, Shevkoplyas *et al.* [2005] achieved efficient separation of WBCs from whole blood using a simple network of microfluidic channels. Other examples include separation of stiffened RBCs such as those infected in malaria from the healthy ones utilizing margination or lateral displacement of the stiff cells [Hou *et al.*, 2010, Guo *et al.*, 2016, Chen *et al.*, 2017].

The segregation behavior in blood flow, i.e., the discrepancy in cross-stream distribution propensity of different species of blood cells, substantially arises from their shape, size, and rigidity contrasts [Kumar and Graham, 2011, Kumar *et al.*, 2014, Sinha and Graham, 2016]. In a more general context, these factors, among other properties of the particles, are the determinants of the segregation behavior in an arbitrary

flowing multicomponent suspension. A series of computational efforts have been made in the past years to examine the individual roles of various physical properties of the components in the segregation behavior. Kumar *et al.* [Kumar and Graham, 2011, Kumar *et al.*, 2014] numerically investigated the isolated role of rigidity difference in a binary suspension of neo-Hookean capsules subjected to either simple shear flow or pressure-driven flow in a planar slit. Here the rigidity (or deformability) of a capsule is characterized by the dimensionless capillary number, which represents the ratio of viscous stresses to elastic restoring stresses on the particle. They found that when the stiffer capsules are the dilute component, they display a substantial margination. In contrast, flexible capsules tend to enrich around the centerline of the channel when they are dilute, a behavior termed demargination. The effect of size contrast was also revealed [Kumar *et al.*, 2014]: in a mixture of large and small capsules with equal capillary number, the small capsules marginate while the large particles demarginate, in their respective dilute suspensions. Similarly, Sinha and Graham [2016] explored the shape-mediated segregation behavior in binary suspensions of spherical and ellipsoidal capsules in simple shear flow. In this work, all capules have the same capillary number, while the aspect ratio $\kappa$ of the ellipsoids is varied with either the equatorial radius or the volume of the capsules held constant; here $\kappa > 1$ and $\kappa < 1$ represent prolate and oblate spheroids, respectively. They showed that when the ellipsoids have the same equatorial radius as the spheres, capsules with lower $\kappa$ marginate as the dilute component in a suspension containing primarily capsules with higher $\kappa$. When all capsules have the same volume, however, spherical capsules always marginate when they are dilute, while ellipsoidal (both oblate and prolate) capsules demarginate as the dilute component. In addition, these controlled studies [Kumar and Graham,

2011, Kumar *et al.*, 2014, Sinha and Graham, 2016] all revealed that the near-wall peak in the number density distribution profile for the marginated component shifts towards the wall as the volume fraction of the suspension increases, with a decrease in the cell-free layer thickness.

Inspired by all of the findings from the aforementioned experimental and computational investigations, a number of phenomenological theories have been developed aiming to provide insight into understanding the segregation behavior in flowing multicomponent suspensions of deformable particles. Most of the theories have been grounded on taking into account two key sources of cross-stream particle fluxes in flowing suspensions under confinement: wall-induced migration flux away from the wall, which is ubiquitous for any deformable particles in a bounded flow [Smart and Leighton, 1991], and shear-induced diffusive flux due to hydrodynamic pair collisions between particles. Incorporating the effects of both sources of particle motion, Kumar and Graham [2012c] presented an idealized kinetic master equation model for a binary suspension of capsules with varying rigidity, and obtained the steady-state solution using a Monte Carlo simulation technique. They found that at low volume fractions, heterogeneous pair collisions between capsules of different components drive the segregation by rigidity difference, while at higher volume fractions, wall-induced migration and heterogeneous pair collisions have comparable contributions. The authors further revealed [Kumar *et al.*, 2014] that in a binary suspension of capsules with size contrast, the segregation behavior is mainly caused by the greater wall-induced migration velocity of the larger capsules. Similar methods have been employed to understand the dynamics and particle concentration distributions in either homogeneous suspensions or more complex binary systems [Zurita-Gotor *et al.*, 2012, Narsimhan

*et al.*, 2013, Qi and Shaqfeh, 2017]. An example is a recent work by Qi and Shaqfeh [2017], who predicted the distributions of RBCs and platelets in a binary suspension subjected to pressure-driven flow.

Based on approximations that collisions only occur between closely adjacent particles and result in very small post-collisional displacements, a mechanistic theory was developed by Henríquez Rivera *et al.* [2015] in which the master equation [Kumar and Graham, 2012c, Zurita-Gotor *et al.*, 2012, Narsimhan *et al.*, 2013] was simplified into a pair of drift-diffusion equations that have been denoted as the "simplified drift-diffusion (SDD)" model. In simple shear flow, closed-form analytical solutions for this model are attainable to describe cell-free layer formation and flow-induced segregation in binary suspensions of deformable particles. The predictions of cell-free layer thickness by this model are found [Henríquez Rivera *et al.*, 2016] to agree well with the values reported in other experimental [Bugliarello and Hayden, 1963], numerical [Kumar *et al.*, 2014] and theoretical [Narsimhan *et al.*, 2013] studies. Moreover, several regimes of segregation arise, depending on the value of a so-called "margination parameter", a determinant of the segregation propensity that characterizes the relative significance of the wall-induced migration and the collisional fluxes. Besides, a sharp "drainage transition", characterized by complete depletion of one component from the bulk flow towards the walls, is also identified. This drift-diffusion model was then utilized to understand the segregation behavior in binary suspensions of spherical and ellipsoidal capsules [Sinha and Graham, 2016], as described above, and found to well capture the key qualitative features of the shape-mediated margination and demargination. Later, this model was extended [Henríquez Rivera *et al.*, 2016] to describe suspension dynamics in pressure-driven flow, which is complicated due

to the nonuniform shear rate and in particular the fact that it vanishes at the centerplane. Numerical solutions predict margination regimes and a drainage transition qualitatively similar to those in the simple shear flow case.

The substantial progress by the extensive numerical and theoretical studies has not only disentangled the individual effects of the physical aspects of the particles and the suspensions in the segregation behavior, but also laid the groundwork for understanding the dynamics in more complex systems. Blood flow in SCD, as mentioned above, can considerably differ from the normal due to significant alterations in the physical properties of sickle cells compared to healthy RBCs. Deoxygenation of sickle hemoglobin (HbS) results in hydrophobic interactions among hemoglobin molecules, causing formation of long hemoglobin polymers. This polymer formation results in a variety of shapes for deoxygenated sickle cells [Byun *et al.*, 2012], including the classic sickle shape [Bertles and Milner, 1968]. Sickle cells also have a much smaller volume than healthy RBCs due to dehydration [Zucker and Cameron, 1976, Glader *et al.*, 1978]. In addition, a general increase in membrane rigidity has been determined for sickle cells compared to that of healthy RBCs [Messer and Harris, 1970, Nash *et al.*, 1984, Evans and Mohandas, 1987, Bunn, 1997, Byun *et al.*, 2012].

Complications associated with SCD related to RBC stiffening, which cause altered microvascular blood flow and acute vaso-occlusion followed by consequent tissue ischemia and infarction, have long been observed clinically. These effects only partially describe the pathophysiology of SCD, however, particularly as SCD is also known to be a vasculopathic disease in which endothelial cells that line the blood vessels are dysfunctional and in a pro-inflammatory state in most regions in the circulation. In many ways, SCD vasculopathy bears resemblance to that in cardiovascular dis-

ease characterized by the development of atherosclerosis, and relatedly, subsequent stroke remains a major cause of mortality in SCD. Despite such similarities, the underlying cause of chronic SCD vasculopathy remains unknown. Indeed, the fact that vasculopathy pervasively occurs even in the oxygenated conditions in both small and large vessels necessitates a new understanding of SCD pathophysiology that extends beyond and is independent of vaso-occlusion, which, in contrast, occurs only in the deoxygenated conditions in microvessels. In light of the advances in understanding the segregation behavior of flowing suspensions such as blood flow, how the abnormality in physical properties of sickle cells alters the dynamics of blood flow, and ultimately, how this alteration may be linked to the underlying mechanism for the complications in SCD, are questions to address.

Progress in the past decades in uncovering the pathophysiology of cardiovascular disease such as atherosclerosis may shed some light on the mechanism for vasculopathy in SCD. In particular, cardiovascular bioengineering research has demonstrated that endothelial cells mechanotransduce biophysical cues, such as the shear forces of the hemodynamic microenvironment, into cellular biological signals [Harrison *et al.*, 2006, Chien, 2007, Abe and Berk, 2014]. Additionally, pathological alterations of those forces lead to activation of pro-inflammatory signals within endothelial cells and subsequent development of atherosclerotic plaques *in situ* that are prone to myocardial infarction and stroke [Abe and Berk, 2014]. For example, Bao *et al.* [1999] measured the mRNA expression of MCP-1 and PDGF-A, two atherogenic genes related to endothelial inflammation, by endothelial cells subjected to laminar flows with different well-defined wall shear stress profiles, namely (1) ramp flow in which shear stress was smoothly changed from zero to a maximum value and then sustained, (2)

step flow in which shear stress was abruptly applied at flow onset followed by steady shear stress for a sustained period, and (3) impulse flow in which shear stress was abruptly applied and then removed. A steady shear stress profile was also considered for comparison. They showed that in general, rapid changes in shear stress (as in impulse flow and the onset of step flow) and steady shear stress (as in ramp flow and the steady component of step flow) stimulate and diminish the expression of both genes, respectively. In particular, the impulse flow case was found to induce the highest level endothelial expression of the pro-infammatory signals compared to the other profiles. Other studies [Davies, 1997, De Keulenaer *et al.*, 1998, Chen *et al.*, 1999, Akimoto *et al.*, 2000, Davis *et al.*, 2001, Dekker *et al.*, 2002, Hsiai *et al.*, 2003, Sorescu *et al.*, 2004, Li *et al.*, 2005, Harrison *et al.*, 2006] have also elucidated a variety of shear stress-induced signal transduction pathways of the endothelium, and revealed the opposing effects of steady and unsteady shear stresses on endothelial dysfunction and atherogenic events.

While well-studied in the context of cardiovascular disease, this issue has yet to be explored in SCD. To the best of our knowledge, there exist only a limited number of computational studies regarding the behavior of sickle cells in suspensions in association with probing the mechanism for SCD complications. Examples are [Lei and Karniadakis, 2013, 2015, Deng *et al.*, 2019], which aimed to investigate the mechanism for vaso-occlusive crisis. In these studies, simulations were performed for suspensions containing sickle cells in a cylindrical tube of diameter $D = 10$ $\mu$m, mimicking post-capillary flow, to quantify the consequences of adhesive interactions between sickle cells and the endothelium (tube wall) during flow, and determine the effects of cell morphology and rigidity. However, in accordance with the particular

focus on blood flow in post-capillaries, these studies considered suspensions with only a very small number of cells under strong confinement, so that characteristic dynamics of multicomponent suspensions such as flow-induced segregation and margination were not incorporated.

The aim of the present study is to take a first step towards understanding the dynamics of blood flow in more complex scenarios such as SCD. Using large-scale direct simulations, we investigate a number of binary suspensions containing primarily flexible healthy RBCs with a small fraction of stiff cells with different rest shapes in confined pressure-driven flow at zero Reynolds number. WBCs and platelets are not included in the suspensions due to their extremely small number fractions in blood flow. We predict that sickle cells display strong margination toward the walls due to their increased rigidity and reduced size compared to healthy RBCs. The effects of shape, size, and rigidity differences between the components on the behavior of different suspensions are studied. We also characterize the orbital dynamics of single cells in the suspensions. Furthermore, the hydrodynamic effects of the cell suspensions on the walls, particularly the additional wall shear stress induced by the marginated cells are quantified to establish a connection with issues in SCD such as shear-induced endothelial dysfunction.

The rest of the chapter is organized as follows: in Section 5.2 we describe the models for the cells and suspension systems considered in this work, as well as the numerical methods and algorithms employed to compute the flow field and cell motion; in Section 5.3 we present detailed results and discussion on the behavior of different suspensions and the dynamics of single cells, followed by a characterization of the hydrodynamic effects of the suspensions on the walls. Implications of these results

on the endothelial inflammation in SCD are also discussed. Concluding remarks are presented in Section 5.4.

## 5.2 Model formulation

### 5.2.1 Model and discretization

We consider a flowing suspension of deformable fluid-filled elastic capsules in a planar slit bounded by two parallel rigid walls (FIG. 3.1). In the wall-normal ($y$) direction, no-slip boundary conditions are applied to the two rigid walls at $y = 0$ and $y = 2H$, where $H$ is the distance from each wall to the centerplane of the slit domain. In the flow ($x$) and the vorticity ($z$) directions, periodic boundary conditions are imposed, with spatial periods $L_x$ and $L_z$, respectively. The suspension is subjected to a unidirectional pressure-driven (Poiseuille) flow, and the undisturbed flow velocity field is given by

$$\mathbf{u}^{\infty}(x, y, z) = 2U_0 \frac{y}{H}\Big(1 - \frac{y}{2H}\Big)\mathbf{e}_x, \tag{5.1}$$

where $U_0$ is the undisturbed flow velocity at the centerplane of the channel, and $\mathbf{e}_x$ is the unit vector in the $x$ direction. In the present study a constant pressure drop is imposed, which is equivalent to fixing the mean wall shear rate at $\dot{\gamma}_w = 2U_0/H$. We take the fluids outside and within the capsules to be incompressible and Newtonian with viscosity $\eta$ and $\lambda\eta$, respectively, so $\lambda$ denotes the viscosity ratio between the fluids inside and outside the capsules.

Different suspension systems comprising various types of cells are investigated in this work. Figure 5.1 shows the rest shapes of the cell models. A healthy RBC is

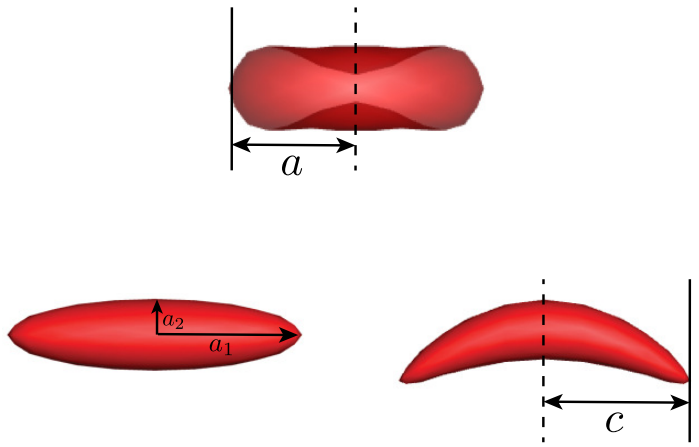



**Figure 5.1:** Rest shapes of a biconcave discoidal capsule (top) as a model for healthy RBCs, a straight prolate capsule (bottom left), and a curved prolate capsule (bottom right) as a model for typical sickle cells.

modeled as a flexible capsule with a biconcave discoidal rest shape [Evans and Fung, 1972, Sinha and Graham, 2015], with the geometry given by

$$y = \frac{a}{2}\sqrt{1-r^2}(C_0 + C_2 r^2 + C_4 r^4), \tag{5.2}$$

where $r^2x^2 + z^2 \leqslant 1$, $C_0 = 0.2072$, $C_2 = 2.0026$, and $C_4 = -1.1228$; $a$ denotes the radius of the biconcave discoid, which is $\sim 3.8 - 4.0$ $\mu$m for human RBCs. In contrast to a healthy RBC, a typical sickle cell is crescent-shaped with a characteristic length $c$ slightly greater than $a$ [Byun *et al.*, 2012, Jung *et al.*, 2016]. In this study, a sickle cell is modeled as a stiff capsule with a curved prolate spheroidal rest shape. This shape is constructed by first polar stretching and equatorial compression of a spherical capsule with radius $a$, which results in a slender prolate capsule with polar radius $a_1 = c = 1.2a$ and equatorial radius $a_2 = 0.25a$ (aspect ratio AR $= a_1/a_2 = 4.8$). The resulting straight prolate capsule is then subjected to a quadratic unidirectional displacement of membrane points perpendicular to the polar axis of the capsule, which eventually generates a curved prolate capsule. Details regarding

the transformation procedure for the sickle RBC model are found in Section 4.2.1. For our models, the volume of a straight or curved prolate capsule is $\sim 20\%$ that of a biconcave discoid.

Having introduced the models for the morphologies of different cells, we now describe the membrane mechanics of the capsules. In this work, the capsule membrane is modeled as an isotropic and hyperelastic surface that incorporates shear elasticity, area dilatation, and bending resistance; details of this membrane model are found in Section 3.2. Specifically, we use the Skalak law [Skalak *et al.*, 1973] (Eq. 3.10) to describe the in-plane shear elasticity of the capsule membrane, which includes an energy penalty for area change of the membrane and thus predicts a strain hardening behavior that is consistent with the experimentally determined response of an RBC membrane to stretching [Mills *et al.*, 2004, Sinha and Graham, 2015]. The deformability of a capsule in pressure driven flow is characterized by the dimensionless wall capillary number $\mathrm{Ca} = \eta\dot{\gamma}_w l/G$, where $\eta$ is the viscosity of the suspending fluid, $G$ the in-plane shear modulus of the membrane, and $l$ the characteristic length of the capsule. The bending modulus of a capsule, on the other hand, is expressed nondimensionally by $\hat{\kappa}_B = K_B/l^2G$, which is $\sim O(10^{-4} - 10^{-2})$ in the physiological context [Evans *et al.*, 2008, Betz *et al.*, 2009]; here we set $\hat{\kappa}_B = 0.04$ for all capsules, which also prevents the cell membranes from any buckling instabilities. For any capsule in this work, unless noted otherwise, the natural shape for shear and the spontaneous shape for bending elasticities of the capsule membrane are both chosen to be the same as the rest shape of the capsule, so that any in-plane or out-of-plane deformation would lead to an increase in the membrane energy and thus to an elastic restoring force. The capsule membrane is discretized into $N_\triangle$ piecewise flat triangular elements; in

this work $N_{\triangle} = 320$, resulting in 162 nodes. We have verified that increasing the number of nodes makes no difference to the cell dynamics, and this mesh resolution keeps the computational cost manageable given that very long simulation times are required for the dynamics of the suspensions to reach steady state. Note that in this work, steady state refers to the state in which the suspension dynamics are statistically invariant or stationary. Based on this discretization, the calculation of the total membrane force density $\mathbf{f^m} = \mathbf{f^b} + \mathbf{f^s}$, which derives from taking the first variation of the total membrane energy (Eq. 3.9), follows the work of Kumar and Graham [2012a] and Sinha and Graham [2015] using approaches given by Charrier *et al.* [1989] for the in-plane shear force density $\mathbf{f^s}$ and Meyer *et al.* [2002] for the out-of-plane bending force density $\mathbf{f^b}$, respectively. Details regarding these calculations are found in [Kumar and Graham, 2012a] and [Sinha and Graham, 2015].

Now we describe the suspension systems considered in this work. A base case is a homogeneous suspension of flexible biconcave discoidal capsules representing purely healthy RBCs. In our simulations Ca is always set to 1.6 for flexible biconcave discoids in all suspensions, which is in accordance with the biomechanical properties of the membrane of a healthy RBC within the physiological ranges, assuming the shear rate of blood flow in the microcirculation $\dot{\gamma}_w \sim O(10^2 - 10^3)$ s$^{-1}$ [Lipowsky, 2013], the viscosity of plasma $\eta \sim 1.2$ mPa s [Harkness and Whittington, 1970], and the in-plane shear modulus of a healthy RBC membrane $G \sim 7.1 \pm 1.6$ $\mu$N/m [Byun *et al.*, 2012].

One of the major aims of this study is to understand the effects of deformability, shape, and size contrast on the dynamics of a flowing suspension of capsules. To this end, different cases of binary suspensions are considered. The "primary" component, i.e., the component with a larger population, is always flexible biconcave discoids

(healthy RBCs), and denoted as '$p$'; for all binary suspensions, $\mathrm{Ca}_p$ is set to 1.6. The other component is stiff, termed "trace" and denoted as '$t$'. The number fractions for the capsules of these two components in all binary suspensions considered in this work are set to $X_p = 0.9$ and $X_t = 0.1$, respectively, with a number density ratio $n_p/n_t = 9$. These values are within the physiological ranges in the context of SCD, as all patients have a small population $(1-10\%)$ of sickle cells that are permanently stiff and misshapen [Caruso *et al.*, 2019]. In the first binary suspension, the '$t$' component is stiff biconcave discoidal capsules with the same rest shape as the flexible (healthy) ones to investigate the isolated role of rigidity difference in the dynamics of the binary suspension. In the second case, we study a binary suspension with the '$t$' component being stiff curved prolate capsules that represent typical sickle cells, and this system serves as an idealized model for blood flow in SCD. For comparison, we also consider a suspension containing stiff straight prolate capsules with no curvature to illustrate the effect of curvature on the behavior of the suspension. In all cases of the binary suspensions, $\mathrm{Ca}_t$ is always set to 0.4 for the '$t$' component to control variables. Indeed, this value is physiological given that the membrane shear modulus of a typical sickle cell is experimentally determined to be roughly four times that of a healthy RBC [Byun *et al.*, 2012].

In this study, the total volume fraction of the capsules is $\phi \approx 0.15$ for all suspensions, with $\phi$ being slightly lower for the cases containing curved and straight prolate capsules due to their smaller volume than a biconcave discoid, as noted above. This volume fraction is consistent with the physiological hematocrit in small vessels ($\sim 40$ $\mu$m across) in the microcirculation [Lipowsky *et al.*, 1980, Sarelius and Duling, 1982]. The domain is periodic in $x$ and $z$ with lengths $L_x = L_z = 2H = 10a$, where $a$ again

is the radius of a biconcave discoid as described above. The half-height of the domain $H = 5a$ so the confinement ratio $C = H/a = 5$. We show later (Section 5.3.1) that changing the spatial period ($L_x$) of the simulation domain makes negligible difference on the dynamics of the suspension. Furthermore, the suspending fluid and the fluid inside the capsules are always assumed to have the same viscosity, i.e., $\lambda = 1$ for all suspensions, to keep the computational cost manageable. This is different than the physiological viscosity ratio of $\sim 5$. However, our previous investigations have revealed that the dynamics of a single sickle cell [Zhang *et al.*, 2019] or straight prolate capsule [Zhang and Graham, 2019] remain qualitatively unchanged as the viscosity ratio $\lambda$ is increased from 1 to 5. Furthermore, as shown by the simulation results below (Section 5.3.1), the dynamics of single healthy RBCs in the suspensions assuming $\lambda = 1$ are consistent with the orbital behavior observed in a number of prior experimental [Goldsmith *et al.*, 1972, Bitbol, 1986, Lanotte *et al.*, 2016] and numerical [Cordasco and Bagchi, 2013, Mendez and Abkarian, 2018] studies with $\lambda = 5$.

### 5.2.2 Fluid motion

In our simulations, the particle and channel Reynolds numbers, defined as $\mathrm{Re}_p = \rho\dot{\gamma}_w l^2/\eta$ and $\mathrm{Re}_c = \rho\dot{\gamma}_w H^2/\eta$, respectively, both have magnitude of $\sim O(10^{-3} - 10^{-2})$ based on the physiological range of the parameter values for blood flow in the microcirculation as noted in Section 5.2.1. The Reynolds numbers are assumed to be sufficiently small so that the fluid motion is governed by the Stokes equation, and the fluid velocity field in the simulation domain can be expressed in boundary integral form given by Eq. 3.13. To compute the velocity field at each time instant, we use an accelerated implementation of the boundary integral method [Kumar and Graham,

2012a] for simulations of capsule suspensions in this work. Details of this method are found in Section 3.3, and here we only reiterate the key idea. The acceleration in this implementation is achieved by using the General Geometry Ewald-like Method (GGEM) [Hernandez-Ortiz *et al.*, 2007]. The essence is to split the overall problem into a local and a global problem. Specifically, the solution associated with the local problem is obtained assuming free-space boundary conditions. It is short-ranged and thus can be neglected beyond a length scale $\sim \alpha^{-1}$ from the pole of the local density; in this work, a cutoff length is taken as $r_{\text{cut}} = 4/\alpha$ with good accuracy. The solution associated with the global problem, on the other hand, is nonsingular and ensures that the boundary conditions for the overall problem are satisfied. In this work, we compute the global solution by employing the discrete Fourier series approximation in the periodic $x$ (flow) and $z$ (vorticity) directions and the discrete Chebyshev polynomial approximation in the $y$ (wall-normal) direction. An important feature of this approach is that the pressure drop associated with the flow field induced by the capsules is always zero over the spatial period of the simulation domain, so that the pressure drop obtained from this boundary integral implementation for a flowing suspension always equals the pressure drop in the flow in the absence of the capsules; in other words, these simulations are performed at constant pressure drop. The overall solution for the velocity or stress field is the sum of the local and global solutions. The computational cost of the algorithm scales as $O(N\log N)$ for a flowing suspension in a slit geometry as considered in the present study, where $N$ is proportional to the product of the total number of capsules $N_p$ and the number of triangular elements $N_\triangle$ upon surface discretization. Details of this accelerated boundary integral implementation are found in [Kumar and Graham, 2012a].

Once the flow field is determined, the positions of the element nodes on the discretized capsule membrane are advanced in time using the second-order explicit Adams-Bashforth method with adaptive time step $\Delta t = 0.02\mathrm{Ca}d$, where $d$ is the minimum node-to-node distance. Time is nondimensionalized with the wall shear rate $\dot{\gamma}_w$, and in this work, $t$ always represents dimensionless time.

## 5.3 Results and discussion

In this section, we first present and discuss simulation results (Section 5.3.1) for the dynamics of different suspension systems as described above. Specifically, we focus on understanding the flow-induced segregation behavior as well as determining the orbital dynamics of single cells, especially the stiff cells, in each suspension. Substantial margination of the stiff cells is observed in all binary suspensions. Following these results, we further characterize the hydrodynamic effects of the suspensions on the walls, particularly the additional wall shear stress induced by the marginated stiff cells (Section 5.3.2). We reveal that compared to the small fluctuations in wall shear stress observed in the case of a homogeneous suspension of healthy RBCs, the marginated cells in the binary suspensions induce intermittent local wall shear stress peaks. A mechanistic framework based on the competition between wall-induced migration and shear-induced collisions is presented (Section 5.3.3) to understand these results. We further discuss the implications of these findings on the mechanism for endothelial inflammation in SCD (Section 5.3.4).

### 5.3.1 Cross-stream distribution and dynamics of cells in different suspensions

**Homogeneous suspension of healthy (flexible) RBCs**

We first consider the base case with a homogeneous suspension of flexible biconcave discoidal capsules representing purely healthy RBCs, and assume that the spontaneous shape ($c_0$ in Eq. 3.9) of the capsules is the same as their rest shape, i.e., a biconcave discoid. The effect of spontaneous shape will be discussed shortly. Again, the capillary number of healthy RBCs is Ca = 1.6. To obtain the cross-stream distribution for the cells of component $\alpha$ in a general suspension, we compute the normalized number density profile of the cells based on their wall-normal center-of-mass positions, given by $\hat{n}_\alpha(y) = n_\alpha(y)/n_\alpha^0$, where $n_\alpha^0$ is the mean number density of the cells of component $\alpha$ in the suspension; for a uniform distribution, $\hat{n}_\alpha(y) = 1$ at all $y$ positions. Figure 5.2a shows the time-averaged cross-stream distribution profile for healthy RBCs in a homogeneous suspension. The error bars represent estimated error using the "blocking" method [Flyvbjerg and Petersen, 1989]. A cell-free layer is evidently observed next to the wall ($y/a = 0$), which is a consequence of the competition between the effects of wall-induced migration [Goldsmith, 1971, Smart and Leighton, 1991] and hydrodynamic pair collisions. The two substantial peaks in the profile, which have been observed in prior experiments [Tatsumi *et al.*, 2019], simulations [Fedosov *et al.*, 2010b, Kumar *et al.*, 2014, Katanov *et al.*, 2015, Sinha and Graham, 2016, Mehrabadi *et al.*, 2016], and theoretical predictions [Henríquez Rivera *et al.*, 2016, Tatsumi *et al.*, 2019] for suspensions of RBCs and other deformable capsules, indicate that the healthy RBCs accumulate both around the centerplane of the

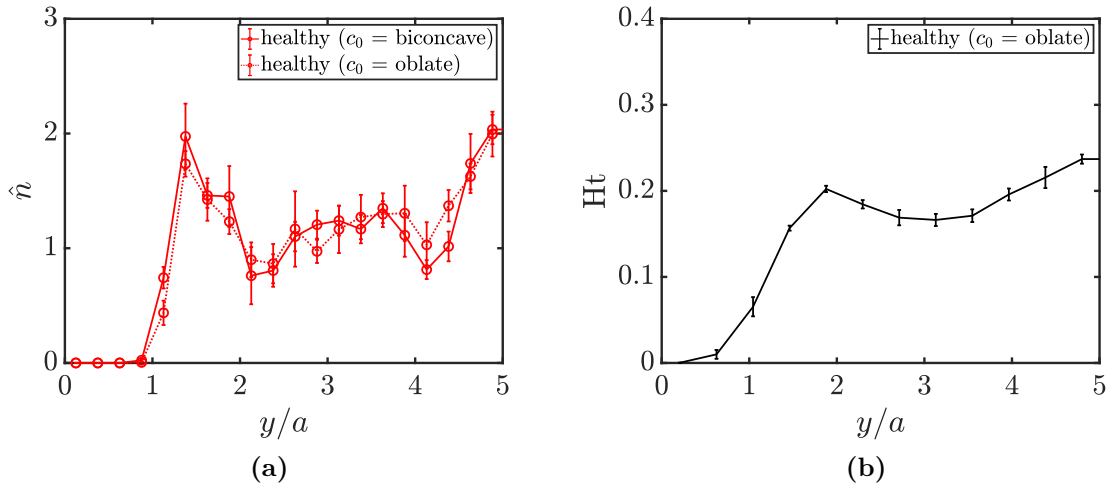
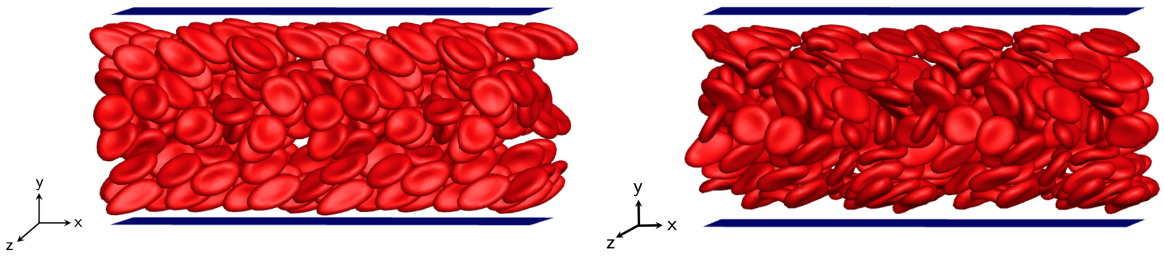



**Figure 5.2:** (a) Wall-normal number density profile $\hat{n}$ for healthy RBCs assuming different spontaneous shapes ($c_0$) in a homogeneous suspension at steady state. (b) Hematocrit profile for the healthy RBC suspension. The two positions at $y/a = 0$ and $y/a = 5$ correspond to the wall and centerplane of the channel, respectively.

channel and near the wall right beyond the cell-free layer. In addition, we also determine the hematocrit profile by computing the local volume fraction of the RBCs. The time-averaged hematocrit profile is shown in FIG. 5.2b. We note that this profile closely resembles those in a previous numerical study by Zhao *et al.* [2012] for an RBC suspension with similar parameters.

Furthermore, in the near-wall region where the local shear rate is high, healthy RBCs approximate a rolling motion, as observed in the simulation snapshot (FIG. 5.3a). Two periods of the simulation domain are shown in both $x$ and $z$ directions in this snapshot as well as all future snapshots for other suspensions. Similar to our observation, this rolling orbit assumed by an RBC at high shear rate, or a transition of the cell dynamics towards the rolling orbit upon increasing shear rate, has been revealed in both experimental [Goldsmith *et al.*, 1972, Bitbol, 1986, Lanotte *et al.*, 2016] and numerical [Cordasco and Bagchi, 2013, Cordasco *et al.*, 2014, Mendez and Abkarian,




**(a)** **(b)**

**Figure 5.3:** Simulation snapshots for a homogeneous suspension at steady state of flexible biconcave discoidal capsules (healthy RBCs) with Ca = 1.6 assuming either a biconcave discoidal (a) or an oblate spheroidal (b) spontaneous shape.

2018] studies for single RBCs under physiological conditions in which the viscosity ratio between the fluids inside and outside the cell is typically $\lambda \approx 5$, although the viscosity ratio is set to $\lambda = 1$ in this work, again, to make the computational cost manageable. We note, though, that the spontaneous shape has a nontrivial effect on the dynamics of single RBCs. For example, as shown in FIG. 5.3, the near-wall healthy RBCs are observed to reorient from a rolling orbit into a tank-treading configuration when their spontaneous shape is changed from a biconcave discoid to an oblate spheroid, consistent with the findings in a prior numerical investigation by Sinha and Graham [2015]. In spite of the change in orientational dynamics when the spontaneous shape is changed, no substantial change is observed in the wall-normal number density profile for healthy RBCs (FIG. 5.2a). Indeed, we have further verified that for the binary suspensions that will be presented next, the segregation behavior and dynamics of stiff cells are only weakly affected by the orientational dynamics of healthy (flexible) RBCs.

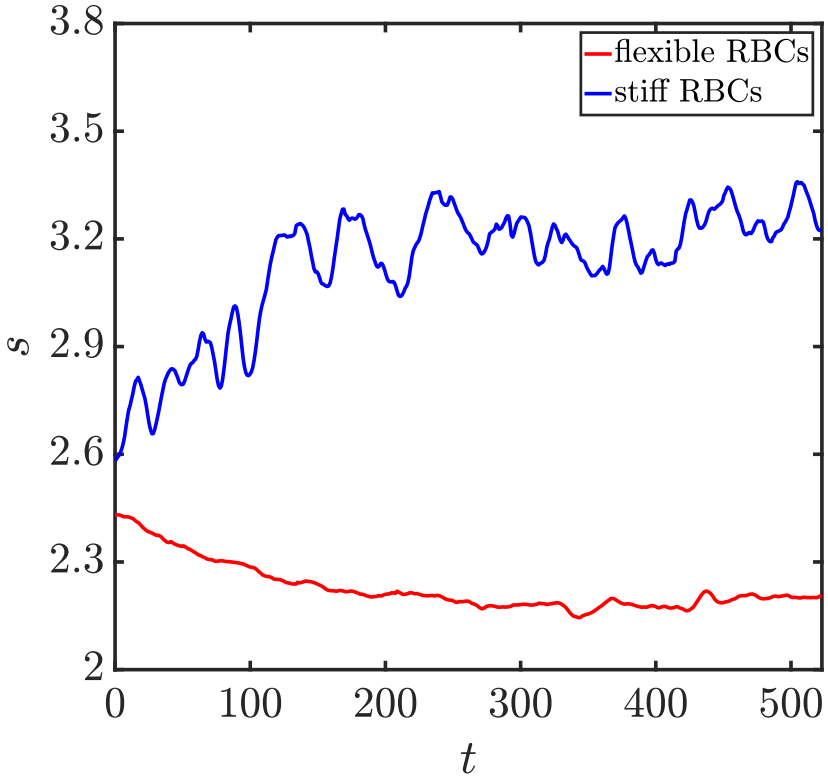



**Figure 5.4:** Time evolution of the parameter $s = \left\langle (y_{cm} - H)^2 \right\rangle^{1/2}/a$ for flexible (red) and stiff (blue) RBCs in a binary suspension.

### Binary suspension of flexible and stiff RBCs: isolated effect of rigidity difference

We now consider a binary suspension of flexible ($\mathrm{Ca}_p = 1.6$) and stiff ($\mathrm{Ca}_t = 0.4$) RBCs with a number density ratio $n_p/n_t = 9$. To characterize the collective dynamics of the cells of each component, we define a parameter $s = \left\langle (y_{cm} - H)^2 \right\rangle^{1/2}/a$, which measures the root-mean-square (RMS) distance of the cells from the centerplane of the channel; here $y_{cm}$ is the center-of-mass position of an arbitrary cell in the wall-normal direction. The time evolution of $s$ for the cells of each component is plotted in FIG. 5.4. It is obvious that though starting with comparable values for both

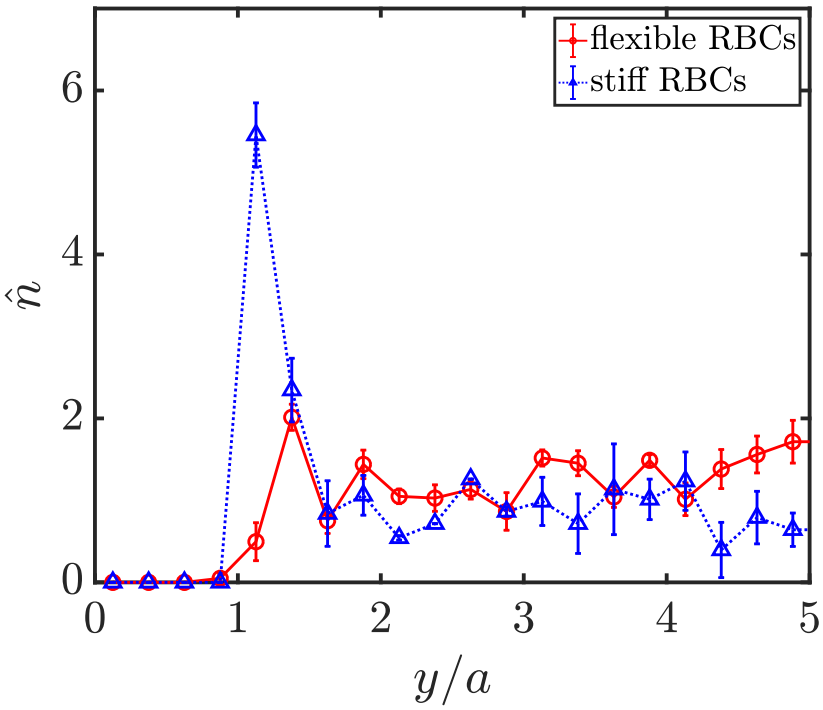
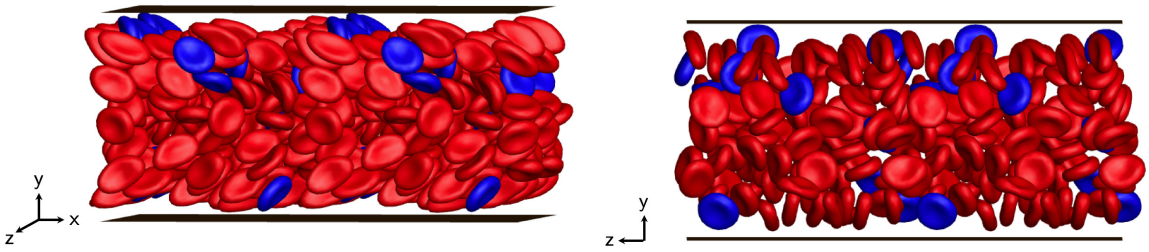



**Figure 5.5:** Wall-normal number density profiles $\hat{n}$ for flexible (solid red) and stiff (dotted blue) RBCs in a binary suspension at steady state.

components, $s$ decreases for flexible RBCs while increasing for stiff RBCs, before reaching a plateau (steady state) at $s_p \approx 2.2$ and $s_t \approx 3.2$, respectively, indicating a segregation behavior in the binary suspension.

Furthermore, to quantify the cell distributions, the steady-state wall-normal number density profiles $\hat{n}(y)$ are computed for both components and shown in FIG. 5.5. In this case where stiff RBCs are dilute, the key observation is that, in contrast to flexible RBCs that exhibit a profile similar to that in their pure suspension, a majority of stiff RBCs are drained from the center of the channel and aggregate in the near-wall region, undergoing substantial margination. This margination and segregation behavior is also evident in snapshots from simulation for this binary suspension




**(a)** **(b)**

**Figure 5.6:** Simulation snapshots ((a) side view, (b) front view) for a binary suspension of flexible (red) and stiff (blue) RBCs at steady state.

(FIG. 5.6). These results demonstrate that rigidity difference by itself is sufficient to induce the segregation behavior in a binary suspension, which is consistent with the findings in prior studies [Kumar and Graham, 2011, Kumar *et al.*, 2014, Henríquez Rivera *et al.*, 2016] considering a suspension of spherical capsules that differ only in rigidity. The marginated stiff RBCs are found to take an approximate in-plane tumbling orbit near the walls. In addition, we have verified that the existence of a small number fraction of stiff RBCs makes little difference to the orbital dynamics of flexible RBCs (not shown).

### Binary suspension of healthy and sickle RBCs: combined effect of rigidity, shape, and size differences

In this section we present simulation results for a binary suspension of healthy and sickle RBCs, which is the focus of this work. Again, healthy RBCs are modeled as flexible biconcave discoidal capsules ($\mathrm{Ca}_p = 1.6$), while sickle cells as stiff curved prolate capsules ($\mathrm{Ca}_t = 0.4$); the number density ratio between these two components is $n_p/n_t = 9$. In the meantime, results for the case in which sickle cells, the trace component, are replaced by stiff straight prolate capsules ($\mathrm{Ca}_t = 0.4$ and $X_t = 0.1$)

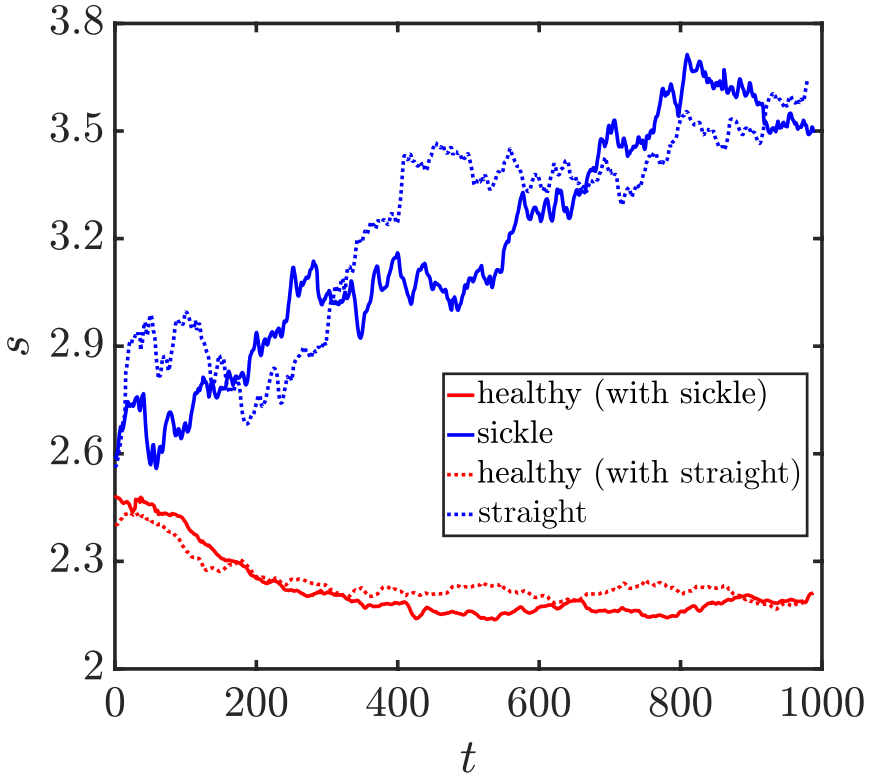



**Figure 5.7:** Time evolution of $s$ for healthy RBCs in suspension with sickle cells (solid red) and straight prolate capsules (dotted red), and for sickle cells (solid blue) and straight prolate capsules (dotted blue) in suspension with healthy RBCs, respectively.

are also presented for comparison to illustrate the effect of curvature for the trace component.

The time evolution of the parameter $s = \left\langle (y_{cm} - H)^2 \right\rangle^{1/2} / a$ is shown in FIG. 5.7 for each component in both suspensions. Similar to the previous case with flexible and stiff RBCs, here the segregation behavior is observed for both cases. It shows from direct comparison that the evolution of $s$ for healthy RBCs is not greatly affected by the curvature of the trace component. The trends of increase in $s$ display minor differences for sickle cells and straight prolate capsules, both reaching a plateau (steady state) at $s_t \approx 3.6$. This steady-state value is greater than that for stiff RBCs

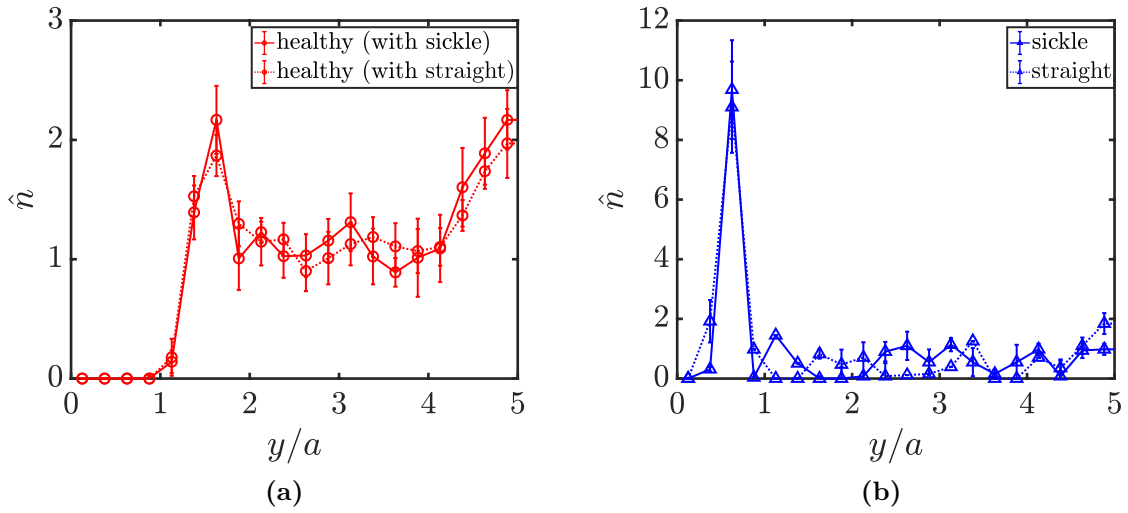



**Figure 5.8:** Wall-normal number density profiles $\hat{n}$ for (a) healthy RBCs in suspension with sickle cells (solid red) and straight prolate capsules (dotted red), and (b) for sickle cells (solid blue) and straight prolate capsules (dotted blue) in suspension with healthy RBCs, respectively.

($s_t \approx 3.2$) in a binary suspension. We also note that compared to the case with stiff RBCs, the cases with sickle cells and straight prolate capsules take a longer time to reach steady state.

More details can be revealed by computing the cross-stream distribution profiles for each component in both suspensions. In FIG. 5.8a, a cell-free layer is observed in the wall-normal number density profiles $\hat{n}$ for healthy RBCs in both cases, as well as the two peaks both around the centerplane of the channel and right beyond the cell-free layer. In general, the $\hat{n}$ profiles for healthy RBCs in these two suspensions are similar to those in previous cases. For sickle cells and straight prolate capsules, the profiles both show a high near-wall peak inside the cell-free layer (FIG. 5.8b), which suggests that the trace component in both cases is largely drained from the bulk of the suspension, displaying strong margination as seen in the simulation snapshots in FIG. 5.9. No substantial differences are observed in the $\hat{n}$ profiles for both

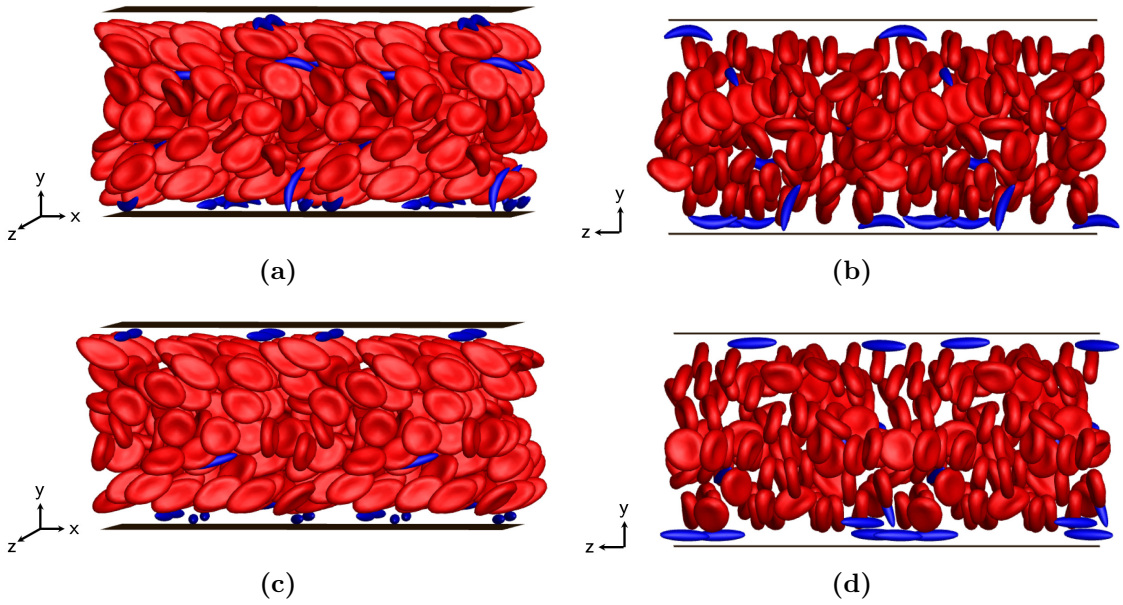



**Figure 5.9:** Simulation snapshots (left: side view; right: front view) for binary suspensions of healthy RBCs with sickle cells (a,b) and straight prolate capsules (c,d), respectively, at steady state.

cases. Besides, we have also found that the $\hat{n}$ profiles remain nearly unchanged as the spatial period in the $x$ direction of the simulation domain is doubled from $L_x = 10a$ to $L_x = 20a$ (FIG. 5.10). We also show in FIG. 5.11 that as the spontaneous shape ($c_0$) of healthy RBCs changes from a biconcave discoid to an oblate spheroid, although an orientational transformation is observed for the dynamics of healthy RBCs (FIGs. 5.11a and 5.11b), insignificant differences are found in the distribution profiles for both healthy RBCs and sickle cells in a binary suspension (FIGs. 5.11c and 5.11d).

It is noteworthy that the near-wall peaks in the $\hat{n}$ profiles for sickle cells and straight prolate capsules (FIG. 5.8b) are both of greater magnitude and closer to the wall compared to that in the profile for stiff RBCs (FIG. 5.5). To explain this, we first characterize the orbital dynamics of sickle cells and straight prolate capsules in the respective suspension. Here the cells (capsules) are classified into two groups based

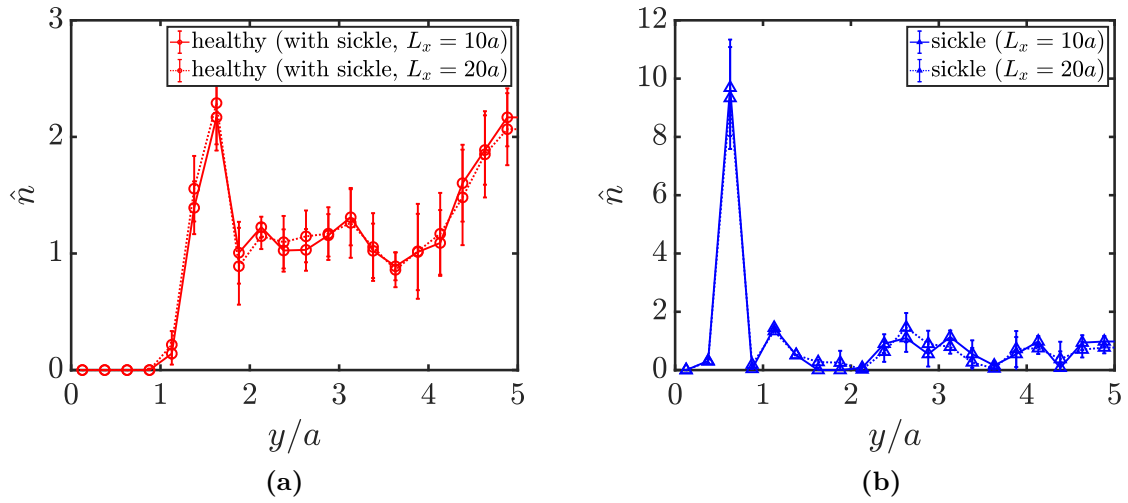



**Figure 5.10:** Effect of the spatial period $L_x$ of the simulation domain on wall-normal number density profiles $\hat{n}$ for healthy RBCs (a) in suspension with sickle cells (b).

on their wall-normal center-of-mass positions $y_{cm}$: one for the cells inside the cell-free layer, and the other for those in the bulk of the suspension. The instantaneous orientation of a single sickle cell or straight prolate capsule in flow is given by a unit end-to-end vector $\mathbf{p}$ that connects the two tips of the cell (capsule). We then define a tensor $\mathbf{S}$ to quantify the ensemble-averaged orientation of the cells in each group, given as

$$\mathbf{S} = \langle \mathbf{pp} \rangle = \begin{pmatrix} \langle p_x p_x \rangle & \langle p_x p_y \rangle & \langle p_x p_z \rangle \\ \langle p_y p_x \rangle & \langle p_y p_y \rangle & \langle p_y p_z \rangle \\ \langle p_z p_x \rangle & \langle p_z p_y \rangle & \langle p_z p_z \rangle \end{pmatrix}. \tag{5.3}$$

In particular, we care about the magnitude of the components $\langle p_x p_x \rangle$, $\langle p_x p_y \rangle (= \langle p_y p_x \rangle)$, $\langle p_y p_y \rangle$, and $\langle p_z p_z \rangle$, assuming that the values for the other components are essentially zero given the equal probability of $p_z$ being positive or negative for an arbitrary cell. The steady-state magnitude of each of these components is presented using a bar graph in FIG. 5.12 for sickle cells and straight prolate capsules inside the

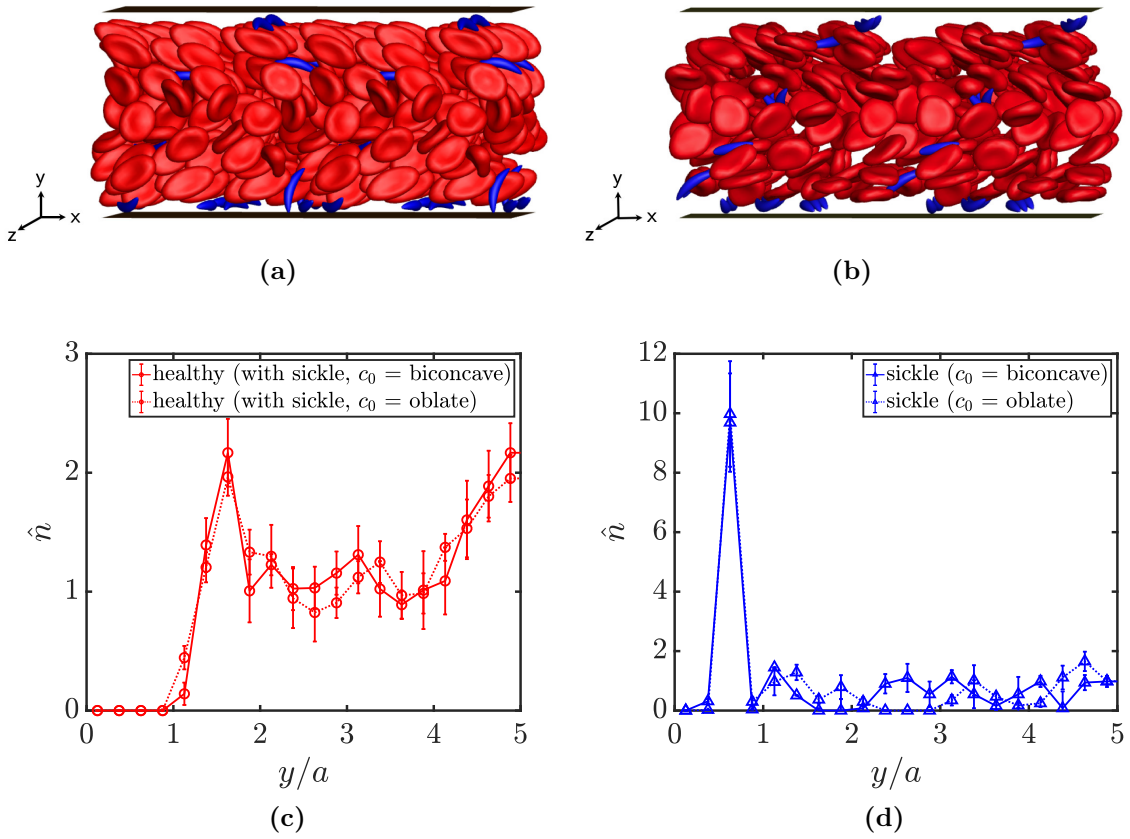



**Figure 5.11:** Simulation snapshots (a,b) for a steady-state binary suspension of healthy RBCs with sickle cells, as well as wall-normal number density profiles $\hat{n}$ (c,d) for both components, assuming a biconcave discoidal (a) and an oblate spheroidal (b) spontaneous shape ($c_0$) for healthy RBCs, respectively.

cell-free layer and in the bulk of the suspension, respectively. We observe that for the cells inside the cell-free layer, the component $\langle p_z p_z \rangle$ dominates with the magnitude close to 1, while the other components are vanishingly small. This suggests that the marginated sickle cells and straight prolate capsules tend to approximate a log-rolling orbital motion inside the cell-free layer, with the end-to-end vector $\mathbf{p}$ nearly aligned with the $z$ axis, which is in agreement with the observations from the simulation snapshots in FIG. 5.9. Compared to the marginated stiff RBCs that approximate a tumbling motion, the near-wall sickle cells or straight prolate capsules are able to

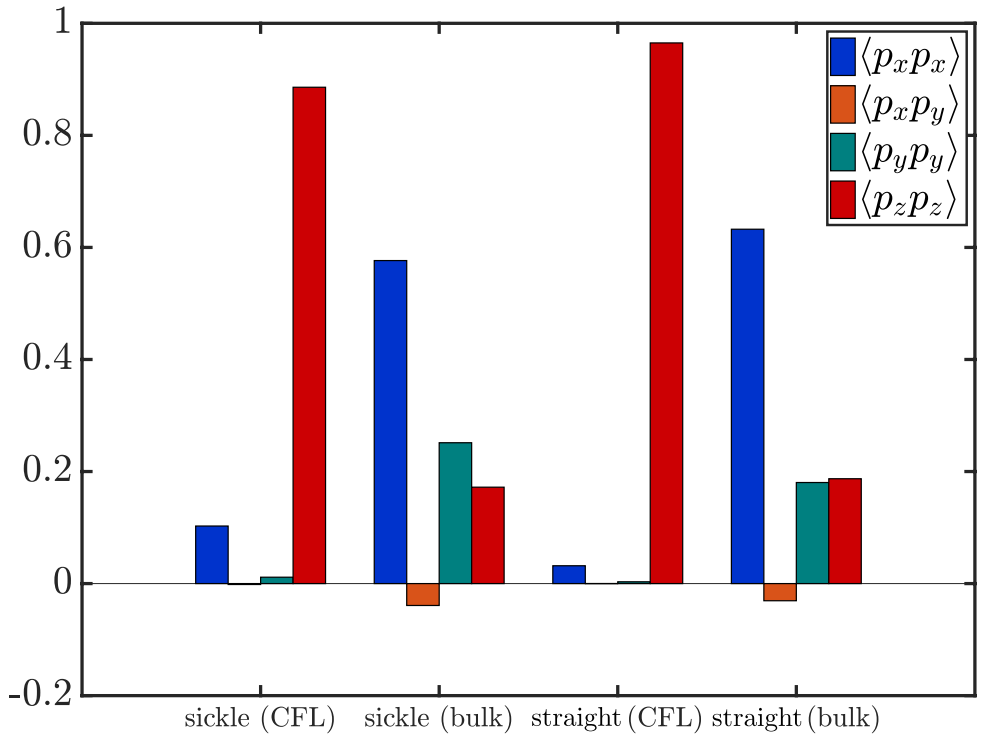



**Figure 5.12:** Magnitude of the $x$-$x$, $x$-$y$, $y$-$y$, and $z$-$z$ components of the tensor $\mathbf{S} = \langle \mathbf{pp} \rangle$ for sickle cells and straight prolate capsules inside the cell-free layer (labelled "CFL") and in the bulk of the suspension (labelled "bulk"), respectively.

approach closer to the walls owing to a minimal volume exclusion effect because of their near-rolling orbits, smaller volume, and slenderness in shape, which leads to a near-wall peak in the $\hat{n}$ profile that is both greater in magnitude and closer to the wall.

For sickle cells and straight prolate capsules in the bulk of the suspension, in contrast, $\langle p_x p_x \rangle$ dominates, with $\langle p_y p_y \rangle$ and $\langle p_z p_z \rangle$ being smaller but non-zero, indicating that the cells in the bulk generally take an averaged kayaking orbit with a small angle off the shear ($x$-$y$) plane, consistent with our previous findings on the dynamics of a single sickle cell in unbounded simple shear flow [Zhang *et al.*, 2019]. During the

evolution of the suspension dynamics, this orbit becomes favorable for these slender cells with a high aspect ratio, given limited space between cells (majorly healthy RBCs) in suspension. The dynamics of healthy RBCs, nevertheless, do not show much difference compared to previous cases.

### 5.3.2 Effect of marginated cells on the walls in binary suspensions

Having determined the cross-stream distribution and cell dynamics in different suspensions, in this section we characterize the hydrodynamic effects of the suspensions on the walls, and compare the results for the binary suspensions with the case containing purely healthy RBCs to illustrate the impact of the marginated stiff cells in the binary suspensions. Particularly, we compute the shear stress at the walls associated with different suspensions. For an undisturbed planar pressure-driven flow in the absence of the capsules confined by two walls at $y = 0$ and $y = 2H$, the mean wall shear stress is given by $\tau_w = 2\eta U_0/H$. In the case of a flowing suspension of capsules, however, additional wall shear stress $\tau_w'$ can be induced by the presence of the capsules. In this work $\tau_w'$ is computed numerically using an accelerated boundary integral method [Kumar and Graham, 2012a], as introduced in Section 3.3. It is worth emphasizing, though, that since the simulations are performed at constant pressure drop, the mean wall shear stress is the same for all suspensions considered here, and is equal to the undisturbed wall shear stress $\tau_w$, which is nondimensionalized to 2. Figure 5.13 shows examples of the spatial distribution of $\hat{\tau}_w = \tau_w'/\tau_w$ on the bottom wall ($y = 0$) induced by different suspensions at steady state. Note that this quantity and all the wall shear stress quantities reported below have been normalized by the

undisturbed wall shear stress $\tau_w$ unless noted otherwise. It is clear that except for the case with purely healthy RBCs in which barely any fluctuations in wall shear stress are observed, the binary suspensions all induce local shear stress peaks on the wall, which is certainly accredited to the marginated cells in each suspension.

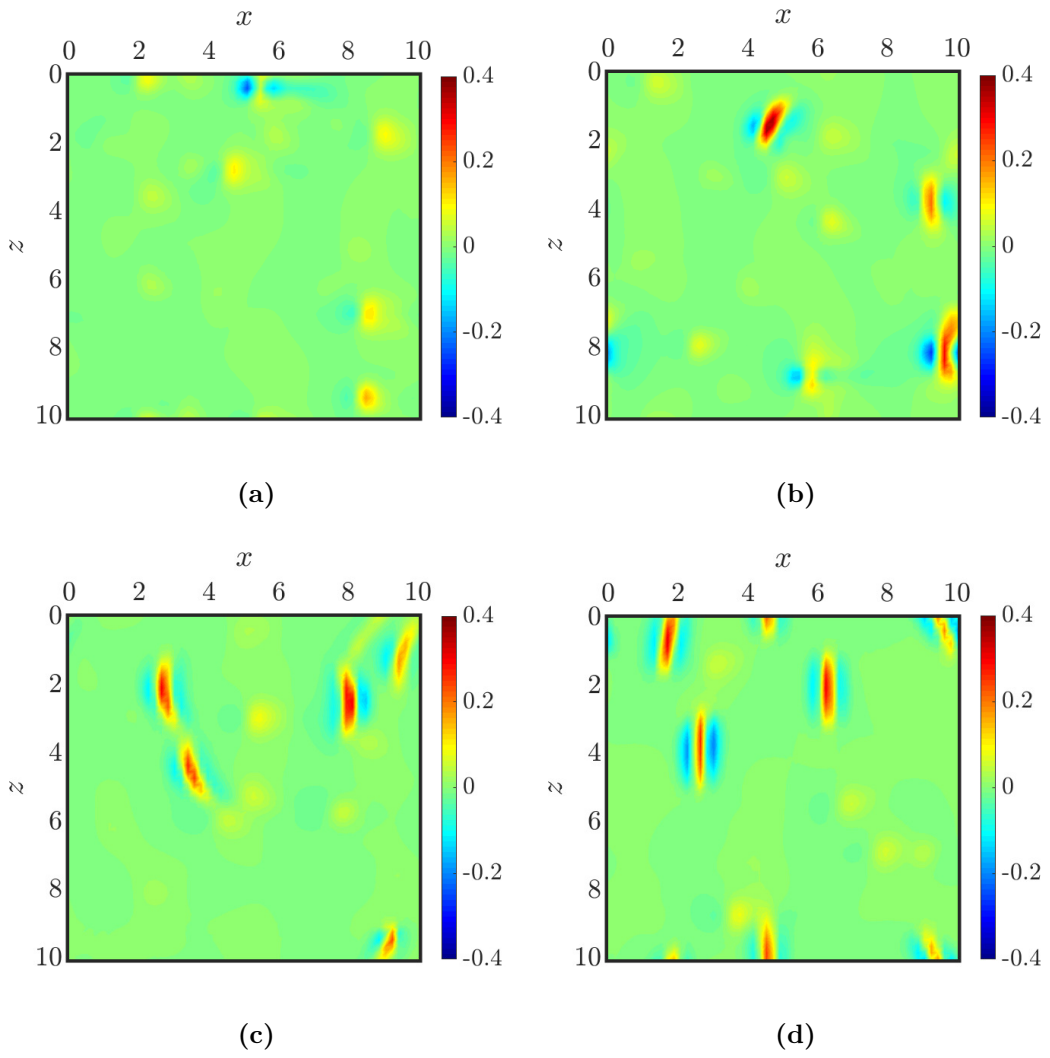



**Figure 5.13:** Examples of the spatial distribution of the additional wall shear stress $\hat{\tau}_w$ on the bottom wall ($y = 0$) induced by a homogeneous suspension of healthy RBCs (a) and binary suspensions of healthy (flexible) RBCs with stiff RBCs (b), sickle cells (c), and straight prolate capsules (d), respectively, at steady state.

In general, an arbitrary wall position can experience dramatic fluctuations in $\hat{\tau}_w$

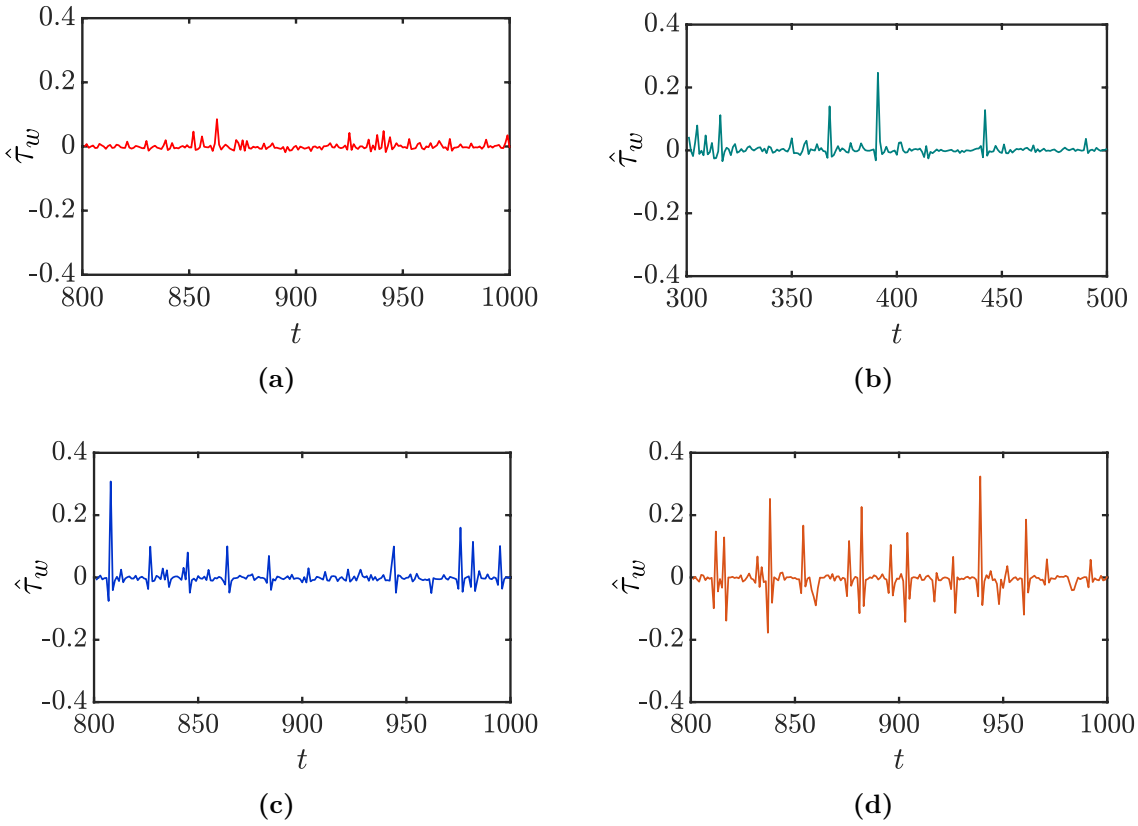



**Figure 5.14:** Time evolution of the additional wall shear stress $\hat{\tau}_w$ at a fixed wall position $(x, y, z) = (0.74a, 0, 1.67a)$ for the cases of a homogeneous suspension of healthy RBCs (a) and binary suspensions of healthy (flexible) RBCs with stiff RBCs (b), sickle cells (c), and straight prolate capsules (d), respectively, at steady state.

due to the dynamical motion of the near-wall cells in a flowing suspension. Examples are shown in FIG. 5.14 for the evolution of $\hat{\tau}_w$ experienced at a fixed wall position $(x, y, z) = (0.74a, 0, 1.67a)$ for different suspensions at steady state. A number of peaks with large magnitude are observed in each case of the binary suspensions, suggesting that this wall position experiences high additional shear stress intermittently. We now detailedly characterize the hydrodynamic effect of each suspension on the walls. First, we compute the RMS of the additional wall shear stress $\hat{\tau}_w$ for each wall position, and the results for the spatially-averaged RMS wall shear stress, $\langle(\hat{\tau}_w)_{\mathrm{RMS}}\rangle$,

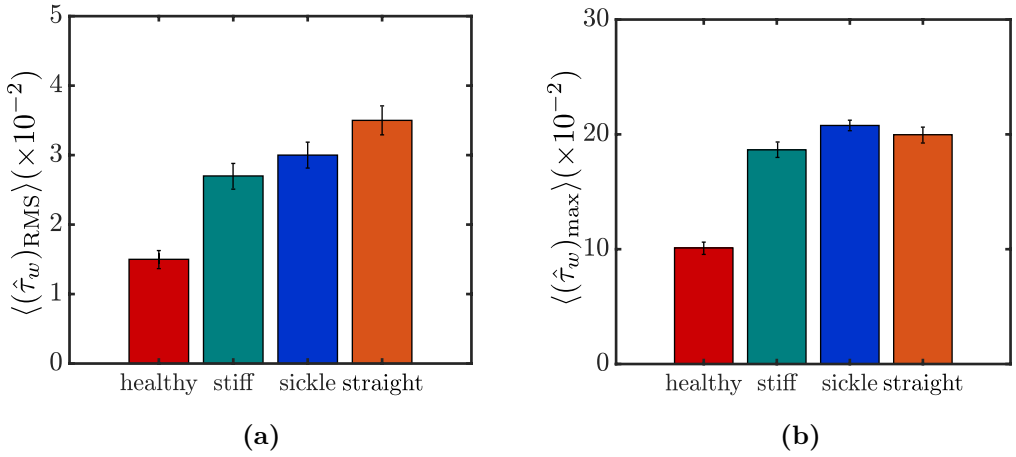



**Figure 5.15:** The spatially-averaged RMS $\langle(\hat{\tau}_w)_{\mathrm{RMS}}\rangle$ (a) and maximum $\langle(\hat{\tau}_w)_{\mathrm{max}}\rangle$ (b) of the additional wall shear stress for different suspensions at steady state. For each quantity, the error bars represent standard error.

are plotted in FIG. 5.15a for different suspensions. It is observed that all three types of cells as the trace component, i.e., stiff RBCs, sickle cells, and straight prolate capsules, cause an increase (of approximately two folds) in the averaged RMS wall shear stress in the case of the corresponding binary suspension compared to the case with purely healthy RBCs. The magnitude of the increase is the greatest for the case with straight prolate capsules, though the differences are small among the binary cases. In addition, the spatially-averaged maximum additional wall shear stress, $\langle(\hat{\tau}_w)_{\mathrm{max}}\rangle$, is also computed for different cases (FIG. 5.15b). Again, no substantial differences are observed among the binary cases, although the magnitude of this quantity is slightly greater for the case with sickle cells than with stiff RBCs or straight prolate capsules.

However, despite the general indications, neither the RMS nor the maximum is able to reveal the influence of the marginated cells in a binary suspension on the walls in detail. Indeed, it is mainly these near-wall cells that arouse the intermittent peaks in the additional wall shear stress, as shown in the examples in FIG. 5.14. To

this end, we now compute three quantities for each of the suspensions: the ensemble-averaged magnitude, duration, and frequency of the peaks in the additional wall shear stress. To do this, we consider only those wall shear stress peaks in each case that are greater than the expected maximum value for the healthy case, and the associated quantities are denoted using the subscript "$pk$". The ensemble-averaged magnitude, duration, and frequency of these peaks are then computed, which gives $\langle(\hat{\tau}_w)_{pk}\rangle$, $\langle\Delta t_{pk}\rangle$, and $\langle f_{pk}\rangle$, respectively. Note that an arbitrary peak in $\hat{\tau}_w$, as defined above, is always characterized by a spike and two dips right before and after it (FIG. 5.14). Accordingly, the duration of a peak is defined as the time difference between the onset of the dip before the spike and the end of the one after. Finally, we take the product $A_{pk}$ of these three quantities, defined as

$$A_{pk} = \langle(\hat{\tau}_w)_{pk}\rangle \times \langle\Delta t_{pk}\rangle \times \langle f_{pk}\rangle, \tag{5.4}$$

which quantifies the overall effect of each suspension on the wall shear stress.

The results are summarized in FIG. 5.16. It is obvious that compared to the case with purely healthy RBCs where $A_{pk}$ is vanishingly small, all three binary suspensions exert a substantial overall effect on the wall shear stress (FIG. 5.16d). The averaged magnitude and duration of the wall shear stress peaks, $\langle(\hat{\tau}_w)_{pk}\rangle$ and $\langle\Delta t_{pk}\rangle$, show minor differences among the cases of binary suspensions, although both are slightly greater for the case with stiff RBCs than with sickle cells or straight prolate capsules. Significant differences, however, are observed in the averaged frequency of the wall shear stress peaks, with $\langle f_{pk}\rangle$ being the greatest when the trace component is straight prolate capsules. As a result, the product $A_{pk}$ also yields the greatest value for the

case with straight prolate capsules, while being slightly greater for the case with sickle cells than with stiff RBCs.

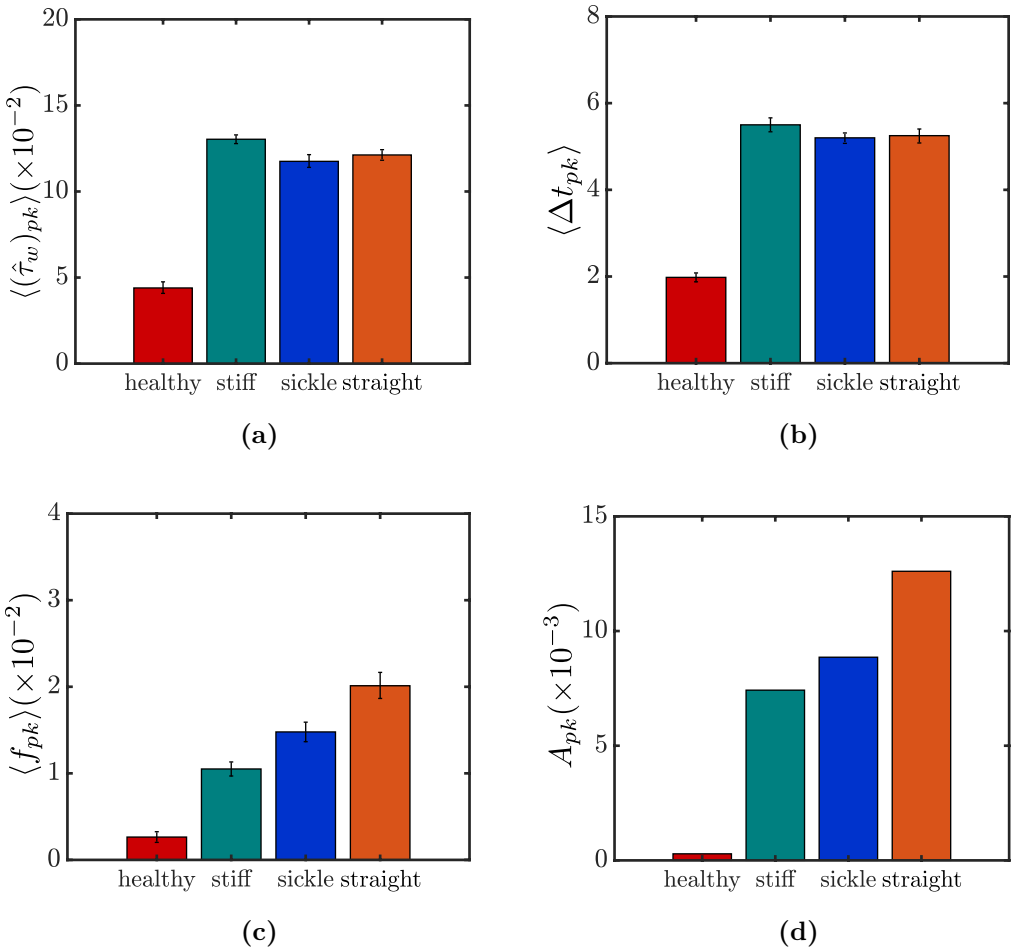



**Figure 5.16:** The ensemble-averaged magnitude $\langle(\hat{\tau}_w)_{pk}\rangle$ (a), duration $\langle \Delta t_{pk} \rangle$ (b), and frequency $\langle f_{pk} \rangle$ (c), respectively, of the wall shear stress peaks experienced by all wall positions for different suspensions at steady state, and the product $A_{pk}$ of these three quantities (d). The error bars in (a), (b), and (c) represent standard error for each quantity.

The differences in $\langle f_{pk} \rangle$ among the binary suspension cases, as shown in FIG. 5.16c, may be explained by the orbital dynamics of the marginated cells. As determined in Section 5.3.1, marginated stiff RBCs tend to approximate an in-plane tumbling orbit. Theoretically, substantial additional wall shear stress is induced when the cell

is oriented perpendicular to the wall with a minimal distance between the edge of the cell and the wall. However, during the periodic orbital motion of the cell, this orientation is transient before the cell is quickly flipped by the shear effect of the flow and spend longer time at the edge of the cell-free layer becoming parallel with the wall, which conversely leads to negligible additional wall shear stress and, as a consequence, the lowest frequency of the wall shear stress peaks among the binary suspension cases. The difference in $\langle f_{pk} \rangle$ between the cases with sickle cells and straight prolate capsules, on the other hand, is majorly an effect of curvature: the steady rolling motion of marginated straight prolate capsules inside the cell-free layer, with negligible fluctuations in the wall-normal position of the cell body compared to the larger fluctuations for near-wall rolling sickle cells caused by curvature, ensures that at any wall position, a peak in wall shear stress is induced whenever a straight prolate capsule goes by.

As mentioned in Introduction, in this work WBCs and platelets are not considered in the suspensions assuming negligible effects due to their extremely small number fractions in blood. To justify this assumption, we have tested the case in which one stiff spherical capsule slightly larger than a biconcave discoid, which serves as a model for the WBC, is placed near the wall in suspension with healthy RBCs ($X_p = 0.99$, $X_t = 0.01$). We reveal that the overall effect of this suspension on wall shear stress, characterized by $A_p$ as defined above, is indeed negligible compared to that for the case containing sickle cells; note that this number fraction of WBCs is even higher than the physiological range [Dean, 2005]. Therefore, it is reasonable to exclude WBCs in our simulations. Similarly, we expect that platelets should also have a negligible effect on wall shear stress due to both the small number fraction and the

tumbling motion taken near the walls [Zhao *et al.*, 2012] as noted and discussed above for marginated stiff RBCs.

### 5.3.3 Mechanism for flow-induced segregation and margination

In Section 5.3.1 we have presented detailed results for the dynamics of different binary suspensions considered in this work, and particularly focused on the flow-induced segregation and margination of stiff cells in each suspension. In this section we briefly provide a mechanistic understanding for this segregation behavior by characterizing the effects of two key sources of cross-stream particle fluxes in a confined particle suspension: (a) wall-induced migration of deformable particles, which tends to cause a flux away from the walls towards the centerplane of the channel, and (b) shear-induced pair collisions, which tend to drive a diffusive flux of the particles. We show that the relative significance of these two competing effects for each particle species gives rise to the segregation in a binary suspension.

#### Wall-induced migration

In general, in bounded simple shear flow, a deformable object (e.g. capsule, droplet, vesicle, flexible macromolecule) near the wall exhibits a cross-stream migration away from the wall even at zero Reynolds number [Smart and Leighton, 1991, Jendrejack *et al.*, 2004, Ma and Graham, 2005, Chen *et al.*, 2005, Danker *et al.*, 2009, Graham, 2011]. To leading order, a deformable neutrally-buoyant particle in flow near a wall can be described by a point force dipole [Smart and Leighton, 1991, Ma and Graham, 2005]. The migration velocity of the deformable particle is a linear function of the

$yy$-component of the stresslet $\mathbf{S}$ generated by the particle, denoted as $S_{yy}$, which depends on the deformability, size, and shape of the particle. It also scales inversely with $y^2$, where $y$ is the distance of the center-of-mass position of the particle from the wall.

In this work, we characterize the effect of wall-induced capsule migration using direct simulations. We consider isolated capsules of different species as in the binary suspensions described above, namely biconcave discoid (or healthy RBC), curved prolate spheroid (or sickle RBC), and straight (non-curved) prolate spheroid, subjected to simple shear flow in a slit domain of size $10a \times 10a \times 10a$, where $a$ again is the radius of a biconcave discoid. Each isolated capsule is initially placed at $y_{cm} = 1.5a$, where $y_{cm}$ is the center-of-mass position of the capsule in the wall-normal direction. For simplicity, a biconcave discoidal capsule is initially oriented with the major axis of revolution aligned with the $y$ axis. For a curved or straight prolate capsule, two initial orientations are considered: (i) the end-of-end vector $\mathbf{p}$ of the capsule initially aligned with the $x$ direction (i.e. $\mathbf{p}^0 = (1, 0, 0)$), and (ii) $\mathbf{p}$ initially aligned with $z$ (i.e. $\mathbf{p}^0 = (0, 0, 1)$). Specifically, using our previous definition (Section 4.2.1), for a curved prolate capsule $[\alpha, \beta] = [0,\pi/2]$ in case (i) and $[\alpha, \beta] = [\pi/2,\pi/2]$ in case (ii); for a straight prolate capsule $\beta$ is irrelevant to its orientation. These two cases are illustrated in FIG. 5.17.

Figure 5.18a shows the time evolution of the wall-normal center-of-mass position $y_{cm}$ of a stiff sickle RBC (Ca = 0.4, $[\alpha, \beta] = [0,\pi/2]$) in comparison with a healthy RBC (at varying Ca). The plots indicate the migration rate of each species. For the healthy RBC, the migration rate increases with increasing Ca, though this effect is not dramatic given the large increase from Ca = 0.4 to Ca = 1.6. A substantial

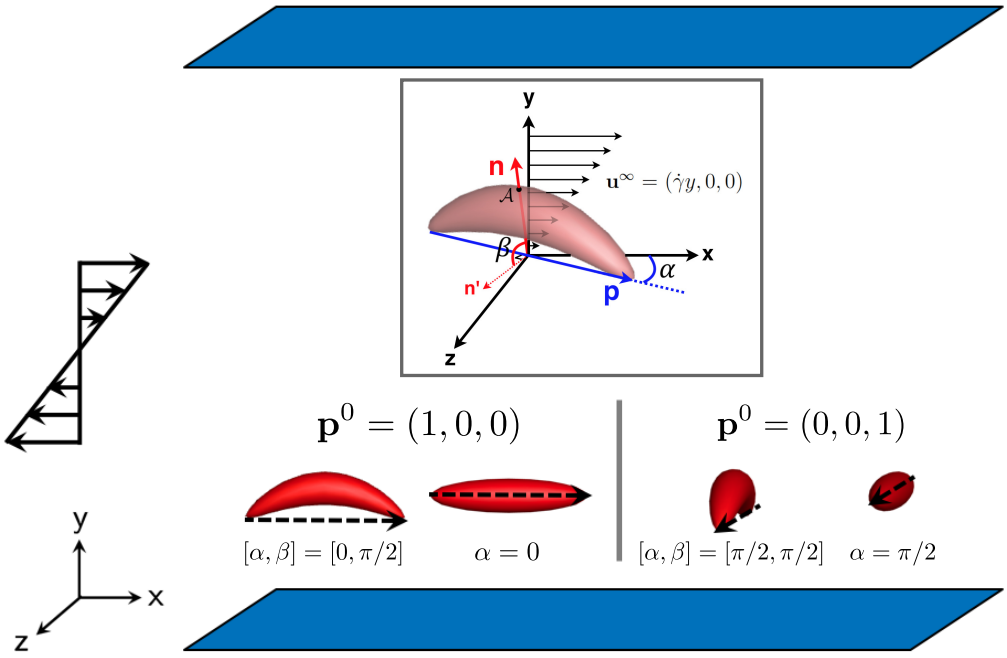



**Figure 5.17:** Schematic of a curved or straight prolate capsule with different initial orientations subjected to simple shear flow in a planar slit. The inset illustrates the initial orientation of a curved prolate capsule (same as FIG. 4.1).

difference, however, is observed between the cross-stream displacements of the sickle and healthy RBCs. It is obvious that the sickle RBC migrates with a much lower rate than the healthy RBC (by about one order of magnitude), even at the same Ca. The evolution profile of $y_{cm}$ for the sickle RBC indicates a quasiperiodic kayaking orbit of the cell, which is similar to the dynamics of a sickle RBC in unbounded shear flow (FIG. 4.10b), except for a very small wall-induced cross-stream displacement.

Now we discuss the effects of initial orientation and curvature of the stiff cell on the migration rate. We first report the orbital dynamics of the sickle RBC and straight prolate capsule with different initial orientations. In case (i) described above, i.e. when the end-of-end vector $\mathbf{p}$ is initially aligned with the $x$ direction, the sickle RBC ($[\alpha, \beta] = [0,\pi/2]$) assumes a kayaking orbit, while the straight prolate capsule ($\alpha = 0$) tumbles in the shear ($x$-$y$) plane during the time period considered. In case (ii) where

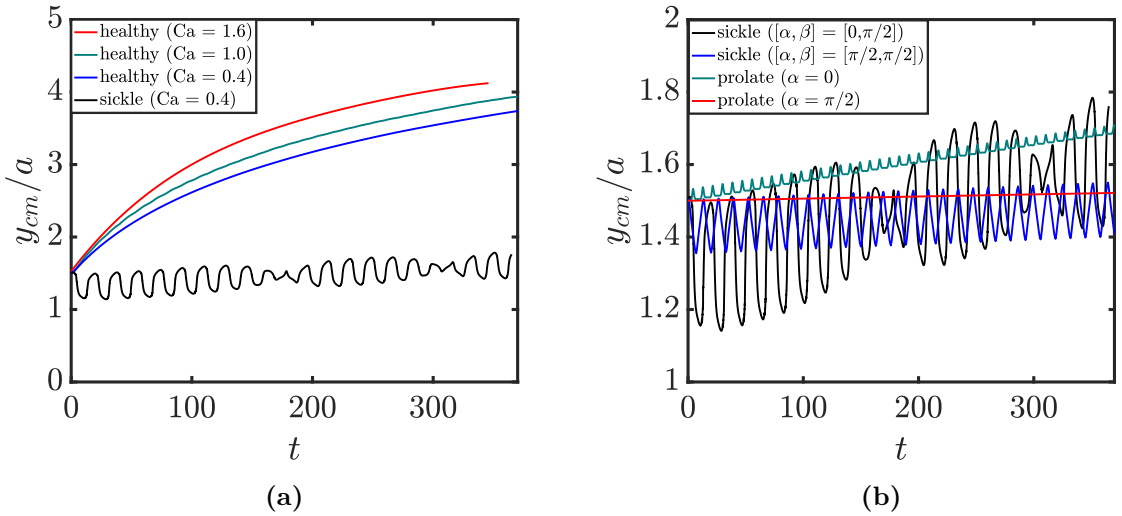



**Figure 5.18:** Evolution of the wall-normal center-of-mass position $y_{cm}$ of a sickle RBC (Ca = 0.4) in comparison with a healthy RBC at varying Ca (a) and a straight prolate capsule with different initial orientations (b).

**p** is initially aligned with the $z$ direction, both sickle RBC ($[\alpha, \beta] = [\pi/2,\pi/2]$) and straight prolate capsule ($\alpha = \pi/2$) take a log-rolling motion. Figure 5.18b shows that the migration rate of the stiff cell depends on the initial orientation and the subsequent cell dynamics. For both sickle RBC and straight prolate capsule, the migration rate is much lower when it is taking a log-rolling motion (with almost zero magnitude) than assuming a kayaking or tumbling orbit. On the other hand, no substantial difference is observed between the wall-normal displacements of these two species with the same initial orientation, suggesting that curvature has a trivial effect on the migration rate.

### Shear-induced pair collisions

In addition to the migration flux, shear-induced hydrodynamic interparticle collisions in a flowing suspension, on the other hand, drive post-collisional displacements of the

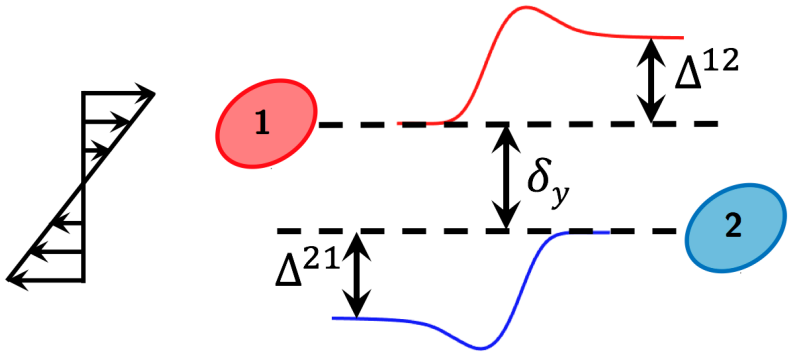



**Figure 5.19:** Schematic of trajectories of capsules ('1' and '2') in a pair collision. The capsules are initially apart from each other with an offset $\delta_y$ in the $y$ direction, and experience cross-stream displacements, $\Delta^{12}$ and $\Delta^{21}$, respectively, after the collision.

capsules from their original trajectories (FIG. 5.19), giving rise to a diffusive flux. With the volume fraction ($\phi \sim 0.15$) of the suspensions in this work, we assume that uncorrelated pair collisions dominate the capsule-capsule interactions [Da Cunha and Hinch, 1996, Zurita-Gotor *et al.*, 2012]. Specifically, two types of pair collisions can occur in a suspension: homogeneous pair collisions between two particles of the same species, and heterogeneous pair collisions between two particles of different species. In a binary suspension containing primarily healthy RBCs ($\mathrm{Ca}_p = 1.6$) and a trace amount of stiff curved or straight prolate capsules ($\mathrm{Ca}_t = 0.4$) as considered in this work, the probability of interactions between the stiff capsules is assumed to be very small. Hence, in this section we only consider homogeneous pair collisions between two healthy RBCs and heterogeneous pair collisions between a healthy RBC and a stiff capsule.

To characterize these pair collisions, direct simulations are performed in simple shear flow in a domain of size $30a \times 30a \times 30a$, which is effectively unbounded. Initially, the two capsules of each pair are placed on either side of the centerplane (i.e. the plane with zero undisturbed flow velocity) with their center-of-mass positions

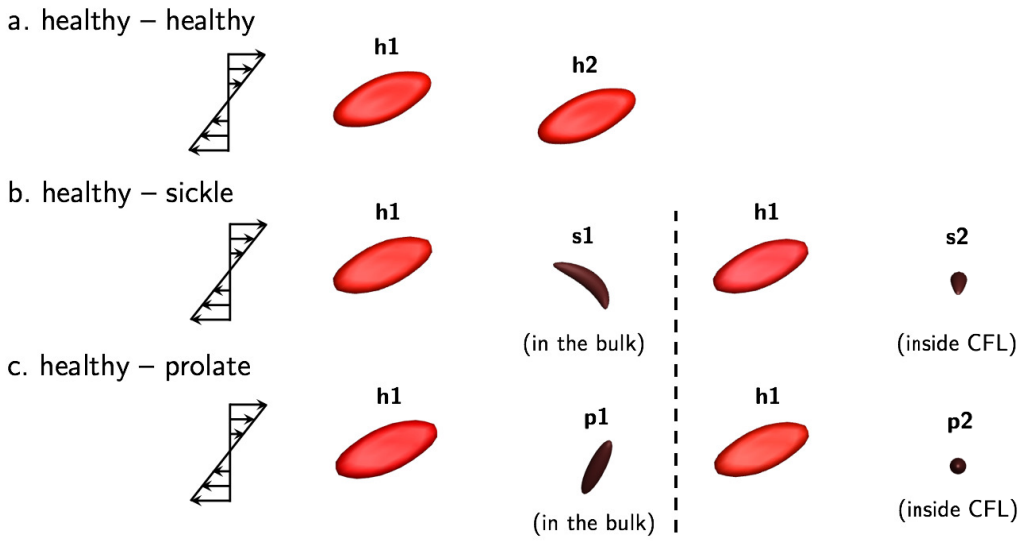



**Figure 5.20:** Schematic of capsules in homogeneous (a) and heterogeneous (b,c) pair collisions with specified orientations. Healthy ('h') – healthy RBC; sickle ('s') – curved prolate capsule; prolate ('p') – straight prolate capsule.

being symmetric with regard to the centerplane. The pre-collisional offset of the two capsules in the flow ($x$), wall-normal ($y$), and vorticity ($z$) direction is denoted as $\delta_x$, $\delta_y$, and $\delta_z$, respectively; here $\delta_x = 6a$, $\delta_y = 0.5a$, and $\delta_z = 0$. In a pair collision, the capsules first approach each other due to the shear effect of the flow, and experience post-collisional displacements $\Delta$ after the collision. In either homogeneous or heterogeneous pair collisions, healthy RBCs are assumed to adopt the steady-state rolling orbit, as is observed above for the dynamics of single healthy RBCs in a suspension. Two orbital motions, however, are considered for curved or straight prolate capsules in heterogeneous pair collisions with healthy RBCs. One is the kayaking motion that is characteristic of the capsule dynamics in the bulk of the suspension, and the other is the rolling orbit taken by the marginated capsules inside the cell-free layer. Figure 5.20 shows the pre-collisional state of different colliding pairs considered in this section with specified capsule orientations.

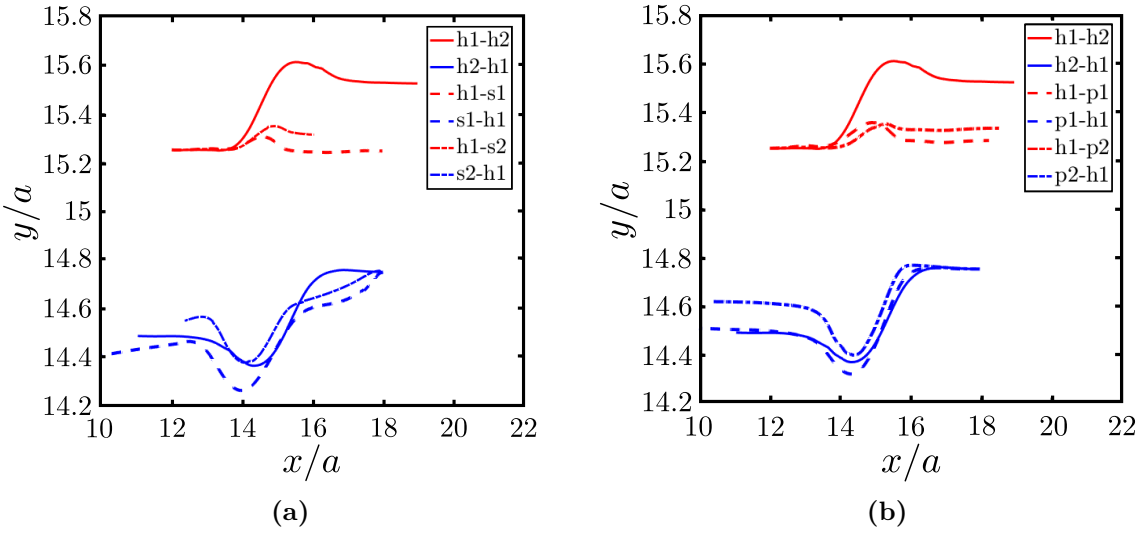



**Figure 5.21:** Trajectories of healthy RBCs as well as curved (a) and straight (b) prolate capsules assuming specified orbits in homogeneous and heterogeneous pair collisions.

The trajectories of capsules in homogeneous and heterogeneous pair collisions are plotted in FIG. 5.21. For the homogeneous pair collision, the post-collisional displacements of the two healthy RBCs are the same, i.e., $\Delta^{\mathrm{h1h2}} = \Delta^{\mathrm{h2h1}}$. For heterogeneous pair collisions, the stiff curved and straight prolate capsules, either kayaking or rolling, are always displaced more than the healthy RBC. More detailedly, a kayaking curved or straight prolate capsule exhibits a greater displacement than when it is rolling. The order of displacements in heterogeneous pair collisions is as follows: $\Delta^{\mathrm{s1h1}} > \Delta^{\mathrm{s2h1}} > \Delta^{\mathrm{h1s2}} > \Delta^{\mathrm{h1s1}}$ for collisions between healthy RBCs and curved prolate capsules, and similarly, $\Delta^{\mathrm{p1h1}} > \Delta^{\mathrm{p2h1}} > \Delta^{\mathrm{h1p2}} > \Delta^{\mathrm{h1p1}}$ for collisions between healthy RBCs and straight prolate capsules. Curvature is found to have a minor effect on heterogeneous pair collisions, except for causing a small drift of the curved capsules in the wall-normal direction.

The results presented above for the wall-induced migration and shear-induced

pair collisions may provide mechanistic insight into understanding the flow-induced segregation and margination observed in the binary suspensions. The stiff curved or straight prolate capsule migrates much slower, on one hand, and displaces more in collision, on the other hand, than the healthy RBC. As a result, stiff capsules tend to be pushed towards the walls by surrounding healthy RBCs in iterative collisions, and the time scale for this process is much shorter compared to that for the extremely slow migration away from the walls, leading to the margination of stiff capsules eventually. Furthermore, using this mechanistic framework, we can predict that the stiff cells that are already marginated would likely remain stable inside the cell-free layer instead of escaping back to the bulk flow. In return, this entrapment would facilitate the steady hydrodynamic interactions between the marginated cells and the walls, as indicated by the continuous fluctuations in wall shear stress.

### 5.3.4 Implications on SCD vasculopathy

The findings in the present work may aid in understanding the pathophysiology of chronic endothelial inflammation in SCD from a biophysical perspective. Indeed, the intermittent peaks in wall shear stress induced by the marginated stiff sickle cells, as observed in this work, resemble the spiky wall shear stress profile considered in [Bao *et al.*, 1999] on flow-mediated endothelial mechanotransduction. This spiky profile, characterized by abrupt onset and termination of shear stress, was found to induce the greatest upregulation of pro-inflammatory signals compared to the other shear stress profiles. More generally, rapid changes in shear stress, as opposed to steady shear stress, have been demonstrated to contribute to endothelial inflammation and subsequent atherogenesis via specific mechanotransduction pathways of the endothe-

lium [De Keulenaer *et al.*, 1998, Dekker *et al.*, 2002, Hsiai *et al.*, 2003, Sorescu *et al.*, 2004, Harrison *et al.*, 2006]. In this sense, our results provide a possible mechanism for chronic SCD vasculopathy.

The present work does not incorporate adhesive interactions between diseased cells and vessel walls. While these play a significant role in the acute vaso-occlusive crisis [Kaul *et al.*, 1989, 1994, Frenette, 2002, Lei and Karniadakis, 2013, 2015], which in turn, may cause endothelial dysfunction, our aim here was to address the question of whether non-adhesive effects may also lead to a pro-inflammatory state of the endothelium via mechanotransductive mechanisms. In fact, the aforementioned experimental studies on shear stress-induced endothelial expression were all performed in the absence of adhesive events. Hence, this work suggests that purely physical (non-adhesive) interactions between endothelial cells and sickle cells may be sufficient to cause endothelial inflammation, which provides innovative and vital insight into SCD pathophysiology that extends beyond, and is independent of, vaso-occlusion. In the case where adhesive events become important, the phenomena revealed here would still be of prime importance, as the strong sickle cell margination demonstrated here brings the cells into the vicinity of the walls, which is of course a prerequisite for adhesion to them.

## 5.4 Conclusion

In this study, we investigated different flowing suspensions of deformable capsules subjected to pressure-driven flow in a planar slit using boundary integral simulations, assuming that the flow is in the Stokes regime. The focus of this study is a binary

suspension of healthy RBCs and sickle cells, which describes the microvascular blood flow in sickle cell disease (SCD). The parameter regime is mostly based on the range of experimentally determined values for RBCs and blood flow in the microcirculation, except that the suspending fluid and the fluids enclosed by all capsules are assumed to have the same viscosity, i.e., the viscosity ratio $\lambda = 1$, for the purpose of keeping the computational cost manageable for the simulations.

We first characterized the cross-stream distributions and orbital dynamics of different types of capsules in each suspension, and revealed a number of key features.

(i) In the homogeneous suspension of healthy (flexible) RBCs, a cell-free layer is formed next to the channel walls. Healthy RBCs accumulate both around the centerplane of the channel and near the wall right beyond the cell-free layer, showing two corresponding peaks in the number density distribution profile. The spontaneous shape of RBCs plays a nontrivial role in the orientational dynamics of single cells in the suspension, but has a negligible effect on the number density distribution.

(ii) In the binary suspension of flexible and stiff RBCs with the same rest shape but large contrast in membrane rigidity, the dilute stiff RBCs are largely drained from the center of the channel and display substantial margination towards the walls, showing a high near-wall peak in the number density profile. This suggests that rigidity contrast by itself is sufficient to induce the segregation behavior in a binary suspension. The marginated stiff RBCs assume an approximate in-plane tumbling orbit.

(iii) In the binary suspension of healthy RBCs and sickle cells, the dilute stiff sickle cells are almost completely drained from the bulk of the suspension, and strongly aggregate close to the walls inside the cell-free layer. The near-wall peak in the

number density profile for sickle cells is both greater in magnitude and closer to the walls than that for stiff RBCs, mainly attributed to the much smaller volume and slenderness in shape of sickle cells. The marginated sickle cells tend to roll in flow with the major axis aligned with the vorticity ($z$) direction. No substantial differences are observed for the number density profile and orbital dynamics of dilute stiff straight prolate capsules in the binary suspension compared to those in the case with sickle cells, indicating that curvature plays a minor role.

The segregation behavior can be understood by characterizing the wall-induced migration of different capsule species and shear-induced pair collisions in the suspensions. Compared to a healthy RBC, a stiff curved or straight prolate capsule migrates at a much lower rate away from the wall, while experiencing a greater post-collisional displacement in a heterogeneous pair collision. The counterbalance between these two effects eventually leads to the margination of stiff capsules in a binary suspension with healthy RBCs.

Having revealed the segregation behavior and margination of the dilute stiff component in different binary suspensions, we also quantified the physical effect of each suspension on the walls. Particularly, the additional wall shear stress, i.e., the deviation from the undisturbed wall shear stress induced by the presence of capsules, was computed for each suspension. We found that compared to the small fluctuations in wall shear stress for the case with purely healthy RBCs, large local peaks in wall shear stress are induced by all binary suspensions, which is believed to be a hydrodynamic effect of the marginated cells on the walls. Detailed quantification showed that the shape and size of the stiff component have a secondary role, even though for the parameter space considered in this study, straight prolate capsules seem to have a

greater overall effect on the wall shear stress than do stiff RBCs and sickle cells, which may be accredited to the steady near-wall rolling motion with little fluctuations in the wall-normal position and the slenderness in shape with no curvature.

Overall, all these results represent a pioneering effort to gain a mechanistic understanding of the behavior of flowing suspensions of cells or capsules in complex scenarios, such as blood flow in SCD which is the focus of the current study. More importantly, this work is of essential interest from the medical point of view in that the results, from a purely physical (non-chemical) perspective, may help explain the mechanism for complications associated with SCD, such as endothelial inflammation, that are still poorly understood. Particularly, this work addresses how circulating stiffened and misshapen RBC subpopulations may directly contribute to vasculopathy in SCD, not via vaso-occlusion or cell adhesion as canonically depicted, but via biophysical effects due to the margination of diseased cells.

One limitation of this work is that the properties of cells of each type were identical and unchanging – physiologically, sickle cells vary considerably in cell morphology and membrane stiffness, which should be addressed in future studies. Other parameters of the suspensions, such as the total volume fraction and the number fraction of each component in a binary system, can also be altered in extended studies to investigate the effects of these parameters on the suspension dynamics. Another limitation is that the flow domain considered here is a planar slit bounded by two rigid walls. Vessel walls are actually elastic, which may in turn affect the hydrodynamic interactions between the marginated sickle cells and the endothelium. Future simulations should investigate the effects of vessel wall elasticity on the dynamics of blood flow in SCD.

The present work may be extended in a number of directions. For example, it

has been observed in experiments [Loiseau *et al.*, 2015] that the flow of a suspension of sickle cells around an acute corner of a triangular pillar or a bifurcation leads to an enhanced deposition and aggregation of cells. Therefore, complex geometries of the flow domain other than a planar slit can be considered in future simulations. In addition, intravascular hemolysis, a fundamental feature of SCD, is also known to play a role in endothelial dysfunction. Though the link between hemolysis and SCD pathophysiology has been probed experimentally [Reiter *et al.*, 2002, Minneci *et al.*, 2005, Taylor *et al.*, 2008], computational efforts should also be made to provide a mechanistic insight into the role of hemolysis in SCD vasculopathy. Finally, future experiments are needed to elucidate if the cross-stream distribution of RBCs in SCD would be adversely altered in the microcirculation, and if so, how this process may contribute to SCD vasculopathy. Such work could directly lead to a new paradigm of biophysical therapeutic strategies by mitigating the potential margination of aberrant sickle RBCs in SCD.

# Chapter 6

# Dynamics of deformable prolate capsules in shear flow: multiplicity of stable orbits[a]

## 6.1 Introduction

Microcapsules, small liquid droplets enclosed by a thin solid membrane, have been of increasing significance in the bioengineering, pharmaceutics, and food industries. Examples include cell encapsulation for tumor progression monitoring [Alessandri *et al.*, 2013], encapsulation of cosmetic active ingredients for topical application [Casanova and Santos, 2016], development of drug delivery systems [Masuda, 2011, Degen, 2014], and artificial food particles for aquatic filter feeders [Jones *et al.*, 1974].

To satisfy engineering needs, many fabrication techniques for artificial capsules

[a]This chapter includes content from: Zhang, X., and Graham, M. D. (2019). Accepted.

have emerged. Polyelectrolyte capsules (PECs), for example, are a promising vehicle in the biomedical field to carry a variety of therapeutic molecules (peptides, proteins, etc.) for targeted delivery to a desired site in the body [De Geest *et al.*, 2007]. Avoidance of immune clearance (cellular uptake by macrophages), which is critical for the efficiency of carrier particles in delivery system, has been revealed to greatly depend on particle physical and chemical properties such as size, shape, deformability, and surface chemistry. A number of studies have reported that high-aspect-ratio (prolate) microparticles exhibited considerably reduced immune clearance and increased circulation half-time compared to spheres [Geng *et al.*, 2007, Champion and Mitragotri, 2009]. To this end, Zan *et al.* [2015] developed a fabrication method to obtain PECs with constant surface chemistry but independently controlled size and shape by combining soft organic templates created by the particle stretching method and a modified layer-by-layer (LBL) deposition process, which may enable both a more systematic investigation on the roles of capsule properties on its efficiency and the optimization of the design of a delivery system. Furthermore, non-spherical capsules, because of a higher surface-to-volume ratio than their spherical counterparts, can be preferable to enhance the transfer of cargoes across the capsule membrane upon arrival at the target; an example is the fabrication of prolate capsules containing a calcium ion solution by Schneeweiss and Rehage [2005] using a microfluidic channel.

All of the aforementioned situations involve capsule suspensions in a fluid environment, and the dynamics of these suspensions can be greatly affected by the behavior of single capsules. Therefore, it is essential to gain a comprehensive understanding of the single capsule dynamics in a flow. For example, an initially spherical deformable capsule is found to take a so-called tank-treading motion in simple shear flow with

the membrane rotating periodically around its stationary elongated shape [Barthès-Biesel and Rallison, 1981]. Here the deformability of the capsule is characterized by the capillary number Ca, which represents the ratio of viscous stresses to elastic restoring stresses on the particle. Non-spherical capsules, such as oblate spheroids [Ramanujan and Pozrikidis, 1998, Sui *et al.*, 2008, Kessler *et al.*, 2008, Bagchi and Kalluri, 2009, Le and Tan, 2010, Walter *et al.*, 2011, Yazdani *et al.*, 2011, Omori *et al.*, 2012, Cordasco and Bagchi, 2013, Wang *et al.*, 2013, Dupont *et al.*, 2016] and biconcave discoids, a model for red blood cells (RBCs) [Goldsmith *et al.*, 1972, Fischer *et al.*, 1978, Abkarian *et al.*, 2007, Skotheim and Secomb, 2007, Dupire *et al.*, 2010, Fedosov *et al.*, 2010a, 2011, Peng *et al.*, 2011, Yazdani and Bagchi, 2011, Dupire *et al.*, 2012, Cordasco *et al.*, 2014, Peng *et al.*, 2014, Sinha and Graham, 2015], have also been investigated extensively in both experimental and computational studies. These studies have explored a wide range of parameters for the capsule membrane mechanics and flow properties, and revealed rich and complex orbital dynamics for the capsules. Indeed, the increasing attention that oblate capsules have gained in the past decades may be attributed to the findings by several studies on RBCs [Dupire *et al.*, 2012, Cordasco *et al.*, 2014, Peng *et al.*, 2014, Sinha and Graham, 2015] that an oblate spheroidal spontaneous shape has to be assumed for RBCs to maintain the stability of their biconcave shape during motions, and it provides a better prediction than other spontaneous shapes for cell dynamics in comparison with experimental observations.

In contrast, to the best of our knowledge, there only exist a limited number of works on the motion of prolate capsules in shear flow, most of which have focused on the special case where the fluids inside and outside the capsules have the same

viscosity. Walter *et al.* [2011] numerically studied the motion of an inertialess prolate capsule in shear flow with the major axis initially positioned in the shear plane. The membrane was modeled as a thin hyperelastic surface with no bending resistance. Two stable in-plane orbital motions were found: a rigid-body-like tumbling motion at low Ca, in which the capsule flips continuously, and a fluid-like motion named swinging at high Ca, which is similar to a tank-treading motion only with small oscillations in both the deformation and orientation of the capsule. Richer orbital dynamics have been revealed for a prolate capsule with out-of-shear-plane initial orientations. In a numerical investigation by Dupont *et al.* [2013], the membrane mechanics of the capsule was described using a model that includes shear elasticity and area dilatation described by either the Skalak law [Skalak *et al.*, 1973] or the neo-Hookean law, but again no bending resistance. They showed that for any initial orientation with respect to the vorticity axis, the capsule always converges towards a unique stable long-time orbit depending on Ca. At low Ca, the stable orbit corresponds to a rolling motion about the vorticity axis. As Ca increases, the capsule precesses around the vorticity axis, and undergoes a so-called wobbling motion. At high Ca, the capsule assumes a complex motion with oscillations about the shear plane termed oscillating-swinging, which eventually evolves into a swinging motion, as described in [Walter *et al.*, 2011], as Ca further increases. The same qualitative motions were generally observed in the parameter regimes considered in this work, irrespective of the capsule membrane law or aspect ratio. Cordasco and Bagchi [2013] later incorporated a small constant bending stiffness into the membrane for an inertialess prolate capsule with zero spontaneous curvature, and observed a transition of the stable orbit from a drift precession (rolling) to a stable precession with a tank-treading motion of the

membrane (oscillating-swinging) as Ca increases, which is qualitatively similar to the observations in [Dupont *et al.*, 2013].

The effect of a small particle inertia was considered by Wang *et al.* [2013] for the three-dimensional orbital behavior of an isolated prolate capsule in shear flow, in which, again, bending resistance was neglected and a unity viscosity ratio between the inner and outer fluids was assumed. With increasing Ca, the dominant stable orbital modes were found to be tumbling, precessing, rolling, and oscillating-swinging. In contrast to the findings in [Dupont *et al.*, 2013] and [Cordasco and Bagchi, 2013], they revealed that multiple stable orbits coexist in the transition regimes, even at the same capillary number.

None of the preceding studies regarding deformable prolate capsules have addressed the effects of bending stiffness and viscosity ratio, which may both play a nontrivial role in the orbital dynamics of the capsules. In fact, in applications, the mechanical properties of the capsule membrane can vary greatly depending on the materials and fabrication techniques, and the suspending fluid or solution and the fluid enclosed inside the capsules will generally have different viscosities. The present work aims to gain an improved understanding of the dynamics of prolate capsules in shear flow by performing a systematic numerical investigation over a broad domain of parameter space and determining the effects of membrane deformability, bending stiffness, initial orientation, aspect ratio of the capsule and the viscosity ratio between the inner and outer fluids. In this work, we reveal parameter regimes for an inertialess deformable prolate capsule in shear flow in which either a single or multiple attractors exist, and show in particular that the orbits for a capsule lying in the shear plane and aligned with the vorticity axis are not always stable as the capsule evolves towards

the equilibrium configuration. By computing the particle contribution to the stress, we illustrate how the multiplicity of stable orbits for a prolate capsule is reflected in the rheology for a suspension of such capsules in the dilute limit. The connection between orbit dynamics and rheology for capsules has been reported in a number of prior studies [Barthès-Biesel and Chhim, 1981, Pozrikidis, 1995, Ramanujan and Pozrikidis, 1998, Pozrikidis, 2003, Drochon, 2003, Bagchi and Kalluri, 2010, Clausen and Aidun, 2010, Bagchi and Kalluri, 2011, Takeishi *et al.*, 2019], but only a small number have considered prolate capsules.

The rest of the chapter is organized as follows: in Section 6.2 we present the models for a deformable prolate capsule and the membrane mechanics, and the numerical method adopted to calculate the fluid motion; in Section 6.3 we provide detailed results and discussion for the orbital dynamics of a prolate capsule over a broad range of various parameters, including membrane deformability, bending stiffness, initial orientation, aspect ratio of the capsule and the viscosity ratio between the inner and outer fluids. Predictions of the rheological properties for a dilute suspension of prolate capsules are also reported. Concluding remarks are presented in Section 6.4.

## 6.2 Model formulation

### 6.2.1 Model and discretization

We consider an isolated inertialess fluid-filled deformable capsule with a prolate spheroidal rest shape immersed in unbounded simple shear flow with shear rate $\dot{\gamma}$ (FIG. 6.1). The undisturbed flow velocity is given by $\mathbf{u}^{\infty} = (\dot{\gamma}y, 0, 0)$. Both the suspending fluid and the fluid inside the capsule are assumed to be incompressible and

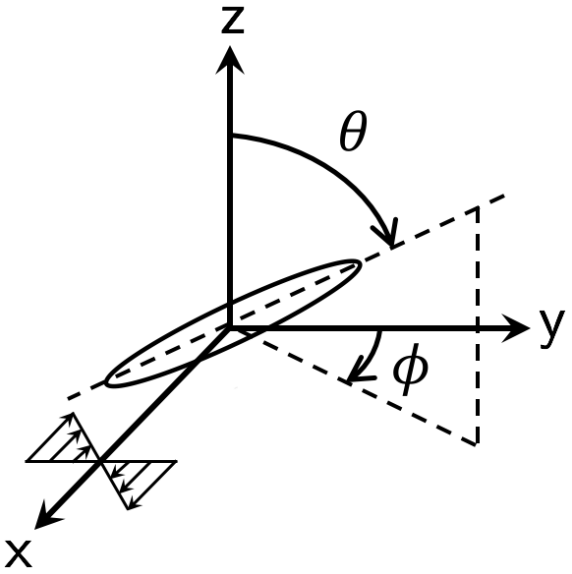



**Figure 6.1:** Schematic of the 3D orientation of a prolate capsule in unbounded simple shear flow.

Newtonian, with viscosity $\eta$ and $\lambda\eta$, respectively, where $\lambda$ is the viscosity ratio. At rest, the prolate capsule has a polar radius $a_1$ and an equatorial radius $a_2$, with an aspect ratio $\mathrm{AR} = a_1/a_2 > 1$. Here we define a characteristic length scale $a = (a_1 a_2^2)^{1/3}$; this is the radius of a sphere having the same volume as the prolate capsule. The particle Reynolds number $\mathrm{Re}_p = \rho\dot{\gamma}a^2/\eta$ is assumed to be sufficiently small so that the fluid motion is governed by the Stokes equation. The instantaneous orientation of the prolate capsule is given by two angles, as defined by Jeffery [1922]: $\phi$ is the azimuthal angle with respect to the $y$ axis, and $\theta$ is the polar angle with respect to the $z$ axis.

To describe the membrane mechanics, we adopt a model that incorporates shear elasticity, area dilatation, and bending resistance. Details regarding this membrane model are presented in Section 3.2. In brief, the behavior of the capsule membrane in response to the in-plane shear elastic force and area change is described using a

model by Skalak *et al.* [1973] (Eq. 3.10). The deformability and bending stiffness of the capsule are characterized by the dimensionless capillary number $\mathrm{Ca} = \eta\dot{\gamma}a/G$ and bending modulus $\hat{\kappa}_B = K_B/a^2G$, respectively, where $G$ is the in-plane shear modulus of the membrane and $K_B$ the out-of-plane bending modulus. The capsule membrane is discretized into 320 piecewise flat triangular elements, resulting in 162 nodes. We have verified that increasing the number of membrane elements from 320 to 1280 makes no difference to the orbital dynamics of capsules with varying bending stiffness and viscosity ratio. Based on this discretization, the total membrane force density $\mathbf{f^m}$ is calculated following the manner described in Section 3.2.

### 6.2.2 Fluid motion

In the Stokes flow regime, the fluid velocity $\mathbf{u}$ at any point $\mathbf{x_0}$ in the unbounded domain can be written in boundary integral form [Pozrikidis, 1992, Kumar and Graham, 2012a] as:

$$u_j(\mathbf{x_0}) = u_j^{\infty}(\mathbf{x_0}) + \int_S q_i(\mathbf{x}) G_{ji}(\mathbf{x_0}, \mathbf{x}) dS(\mathbf{x}), \tag{6.1}$$

where $\mathbf{q}(\mathbf{x_0})$ is a single-layer density that satisfies

$$\begin{aligned} &q_j(\mathbf{x_0}) + \frac{\lambda - 1}{4\pi(\lambda+1)} n_k(\mathbf{x_0}) \sum_{m=1}^{N_p} \int_{S^m} q_i(\mathbf{x}) T_{jik}(\mathbf{x_0}, \mathbf{x}) dS(\mathbf{x}) \\ &= -\frac{1}{4\pi\mu}\Big(\frac{\Delta f_j(\mathbf{x_0})}{\lambda+1} + \frac{\lambda-1}{\lambda+1} f_j^{\infty}(\mathbf{x_0})\Big). \end{aligned} \tag{6.2}$$

Here $\mathbf{u}^{\infty}(\mathbf{x_0})$ is the undisturbed fluid velocity at a given point $\mathbf{x_0}$, $S$ denotes the surface of the particle; $\mathbf{f}^{\infty}(\mathbf{x_0})$ is the traction at a given point due to the stress generated in the fluid corresponding to the undisturbed flow $\mathbf{u}^{\infty}(\mathbf{x_0})$; $\Delta\mathbf{f}(\mathbf{x})$ is the

hydrodynamic traction jump across the membrane interface, which relates to the total membrane force density by $\Delta\mathbf{f}(\mathbf{x}) = -\mathbf{f^m}$ assuming the membrane equilibrium condition; $\mathbf{G}$ and $\mathbf{T}$ are the Green's function and its associated stress tensor for Stokes flow in an unbounded domain. Details of the numerical method are described in [Kumar and Graham, 2012a]. Once the flow field is determined, the positions of the element nodes on the discretized capsule membrane are advanced in time using a second-order Adams-Bashforth method with adaptive time step $\Delta t = 0.02\mathrm{Ca}l$, where $l$ is the minimum node-to-node distance. Time is nondimensionalized by the shear rate $\dot{\gamma}$, and in this work we define $t$ as the dimensionless time.

The implementation of the boundary integral method used in this work has been extensively validated with test problems considering both a rigid sphere and a spherical drop between parallel walls subjected to pressure driven flow [Kumar and Graham, 2012a], and the numerical algorithms applied to calculate the shear and bending elastic force densities in the capsule membrane have been validated on the deformation of spherical capsules in simple shear flow [Kumar and Graham, 2012a, Sinha and Graham, 2015]. In addition, we have also compared the numerically determined inclination profile for a highly stiff prolate capsule with the prediction by Jeffery's theory [Jeffery, 1922] for an inertialess rigid prolate particle in shear flow, and observed good agreement (Section 4.2.3)

### 6.2.3 Particle stress in a dilute suspension of capsules

In addition to the capsule motions, we also compute the particle stress tensor in order to understand the rheology for a suspension of such capsules in the dilute limit. For a suspension of $N_p$ capsules in a volume $V$, the contribution of the suspended capsules

to the bulk stress of the suspension, in dimensional form, is given by [Batchelor, 1970, Kennedy *et al.*, 1994, Ramanujan and Pozrikidis, 1998, Bagchi and Kalluri, 2010, Graham, 2018]:

$$\Sigma_{ij}^{p} = \frac{1}{V}\sum_{m=1}^{N_p}\int_{S_m}[\Delta f_i x_j + \eta(\lambda-1)(u_i n_j + u_j n_i)]dS, \tag{6.3}$$

where $\boldsymbol{\Sigma^p}$ is the particle stress tensor. Rewritten in nondimensional variables, $\widetilde{\mathbf{x}} = \mathbf{x}/a$, $\widetilde{\mathbf{u}} = \mathbf{u}/(a\dot{\gamma})$, $\widetilde{V} = V/a^3$, $\widetilde{S} = S/a^2$, and $\widetilde{\Delta\mathbf{f}} = \Delta\mathbf{f}/(\eta\dot{\gamma})$, Eq. 6.3 becomes

$$\Sigma_{ij}^{p} = \frac{\eta\dot{\gamma}}{\widetilde{V}}\sum_{m=1}^{N_p}\int_{\widetilde{S}_m}[\widetilde{\Delta f}_i\widetilde{x}_j + (\lambda-1)(\widetilde{u}_i n_j + \widetilde{u}_j n_i)]d\widetilde{S}. \tag{6.4}$$

Now we assume that the suspension is dilute, containing $N_p$ identical prolate capsules all undergoing the same stable orbital motion, and that the interparticle hydrodynamic interactions are negligible. The volume fraction of the suspension is given by $\Phi = N_p V_p/V = N_p\widetilde{V}_p/\widetilde{V}$, where $V_p$ is the volume of a single capsule and $\widetilde{V}_p = V_p/a^3$ is dimensionless. Eq. 6.4 now becomes

$$\begin{aligned}\Sigma_{ij}^{p} &= \frac{\eta\dot{\gamma}N_p}{\widetilde{V}}\int_{\widetilde{S}_m}[\widetilde{\Delta f}_i\widetilde{x}_j + (\lambda-1)(\widetilde{u}_i n_j + \widetilde{u}_j n_i)]d\widetilde{S} \\ &= \frac{\eta\dot{\gamma}\Phi}{\widetilde{V}_p}\int_{\widetilde{S}_m}[\widetilde{\Delta f}_i\widetilde{x}_j + (\lambda-1)(\widetilde{u}_i n_j + \widetilde{u}_j n_i)]d\widetilde{S},\end{aligned} \tag{6.5}$$

which naturally gives the dimensionless particle stress tensor

$$\widetilde{\Sigma_{ij}^{p}} = \frac{\Sigma_{ij}^{p}}{\eta\dot{\gamma}} = \frac{\Phi}{\widetilde{V}_p}\int_{\widetilde{S}_m}[\widetilde{\Delta f}_i\widetilde{x}_j + (\lambda-1)(\widetilde{u}_i n_j + \widetilde{u}_j n_i)]d\widetilde{S}. \tag{6.6}$$

The dimensionless particle shear stress $\widetilde{\Sigma^p_{xy}}$ is identical to the specific viscosity $\eta_{sp}$; for a dilute suspension of rigid spherical particles $\eta_{sp} = [\eta]\Phi = 2.5\Phi$ [Einstein, 1911], where $[\eta]$ is the intrinsic viscosity. The dimensionless first and second normal stress differences are $N_1 = \widetilde{\Sigma^p_{xx}} - \widetilde{\Sigma^p_{yy}}$ and $N_2 = \widetilde{\Sigma^p_{yy}} - \widetilde{\Sigma^p_{zz}}$.

## 6.3 Results and discussion

In this section, the orbital dynamics of a prolate capsule in unbounded simple shear flow are systematically investigated over a broad domain of parameter space. We focus on addressing the issue of long-time behavior of the orbits. For a capsule with small bending stiffness (Section 6.3.1), all initial conditions we consider evolve towards the same orbit at long times. For a capsule with large bending stiffness (Section 6.3.2), in contrast, we reveal parameter regimes with multiple attractors, i.e., there are multiple stable orbits, and which one is reached at long times depends on the initial orientation. A corresponding multiplicity in the rheological properties is predicted for a dilute suspension of such capsules.

### 6.3.1 Dynamics of prolate capsules with small bending stiffness

We first report the dynamics of a deformable prolate capsule with small bending stiffness ($\hat{\kappa}_B = 0.02$). The initial orientation of the capsule is set to $[\phi^0, \theta^0] = [\pi/2, \alpha]$. We begin with the case where $\lambda = 1$ and AR $= 2.0$, and assume that the spontaneous shape of the capsule is the same as its rest shape. The effect of spontaneous curvature will be discussed later. Figure 6.2 shows the evolution of the capsule orbit in various

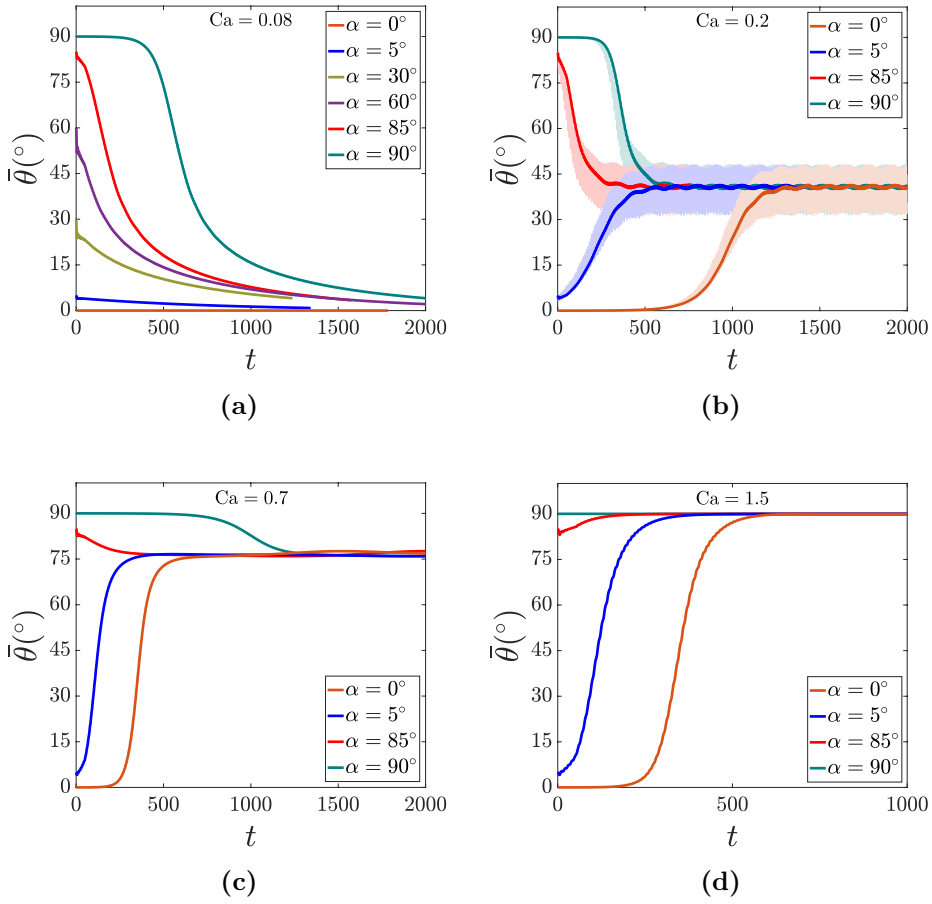



**Figure 6.2:** Evolution of $\bar{\theta}$ of a prolate capsule (AR = 2.0) with $\hat{\kappa}_B = 0.02$ and $\lambda = 1$ at (a) Ca = 0.08, (b) Ca = 0.2, (c) Ca = 0.7, and (d) Ca = 1.5. Here the spontaneous shape of the capsule is assumed to be the same as its rest shape.

regimes of Ca. We are interested in the long-time limit (dimensionless time $t \gg 1$) of the capsule dynamics, so the evolution data is presented using a running average of $\theta$, defined as $\bar{\theta} = \frac{1}{t_{\text{avg}}} \int_{t-t_{\text{avg}}}^{t} \theta(t)dt$ that averages over the oscillations in $\theta$ caused by the rotational motions of the capsule on the time scale $1/\dot{\gamma}$. Here we set $t_{\text{avg}} = 50$; FIG. 6.2b shows an example of the evolution data before (light-colored "clouds") and after (solid colored lines) taking the running average.

The key observation here is that the capsule, irrespective of the initial orientation

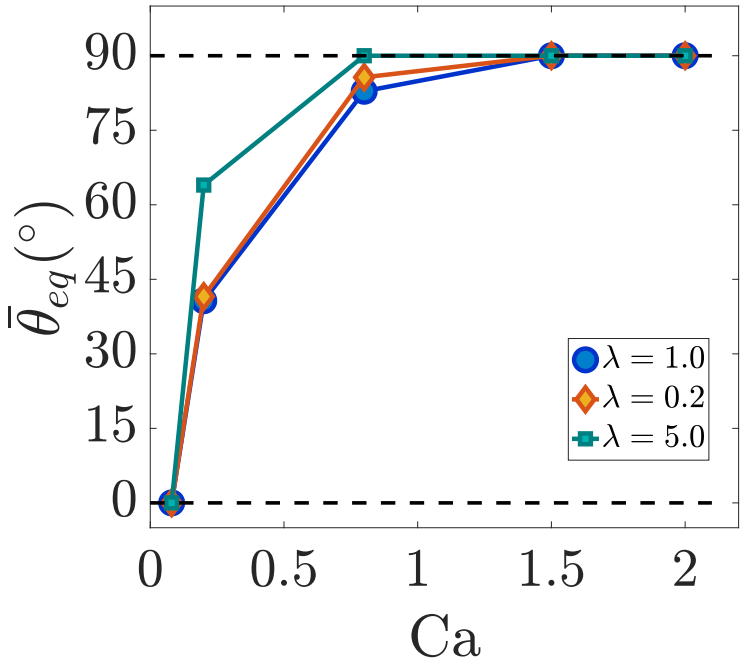



**Figure 6.3:** Bifurcation behavior for a prolate capsule (AR = 2.0) with $\hat{\kappa}_B = 0.02$ and varying $\lambda$. The black dashed lines at $\theta = 0°$ and $\theta = 90°$ represent the orbits for a capsule aligned with the $z$ axis and in the shear plane, respectively.

$\alpha$, evolves towards the same orbit at long times, denoted as $\bar{\theta}_{eq}$. In FIG. 6.2a (Ca = 0.08), six values of $\alpha$ are considered, and the orbit of the capsule always converges towards $\bar{\theta}_{eq} = 0°$. For simplicity, results are only shown for four values of $\alpha$ in FIGs. 6.2b, 6.2c and 6.2d. As Ca increases, $\bar{\theta}_{eq}$ increases from 0° to 90°. This trend holds qualitatively for $\lambda = 0.2$ and $\lambda = 5$, and also as AR increases from 2.0 to 3.0 (not shown). The dependence of $\bar{\theta}_{eq}$ on Ca for a prolate capsule (AR = 2.0) with $\hat{\kappa}_B = 0.02$ is illustrated in a bifurcation diagram with varying $\lambda$, as shown in FIG. 6.3. Note that by symmetry, the orbits for a capsule lying in the shear plane ($\theta = 90°$) and aligned with the $z$ axis ($\theta = 0°$) are always solutions for all parameter values. However, these two solutions may not be stable with respect to symmetry-breaking

perturbations; indeed, in the case of $\lambda = 1$ (solid blue line with circles), for example, there is a symmetry-breaking bifurcation away from $\theta = 0^\circ$ between Ca $= 0.08$ and Ca $= 0.2$, and another one away from $\theta = 90^\circ$ between Ca $= 0.7$ and Ca $= 1.5$.

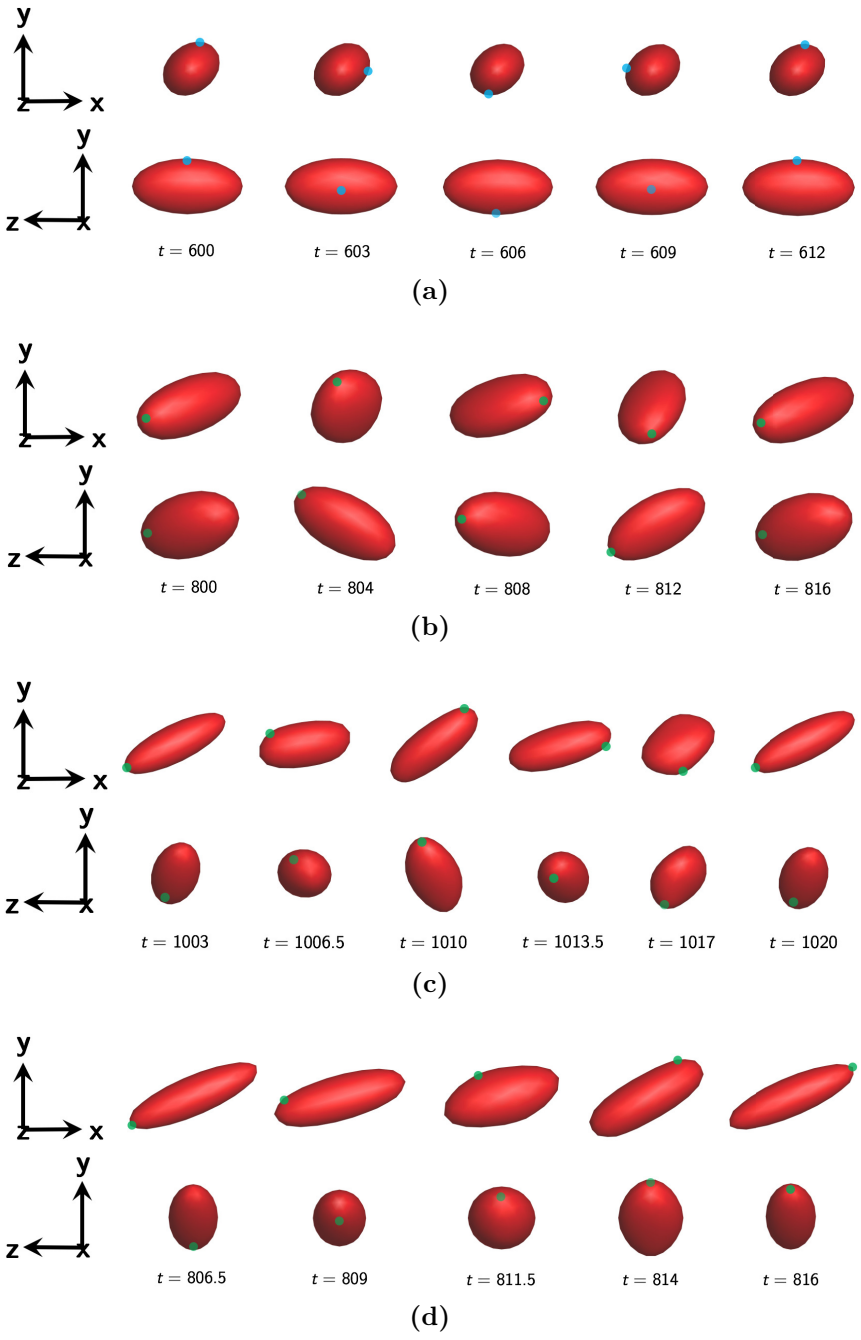



**Figure 6.4:** Time sequence images (side and front views) of a prolate capsule (AR = 2.0) with $\hat{\kappa}_B = 0.02$ and $\lambda = 1$ taking a rolling (a, Ca = 0.08), wobbling (b, Ca = 0.2), oscillating-swinging (c, Ca = 0.7), and swinging (d, Ca = 1.5) motion, respectively. The initial orientation of the capsule is $\alpha = 5°$. The markers indicate the positions of a membrane point initially on the equator of the capsule for (a), and a membrane point initially on the major axis of the capsule for (b), (c) and (d).

We now look into the detailed motions of the capsule in different Ca regimes. With increasing Ca, four orbital modes are determined corresponding to the stable orbits in different regimes. At very low Ca, the major axis of the capsule is observed to evolve towards the vorticity axis via a process termed drifting precession [Cordasco and Bagchi, 2013], till the capsule takes a stable rolling motion (FIG. 6.4a). As Ca increases, the capsule orbit drifts towards an intermediate equilibrium configuration where the capsule exhibits a wobbling behavior while precessing about the vorticity axis (FIG. 6.4b); this motion is named stable precession in [Cordasco and Bagchi, 2013]. In the regime of higher Ca, the capsule adopts a complex motion termed oscillating-swinging (FIG. 6.4c), in which the long axis of the elongated capsule oscillates both about the shear plane and about a mean inclination with respect to the flow direction, while the membrane of the capsule rotates around its deformed shape with the capsule elongation oscillating over time, as described by Dupont *et al.* [2013]. With a further increase in Ca (FIG. 6.4d), the oscillations about the shear plane in the oscillating-swinging motion vanish, and a pure in-plane fluid-like swinging motion, as described by Walter *et al.* [2011], is assumed eventually. This qualitative transition of stable orbital motions for a prolate capsule agrees well with the findings by Dupont *et al.* [2013], which did not include bending resistance.

In addition, we examine the effect of spontaneous curvature on the orbital dynamics of the prolate capsule. Figure 6.5 shows the orbit evolution for a capsule with zero spontaneous curvature (i.e. $c_0 = 0$ in Eq. 3.9) everywhere on the membrane surface. For each Ca, the long-time orbit is independent of the initial orientation, and thus only the results for $\alpha = 5°$ and $\alpha = 85°$ are shown here. Similar to the previous case, $\bar{\theta}_{eq}$ is observed to increase from 0° to 90° at increasing Ca. Same stable motion modes

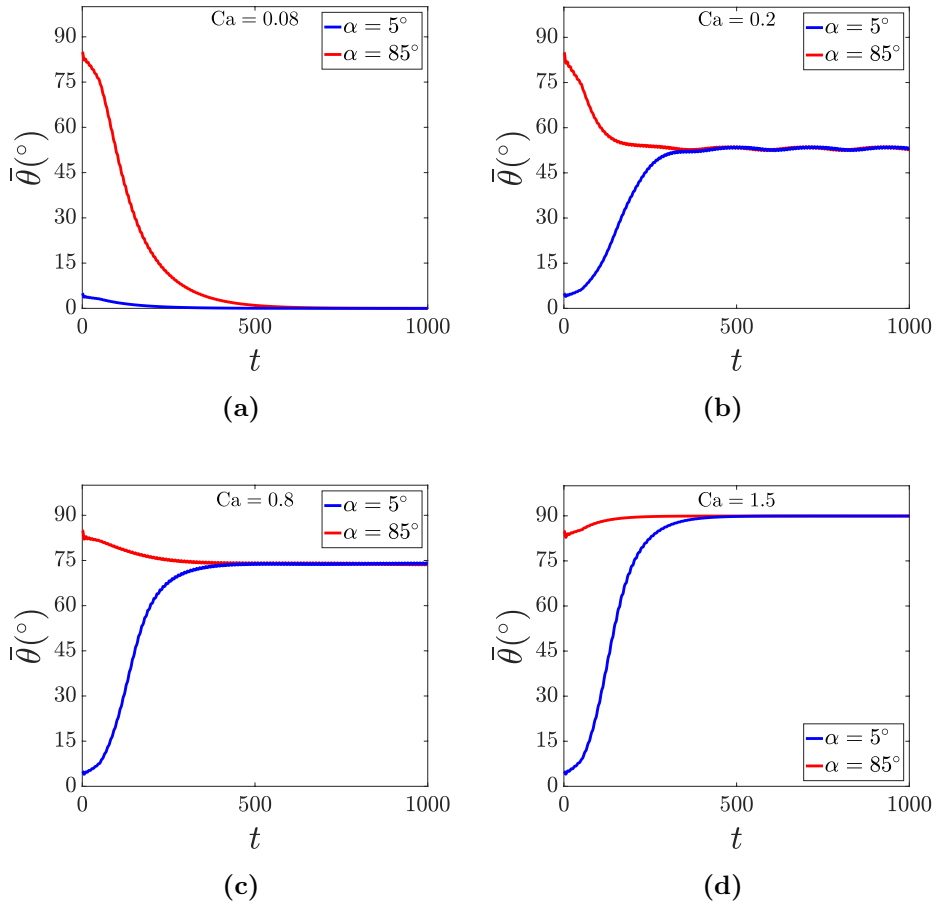



**Figure 6.5:** Evolution of $\bar{\theta}$ of a prolate capsule (AR = 2.0) with $\hat{\kappa}_B = 0.02$ and $\lambda = 1$ at (a) Ca = 0.08, (b) Ca = 0.2, (c) Ca = 0.8, and (d) Ca = 1.5. Here the spontaneous curvature is assumed to be zero ($c_0 = 0$ in Eq. 3.9) everywhere on the membrane surface.

are determined, namely, rolling, wobbling, oscillating-swinging, and swinging, associated with different Ca regimes. Cordasco and Bagchi [2013] also found a qualitatively similar transition of the orbital dynamics at increasing Ca from drift precession (the rolling regime) to stable precession accompanied by a tank-treading behavior of the membrane (the oscillating-swinging regime) for a prolate capsule (AR = 2.0, $\lambda = 1$) with zero spontaneous curvature and small bending stiffness ($\hat{\kappa}_B = 0.01$). These results suggest that the spontaneous curvature has a minor effect on the orbital behavior

of the capsule.

Using Eq. 6.6, we can predict the rheology for a suspension of prolate capsules in the dilute limit. Figure 6.6 shows the capillary-number dependence of the time-averaged intrinsic viscosity and the dimensionless normal stress differences predicted for a dilute suspension of such capsules all of which assume that same orbit for AR = 2.0 and $\hat{\kappa}_B = 0.02$. A decrease in the intrinsic viscosity $[\eta]$ with increasing Ca, i.e. shear-thinning, is observed for all viscosity ratios considered here, and $[\eta]$ decreases with increasing $\lambda$ at each Ca (FIG. 6.6a). Shear-thinning is the generally-expected behavior for dilute suspensions of deformable particles, and indeed has also been observed for dilute suspensions of other types of capsules, such as spherical capsules [Barthès-Biesel and Chhim, 1981, Pozrikidis, 1995, Ramanujan and Pozrikidis, 1998, Bagchi and Kalluri, 2010, Clausen and Aidun, 2010], oblate capsules [Bagchi and Kalluri, 2011], and biconcave discoidal capsules [Pozrikidis, 2003, Drochon, 2003, Takeishi *et al.*, 2019]. Results for the dimensionless normal stress differences $N_1$ and $N_2$ are shown in FIGs. 6.6b and 6.6c, respectively. For all cases, $N_1 > 0$ and $N_2 < 0$, with $|N_2| \ll N_1$. In general, both $N_1$ and $|N_2|$ decrease with increasing $\lambda$ at each Ca, and increase monotonically with Ca for $\lambda = 1.0$ and $\lambda = 0.2$. For $\lambda = 5.0$, however, $N_1$ is observed to show a non-monotonic dependency on Ca, while $|N_2|$ decreases with Ca.

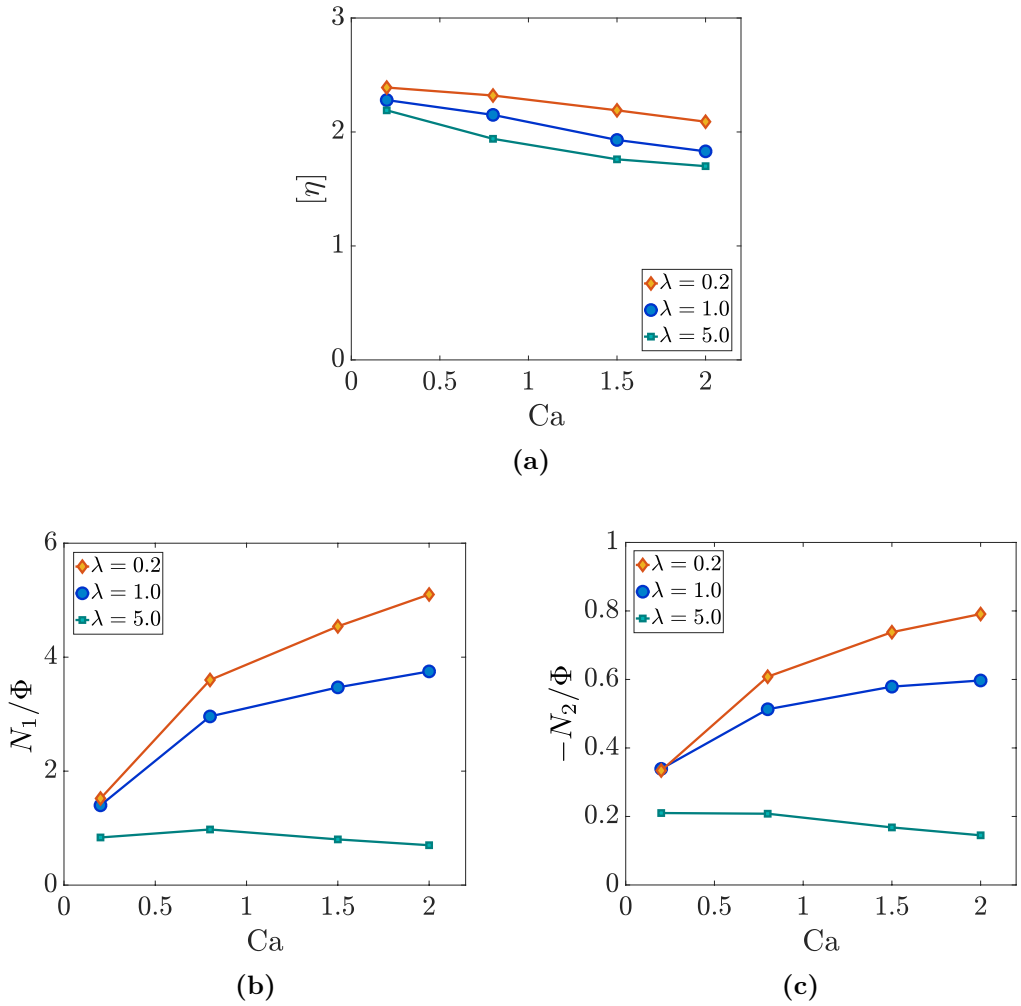



**Figure 6.6:** Intrinsic viscosity (a) and dimensionless normal stress differences (b,c) predicted for a dilute suspension (with volume fraction $\Phi$) of identical prolate capsules (AR = 2.0) with $\hat{\kappa}_B = 0.02$ taking the same corresponding stable orbit at varying Ca.

### 6.3.2 Dynamics of prolate capsules with large bending stiffness

We found in the previous section that the long-time orbits for a prolate capsule with small bending stiffness are always independent of the initial conditions, although the stable orbital motions vary with capillary number. In this section, we investigate the

dynamics of a prolate capsule with large bending stiffness. The spontaneous shape of the capsule is always assumed to be the same as its rest shape unless stated otherwise. We vary the viscosity ratio $\lambda$, capillary number Ca, initial orientation $\alpha$ and aspect ratio AR of the capsule while keeping the bending modulus $\hat{\kappa}_B = 0.2$. We reveal that large bending stiffness coupled with high viscosity ratio can give rise to a multiplicity of attractors for the capsule dynamics, which will be presented and discussed below.

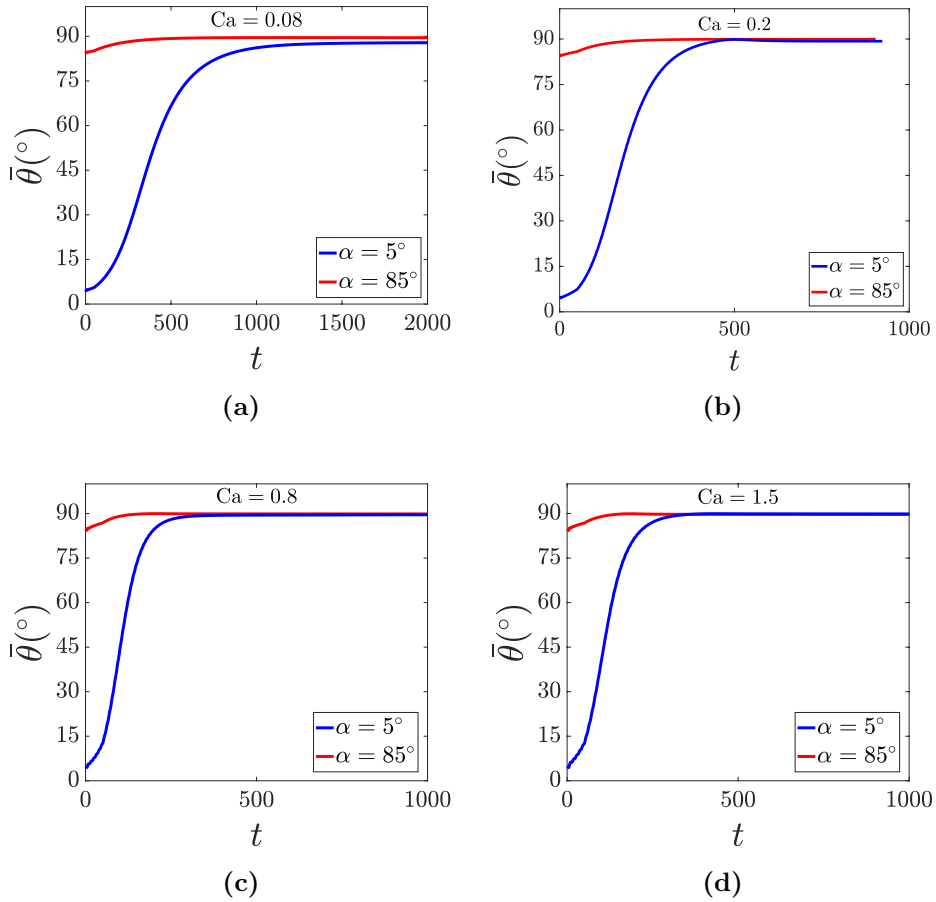



**Figure 6.7:** Evolution of $\bar{\theta}$ of a prolate capsule (AR = 2.0) with $\hat{\kappa}_B = 0.2$ and $\lambda = 1$ at varying Ca. At low Ca the capsule takes a stable tumbling motion at long times ((a) Ca = 0.08 and (b) Ca = 0.2)). A tumbling-to-swinging transition is observed at moderate Ca ((c) Ca = 0.8) before swinging becomes the attractor at high Ca ((d) Ca = 1.5).

Again, we begin with $\lambda = 1$ and AR = 2.0. Unlike the case with $\hat{\kappa}_B = 0.02$, in this case the stable orbit for the capsule is always in the shear plane, as shown by the $\alpha$-independent convergence of $\bar{\theta}$ towards 90° at varying Ca in FIG. 6.7. The time it takes for this transient convergence decreases in general with increasing Ca. This conclusion holds as $\lambda$ decreases from 1 to 0.2, and also as AR increases from 2.0 to 3.0 (not shown). In a previous numerical study by Walter *et al.* [2011], two regimes of stable orbital motion were found for a prolate capsule with the major axis initially lying in the shear plane: a rigid-body-like tumbling motion at low capillary number, and a fluid-like swinging motion at high shear rate, in which the capsule elongation and orientation both oscillate in shear flow with the membrane continuously rotating around its deformed shape. Here we observe similar dynamics. At low Ca, the capsule takes tumbling as the stable orbit (FIGs. 6.7a and 6.7b), while at high Ca swinging becomes the attractor (FIG. 6.7d); a tumbling-to-swinging transition is observed at moderate Ca (FIG. 6.7c), which is characterized by a nearly circular profile of the deformed capsule in the shear plane and roughly the same length of the two principal axes of the capsule during each half-period. A similar transition was also observed for a prolate solid elastic particle in shear flow in both a theoretical prediction by Gao *et al.* [2012] and a numerical investigation by Villone *et al.* [2015].

Now we consider the cases where the viscosity ratio $\lambda$ is greater than unity. Figure 6.8 shows the evolution of $\bar{\theta}$ over time for a prolate capsule with AR = 2.0 and $\lambda = 5$ at varying Ca. At low and high Ca regimes, the orbit of the capsule converges towards $\bar{\theta}_{eq} = 90°$ and $\bar{\theta}_{eq} = 0°$, representing a stable tumbling and rolling motion, respectively (FIGs. 6.8a and 6.8c). At intermediate Ca, however, the orbit taken by the capsule at long times is found to depend on the initial orientation, as observed in

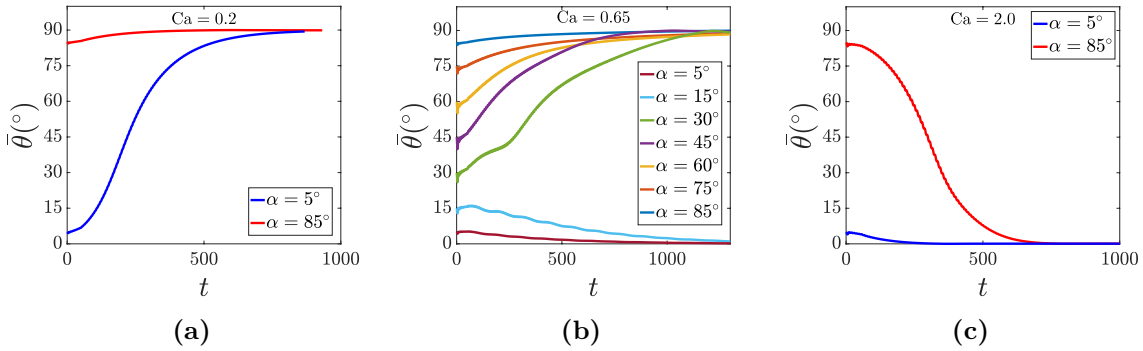



**Figure 6.8:** Evolution of $\bar{\theta}$ of a prolate capsule (AR = 2.0) with $\hat{\kappa}_B = 0.2$ and $\lambda = 5$ at (a) Ca = 0.2, (b) Ca = 0.65, and (c) Ca = 2.0.

FIG. 6.8b. Several values of $\alpha$ ranging from 5° to 85° are considered here to illustrate the dependence of the long-time orbit on the initial orientation, and the results for a range of Ca are displayed in FIG. 6.9. The key characteristic of this regime is that multiple stable orbits coexist, as observed in FIGs. 6.9a, 6.9b and 6.9c. In this multiplicity regime, two stable solution branches are found as the capsule with varying $\alpha$ evolves towards the long-time orbit. The lower branch always corresponds to a stable rolling motion with $\bar{\theta}_{eq} = 0^\circ$. For the upper branch, $\bar{\theta}_{eq}$ decreases with increasing Ca from 90°, which corresponds to a stable tumbling motion, to intermediate values representing stable precessing motions about the shear plane. The multiplicity of attractors disappears as Ca further increases, and $\bar{\theta}_{eq} = 0^\circ$ (rolling) becomes the only stable orbit (FIG. 6.9d). Another important observation is that the critical value of $\alpha$ for the two branches of the evolution results, denoted as $\alpha_c$, increases as Ca increases. Here it is not necessary to determine the exact values for $\alpha_c$; actually, a range for $\alpha_c$ at each Ca is sufficient to show this trend: $\alpha_c \in (15^\circ, 30^\circ)$ at Ca = 0.65 (FIG. 6.9a), $\alpha_c \in (30^\circ, 45^\circ)$ at Ca = 0.8 (FIG. 6.9b), and $\alpha_c \in (45^\circ, 60^\circ)$ at Ca = 0.9 (FIG. 6.9c).

The global effects of Ca on $\bar{\theta}_{eq}$ for the attractors and $\alpha_c$ for the multiplicity regime

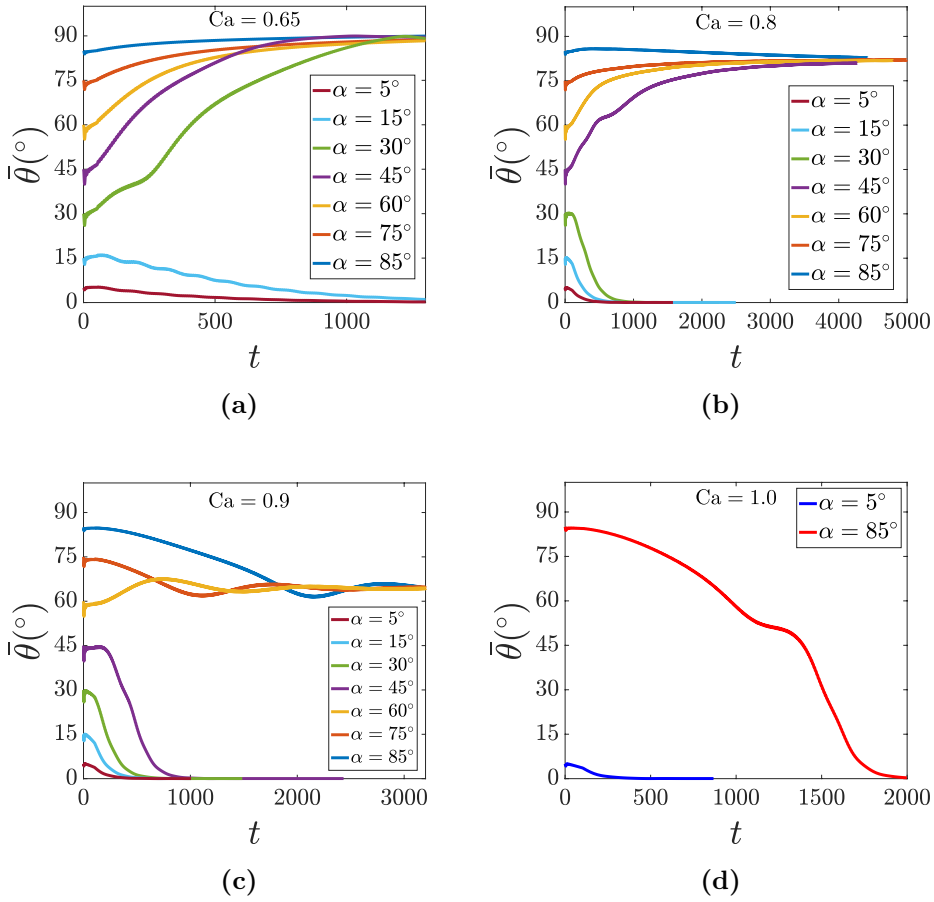



**Figure 6.9:** Evolution of $\bar{\theta}$ of a prolate capsule (AR = 2.0) with $\hat{\kappa}_B = 0.2$ and $\lambda = 5$ at (a) Ca = 0.65, (b) Ca = 0.8, (c) Ca = 0.9, and (d) Ca = 1.0.

described above are summarized as a bifurcation diagram in FIG. 6.10a. The values for $\bar{\theta}_{eq}$ corresponding to the attractors in different regimes, either single or multiple, are represented by the solid blue lines with circles, and the estimated values for $\alpha_c$ by the dashed blue line with circles. Again, there are always solutions at $\theta = 0^\circ$ and $\theta = 90^\circ$ that correspond to the orbits for a capsule aligned with the $z$ axis and in the shear plane, respectively. These solutions are found to be unstable in certain regimes of Ca, as indicated by the dashed black lines with crosses. Indeed, there is a

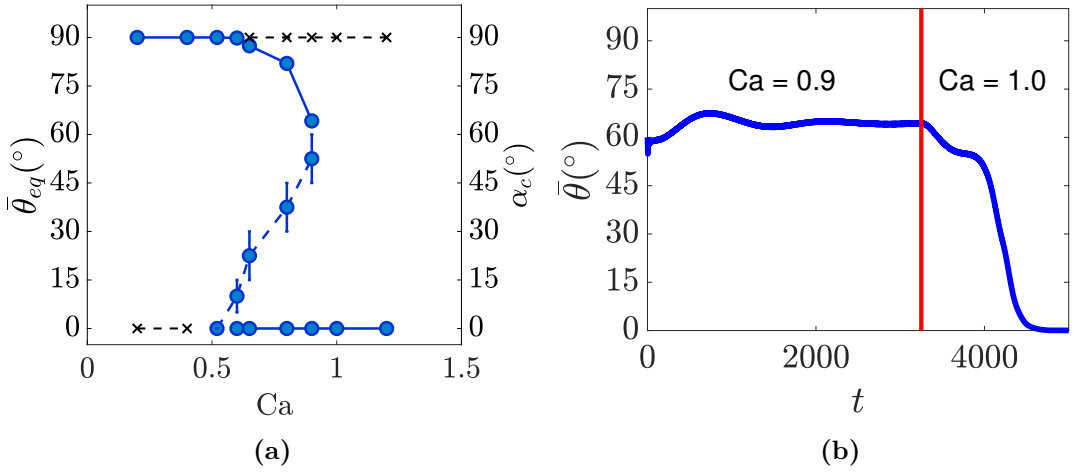



**Figure 6.10:** (a) Bifurcation behavior for a prolate capsule (AR = 2.0) with $\hat{\kappa}_B = 0.2$ and $\lambda = 5$. The values for $\bar{\theta}_{eq}$ corresponding to the attractors are represented by the solid blue lines with filled circles, and the estimated values for $\alpha_c$ by the dashed blue line with filled circles (the error bars indicating the range for $\alpha_c$ at each Ca in the multiplicity regime). The unstable solutions at $\theta = 0°$ and $\theta = 90°$ are indicated by the dashed black lines with crosses. (b) Evolution of $\bar{\theta}$ for a capsule with $\alpha = 60°$ initially at Ca = 0.9. When a stable orbit is reached, the value of Ca is suddenly increased to 1.0, and the capsule evolves towards a new stable orbit.

symmetry-breaking bifurcation away from $\theta = 90°$ between Ca = 0.6 and Ca = 0.65, and away from $\theta = 0°$ between Ca = 0.4 and Ca = 0.52. Two branches of attractors are observed. With any instantaneous orientation $\theta$ above the dashed blue line, the capsule would be attracted to a stable orbit on the upper branch of the attractors at the corresponding Ca, while any value for $\theta$ below the dashed blue line converges towards a rolling orbit on the lower branch with $\bar{\theta}_{eq} = 0°$. The turning point at Ca $\approx$ 0.9 corresponds to a saddle-node bifurcation – for higher Ca this intermediate solution loses existence. This loss of existence is indicated by computing the solution at Ca = 0.9 and suddenly increasing Ca from 0.9 to 1.0 (FIG. 6.10b). The capsule now evolves from a stable precession to a rolling motion as taken by a capsule with the same initial orientation initially at Ca = 1.0.

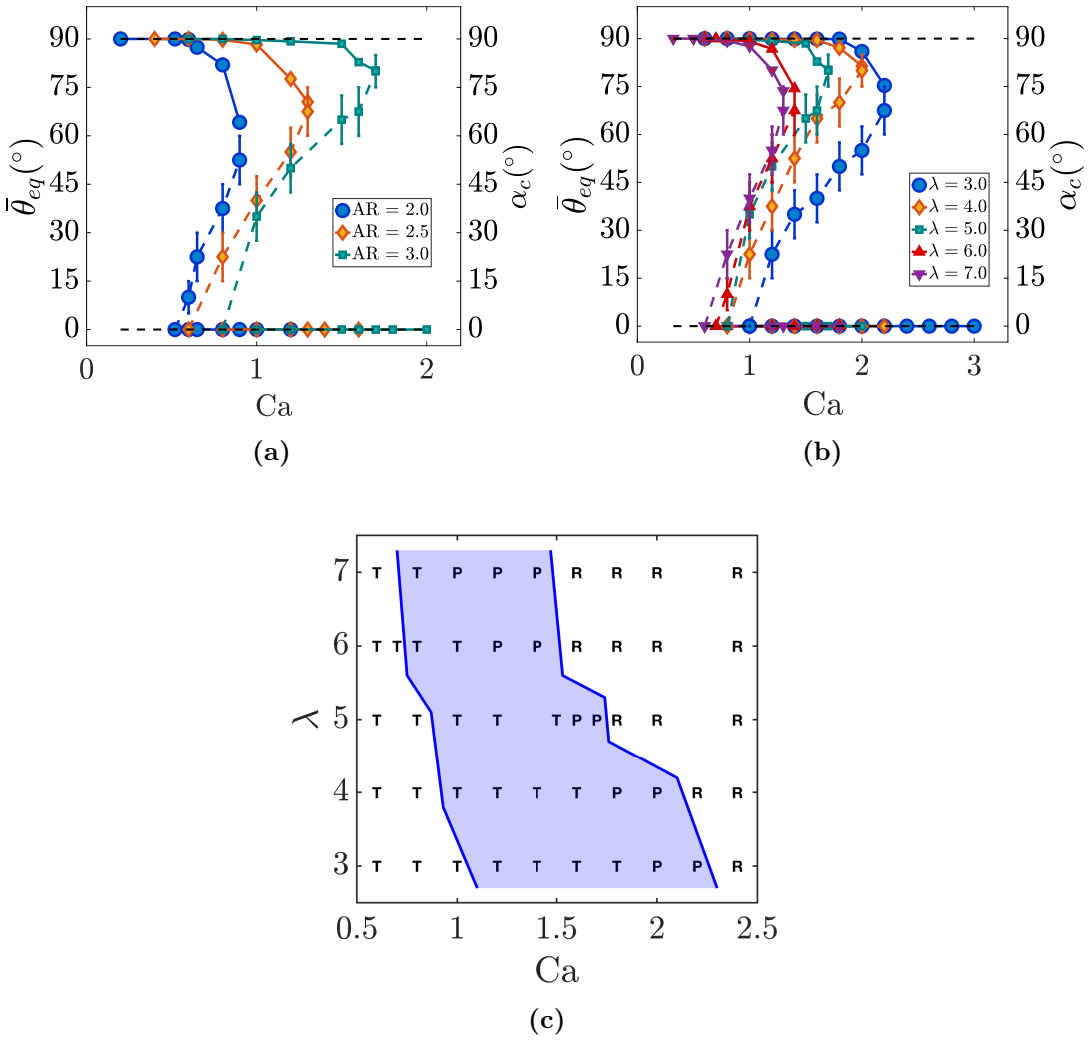



**Figure 6.11:** Effects of capsule aspect ratio (a, $\lambda = 5$) and the viscosity ratio (b, AR = 3.0) on the bifurcation behavior of the attractors for a prolate capsule with $\hat{\kappa}_B = 0.2$. Again, the black dashed lines at $\theta = 0°$ and $\theta = 90°$ correspond to the orbits for a capsule aligned with the $z$ axis and in the shear plane, respectively. (c) Phase diagram of stable orbital motions for a prolate capsule (AR = 3.0) with $\hat{\kappa}_B = 0.2$ over a range of Ca and $\lambda$. The multiplicity regime is shaded in blue, and only the motion modes for the attractors on the upper branch are shown here (the attractors on the lower branch always correspond to rolling and thus are not shown here). T denotes tumbling, P precessing, and R rolling.

Similar to our findings, a tumbling-to-rolling transition was also observed for a prolate capsule (AR = 2.0, $\lambda = 1$) with zero bending resistance but in the presence of a small particle inertia [Wang *et al.*, 2013], and a multiplicity of attractors was

found in the transition regime. Other studies [Yu *et al.*, 2007, Huang *et al.*, 2012, Rosen *et al.*, 2014] have also reported a dependence of the stable orbit on the initial orientation for a solid prolate particle at certain Reynolds number regimes. A recent experimental investigation of red blood cells under shear flow in the dilute regime by Minetti *et al.* [2019] has revealed hysteresis loops in the fraction of tank-treading cells upon increasing or decreasing shear rate. This result implies the presence of at least two populations of cells with different orbital dynamics that stably coexist in the same shear flow. This is exactly the situation that our computational results imply. Figure 6.11a shows the bifurcation behavior of the attractors for a prolate capsule ($\lambda = 5$) with various aspect ratios. It is observed that as AR increases from 2.0 to 3.0, the onset of the multiplicity regime occurs at a higher Ca, and this regime becomes broader. The effect of the viscosity ratio $\lambda$ is illustrated in FIG. 6.11b for a capsule with AR = 3.0. In the parameter regime considered here, the multiplicity regime starts at a lower Ca and becomes narrower with increasing $\lambda$, showing an effect opposite to that of the aspect ratio. The orbital modes are determined for the attractors on the upper branch of the multiplicity, and summarized in a phase diagram over a wide range of Ca and $\lambda$ (FIG. 6.11c). Snapshots of a capsule ($\lambda = 6$) taking a stable tumbling, precessing, and rolling motion are shown in FIGs. 6.12a, 6.12b and 6.12c, respectively, as examples.

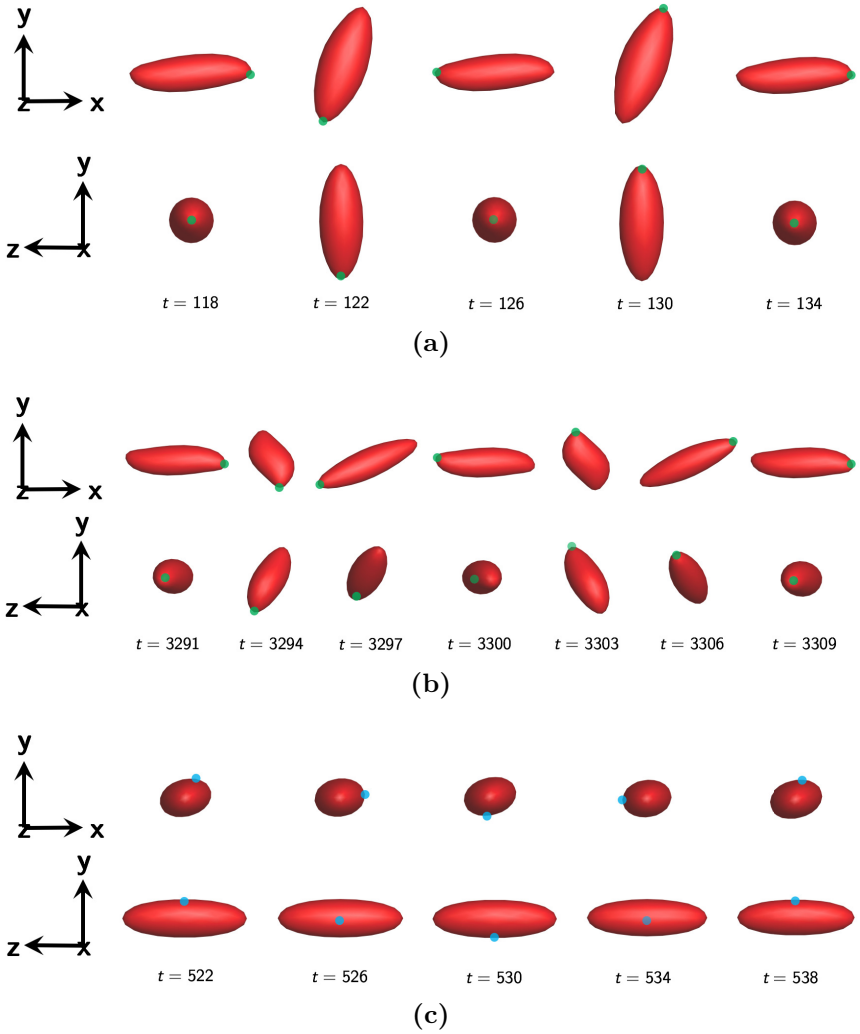



**Figure 6.12:** Time sequence images (side and front views) of a prolate capsule (AR = 3.0) with $\hat{\kappa}_B = 0.2$ and $\lambda = 6.0$ taking a tumbling (a, Ca = 0.6), precessing (b, Ca = 1.4), and rolling (c, Ca = 2.0) motion, respectively. The initial orientation of the capsule is $\alpha = 75°$. The markers indicate the positions of a membrane point initially on the major axis of the capsule for (a) and (b), and a membrane point initially on the equator of the capsule for (c).

The multiplicity in attractors for a single prolate capsule, as described above, implies a multiplicity in the rheological properties for a dilute suspension of such capsules (AR = 3.0 and $\hat{\kappa}_B = 0.2$). Results are summarized in FIG. 6.13 for two viscosity ratios, $\lambda = 3.0$ and $\lambda = 5.0$. For each $\lambda$, the squares represent the pure tumbling regime at lower Ca, while the circles represent the pure rolling regime at

higher Ca; the multiplicity regime at intermediate Ca is bounded by vertical dotted lines, the downward and upward triangles representing the attractors on the upper branch (either tumbling or precessing) and the stable rolling orbits on the lower branch, respectively. All capsules are assumed to take the same stable orbit at each Ca. In this idealized situation, two different stable values for the particle stress can coexist when Ca is in the multiplicity regime. A general shear-thinning behavior is observed in FIG. 6.13a for both viscosity ratios, and minor differences are observed between these two cases. This shear-thinning behavior is also observed for $\lambda = 1.0$ and $\lambda = 0.2$ (not shown). Another observation is that $[\eta]$ is higher when the capsules are taking a stable tumbling (or precessing) motion than it is when they are rolling. Mueller *et al.* [2010] numerically determined the Einstein coefficient for a dilute suspension of inertialess non-spherical solid particles with a distribution of orientations, and reported similar findings: the contribution of a prolate particle to the suspension viscosity (i.e. the $yx$-component of the particle's force dipole) decreases as the orbit of the capsule evolves from tumbling to rolling. Huang *et al.* [2012] showed that this conclusion still holds in the presence of small inertia.

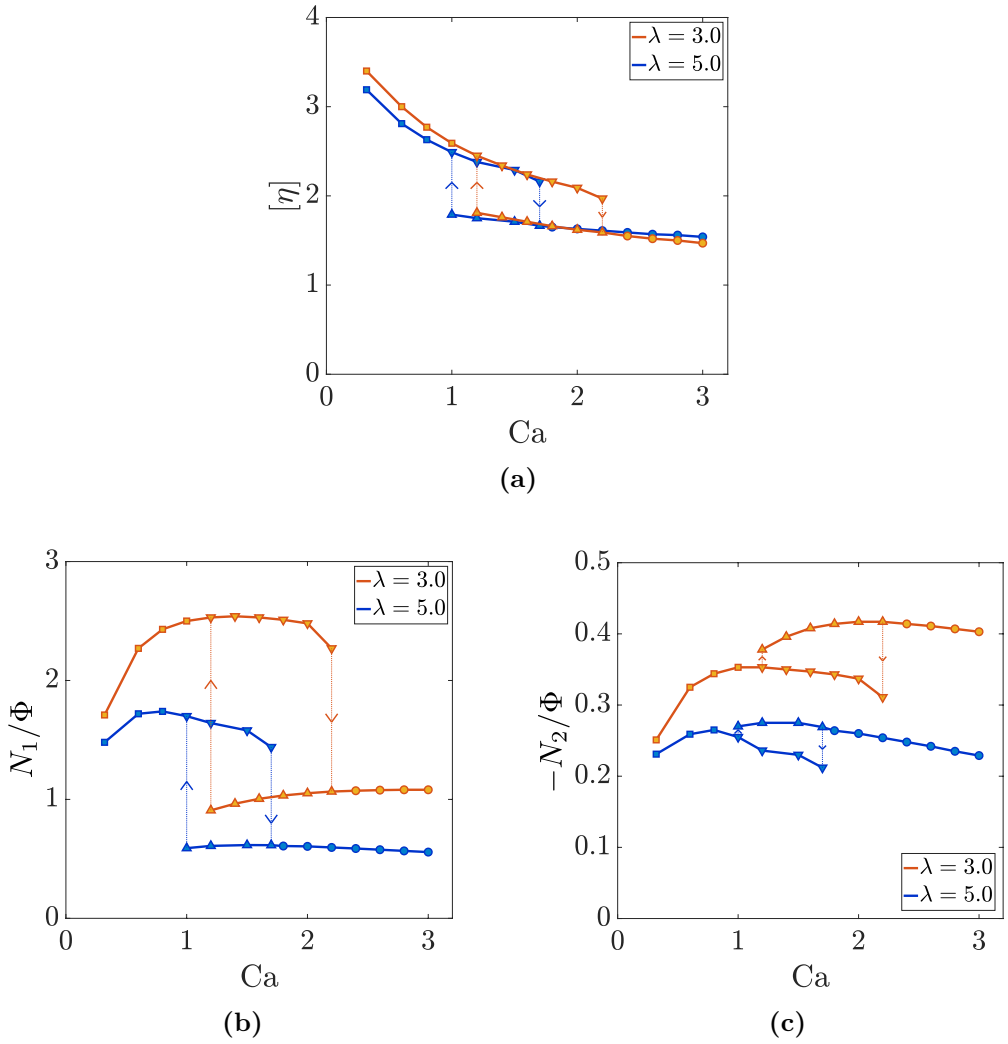



**Figure 6.13:** Intrinsic viscosity (a) and dimensionless normal stress differences (b,c) predicted for a dilute suspension (with volume fraction $\Phi$) of identical prolate capsules (AR = 3.0) with $\hat{\kappa}_B = 0.2$ taking the same corresponding stable orbit(s) at varying Ca for $\lambda = 3.0$ and $\lambda = 5.0$. In each case, the squares represent the pure tumbling orbits at lower Ca, and the circles represent the pure rolling orbits at higher Ca; the downward and upward triangles represent the attractors on the upper branch (either tumbling or precessing) and the stable rolling orbits on the lower branch of the multiplicity regime (bounded by vertical dotted lines), respectively.

For the dimensionless normal stress differences $N_1$ and $N_2$ (FIGs. 6.13b and 6.13c), again, the values are always positive for $N_1$ and negative for $N_2$, with $|N_2| \ll N_1$. Specifically, $N_1$ displays an obvious non-monotonic dependency on Ca when the capsules are tumbling or precessing, while having smaller values and showing a small

variation with Ca for a suspension of rolling capsules. This trend with Ca is qualitatively similar for both viscosity ratios, even though the magnitude of $N_1$ corresponding to each line is much smaller for the higher viscosity ratio ($\lambda = 5.0$). A non-monotonicity is also observed for $N_2$. Overall, as a result of the existence of the multiplicity regime, the values for each quantity of the rheology follow the path along the upper branch, and eventually fall onto the lower branch through the right vertical dotted line upon quasi-statically increasing Ca; conversely, the values move along the lower branch and jump onto the upper branch via the left vertical dotted line upon quasi-statically decreasing Ca. These processes are illustrated by the arrows in each figure of FIG. 6.13.

The presence of this complex rheological behavior naturally raises the question of whether there might be important fluid-mechanical consequences such as shear banding. In the dilute regime these phenomena cannot arise because the particle contribution to the total stress is much smaller than the stress due to the solvent, so the flow curve (shear stress vs. strain rate) will not deviate substantially from linear. If the multiplicity were to persist to large concentration, the resulting flow curve is of the type that would lead not to shear banding (where two shear rates exist for the same shear stress) but to vorticity banding (where two shear stresses exist for the same shear rate) [Dhont and Briels, 2008].

More generally, at finite concentration the particles are hydrodynamically coupled, which may result in changes to the dynamics. One natural question is whether the orbits of particles can become synchronized. While possible, we consider this unlikely, as while the particles are rotating, they are also moving past one another due to the mean shear and thus only in close proximity for a time scale of a few strain units.

## 6.4 Conclusion

In this work we have systematically explored the orbital dynamics of an inertialess neutrally-buoyant deformable prolate capsule in unbounded simple shear flow using direct simulations. For a capsule with small bending stiffness, we revealed that the orbit always converges towards a unique stable equilibrium state independent of the initial orientation. As Ca increases, the stable orbit evolves from the $z$ (vorticity) axis to the shear plane. This trend holds qualitatively for all values of $\lambda$ and AR considered in this study. Four dynamical modes for the stable orbit, namely, rolling, wobbling, oscillating-swinging, and swinging, are determined at increasing Ca, similar to the findings by Dupont *et al.* [2013]. The spontaneous curvature is shown to have a minor effect on the orbital dynamics of the capsule, although we believe that the artificial capsules in experiments are more likely to adopt a spontaneous shape the same as or close to the rest shape, instead of a flat sheet, which would lead to higher stress and strain energy in the membrane surface.

For a capsule with large bending stiffness, we found that the viscosity ratio $\lambda$ plays a significant role in the determination of the stable orbits. When $\lambda \lesssim 1$, the stable orbit is always in the shear plane. Two regimes of stable orbital motions are identified: a rigid-body-like tumbling motion at low Ca, and a fluid-like swinging motion at high Ca. When $\lambda > 1$, the stable motion is tumbling and rolling at low and high Ca regimes, respectively, independent of the initial orientation. During the transition, however, the capsule is found to adopt multiple stable orbital modes including tumbling, precessing and rolling, depending on the initial orientation. This multiplicity regime becomes broader as the aspect ratio of the capsule increases, while showing an opposite dependency on the viscosity ratio. We also predicted a

general shear-thinning behavior and a multiplicity in the rheological properties for a dilute suspension of prolate capsules all assuming the same orbit, as a result of the multiplicity in the attractors for the capsule dynamics.

We note, though, that the membrane model adopted in this work has limitations. The model assumes that the capsule membrane is infinitely thin, while incorporating bending resistance by simply adding a bending energy cost function to account for the effect of finite thickness of the capsule membrane. Such a decoupled energy-based model, as pointed out in a prior work by Dupont *et al.* [2015], may be most suitable for particles with a composite membrane such as RBCs, which have a membrane comprising a fluid lipid bilayer tethered to an elastic spectrin network [Mohandas and Evans, 1994]. However, for artificial capsules that may likely have a homogeneous membrane with finite thickness, the accuracy of this model may need further investigation. In addition, the feasibility of this model in terms of describing large bending resistance of the membrane, as considered in this study, may be questionable. Future works should examine the robustness of this model against other membrane models that consider non-zero thickness.

Overall, this work has revealed rich orbital dynamics for single prolate capsules in shear flow over a broad domain of parameter space, and illustrated how the stable orbits for a prolate capsule can be linked to the rheological properties for a suspension of such capsules in the dilute limit. We hope that these results will motivate experiments to probe the phenomenon of multiplicity of stable orbits predicted here.

# Chapter 7

# Conclusions

Flow-induced segregation occurs prevalently in multicomponent systems, of which blood is a classic example. The segregation behavior in blood flow is substantially driven by the differences in their physical properties. Under pathological conditions, however, the dynamics of blood flow can be greatly altered due to the aberrant properties of blood cells. In sickle cell disease (SCD), which is the focus of the present work, diseased red blood cells (RBCs) are misshapen and stiffened. The alterations in cell properties may contribute to the pathophysiology of SCD and associated complications such as endothelial inflammation, which yet remains poorly understood. In this work, we took a first step towards understanding the dynamics of blood flow and RBCs in SCD, taking into account the pathologically altered properties of the diseased cells. Our findings will have clear implications, from a purely physical perspective, on the mechanisms underlying chronic endothelial inflammation in SCD.

To begin with, in Chapter 4 we investigated the motion of isolated neutrally-buoyant, slightly deformable curved prolate fluid-filled capsules in unbounded simple

shear flow at zero Reynolds number using direct simulations. In this work the curved prolate capsule serves as a model for the typical crescent-shaped sickle cells in SCD. The deformability of the capsule is characterized by the nondimensional capillary number Ca, which represents the ratio of viscous stresses to elastic restoring stresses on the capsule. We showed that at long times, the dynamics of the capsule always evolve into a Jeffery-like quasiperiodic orbit regardless of the initial orientation, and the average of this long-time trajectory can be well approximated using the analytical solution for Jeffery orbits with an effective orbit constant $C_{\text{eff}}$ and aspect ratio $\ell_{\text{eff}}$. A parameter study further revealed that as the capsule becomes more deformable or curved, $C_{\text{eff}}$ decreases, indicating a shift of the orbit towards log-rolling motion, while $\ell_{\text{eff}}$ increases weakly as the degree of curvature increases but shows negligible dependency on deformability. These features are not changed substantially as the viscosity ratio $\lambda$ between the inner and outer fluids is changed from 1 to the physiological value of 5. These results demonstrate how the aberrant mechanical properties and distorted shape of sickle cells can lead to distinct trajectories that may, in turn, cause pathological activation of other cells, and serve as a groundwork for studying more complex systems such as flowing suspensions containing sickle cells.

In Chapter 5, detailed boundary integral simulations were then performed to investigate the dynamics of a binary suspension of flexible biconcave discoidal fluid-filled capsules and stiff curved prolate capsules that represent healthy and sickle RBCs, respectively, subjected to a pressure-driven flow confined in a planar slit. The stiff component is dilute in the binary suspension. This system serves as an idealized model for microvascular blood flow in SCD. The key observation is that, unlike healthy RBCs that concentrate around the center of the channel and form an RBC-depleted layer

(i.e. cell-free layer) next to the walls, sickle cells are largely drained from the bulk of the suspension and aggregate inside the cell-free layer, displaying a strong margination phenomenon. The marginated sickle cells approximate a rigid-body-like log-rolling orbit near the walls. For comparison, a binary suspension of flexible biconcave discoidal capsules and stiff straight (non-curved) prolate capsules is also considered, and we showed that the curvature of the stiff component has a insignificant effect on the behavior of the binary suspension and the orbital dynamics of single cells. Additionally, by considering a mixture of flexible and stiff biconcave discoids, we revealed that rigidity difference by itself is sufficient to induce the segregation behavior in a binary suspension. Furthermore, we computed the additional shear stress on the walls induced by different suspensions. Compared to the small fluctuations in wall shear stress for the case with purely healthy RBCs, large local peaks in wall shear stress are observed for all binary suspensions, accredited to the proximity of the marginated stiff cells to the walls. Detailed characterization showed that the shape and size of the stiff component have a secondary role, though straight prolate capsules, which roll downstream very close to the walls, seem to have the greatest overall effect on wall shear stress for the parameter space considered in this study. As endothelial cells are known to mechanotransduce physical forces such as disturbance in shear stress and convert them to physiological processes such as activation of inflammatory signals, these results will aid in understanding the pathophysiology of SCD vasculopathy, suggesting that the purely physical (non-adhesive) interactions between sickle cells and endothelial cells alone may be sufficient to cause chronic endothelial dysfunction that is pervasive throughout the body.

The model for sickle cells in this work derives from modifications to a straight

prolate capsule. As an extended study, in Chapter 6 we numerically investigated the orbital dynamics of a fluid-filled deformable straight prolate capsule in unbounded simple shear flow assuming the Stokes regime. Aiming to fill the gap in prior studies, we explored over a broad domain of parameter space and determined the effects of membrane deformability, bending stiffness, initial orientation, aspect ratio of the capsule and the viscosity ratio between the inner and outer fluids. We found that for a capsule with small bending stiffness, at a given Ca, the orientation converges over time towards a unique stable orbit independent of the initial orientation. With increasing Ca, four dynamical modes were determined as the stable orbit, namely, rolling, wobbling, oscillating-swinging, and swinging. On the other hand, for a capsule with large bending stiffness, we revealed parameter regimes in which either a single or multiple attractors exist. When the viscosity ratio $\lambda \lesssim 1$, the long axis of the capsule always tends towards a stable orbit in the flow-gradient plane, either tumbling or swinging, depending on Ca. When $\lambda \gtrsim 1$, the stable orbit of the capsule is a tumbling motion at low Ca, irrespective of the initial orientation. Upon increasing Ca, there is a symmetry-breaking bifurcation away from the tumbling orbit, and the capsule is observed to adopt multiple stable orbital modes including nonsymmetric precessing and rolling, depending on the initial orientation. As Ca further increases, the nonsymmetric stable orbit loses existence at a saddle-node bifurcation, and rolling becomes the only attractor at high Ca, whereas the rolling state coexists with the nonsymmetric state at intermediate values of Ca. A symmetry-breaking bifurcation away from the rolling orbit was also found upon decreasing Ca. The regime with multiple attractors becomes broader as the aspect ratio of the capsule increases, while narrowing as the viscosity ratio increases. In addition, by computing the particle

contribution to the stress, we also predicted a general shear-thinning behavior and a multiplicity in the rheological properties for a dilute suspension of prolate capsules all assuming the same orbit, as a result of the multiplicity in the attractors for the capsule dynamics. These results will motivate future experiments to probe the phenomenon of multiplicity predicted in the present work for capsule suspensions.

# Chapter 8

# Future directions: extending the present study on blood flow in sickle cell disease

## 8.1 Effects of heterogeneity in cell properties and flow parameters

In Chapter 5, we attempted to probe the mechanism for endothelial inflammation associated with sickle cell disease (SCD) by considering a binary suspension of flexible biconcave discoidal fluid-filled capsules and stiff curved prolate capsules representing healthy and sickle red blood cells (RBCs), respectively, subjected to a pressure-driven flow confined in a planar slit. This system serves as an idealized model for microvascular blood flow in SCD. A major limitation of this system, however, lies in that all sickle cells are modeled to have the same rest shape and membrane mechanics.

In reality, nonnegligible heterogeneity in these physical properties has been clinically observed within the population of sickle cells in SCD patients, which largely depends on the state and conditions of individual cells. To this end, as one direction for future studies, heterogeneity in cell properties should be incorporated.

### 8.1.1 Direct simulation

The current model system for blood flow in SCD, as noted in Section 5.2.1, consists of a "primary" ('$p$') component, which is the flexible biconcave discoids (healthy RBCs), and a "trace" ('$t$') component being the stiff curved prolate capsules (sickle cells). In future simulations, the current system can be extended to ternary (three-component) suspensions by adding a third component $s$ with intermediate stiffness. This additional component represents another subpopulation of sickle cells that are in general less stiff than the typical crescent-shaped irreversibly sickled cells (ISCs) [Messer and Harris, 1970, Nash *et al.*, 1984, Evans and Mohandas, 1987] and have a different morphology [Kaul and Xue, 1991, Byun *et al.*, 2012]. A few computational studies [Lei and Karniadakis, 2012a,b, 2013] have provided a variety of potential models for non-ISCs with different morphologies other than the classic sickle shape, such as granular and elongated shapes. Once these physical parameters are determined for the additional '$s$' component, detailed boundary integral simulations can be performed for a ternary suspension that models SCD blood flow comprising primarily healthy RBCs with two types of sickle RBCs. Results for this system, such as the cross-stream distribution of each component and additional wall shear stress induced by the suspension, can then be compared with those shown in the present work for the binary case to illustrate the contribution of the additional sickle cell subpopulation to the

dynamics of blood flow in SCD and the associated endothelial inflammation.

### 8.1.2 Mechanistic theory

In parallel with direct simulations, we can also leverage a mechanistic theory to predict and understand the dynamics of such ternary suspensions. A recent theory by Henríquez Rivera *et al.* [2016], which describes the flow-induced segregation in binary suspensions, can be readily extended to ternary systems. Here we briefly present our preliminary study using this extended theory.

Consider a dilute suspension composed of three types of deformable capsules subjected to pressure-driven flow in a slit bounded by two no-slip walls at $y = 0$ and $y = 2H$, and periodic in $x$ and $z$ directions. The three particle components in the suspension, namely $p$, $s$, and $t$, are assumed to have the same characteristic length, i.e., $a_p = a_s = a_t$, but varying deformability and mean volume fraction $\bar{\phi}_\alpha$. Deformability of component $\alpha$ ($\alpha = p$, $s$, or $t$) is characterized by the capillary number $\mathrm{Ca}_\alpha = \eta\dot{\gamma}a_\alpha/G_\alpha$, where $\eta$ is the viscosity of the suspending fluid, $\dot{\gamma}$ the shear rate of the flow, and $G_\alpha$ the membrane shear modulus of component $\alpha$, respectively. Here we set $\mathrm{Ca}_p = 0.5$, $\mathrm{Ca}_s = 0.08$, $\mathrm{Ca}_t = 0.01$, i.e., components $s$ and $t$ are much stiffer than component $p$, with $t$ the stiffest. The volume fraction of component $\alpha$ is defined as $\phi_\alpha = n_\alpha V_\alpha$, where $n_\alpha$ and $V_\alpha$ are the number density and the volume per particle of component $\alpha$, respectively. The particle distributions are assumed to be uniform in the $x$ and $z$ directions. In the $y$ direction, all three components are initially distributed uniformly, with mean volume fractions $\bar{\phi}_p = 0.20$, $\bar{\phi}_s = 0.02$, and $\bar{\phi}_t = 1.0 \times 10^{-3}$, respectively, i.e., components $s$ and $t$ are much more dilute than component $p$, with $t$, the stiffest component, approaching the dilute limit. The nondimensionalized dis-

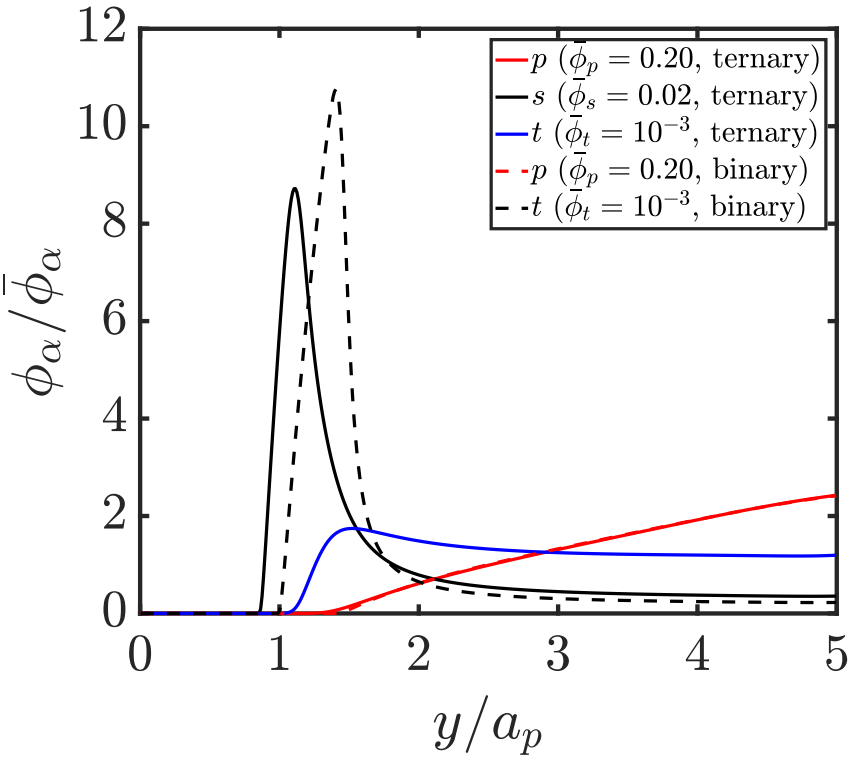



**Figure 8.1:** Steady-state profiles of normalized volume fractions for components in ternary (solid lines) and binary (dash-dot lines) suspensions in planar pressure-driven flow under confinement ($C = 5$). Here $\mathrm{Ca}_p = 0.5$, $\mathrm{Ca}_s = 0.08$, and $\mathrm{Ca}_t = 0.01$; $\bar{\phi}_p = 0.20$, $\bar{\phi}_s = 0.02$, and $\bar{\phi}_t = 1.0 \times 10^{-3}$; $\kappa_1 = 0.16$, $\kappa_{\alpha pc} = 0.02$, and $\kappa_{\alpha pd} = 0.07$.

tance from each wall to the centerplane of the slit is defined as the confinement ratio $C = H/a_p$; here $C = 5$.

The dynamics of this ternary suspension can be described by a theory extended from a so-called simplified drift-diffusion (SDD) model by Henríquez Rivera *et al.* [2016], which incorporates the effects of hydrodynamic migration and pair collisions. The SDD model is focused on the special case of a binary suspension composed of a "primary" component ('$p$') and a "trace" component ('$t$'), such that $n_p \gg n_t$ and only the '$p$' component contributes to the collisional fluxes of both components. Here in this ternary suspension, however, all possible pairs of interparticle interactions, i.e.,

$p-p$, $p-s$, $p-t$, $s-p$, $s-s$, $s-t$, $t-p$, $t-s$, and $t-t$ interactions, are considered for the calculation of the collisional fluxes of all three components. Molecular diffusion of the particles is neglected for the moment. Figure 8.1 shows the steady-state profiles of the normalized volume fractions $\phi_\alpha/\bar{\phi}_\alpha$ for the three components in the ternary suspension (solid lines). Results for components '$p$' and '$t$' in a binary suspension (in the absence of '$s$') are also shown for comparison (dashed lines). In both cases, the '$t$' component is found to strongly marginate, as evident by the near-wall peaks, while the '$p$' component displays a substantial demargination towards the centerplane. Another important observation is that for the ternary suspension, the additional component '$s$', which has intermediate stiffness, displays an intermediate degree of margination, but also drives the stiffest component '$t$' closer to the wall than in the binary case (by comparing black solid and dashed curves).

In [Henríquez Rivera *et al.*, 2016], several regimes of segregation were predicted for the binary suspension, depending on the value of a so-called "margination parameter" $M$, a determinant of the segregation propensity that characterizes the relative significance of the wall-induced migration and the collisional fluxes. For the ternary suspension considered here, the margination parameter for component $\alpha$ ($\alpha = s$ or $t$) is given as

$$M_\alpha = \frac{\kappa_{ppc} + 2\kappa_{ppd}}{\kappa_{\alpha pd}} \left( \frac{\mathrm{Ca}_\alpha}{\kappa_1 + \mathrm{Ca}_\alpha} \frac{\kappa_1 + \mathrm{Ca}_p}{\mathrm{Ca}_p} - \frac{\kappa_{\alpha pc} + \kappa_{\alpha pd}}{\kappa_{ppc} + 2\kappa_{ppd}} \right), \tag{8.1}$$

where $\kappa_1$ quantifies the effect of wall-induced migration, and $\kappa_{\alpha pc}$ and $\kappa_{\alpha pd}$ characterize the contributions of the $\alpha - p$ interaction ($\alpha = p$, $s$, or $t$) to the effects of the collisional drift (subscripted '$c$') and the shear-induced diffusion (subscripted '$d$'),

respectively, both resulting from the collisional fluxes in the governing equations. Here $\kappa_1 = 0.16$, $\kappa_{\alpha pc} = 0.02$, $\kappa_{\alpha pd} = 0.07$. The margination regimes determined for the binary suspension can also be roughly utilized to predict the segregation behavior in the ternary suspension. Specifically, with the parameter values above, the margination parameters for components '$s$' and '$t$' are $M_s = -0.30$ and $M_t = -1.11$, which correspond to regimes of modest and strong margination, respectively. The predictions agree well with the observations in FIG. 8.1.

These preliminary results have suggested the necessity and significance of considering the heterogeneity in cell properties in studying the dynamics of blood flow in SCD. Future simulations and experiments should focus on uncovering the role of an additional component in the segregation behavior and margination in the ternary system during flow. Besides, in the theory predictions above, parameters that quantify the effects of wall-induced migration, collisional drift, and shear-induced diffusion are assumed to be the same for all components, which is an oversimplification given that both migration velocity and collisional dynamics are expected to depend on particle deformability and shape [Smart and Leighton, 1991, Barthès-Biesel *et al.*, 2002, Pranay *et al.*, 2012, Kumar *et al.*, 2014, Sinha and Graham, 2016]. A refined model framework should be established by taking more physical inputs that could be determined with the aid of direct simulations of particle migration and pair collisions.

## 8.2 Effects of vessel geometry

In the present work, the simulation domain for flowing suspensions is a simple planar slit bounded by two parallel walls, which serves as an idealized model for straight

blood vessels. In reality, blood vessels can be highly tortuous, and bifurcated vessel geometries are ubiquitous in the body. It has been long observed clinically that atherosclerosis, which is related to endothelial dysfunction and inflammation, develops preferentially in areas where disturbed blood flow occurs, such as branches, bifurcations, and curvatures of large arteries. Specifically, in these so-called athero-prone areas, disturbed blood flow activates pro-inflammatory signaling of endothelial cells, which results in endothelial dysfunction and subsequent development of atherosclerosis [Abe and Berk, 2014].

In many ways, SCD vasculopathy is similar to that in cardiovascular disease such as atherosclerosis, and relatedly, stroke remains a major cause of mortality in SCD that often occurs in cerebral arteries, which are highly tortuous. In light of our findings in the present work, we expect that the geometric complexities of vessels would mediate the margination of aberrant sickle cells in SCD and the subsequent endothelial pro-inflammatory pathways by altering the local hemodynamic conditions. Indeed, in a recent microfluidic study, Loiseau *et al.* [2015] observed that the flow of a suspension of sickle cells around an acute corner of a bifurcation leads to an enhanced deposition and aggregation of cells. To this end, complex geometries of the flow domain other than a planar slit should be considered in future simulations, with an aim being to shed vital light on the pathophysiology of stroke in SCD.

The current boundary integral implementation for a planar slit geometry can be adapted to more complex geometries. Figure 8.2 shows examples of a bifurcated domain and a tortuous channel for direct simulations. A symmetric bifurcation can be the initial focus. Once the flow dynamics are well understood for this special case, asymmetric bifurcations can be considered. Of particular interest is the Zweifach-

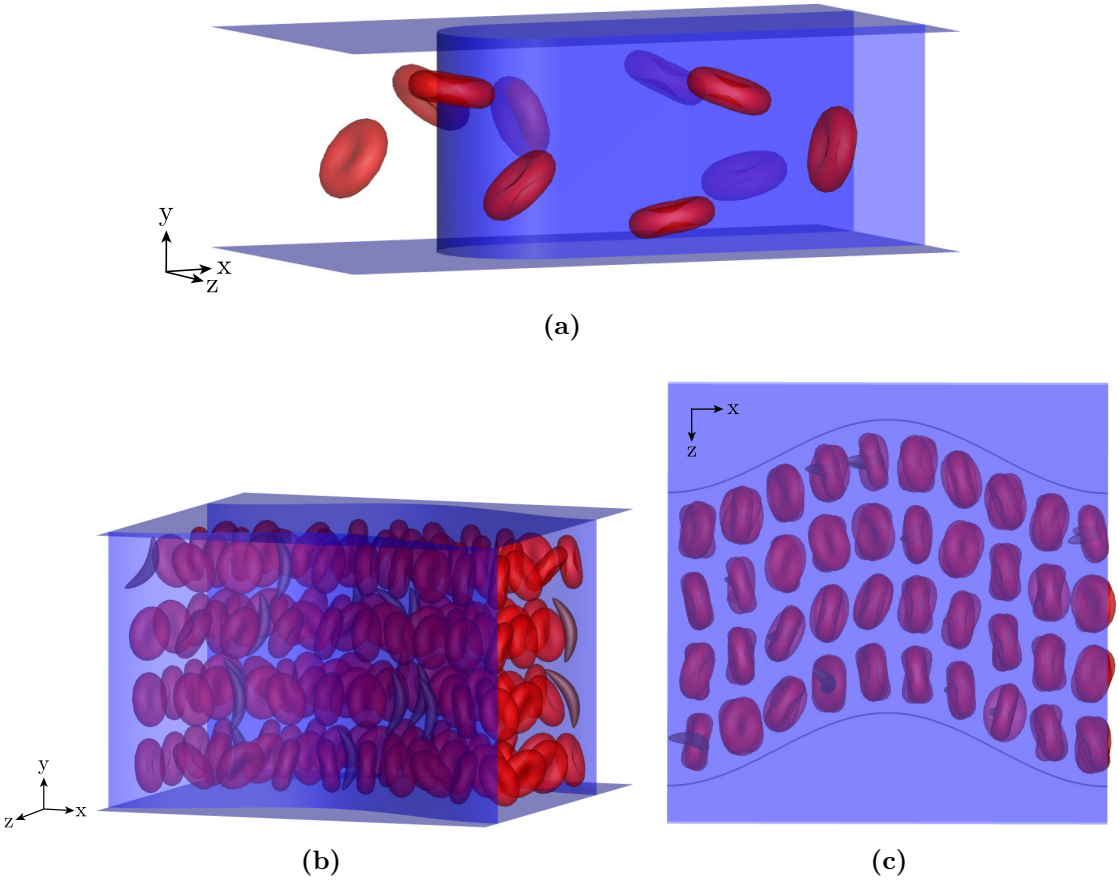



**Figure 8.2:** Schematics of blood flow in a bifurcated domain (a) and a tortuous channel (b: oblique view; c: top view), respectively.

Fung (Z-F) effect, in which the daughter branch with the higher flow rate tends to draw a larger proportion of RBCs than the one with the lower flow rate. We expect that the Z-F effect will be altered in the context of SCD. Specifically, the margination of stiff sickle cells reduces the thickness of cell-free layer, leading to a more uniform distribution of RBCs across the vessels, so that the Z-F effect may be attenuated with a higher hematocrit in the branch with the lower flow rate. For a tortuous channel, systematic investigations can be performed by varying geometry parameters including degree of curvature and channel size. By comparing predictions by numerical

simulations to experimental results from in vitro studies considering similar microfluidic channel geometries, we aim to gain a mechanistic understanding of the effects of geometric complexities on the hemodynamics in SCD and the pathophysiology of the associated vasculopathy and stroke.

## 8.3 Novel biophysical therapeutic strategies

Even though the cause of SCD at a molecular level was uncovered more than half a century ago [Pauling *et al.*, 1949], progress in translating this knowledge into improved treatment has been slow. Only a limited number of FDA-approved drugs are currently available as direct therapies for SCD, which are mostly targeted at vaso-occlusive crisis via down-regulation of adhesion molecules such as selectins to mediate cell binding and sticking. Drugs for SCD vasculopathy are still under-developed for patients, and the subsequent stroke, one of the leading causes of mortality in SCD, is currently treatable only with chronic blood transfusions that depend on donor availability and have their own substantial adverse effects [Hankins *et al.*, 2010, Estcourt *et al.*, 2017].

Our findings in the present study suggest that endothelial inflammation in SCD can be induced in a purely biophysical manner by the aberrant interactions between sickle cells and endothelial cells. This improved understanding of SCD pathophysiology can directly lead to a new paradigm of biophysical therapeutic strategies by mitigating the potential deleterious effects of the aberrant sickle RBCs on endothelium due to margination. Proof-of-concept experiments should first be conducted using blood samples containing both flexible healthy RBCs and a proportion of stiffened diseased cells, comparable to the model systems in our simulations, to validate the

margination of stiff cells predicted in our results. Future drug development and therapeutic strategies based on mitigating the adverse margination effects can consider two ideas. One is leveraging erythrocytapheresis or inducing specific apoptosis to intravenously remove the stiffened RBC subpopulations. The other relies on the softening of sickle cells through membrane modification. A similar idea has been implemented in a recent experimental study [Fay *et al.*, 2016], which showed that glucocorticoid and catecholamine hormones, such as dexamethasone and epinephrine, significantly reduce the stiffness of WBCs and attenuate WBC margination, leading to an increase in the clinical WBC count.

# Appendix A

# Parallel computing using message passing interface

In the present work, an accelerated boundary integral implementation [Kumar and Graham, 2012a] is used to calculate the flow field for simulations of capsule suspensions (Section 3.3). The computational complexity associated with this implementation scales as $O(N\log N)$, where $N$ is proportional to the product of the total number of capsules $N_p$ and the number of triangular elements $N_\triangle$ used for discretizing the membrane of each capsule. For large-scale detailed simulations as in this work, $N$ can be easily $\sim O(10^4)$, and even with this accelerated algorithm, the computational cost for calculating the membrane forces and flow field at each time step can be very expensive. Consequently, the wall-clock time needed for such a capsule suspension to reach a statistically steady state ($\sim$ 1000 strain units or $2 \times 10^6$ time steps) can be extremely long if the simulation is performed on a single core of the compute cluster.

To resolve this, we have achieved a high-level parallelization of the in-house C code

base we developed using message-passing interface (MPI), so that the wall-clock time can be greatly reduced by distributing the total load of calculation over a number of cores. As described in Section 3.3, the acceleration in the boundary integral implementation is achieved by the use of General Geometry Ewald-like Method (GGEM) [Hernandez-Ortiz *et al.*, 2007], the key idea of which is to decompose the overall problem into a local problem and a global problem. Using MPI, we have embarrassingly parallelized most of this algorithm including both local and global parts, i.e., the calculation on each core does not require communication across different cores. The major part that requires communication across processes is the final gathering and operation of data from each process. To achieve the maximal efficiency, the load of calculation for both local and global parts is always evenly distributed across a number of MPI processes. Specifically, the load of calculation for the local part is the sum over all nodes on the membrane of the capsules, while the load of calculation for the global part is the sum over all mesh points in the simulation domain. The parallelization is implemented using the MPI libraries in the public software package provided by the Fastest Fourier Transform in the West (FFTW).

### A.0.1 High performance computing resources

The current in-house computing resource is a compute cluster located in the Mechanical Engineering Building on the University of Wisconsin-Madison campus with appropriate cooling and power supply. It is a Dell PowerEdge high performance computing (HPC) cluster consisting of 1 dual-processor head node (8-core Intel Xeon, 2.00 GHz) and 16 compute dual-processor nodes in total. 5 compute nodes (8-core Intel Xeon E5-2640 v3, 2.60 GHz) were purchased from Dell in 2013, 5 (10-core In-

tel Xeon E5-2640 v4, 2.40 GHz) in 2017, and 6 (12-core Intel Xeon Gold 5118, 2.30 GHz) in 2019. Each compute node has a RAM of 64 GB. The compute nodes are configured with MPI over 40 Gbps InfiniBand. The cluster also includes a storage server with 80 TB of space. This in-house cluster is currently supporting computations for a group of 10 people performing blood simulations as well as turbulence simulations and machine learning tasks. While it is capable of handling the computational needs for simulations of single-cell or small-scale particle suspensions, it has become insufficient for large-scale particle suspension simulations. Additionally, UW-Madison provides research groups with access to two clusters through the Advanced Computing Initiative: a high-throughput and high-performance computing cluster. The high-throughput cluster uses a Condor pool to take advantage of idle CPUs, but it is limited to serial execution that is not suitable for the simulations described here. The high-performance computing cluster has 144 nodes, each equipped with 20 cores (2.5 GHz/core) and 128 GBs of RAM. Unfortunately, this cluster is shared by the entire UW-Madison campus and is highly oversubscribed.

To satisfy our computational needs, we requested additional computing resources from the Extreme Science and Engineering Discovery Environment (XSEDE). In January 2019, we were granted a Startup Allocation (TG-CTS190001, expired 2020-01-10): SDSC Dell Cluster with Intel Haswell Processors (Comet, 24-core Intel Xeon E5-2680v3, 2.50 GHz) with 50,000 service units (SUs), and SDSC Medium-term disk (Data Oasis, 500 GB). In this allocation, we completed successful transfer of our code base from the in-house cluster to Comet, on which benchmark data were collected for the performance and scaling of the code (see below). Later in September 2019, we were awarded a full Research Allocation by XSEDE (TG-MCB190100, expired 2020-

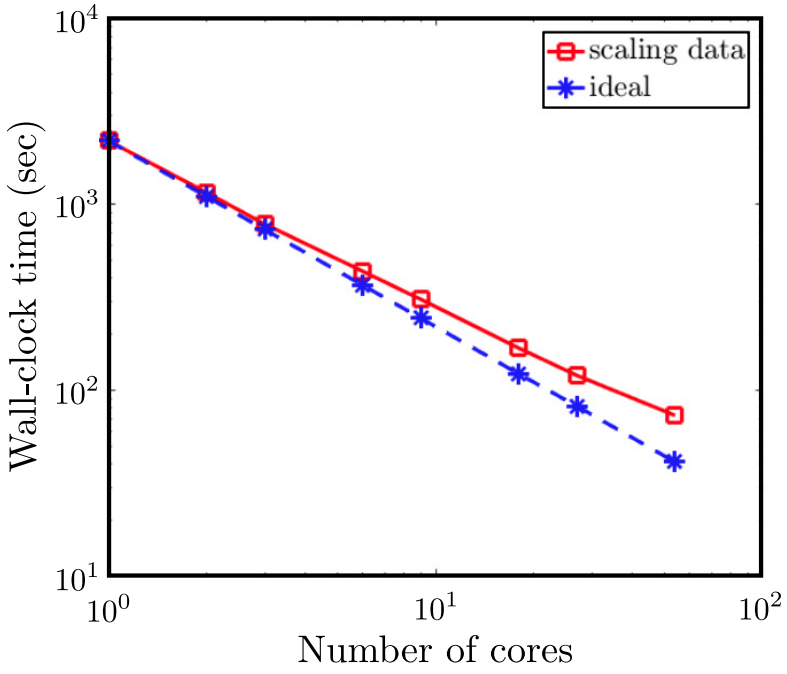



**Figure A.1:** Scaling for benchmark simulations of a single prolate spheroidal capsule in an unbounded simple shear flow. The scaling data were obtained using Comet. It shows that the computational cost decreases approximately linearly with an increasing number of cores.

09-30): SDSC Dell Cluster with Intel Haswell Processors (Comet, 1,433,920 SUs) and SDSC Medium-term disk (Data Oasis, 1000 GB).

### A.0.2 Code performance and scaling

Here we report the scaling of our code for accelerated boundary integral implementation on XSEDE Comet with MPI parallelization, for simulations of both single particles in an unbounded domain and particle suspensions in a bounded domain.

#### Simulations of single particles in an unbounded domain

We first performed benchmark runs with one single slender straight prolate spheroidal capsule (as described in Section 4.2.1) in unbounded simple shear flow with the mem-

brane discretized into 320 elements (resulting in 162 nodes). In this case, the global part of the overall computation is not needed due to the free-space boundary conditions, and the regular Green's function is recovered in the calculation of the local problem. The total load of calculation over all nodes was evenly distributed across a number of MPI processes. The scaling data for 10 strain units of such runs using varying numbers of cores are summarized in FIG. A.1.

**Large-scale simulations of particle suspensions in a bounded domain**

We also considered suspensions with 100 cells (90 healthy RBCs and 10 sickle cells) in a planar pressure-driven flow bounded by two no-slip walls, as described in Section 5.2.1. We set $\alpha = 4$ for all benchmark runs, where $\alpha^{-1}$ represents the length scale beyond which the local solution can be neglected. Again, the membrane of each cell was discretized into 320 elements, resulting in 162 nodes, and the calculation over all nodes was evenly distributed across the assigned MPI processes. The scaling data for 50 time steps of such runs using varying numbers of cores are plotted in FIG. A.2.

**Analysis of code performance and scaling**

As observed in FIGs. A.1 and A.2, for both single cell and suspension simulations, the computational cost decreases monotonically as the number of cores increases. However the scaling degrades. This is mainly a consequence of the overhead caused by the communication among the cores. Also, InfiniBand has to be used to achieve communication among the cores spanning over different nodes when the number of cores is very large, which may lead to a further slowdown compared to the ideal scaling. Thus, as suggested by the scaling data, future simulations of similar systems

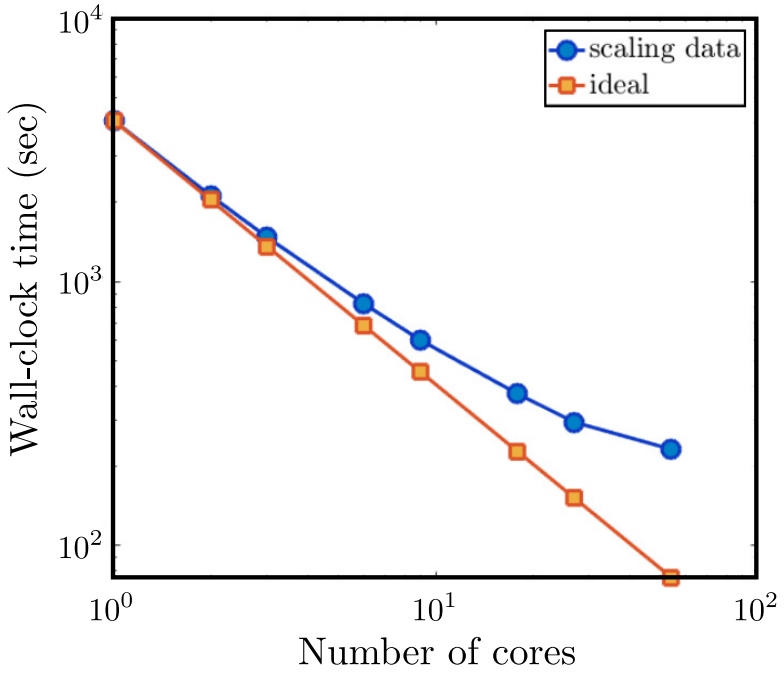



**Figure A.2:** Scaling for benchmark simulations of a suspension of 100 capsules in a bounded domain ($\alpha = 4$). The scaling data were obtained using Comet.

should use 54 cores considering both computational efficiency and resource availability. Besides, the current parallelization should be improved for better performance and scaling of the code.

Furthermore, to achieve an optimal acceleration for large-scale simulations of suspensions in a confined domain, we also performed a benchmarking exercise to find the most efficient way of splitting the total computational load between the local and global parts of the Ewald-sum-like computations. The key parameter that can be used to balance the computation load between these two parts is $\alpha$. As detailed in Section 3.3, the local solution can be neglected beyond a cutoff length $r_{\text{cut}} = 4/\alpha$ away from the pole, and the convergence of the overall solution is guaranteed by setting $\alpha h = 0.5$ ($h$ being the characteristic mesh spacing associated with the global solution).

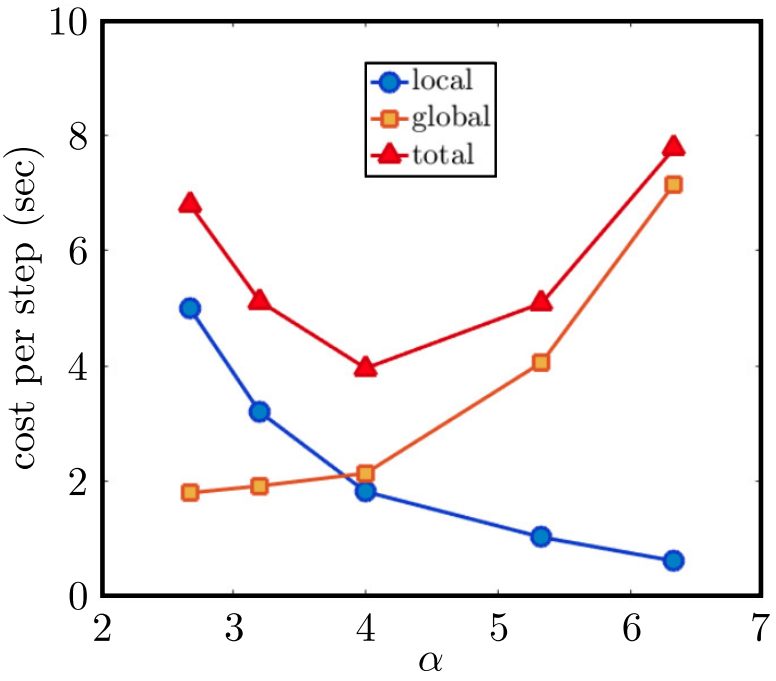



**Figure A.3:** Computational cost per step as a function of $\alpha$ for benchmark simulations of a suspension of 100 capsules in a bounded domain. All data points were obtained using 54 cores on Comet. As $\alpha$ increases, the cost of the local part decreases monotonically, while that of the global part increases monotonically. The total cost is minimal at $\alpha = 4$.

It is easy to see that as $\alpha$ increases, $r_{\text{cut}}$ decreases, meaning a reduced load of computation for the local part, but a finer domain mesh (smaller $h$) is required, resulting in an increase of computation load for the global part. Hence, an optimal value of $\alpha$ can be determined to minimize the computational cost of the overall problem, as shown in FIG. A.3. It suggests that we set $\alpha = 4$ for an optimal acceleration of the computation of the confined particle suspensions while using 54 cores on XSEDE Comet.

# Bibliography

[1] Aarts, P. A., Heethaar, R. M., and Sixma, J. J. (1984). Red blood cell deformability influences platelets–vessel wall interaction in flowing blood. *Blood*, 64(6):1228–1233.

[2] Abbitt, K. B. and Nash, G. B. (2003). Rheological properties of the blood influencing selectin-mediated adhesion of flowing leukocytes. *Am. J. Physiol. Heart Circ. Physiol.*, 285(1):H229–40.

[3] Abe, J. and Berk, B. C. (2014). Novel mechanisms of endothelial mechanotransduction. *Arterioscler. Thromb. Vasc. Biol.*, 34(11):2378–2386.

[4] Abkarian, M., Faivre, M., and Viallat, A. (2007). Swinging of red blood cells under shear flow. *Phys. Rev. Lett.*, 98:188302.

[5] Akimoto, S., Mitsumata, M., Sasaguri, T., and Yoshida, Y. (2000). Laminar shear stress inhibits vascular endothelial cell proliferation by inducing cyclin-dependent kinase inhibitor p21(Sdi1/Cip1/Waf1). *Circ. Res.*, 86(2):185–190.

[6] Alberts, B., Johnson, A., Lewis, J., Raff, M., Roberts, K., and Walter, P. (2007). *Molecular Biology of the Cell*. Garland Science, New York, fifth edition.

[7] Alessandri, K., Sarangi, B. R., Gurchenkov, V. V., Sinha, B., Kießling, T. R., Fetler, L., Rico, F., Scheuring, S., Lamaze, C., Simon, A., Geraldo, S., Vignjević, D., Doméjean, H., Rolland, L., Funfak, A., Bibette, J., Bremond, N., and Nassoy, P. (2013). Cellular capsules as a tool for multicellular spheroid production and for investigating the mechanics of tumor progression in vitro. *Proc. Natl. Acad. Sci. USA*, 110(37):14843–14848.

[8] Allen, M. P. and Tildesley, D. J. (1987). *Computer Simulation of Liquids*. Oxford University Press.

[9] AlMomani, T., Udaykumar, H. S., Marshall, J. S., and Chandran, K. B. (2008). Micro-scale dynamic simulation of erythrocyte-platelet interaction in blood flow. *Ann. Biomed. Eng.*, 36(6):905–920.

[10] Bagchi, P. and Kalluri, R. M. (2009). Dynamics of nonspherical capsules in shear flow. *Phys. Rev. E*, 80:016307.

[11] Bagchi, P. and Kalluri, R. M. (2010). Rheology of a dilute suspension of liquid-filled elastic capsules. *Phys. Rev. E*, 81:056320.

[12] Bagchi, P. and Kalluri, R. M. (2011). Dynamic rheology of a dilute suspension of elastic capsules: Effect of capsule tank-treading, swinging and tumbling. *J. Fluid Mech.*, 669:498–526.

[13] Bao, X., Lu, C., and Frangos, J. A. (1999). Temporal gradient in shear but not steady shear stress induces PDGF-A and MCP-1 expression in endothelial cells: role of NO, NF kappa B, and egr-1. *Arterioscler. Thromb. Vasc. Biol.*, 19(4):996–1003.

[14] Barbee, J. H. and Cokelet, G. R. (1971). The Fahraeus effect. *Microvasc. Res.*, 3(1):6–16.

[15] Barthès-Biesel, D. and Chhim, V. (1981). The constitutive equation of a dilute suspension of spherical microcapsules. *Int. J. Multiph. Flow*, 7(5):493–505.

[16] Barthès-Biesel, D., Diaz, A., and Dhenin, E. (2002). Effect of constitutive laws for two-dimensional membranes on flow-induced capsule deformation. *J. Fluid Mech.*, 460:211–222.

[17] Barthès-Biesel, D. and Rallison, J. M. (1981). The time-dependent deformation of a capsule freely suspended in a linear shear flow. *J. Fluid Mech.*, 113:251–267.

[18] Batchelor, G. K. (1970). The stress system in a suspension of force-free particles. *J. Fluid Mech.*, 41(3):545–570.

[19] Bertles, J. F. and Döbler, J. (1969). Reversible and irreversible sickling: a distinction by electron microscopy. *Blood*, 33(6):884–898.

[20] Bertles, J. F. and Milner, P. F. (1968). Irreversibly sickled erythrocytes: A consequence of the heterogeneous distribution of hemoglobin types in sickle-cell anemia. *J. Clin. Invest.*, 47(8):1731–1741.

[21] Betz, T., Lenz, M., Joanny, J.-F., and Sykes, C. (2009). ATP-dependent mechanics of red blood cells. *Proc. Natl. Acad. Sci. USA*, 106(36):15320–15325.

[22] Bitbol, M. (1986). Red blood cell orientation in orbit C = 0. *Biophys. J.*, 49(5):1055–1068.

[23] Bretherton, F. P. (1962). The motion of rigid particles in a shear flow at low Reynolds number. *J. Fluid Mech.*, 14(2):284–304.

[24] Bugliarello, G. and Hayden, J. W. (1963). Detailed characteristics of the flow of blood in vitro. *Trans. Soc. Rheol.*, 7(1):209–230.

[25] Bunn, H. F. (1997). Pathogenesis and treatment of sickle cell disease. *N. Engl. J. Med.*, 337(11):762–769.

[26] Byun, H., Hillman, T. R., Higgins, J. M., Diez-Silva, M., Peng, Z., Dao, M., Dasari, R. R., Suresh, S., and Park, Y. (2012). Optical measurement of biomechanical properties of individual erythrocytes from a sickle cell patient. *Acta Biomater.*, 8(11):4130–4138.

[27] Canham, P. B. (1970). The minimum energy of bending as a possible explanation of the biconcave shape of the human red blood cell. *J. Theor. Biol.*, 26(1):61 – 81.

[28] Caruso, C., Zhang, X., Sakurai, Y., Li, W., Fay, M. E., Carden, M. A., Myers, D. R., Mannino, R. G., Joiner, C. H., Graham, M. D., and Lam, W. A. (2019). Stiff erythrocyte subpopulations biomechanically induce endothelial inflammation in sickle cell disease. *Blood*, 134(Supplement 1):3560–3560.

[29] Casanova, F. and Santos, L. (2016). Encapsulation of cosmetic active ingredients for topical application – A review. *J. Microencapsul.*, 33(1):1–17.

[30] Champion, J. A. and Mitragotri, S. (2009). Shape induced inhibition of phagocytosis of polymer particles. *Pharm. Res.*, 26(1):244–249.

[31] Chang, T. M., MacIntosh, F. C., and Mason, S. G. (1966). Semipermeable aqueous microcapsules. i. preparation and properties. *Can. J. Physiol. Pharmacol.*, 44(1):115–128.

[32] Charoenphol, P., Huang, R. B., and Eniola-Adefeso, O. (2010). Potential role of size and hemodynamics in the efficacy of vascular-targeted spherical drug carriers. *Biomaterials*, 31(6):1392–1402.

[33] Charrier, J., Shrivastava, S., and Wu, R. (1989). Free and constrained inflation of elastic membranes in relation to thermoforming – non-axisymmetric problems. *J. Strain Anal. Eng. Des.*, 24(2):55–74.

[34] Chen, K. D., Li, Y. S., Kim, M., Li, S., Yuan, S., Chien, S., and Shyy, J. Y. (1999). Mechanotransduction in response to shear stress. Roles of receptor tyrosine kinases, integrins, and Shc. *J. Biol. Chem.*, 274(26):18393–18400.

[35] Chen, Y., Li, D., Li, Y., Wan, J., Li, J., and Chen, H. (2017). Margination of stiffened red blood cells regulated by vessel geometry. *Sci. Rep.*, 7(1):15253.

[36] Chen, Y. L., Graham, M. D., de Pablo, J. J., Jo, K., and Schwartz, D. C. (2005). DNA molecules in microfluidic oscillatory flow. *Macromolecules*, 38(15):6680–6687.

[37] Chien, S. (2007). Mechanotransduction and endothelial cell homeostasis: The wisdom of the cell. *Am. J. Physiol. Heart Circ. Physiol.*, 292(3):H1209–H1224.

[38] Clausen, J. R. and Aidun, C. K. (2010). Capsule dynamics and rheology in shear flow: Particle pressure and normal stress. *Phys. Fluids*, 22(12):123302.

[39] Cordasco, D. and Bagchi, P. (2013). Orbital drift of capsules and red blood cells in shear flow. *Phys. Fluids*, 25(9):091902.

[40] Cordasco, D., Yazdani, A., and Bagchi, P. (2014). Comparison of erythrocyte dynamics in shear flow under different stress-free configurations. *Phys. Fluids*, 26(4):041902.

[41] Crowdy, D. (2016). Flipping and scooping of curved 2D rigid fibers in simple shear: The Jeffery equations. *Phys. Fluids*, 28(5):053105.

[42] Crowl, L. and Fogelson, A. L. (2011). Analysis of mechanisms for platelet near-wall excess under arterial blood flow conditions. *J. Fluid Mech.*, 676:348–375.

[43] Da Cunha, F. and Hinch, E. (1996). Shear-induced dispersion in a dilute suspension of rough spheres. *J. Fluid Mech.*, 309:211–223.

[44] Danker, G., Vlahovska, P. M., and Misbah, C. (2009). Vesicles in Poiseuille flow. *Phys. Rev. Lett.*, 102(14):148102.

[45] Davies, P. F. (1997). Overview: temporal and spatial relationships in shear stress-mediated endothelial signalling. *J. Vasc. Res.*, 34(3):208–211.

[46] Davis, M. E., Cai, H., Drummond, G. R., and Harrison, D. G. (2001). Shear stress regulates endothelial nitric oxide synthase expression through c-Src by divergent signaling pathways. *Circ. Res.*, 89(11):1073–1080.

[47] De Geest, B. G., Sanders, N. N., Sukhorukov, G. B., Demeester, J., and De Smedt, S. C. (2007). Release mechanisms for polyelectrolyte capsules. *Chem. Soc. Rev.*, 36:636–649.

[48] De Keulenaer, G. W., Chappell, D. C., Ishizaka, N., Nerem, R. M., Alexander, R. W., and Griendling, K. K. (1998). Oscillatory and steady laminar shear stress differentially affect human endothelial redox state: role of a superoxide-producing NADH oxidase. *Circ. Res.*, 82(10):1094–1101.

[49] Dean, L. (2005). *Table 1, Complete blood count*. Bethesda (MD): National Center for Biotechnology Information (US).

[50] Degen, P. (2014). Self-propelling capsules as artificial microswimmers. *Curr. Opin. Colloid Interface Sci.*, 19(6):611–619.

[51] Dekker, R. J., van Soest, S., Fontijn, R. D., Salamanca, S., de Groot, P. G., VanBavel, E., Pannekoek, H., and Horrevoets, A. J. G. (2002). Prolonged fluid

shear stress induces a distinct set of endothelial cell genes, most specifically lung Kruppel-like factor (KLF2). *Blood*, 100(5):1689–1698.

[52] Deng, Y., Papageorgiou, D. P., Chang, H., Abidi, S. Z., Li, X., Dao, M., and Karniadakis, G. E. (2019). Quantifying shear-induced deformation and detachment of individual adherent sickle red blood cells. *Biophys. J.*, 116(2):360–371.

[53] Dhont, J. K. G. and Briels, W. J. (2008). Gradient and vorticity banding. *Rheol. Acta*, 47(3):257–281.

[54] Diggs, L. W. and Bibb, J. (1939). The erythrocyte in sickle cell anemia: Morphology, size, hemoglobin content, fragility and sedimentation rate. *JAMA*, 112(8):695–701.

[55] Doddi, S. and Bagchi, P. (2008). Lateral migration of a capsule in a plane Poiseuille flow in a channel. *Int. J. Multiph. Flow*, 34(10):966–986.

[56] Dou, Q. and Ferrone, F. A. (1993). Simulated formation of polymer domains in sickle hemoglobin. *Biophys. J.*, 65(5):2068–2077.

[57] Drochon, A. (2003). Rheology of dilute suspensions of red blood cells: Experimental and theoretical approaches. *Eur. Phys. J. AP*, 22(2):155–162.

[58] Dupire, J., Abkarian, M., and Viallat, A. (2010). Chaotic dynamics of red blood cells in a sinusoidal flow. *Phys. Rev. Lett.*, 104:168101.

[59] Dupire, J., Socol, M., and Viallat, A. (2012). Full dynamics of a red blood cell in shear flow. *Proc. Natl. Acad. Sci. USA*, 109(51):20808–20813.

[60] Dupont, C., Delahaye, F., Barthès-Biesel, D., and Salsac, A.-V. (2016). Stable equilibrium configurations of an oblate capsule in simple shear flow. *J. Fluid Mech.*, 791:738–757.

[61] Dupont, C., Salsac, A., and Barthès-Biesel, D. (2013). Off-plane motion of a prolate capsule in shear flow. *J. Fluid Mech.*, 721:180–198.

[62] Dupont, C., Salsac, A.-V., Barthès-Biesel, D., Vidrascu, M., and Le Tallec, P. (2015). Influence of bending resistance on the dynamics of a spherical capsule in shear flow. *Phys. Fluids*, 27(5):051902.

[63] Eckstein, E. C., Tilles, A. W., and Millero, F. J. (1988). Conditions for the occurrence of large near-wall excess of small particles during blood flow. *Microvasc. Res.*, 36(1):31–39.

[64] Einstein, A. (1911). Berichtigung zu meiner arbeit: "Eine neue bestimmung der moleküldimensionen". *Ann. Phys.*, 339(3):591–592.

[65] Estcourt, L. J., Fortin, P. M., Hopewell, S., Trivella, M., and Wang, W. C. (2017). Blood transfusion for preventing primary and secondary stroke in people with sickle cell disease. *Cochrane. Database Syst. Rev.*, 1:CD003146.

[66] Evans, E. and Fung, Y.-C. (1972). Improved measurements of the erythrocyte geometry. *Microvasc. Res.*, 4(4):335–347.

[67] Evans, E. and Mohandas, N. (1987). Membrane-associated sickle hemoglobin: a major determinant of sickle erythrocyte rigidity. *Blood*, 70(5):1443–1449.

[68] Evans, J., Gratzer, W., Mohandas, N., Parker, K., and Sleep, J. (2008). Fluctuations of the red blood cell membrane: relation to mechanical properties and lack of ATP dependence. *Biophys. J.*, 94(10):4134–4144.

[69] Fåhræus, R. and Lindqvist, T. (1931). The viscosity of the blood in narrow capillary tubes. *Am. J. Physiol.*, 96(3):562–568.

[70] Fay, M. E., Myers, D. R., Kumar, A., Turbyfield, C. T., Byler, R., Crawford, K., Mannino, R. G., Laohapant, A., Tyburski, E. A., Sakurai, Y., Rosenbluth, M. J., Switz, N. A., Sulchek, T. A., Graham, M. D., and Lam, W. A. (2016). Cellular softening mediates leukocyte demargination and trafficking, thereby increasing clinical blood counts. *Proc. Natl. Acad. Sci. USA*, 113(8):1987–1992.

[71] Fedosov, D. A., Caswell, B., and Karniadakis, G. E. (2010a). A multiscale red blood cell model with accurate mechanics, rheology, and dynamics. *Biophys. J.*, 98(10):2215–2225.

[72] Fedosov, D. A., Caswell, B., Popel, A. S., and Karniadakis, G. E. (2010b). Blood flow and cell-free layer in microvessels. *Microcirculation*, 17(8):615–628.

[73] Fedosov, D. A., Fornleitner, J., and Gompper, G. (2012). Margination of white blood cells in microcapillary flow. *Phys. Rev. Lett.*, 108(2):028104.

[74] Fedosov, D. A. and Gompper, G. (2014). White blood cell margination in microcirculation. *Soft Matter*, 10(17):2961–2970.

[75] Fedosov, D. A., Lei, H., Caswell, B., Suresh, S., and Karniadakis, G. E. (2011). Multiscale modeling of red blood cell mechanics and blood flow in malaria. *PLoS Comp. Biol.*, 7(12):e1002270.

[76] Firrell, J. C. and Lipowsky, H. H. (1989). Leukocyte margination and deformation in mesenteric venules of rat. *Am. J. Physiol. Heart Circ. Physiol.*, 256(6):H1667–H1674.

[77] Fischer, T., Stohr-Lissen, M., and Schmid-Schonbein, H. (1978). The red cell as a fluid droplet: Tank tread-like motion of the human erythrocyte membrane in shear flow. *Science*, 202(4370):894–896.

[78] Flyvbjerg, H. and Petersen, H. G. (1989). Error estimates on averages of correlated data. *J. Chem. Phys.*, 91(1):461–466.

[79] Frenette, P. S. (2002). Sickle cell vaso-occlusion: multistep and multicellular paradigm. *Curr. Opin. Hematol.*, 9(2):101–106.

[80] Freund, J. B. (2007). Leukocyte margination in a model microvessel. *Phys. Fluids*, 19(2):023301.

[81] Fung, Y. (1973). Stochastic flow in capillary blood vessels. *Microvasc. Res.*, 5(1):34–48.

[82] Fung, Y. and Zweifach, B. (1971). Microcirculation: mechanics of blood flow in capillaries. *Annu. Rev. Fluid Mech.*, 3(1):189–210.

[83] Fung, Y. C. (1984). *Biodynamics*. Springer New York, New York.

[84] Gao, T., Hu, H. H., and Castañeda, P. P. (2012). Shape dynamics and rheology of soft elastic particles in a shear flow. *Phys. Rev. Lett.*, 108:058302.

[85] Geng, Y., Dalhaimer, P., Cai, S., Tsai, R., Tewari, M., Minko, T., and Discher, D. E. (2007). Shape effects of filaments versus spherical particles in flow and drug delivery. *Nat. Nanotechnol.*, 2:249–255.

[86] Glader, B. E., Lux, S. E., Muller-Soyano, A., Platt, O. S., Propper, R. D., and Nathan, D. G. (1978). Energy reserve and cation composition of irreversibly sickled cell in vivo. *Br. J. Haematol.*, 40(4):527–532.

[87] Goldsmith, H. (1971). Red cell motions and wall interactions in tube flow. *Fed. Proc.*, 30(5):1578–1590.

[88] Goldsmith, H. L., Marlow, J., and MacIntosh, F. C. (1972). Flow behaviour of erythrocytes. I. Rotation and deformation in dilute suspensions. *Proc. R. Soc. Lond., B, Biol. Sci.*, 182(1068):351–384.

[89] Goldsmith, H. L. and Spain, S. (1984). Margination of leukocytes in blood flow through small tubes. *Microvasc. Res.*, 27(2):204–222.

[90] Graham, M. D. (2011). Fluid dynamics of dissolved polymer molecules in confined geometries. *Annu. Rev. Fluid Mech.*, 43:273–298.

[91] Graham, M. D. (2018). *Microhydrodynamics, Brownian Motion, and Complex Fluids*. Cambridge Texts in Applied Mathematics. Cambridge University Press.

[92] Guo, Q., Duffy, S. P., Matthews, K., Deng, X., Santoso, A. T., Islamzada, E., and Ma, H. (2016). Deformability based sorting of red blood cells improves diagnostic sensitivity for malaria caused by plasmodium falciparum. *Lab Chip*, 16:645–654.

[93] Gutierrez, M., Fish, M. B., Golinski, A. W., and Eniola-Adefeso, O. (2018). Presence of rigid red blood cells in blood flow interferes with the vascular wall adhesion of leukocytes. *Langmuir*, 34(6):2363–2372.

[94] Hankins, J. S., Smeltzer, M. P., McCarville, M. B., Aygun, B., Hillenbrand, C. M., Ware, R. E., and Onciu, M. (2010). Patterns of liver iron accumulation

in patients with sickle cell disease and thalassemia with iron overload. *Eur. J. Haematol.*, 85(1):51–57.

[95] Harkness, J. and Whittington, R. B. (1970). Blood-plasma viscosity: An approximate temperature-invariant arising from generalised concepts. *Biorheology*, 6:169–187.

[96] Harrison, D. G., Widder, J., Grumbach, I., Chen, W., Weber, M., and Searles, C. (2006). Endothelial mechanotransduction, nitric oxide and vascular inflammation. *J. Intern. Med.*, 259(4):351–363.

[97] Helfrich, W. (1973). Elastic properties of lipid bilayers: Theory and possible experiments. *Z. Naturforsch C.*, 28(11):693–703.

[98] Henríquez Rivera, R. G., Sinha, K., and Graham, M. D. (2015). Margination regimes and drainage transition in confined multicomponent suspensions. *Phys. Rev. Lett.*, 114(18):188101.

[99] Henríquez Rivera, R. G., Zhang, X., and Graham, M. D. (2016). Mechanistic theory of margination and flow-induced segregation in confined multicomponent suspensions: Simple shear and Poiseuille flows. *Phys. Rev. Fluids*, 1:060501.

[100] Hernandez-Ortiz, J. P., de Pablo, J. J., and Graham, M. D. (2007). Fast computation of many-particle hydrodynamic and electrostatic interactions in a confined geometry. *Phys. Rev. Lett.*, 98(14):140602.

[101] Hinch, E. J. and Leal, L. G. (1979). Rotation of small non-axisymmetric particles in a simple shear flow. *J. Fluid Mech.*, 92(3):591–607.

[102] Hou, H. W., Bhagat, A. A. S., Lin Chong, A. G., Mao, P., Wei Tan, K. S., Han, J., and Lim, C. T. (2010). Deformability based cell margination – A simple microfluidic design for malaria-infected erythrocyte separation. *Lab Chip*, 10:2605–2613.

[103] Hsiai, T. K., Cho, S. K., Wong, P. K., Ing, M., Salazar, A., Sevanian, A., Navab, M., Demer, L. L., and Ho, C.-M. (2003). Monocyte recruitment to endothelial cells in response to oscillatory shear stress. *FASEB J.*, 17(12):1648–1657.

[104] Huang, H., Yang, X., Krafczyk, M., and Lu, X.-Y. (2012). Rotation of spheroidal particles in Couette flows. *J. Fluid Mech.*, 692:369–394.

[105] Hudson, S. (2003). Wall migration and shear-induced diffusion of fluid droplets in emulsions. *Phys. Fluids*, 15(5):1106–1113.

[106] Jain, A. and Munn, L. L. (2009). Determinants of leukocyte margination in rectangular microchannels. *PLoS ONE*, 4(9):e7104.

[107] Jeffery, G. B. (1922). The motion of ellipsoidal particles immersed in a viscous fluid. *Proc. Roy. Soc. London A*, 102:161–179.

[108] Jendrejack, R. M., Schwartz, D. C., de Pablo, J. J., and Graham, M. D. (2004). Shear-induced migration in flowing polymer solutions: Simulation of long-chain dna in microchannels. *J. Chem. Phys.*, 120(5):2513–2529.

[109] Jones, D. A., Munford, J. G., and Gabbott, P. A. (1974). Microcapsules as artificial food particles for aquatic filter feeders. *Nature*, 247(5438):233–235.

[110] Jung, J., Matemba, L. E., Lee, K., Kazyoba, P. E., Yoon, J., Massaga, J. J., Kim, K., Kim, D.-J., and Park, Y. (2016). Optical characterization of red blood cells from individuals with sickle cell trait and disease in Tanzania using quantitative phase imaging. *Sci. Rep.*, 6:31698.

[111] Katanov, D., Gompper, G., and Fedosov, D. A. (2015). Microvascular blood flow resistance: Role of red blood cell migration and dispersion. *Microvasc. Res.*, 99:57–66.

[112] Kaul, D. and Xue, H. (1991). Rate of deoxygenation and rheologic behavior of blood in sickle cell anemia. *Blood*, 77(6):1353–1361.

[113] Kaul, D. K., Chen, D., and Zhan, J. (1994). Adhesion of sickle cells to vascular endothelium is critically dependent on changes in density and shape of the cells. *Blood*, 83(10):3006–3017.

[114] Kaul, D. K. and Fabry, M. E. (2004). In vivo studies of sickle red blood cells. *Microcirculation*, 11(2):153–165.

[115] Kaul, D. K., Fabry, M. E., and Nagel, R. L. (1989). Microvascular sites and characteristics of sickle cell adhesion to vascular endothelium in shear flow conditions: pathophysiological implications. *Proc. Natl. Acad. Sci. USA*, 86(9):3356–3360.

[116] Kaul, D. K., Fabry, M. E., Windisch, P., Baez, S., and Nagel, R. L. (1983). Erythrocytes in sickle cell anemia are heterogeneous in their rheological and hemodynamic characteristics. *J. Clin. Invest.*, 72(1):22–31.

[117] Kelley, W. J., Safari, H., Lopez-Cazares, G., and Eniola-Adefeso, O. (2016). Vascular-targeted nanocarriers: design considerations and strategies for successful treatment of atherosclerosis and other vascular diseases. *WIREs Nanomed. Nanobiotechnol.*, 8:909–926.

[118] Kennedy, M. R., Pozrikidis, C., and Skalak, R. (1994). Motion and deformation of liquid drops, and the rheology of dilute emulsions in simple shear flow. *Comput. Fluids*, 23(2):251–278.

[119] Kessler, S., Finken, R., and Seifert, U. (2008). Swinging and tumbling of elastic capsules in shear flow. *J. Fluid Mech.*, 605:207–226.

[120] Kim, S. and Karrila, S. J. (2013). *Microhydrodynamics: principles and selected applications*. Courier Corporation.

[121] Kumar, A. and Graham, M. D. (2011). Segregation by membrane rigidity in flowing binary suspensions of elastic capsules. *Phys. Rev. E*, 84(6):066316.

[122] Kumar, A. and Graham, M. D. (2012a). Accelerated boundary integral method for multiphase flow in non-periodic geometries. *J. Comput. Phys.*, 231(20):6682–6713.

[123] Kumar, A. and Graham, M. D. (2012b). Margination and segregation in confined flows of blood and other multicomponent suspensions. *Soft Matter*, 8(41):10536–10548.

[124] Kumar, A. and Graham, M. D. (2012c). Mechanism of margination in confined flows of blood and other multicomponent suspensions. *Phys. Rev. Lett.*, 109(10):108102.

[125] Kumar, A. and Graham, M. D. (2015). Cell distribution and segregation phenomena during blood flow. In *Complex Fluids in Biological Systems*, pages 399–435. Springer, New York.

[126] Kumar, A., Henríquez Rivera, R. G., and Graham, M. D. (2014). Flow-induced segregation in confined multicomponent suspensions: Effects of particle size and rigidity. *J. Fluid Mech.*, 738:423–462.

[127] Lanotte, L., Mauer, J., Mendez, S., Fedosov, D. A., Fromental, J.-M., Claveria, V., Nicoud, F., Gompper, G., and Abkarian, M. (2016). Red cells' dynamic morphologies govern blood shear thinning under microcirculatory flow conditions. *Proc. Natl. Acad. Sci. USA*, 113(47):13289–13294.

[128] Laogun, A. A., Ajayi, N. O., Osamo, N. O., and Okafor, L. A. (1980). Plasma viscosity in sickle-cell anaemia. *Clin. Phys. Physiol. Meas.*, 1(2):145.

[129] Le, D.-V. and Tan, Z. (2010). Large deformation of liquid capsules enclosed by thin shells immersed in the fluid. *J. Comput. Phys.*, 229:4097–4116.

[130] Leal, L. (1980). Particle motions in a viscous fluid. *Annu. Rev. Fluid Mech.*, 12(1):435–476.

[131] Lei, H. and Karniadakis, G. E. (2012a). Predicting the morphology of sickle red blood cells using coarse-grained models of intracellular aligned hemoglobin polymers. *Soft Matter*, 8:4507–4516.

[132] Lei, H. and Karniadakis, G. E. (2012b). Quantifying the rheological and hemodynamic characteristics of sickle cell anemia. *Biophys. J.*, 102(2):185–194.

[133] Lei, H. and Karniadakis, G. E. (2013). Probing vasoocclusion phenomena in sickle cell anemia via mesoscopic simulations. *Proc. Natl. Acad. Sci. USA*, 110(28):11326–11330.

[134] Lei, H. and Karniadakis, G. E. (2015). *Multiscale Modeling of Sickle Cell Anemia*, pages 119–156. Springer International Publishing.

[135] Levy, M. C., Lefebvre, S., Andry, M. C., and Manfait, M. (1995). Fourier transform infrared spectroscopic studies of cross-linked human serum albumin microcapsules. 3. Influence of terephthaloyl chloride concentration on spectra and correlation with microcapsule morphology and size. *J. Pharm. Sci.*, 84(2):161–165.

[136] Levy, M. C., Lefebvre, S., Andry, M. C., Rahmouni, M., and Manfait, M. (1994). Fourier-transform infrared spectroscopic studies of cross-linked human serum albumin microcapsules. 2. Influence of reaction time on spectra and correlation with microcapsule morphology and size. *J. Pharm. Sci.*, 83(3):419–422.

[137] Levy, M.-C., Rahmouni, M., Andry, M.-C., Lefebvre, S., and Manfait, M. (1991). Fourier transform infrared spectroscopic studies of human serum albumin microcapsules prepared by interfacial cross-linking with terephthaloylchloride: Influence of polycondensation pH on spectra and relation with microcapsule morphology and size. *J. Pharm. Sci.*, 80(6):578–585.

[138] Li, X., Caswell, B., and Karniadakis, G. E. (2012). Effect of chain chirality on the self-assembly of sickle hemoglobin. *Biophys. J.*, 103(6):1130–1140.

[139] Li, X., Dao, M., Lykotrafitis, G., and Karniadakis, G. E. (2017). Biomechanics and biorheology of red blood cells in sickle cell anemia. *J. Biomech.*, 50:34–41.

[140] Li, Y.-S. J., Haga, J. H., and Chien, S. (2005). Molecular basis of the effects of shear stress on vascular endothelial cells. *J. Biomech.*, 38(10):1949–1971.

[141] Lipowsky, H. H. (2013). In vivo studies of blood rheology in the microcirculation in an in vitro world: Past, present and future. *Biorheology*, 50(1-2):3–16.

[142] Lipowsky, H. H., Usami, S., and Chien, S. (1980). In vivo measurements of "apparent viscosity" and microvessel hematocrit in the mesentery of the cat. *Microvasc. Res.*, 19(3):297–319.

[143] Loiseau, E., Massiera, G., Mendez, S., Martinez, P. A., and Abkarian, M. (2015). Microfluidic study of enhanced deposition of sickle cells at acute corners. *Biophys. J.*, 108(11):2623–2632.

[144] Lu, L., Li, X., Vekilov, P. G., and Karniadakis, G. E. (2016). Probing the twisted structure of sickle hemoglobin fibers via particle simulations. *Biophys. J.*, 110(9):2085–2093.

[145] Luo, Z. and Bai, B. (2016). Dynamics of nonspherical compound capsules in simple shear flow. *Phys. Fluids*, 28(10):101901.

[146] Ma, H. and Graham, M. (2005). Theory of shear-induced migration in dilute polymer solutions near solid boundaries. *Phys. Fluids*, 17:083103.

[147] Madigan, C. and Malik, P. (2006). Pathophysiology and therapy for haemoglobinopathies. Part I: sickle cell disease. *Expert Rev. Mol. Med.*, 8(9):1–23.

[148] Makino, M. and Sugihara-Seki, M. (2013). Segregation by size difference in binary suspensions of fluid droplets in channel flow. *Biorheology*, 50:149–163.

[149] Mao, W. and Alexeev, A. (2014). Motion of spheroidal particles in shear flow with inertia. *J. Fluid Mech.*, 749:145–166.

[150] Masuda, K. (2011). Development of a drug delivery system using microcapsules with ultrasound. *Biocybern. Biomed. Eng.*, 31(2):23–32.

[151] Mehrabadi, M., Ku, D. N., and Aidun, C. K. (2015). A continuum model for platelet transport in flowing blood based on direct numerical simulations of cellular blood flow. *Ann. Biomed. Eng.*, 43(6):1410–1421.

[152] Mehrabadi, M., Ku, D. N., and Aidun, C. K. (2016). Effects of shear rate, confinement, and particle parameters on margination in blood flow. *Phys. Rev. E*, 93:023109.

[153] Mendez, S. and Abkarian, M. (2018). In-plane elasticity controls the full dynamics of red blood cells in shear flow. *Phys. Rev. Fluids*, 3:101101.

[154] Messer, M. J. and Harris, J. W. (1970). Filtration characteristics of sickle cells: Rates of alteration of filterability after deoxygenation and reoxygenation, and correlations with sickling and unsickling. *J. Lab. Clin. Med.*, 76(4):537–547.

[155] Meyer, M., Desbrun, M., Schroeder, P., and Barr, A. H. (2002). Discrete differential geometry operators for triangulated 2-manifolds. *Visualization and Mathematics*, 3:34–57.

[156] Mills, J. P., Qie, L., Dao, M., Lim, C. T., and Suresh, S. (2004). Nonlinear elastic and viscoelastic deformation of the human red blood cell with optical tweezers. *Mech. Chem. Biosyst.*, 1:169–180.

[157] Minetti, C., Audemar, V., Podgorski, T., and Coupier, G. (2019). Dynamics of a large population of red blood cells under shear flow. *J. Fluid Mech.*, 864:408–448.

[158] Minneci, P. C., Deans, K. J., Zhi, H., Yuen, P. S. T., Star, R. A., Banks, S. M., Schechter, A. N., Natanson, C., Gladwin, M. T., and Solomon, S. B. (2005). Hemolysis-associated endothelial dysfunction mediated by accelerated NO inactivation by decompartmentalized oxyhemoglobin. *J. Clin. Invest.*, 115(12):3409–3417.

[159] Möbius, M. E., Lauderdale, B. E., Nagel, S. R., and Jaeger, H. M. (2001). Brazil-nut effect: Size separation of granular particles. *Nature*, 414(6861):270–270.

[160] Mohammadigoushki, H. and Feng, J. J. (2013). Size segregation in sheared two-dimensional polydisperse foam. *Langmuir*, 29(5):1370–1378.

[161] Mohandas, N. and Evans, E. (1994). Mechanical properties of the red cell membrane in relation to molecular structure and genetic defects. *Annu. Rev. Biophys. Biomol. Struct.*, 23(1):787–818.

[162] Mueller, S., Llewellin, E. W., and Mader, H. M. (2010). The rheology of suspensions of solid particles. *P. Roy. Soc. A-Math. Phy.*, 466(2116):1201–1228.

[163] Namdee, K., Thompson, A. J., Charoenphol, P., and Eniola-Adefeso, O. (2013). Margination propensity of vascular-targeted spheres from blood flow in a microfluidic model of human microvessels. *Langmuir*, 29(8):2530–2535.

[164] Namgung, B. and Kim, S. (2014). Effect of uneven red cell influx on formation of cell-free layer in small venules. *Microvasc. Res.*, 92:19–24.

[165] Namgung, B., Ng, Y. C., Leo, H. L., Rifkind, J. M., and Kim, S. (2017). Near-wall migration dynamics of erythrocytes in vivo: Effects of cell deformability and arteriolar bifurcation. *Front. Physiol.*, 8:653.

[166] Narsimhan, V., Zhao, H., and Shaqfeh, E. S. G. (2013). Coarse-grained theory to predict the concentration distribution of red blood cells in wall-bounded Couette flow at zero Reynolds number. *Phys. Fluids*, 25(6):061901.

[167] Nash, G., Johnson, C., and Meiselman, H. (1984). Mechanical properties of oxygenated red blood cells in sickle cell (HbSS) disease. *Blood*, 63(1):73–82.

[168] Ng, Y. C., Fisher, L. K., Salim, V., Kim, S., and Namgung, B. (2016). Visualization and quantification of the cell-free layer in arterioles of the rat cremaster muscle. *JoVE*, (116):e54550.

[169] Nieswandt, B., Aktas, B., Moers, A., and Sachs, U. (2005). Platelets in atherothrombosis: lessons from mouse models. *J. Thromb. Haemost.*, 3(8):1725–1736.

[170] Omori, T., Imai, Y., Yamaguchi, T., and Ishikawa, T. (2012). Reorientation of a nonspherical capsule in creeping shear flow. *Phys. Rev. Lett.*, 108:138102.

[171] Otto, O., Rosendahl, P., Mietke, A., Golfier, S., Herold, C., Klaue, D., Girardo, S., Pagliara, S., Ekpenyong, A., Jacobi, A., Wobus, M., Töpfner, N., Keyser, U. F., Mansfeld, J., Fischer-Friedrich, E., and Guck, J. (2015). Real-time deformability cytometry: on-the-fly cell mechanical phenotyping. *Nature Methods*, 12(3):199–202.

[172] Papageorgiou, D. P., Abidi, S. Z., Chang, H., Li, X., Kato, G. J., Karniadakis, G. E., Suresh, S., and Dao, M. (2018). Simultaneous polymerization and adhesion under hypoxia in sickle cell disease. *Proc. Natl. Acad. Sci. USA*, 115(38):9473–9478.

[173] Pappano, A. J. and Wier, W. G. (2013). 8 - the microcirculation and lymphatics. In *Cardiovascular Physiology*, pages 153–170. Content Repository Only!, Philadelphia, tenth edition edition.

[174] Pauling, L., Itano, H. A., Singer, S. J., and Wells, I. C. (1949). Sickle cell anemia, a molecular disease. *Science*, 110(2865):543–548.

[175] Pearson, M. and Lipowsky, H. (2000). Influence of erythrocyte aggregation on leukocyte margination in postcapillary venules of rat mesentery. *Am. J. Physiol.: Heart Circ. Physiol.*, 279(4):H1460–H1471.

[176] Peng, Z., Asaro, R. J., and Zhu, Q. (2011). Multiscale modelling of erythrocytes in Stokes flow. *J. Fluid Mech.*, 686:299–337.

[177] Peng, Z., Mashayekh, A., and Zhu, Q. (2014). Erythrocyte responses in low-shear-rate flows: Effects of non-biconcave stress-free state in the cytoskeleton. *J. Fluid Mech.*, 742:96–118.

[178] Pozrikidis, C. (1992). *Boundary integral and singularity methods for linearized viscous flow*. Cambridge Texts in Applied Mathematics. Cambridge University Press.

[179] Pozrikidis, C. (1995). Finite deformation of liquid capsules enclosed by elastic membranes in simple shear flow. *J. Fluid Mech.*, 297:123–152.

[180] Pozrikidis, C. (2003). Numerical simulation of the flow-induced deformation of red blood cells. *Ann. Biomed. Eng.*, 31(10):1194–1205.

[181] Pranay, P., Henríquez Rivera, R. G., and Graham, M. D. (2012). Depletion layer formation in suspensions of elastic capsules in Newtonian and viscoelastic fluids. *Phys. Fluids*, 24(6):061902.

[182] Pries, A. R. and Secomb, T. W. (2005). Microvascular blood viscosity in vivo and the endothelial surface layer. *Am. J. Physiol. Heart Circ. Physiol.*, 289(6):H2657–H2664.

[183] Pries, A. R., Secomb, T. W., and Gaehtgens, P. (1996). Biophysical aspects of blood flow in the microvasculature. *Cardiovasc. Res.*, 32(4):654–667.

[184] Qi, Q. M. and Shaqfeh, E. S. G. (2017). Theory to predict particle migration and margination in the pressure-driven channel flow of blood. *Phys. Rev. Fluids*, 2:093102.

[185] Ramanujan, S. and Pozrikidis, C. (1998). Deformation of liquid capsules enclosed by elastic membranes in simple shear flow: large deformations and the effect of fluid viscosities. *J. Fluid Mech.*, 361:117–143.

[186] Reasor, D. A., Mehrabadi, M., Ku, D. N., and Aidun, C. K. (2013). Determination of critical parameters in platelet margination. *Ann. Biomed. Eng.*, 41(2):238–249.

[187] Reiter, C. D., Wang, X., Tanus-Santos, J. E., Hogg, N., Cannon, R. O., Schechter, A. N., and Gladwin, M. T. (2002). Cell-free hemoglobin limits nitric oxide bioavailability in sickle-cell disease. *Nat. Med.*, 8(12):1383–1389.

[188] Rosen, T., Lundell, F., and Aidun, C. K. (2014). Effect of fluid inertia on the dynamics and scaling of neutrally buoyant particles in shear flow. *J. Fluid Mech.*, 738:563–590.

[189] Sarelius, I. H. and Duling, B. R. (1982). Direct measurement of microvessel hematocrit, red cell flux, velocity, and transit time. *Am. J. Physiol. Heart Circ. Physiol.*, 243(6):H1018–H1026.

[190] Schaer, D. J., Buehler, P. W., Alayash, A. I., Belcher, J. D., and Vercellotti, G. M. (2013). Hemolysis and free hemoglobin revisited: exploring hemoglobin and hemin scavengers as a novel class of therapeutic proteins. *Blood*, 121(8):1276–1284.

[191] Schneeweiss, I. and Rehage, H. (2005). Non-spherical capsules for the food industry. *Chem. Ing. Tech.*, 77(3):236–239.

[192] Shen, S. C., Fleming, E. M., and Castle, W. B. (1949). Studies on the destruction of red blood cells: V. irreversibly sickled erythrocytes: Their experimental production in vitro. *Blood*, 4(5):498–504.

[193] Shevkoplyas, S., Yoshida, T., Munn, L., and Bitensky, M. (2005). Biomimetic autoseparation of leukocytes from whole blood in a microfluidic device. *Anal. Chem.*, 77(3):933–937.

[194] Sinha, K. and Graham, M. D. (2015). Dynamics of a single red blood cell in simple shear flow. *Phys. Rev. E*, 92:042710.

[195] Sinha, K. and Graham, M. D. (2016). Shape-mediated margination and demargination in flowing multicomponent suspensions of deformable capsules. *Soft Matter*, 12:1683–1700.

[196] Skalak, R., Ozkaya, N., and Skalak, T. C. (1989). Biofluid mechanics. *Annu. Rev. Fluid Mech.*, 21(1):167–200.

[197] Skalak, R., Tozeren, A., Zarda, R. P., and Chien, S. (1973). Strain energy function of red blood-cell membranes. *Biophys. J.*, 13(3):245–280.

[198] Skotheim, J. M. and Secomb, T. W. (2007). Red blood cells and other nonspherical capsules in shear flow: Oscillatory dynamics and the tank-treading-to-tumbling transition. *Phys. Rev. Lett.*, 98:078301.

[199] Smart, J. R. and Leighton, D. T. (1991). Measurement of the drift of a droplet due to the presence of a plane. *Phys. Fluids A Fluid Dynam.*, 3(1):21–28.

[200] Sorescu, G. P., Song, H., Tressel, S. L., Hwang, J., Dikalov, S., Smith, D. A., Boyd, N. L., Platt, M. O., Lassegue, B., Griendling, K. K., and Jo, H. (2004). Bone morphogenic protein 4 produced in endothelial cells by oscillatory shear stress induces monocyte adhesion by stimulating reactive oxygen species production from a nox1-based NADPH oxidase. *Circ. Res.*, 95(8):773–779.

[201] Spann, A. P., Campbell, J. E., Fitzgibbon, S. R., Rodriguez, A., Cap, A. P., Blackbourne, L. H., and Shaqfeh, E. S. G. (2016). The effect of hematocrit on platelet adhesion: Experiments and simulations. *Biophys. J.*, 111(3):577–588.

[202] Sparkenbaugh, E. and Pawlinski, R. (2013). Interplay between coagulation and vascular inflammation in sickle cell disease. *Br. J. Haematol.*, 162(1):3–14.

[203] Subramanian, G. and Koch, D. L. (2006). Inertial effects on the orientation of nearly spherical particles in simple shear flow. *J. Fluid Mech.*, 557:257–296.

[204] Sui, Y., T. Low, H., T. Chew, Y., and Roy, P. (2008). Tank-treading, swinging, and tumbling of liquid-filled elastic capsules in shear flow. *Phys. Rev. E Stat. Nonlin. Soft Matter Phys.*, 77:016310.

[205] Sun, C. and Munn, L. (2006). Influence of erythrocyte aggregation on leukocyte margination in postcapillary expansions: A lattice Boltzmann analysis. *Physica A*, 362(1):191–196.

[206] Sutera, S. P. and Skalak, R. (1993). The history of Poiseuille's law. *Annu. Rev. Fluid Mech.*, 25:1–19.

[207] Svanes, K. and Zweifach, B. (1968). Variations in small blood vessel hematocrits produced in hypothermic rats by micro-occlusion. *Microvasc. Res.*, 1(2):210–220.

[208] Takeishi, N., Rosti, M. E., Imai, Y., Wada, S., and Brandt, L. (2019). Haemorheology in dilute, semi-dilute and dense suspensions of red blood cells. *J. Fluid Mech.*, 872:818–848.

[209] Tangelder, G. J., Teirlinck, H. C., Slaaf, D. W., and Reneman, R. S. (1985). Distribution of blood platelets flowing in arterioles. *Am. J. Physiol. Heart Circ. Physiol.*, 248(3):H318–H323.

[210] Tatsumi, K., Noguchi, S., Tatsumi, A., Kuriyama, R., and Nakabe, K. (2019). Particle and rigidized red blood cell concentration distributions in microchannel flows. *Phys. Fluids*, 31(8):082006.

[211] Taylor, J. G., Nolan, V. G., Mendelsohn, L., Kato, G. J., Gladwin, M. T., and Steinberg, M. H. (2008). Chronic hyper-hemolysis in sickle cell anemia: association of vascular complications and mortality with less frequent vasoocclusive pain. *PLoS One*, 3(5):e2095–e2095.

[212] Thompson, A. J. and Eniola-Adefeso, O. (2015). Dense nanoparticles exhibit enhanced vascular wall targeting over neutrally buoyant nanoparticles in human blood flow. *Acta biomater.*, 21:99–108.

[213] Thompson, A. J., Mastria, E. M., and Eniola-Adefeso, O. (2013). The margination propensity of ellipsoidal micro/nanoparticles to the endothelium in human blood flow. *Biomaterials*, 34(23):5863–5871.

[214] Vahidkhah, K., Diamond, S. L., and Bagchi, P. (2014). Platelet dynamics in three-dimensional simulation of whole blood. *Biophys. J.*, 106(11):2529–2540.

[215] Villone, M. M., D'Avino, G., Hulsen, M. A., and Maffettone, P. L. (2015). Dynamics of prolate spheroidal elastic particles in confined shear flow. *Phys. Rev. E*, 92:062303.

[216] Walter, J., Salsac, A., and Barthès-Biesel, D. (2011). Ellipsoidal capsules in simple shear flow: Prolate versus oblate initial shapes. *J. Fluid Mech.*, 676:318–347.

[217] Wang, J., Tozzi, E. J., Graham, M. D., and Klingenberg, D. J. (2012). Flipping, scooping, and spinning: Drift of rigid curved nonchiral fibers in simple shear flow. *Phys. Fluids*, 24(12):123304.

[218] Wang, Z., Sui, Y., Spelt, P. D. M., and Wang, W. (2013). Three-dimensional dynamics of oblate and prolate capsules in shear flow. *Phys. Rev. E*, 88:053021.

[219] Wootton, D. M. and Ku, D. N. (1999). Fluid mechanics of vascular systems, diseases, and thrombosis. *Annu. Rev. Biomed. Eng.*, 1(1):299–329.

[220] Xu, M., Papageorgiou, D. P., Abidi, S. Z., Dao, M., Zhao, H., and Karniadakis, G. E. (2017). A deep convolutional neural network for classification of red blood cells in sickle cell anemia. *PLoS Comp. Bio.*, 13(10):1–27.

[221] Yarin, A. L., Gottlieb, O., and Roisman, I. V. (1997). Chaotic rotation of triaxial ellipsoids in simple shear flow. *J. Fluid Mech.*, 340:83–100.

[222] Yawn, B. P., Buchanan, G. R., Afenyi-Annan, A. N., Ballas, S. K., Hassell, K. L., James, A. H., Jordan, L., Lanzkron, S. M., Lottenberg, R., Savage, W. J., Tanabe, P. J., Ware, R. E., Murad, M. H., Goldsmith, J. C., Ortiz, E., Fulwood, R., Horton, A., and John-Sowah, J. (2014). Management of sickle cell disease: Summary of the 2014 evidence-based report by expert panel members. *JAMA*, 312(10):1033–1048.

[223] Yazdani, A. Z. K. and Bagchi, P. (2011). Phase diagram and breathing dynamics of a single red blood cell and a biconcave capsule in dilute shear flow. *Phys. Rev. E*, 84:026314.

[224] Yazdani, A. Z. K., Kalluri, R. M., and Bagchi, P. (2011). Tank-treading and tumbling frequencies of capsules and red blood cells. *Phys. Rev. E*, 83:046305.

[225] Yeh, C. and Eckstein, E. (1994). Transient lateral transport of platelet-sized particles in flowing blood suspensions. *Biophys. J.*, 66(5):1706–1716.

[226] Yu, Z., Phan-Thien, N., and Tanner, R. I. (2007). Rotation of a spheroid in a Couette flow at moderate Reynolds numbers. *Phys. Rev. E*, 76:026310.

[227] Zan, X., Garapaty, A., and Champion, J. A. (2015). Engineering polyelectrolyte capsules with independently controlled size and shape. *Langmuir*, 31(27):7601–7608.

[228] Zhang, X. and Graham, M. D. (2019). Multiplicity of stable orbits for deformable prolate capsules in shear flow. *arXiv*, physics.flu-dyn.

[229] Zhang, X., Lam, W. A., and Graham, M. D. (2019). Dynamics of deformable straight and curved prolate capsules in simple shear flow. *Phys. Rev. Fluids*, 4:043103.

[230] Zhao, H. and Shaqfeh, E. S. G. (2011). Shear-induced platelet margination in a microchannel. *Phys. Rev. E*, 83(6):061924.

[231] Zhao, H., Shaqfeh, E. S. G., and Narsimhan, V. (2012). Shear-induced particle migration and margination in a cellular suspension. *Phys. Fluids*, 24(1):011902.

[232] Zucker, R. and Cameron, B. F. (1976). Separation of irreversibly sickled cells (ISC) from blood of sickle cell anemia patients. *Biochem. Med.*, 15(1):10–16.

[233] Zurita-Gotor, M., Bławzdziewicz, J., and Wajnryb, E. (2012). Layering instability in a confined suspension flow. *Phys. Rev. Lett.*, 108:068301.